

CHAPTER 4. RESERVOIR CHARACTERIZATION

Alan P. Byrnes, Martin K. Dubois, and John H. Doveton

Introduction

As noted, the general workflow for developing the Hugoton geomodel shown in Figure 1.1 can be characterized as comprising four principal steps: 1) Compile data for stratigraphy (formation tops) and core lithologic properties, petrophysical properties, wireline logs, fluid properties, and production and analyze data to certify that the data meet quality and accuracy criteria; 2) Define properties/develop algorithms comprising training of a neural network, predicting lithofacies at node wells, developing wireline-log analysis algorithms (including corrections), and petrophysical properties algorithms (e.g., permeability-porosity (k - ϕ), capillary pressure (P_c), relative permeability(k_r)), 3) Develop databases of properties for use in geomodel construction including lithofacies, porosity, tops, free-water level at node wells, and 4) Develop geomodel by constructing 3-D cellular model using tops database, populating node-well cells with lithofacies and porosity database properties, upscaling properties as appropriate, and populating 3-D model with basic properties, then utilizing petrophysical algorithms, populate 3-D cellular model with lithofacies-specific petrophysical properties and fluid saturations.

To perform steps 2 and 3, it is necessary to have measured or predicted lithofacies at node wells and to use a numerical description system of lithofacies. The digital rock classification system developed for Hugoton rocks is discussed in section 4.1. Steps 2 and 3 involve the development of equations that can provide lithofacies-specific petrophysical properties from widely available data. Section 4.2 discusses the petrophysical properties of Hugoton rocks and the equations developed to predict reservoir porosity, permeability, and water saturation that were used to populate the geomodel. Because wireline-log analysis of porosity and fluid saturations in the Hugoton field is complicated by a variety of formation properties in the Chase and Council Grove Groups, section 4.3 discusses interpretation of wireline-log response.

4.1 LITHOFACIES CLASSIFICATION

Martin K. Dubois and Alan P. Byrnes

Because petrophysical properties vary among lithofacies, the population of cells with lithofacies is fundamental to reservoir characterization and the construction of a cellular-reservoir model. Lithofacies defined in this study are based on visual examination of 6756 ft (2060 m) of continuous core from 28 wells (Figure 4.1.1) with the aid of a binocular microscope and several hundred thin sections and thin-section photomicrographs contributed by partners in the project. Cores from a set of approximately 100 continuous cores were selected for lithofacies analysis on the basis of length (longest selected), geographic position (sampling distribution), and availability of core-analysis and wire-line log data (Figure 4.1.1). In most cases, selected cores included either the entire Chase (12) or Council Grove (11) interval, or covered both intervals (5). Lithofacies from core, associated wire-line log variables, and geologic-constraining

variables served as the training data for neural-network models used to estimate lithofacies in wells without core but having appropriate wire-line log curves (Chapter 6, section 6.3). In training neural networks, we found that the log-curve suite typical of wells since the early 1970's (neutron and density porosity, gamma ray and resistivity) was appropriate for successful use of neural networks in lithofacies prediction. Having a photoelectric curve improves accuracy and was used when available.

Lithofacies Class Boundaries

Determining the number of lithofacies classes and the criteria for defining classes involved four objectives: (1) maximum number of lithofacies recognizable by neural networks using petrophysical wire-line log curves and other variables; (2) minimum number of lithofacies needed to accurately represent lithologic and petrophysical heterogeneity; (3) maximum distinction of core-petrophysical properties among classes; and 4) relative contribution of a lithofacies class to storage and flow. An optimal solution using these criteria resulted in 11 lithofacies. Additional lithofacies (splitting the lithofacies spectrum more finely) adds error to lithofacies prediction by neural networks and a reduction in the model reliability. Fewer lithofacies (lumping) reduces error, but reduces the utility of the model (Figure 4.1.2) in discriminating lithofacies (and properties) in a heterogeneous system.

Lithofacies were distinguished primarily on the basis of rock type (siliciclastic or carbonate), texture (Folk, 1954), grain size for siliciclastics and Dunham (1962) classification for carbonates, and principal pore size (visual estimate). In classifying dolomite rocks we did not consider depositional texture but rather the present texture and pore size, which is primarily a function of crystal size and the presence or absence of molds of leached carbonate grains. Classes based on differences in core-petrophysical properties coincided well with major lithofacies classes of rocks and have fairly distinctive wire-line log response to petrophysical properties, the principal variables used for neural network prediction of lithofacies. Although defining more classes might have improved petrophysical prediction accuracy, the inability of neural networks to effectively distinguish finer lithofacies classes discouraged finer class distinctions (e.g.: discriminating between fine-grained packstone and coarse-grained packstone).

Digital Classification System

A quantitative, digital-lithofacies description system (Table 4.1.1) was utilized in describing core at half-foot intervals. Three of the five factors illustrated in the tables were sufficient to segregate lithofacies classes (Table 4.1.2); however, other digits were considered initially in the process of determining class boundaries. For each interval a total of up to 12 variables were recorded (Table 4.1.3). Seven other attributes recorded in addition to those in Table 4.1.1 included: degree of consolidation and fracturing, subsidiary pore size, cement mineralogy, bedding, water depth, faunal assemblage, and color. Classifying lithofacies in a digital form facilitated changes in classification criteria

and correlation of lithofacies with core and log petrophysical properties involved in the iterative process of determining optimal lithofacies class boundaries. This digital system is designed to provide a continuous numerical classification that corresponds to the continuum in lithologic and petrophysical properties. In using this system rather than a mnemonic system, error in classifying a given sample is generally only one class up or down and therefore the predicted property values are within a class step up or down from the true value. Once an object is numerically classified, mapping to alternate classification schemes can be performed automatically.

Numbers were assigned to lithofacies in a hierarchy taking into consideration gross depositional environment (continental or marine), texture (relative proportion of mud to grains), and properties (permeability-porosity (k-phi) relationship, where higher permeability for a given porosity is considered good). Continental lithofacies are L0, L1, and L2 with grain-mud ratio (and property quality) decreasing with higher number. Marine lithofacies L4 to L9 are carbonate and the grain-mud ratio and property quality trend are reversed with the ratio generally increasing (properties improving) with a higher lithofacies number. Marine lithofacies L3 and L10 are siliciclastic, and, to distinguish them from the marine carbonates, they were placed at the ends of the carbonate spectrum according to their properties and mud content. The hierarchy is not perfect. For example, marine sandstone k-phi relationship would place it near L6 or L7 in a hierarchy based solely on properties.

Model Lithofacies Classes

Examples of the 11 major lithofacies classes are shown in Figures 4.1.3 and 4.1.4. Common sub-classes are represented, but the examples illustrated do not show the range exhibited by a lithofacies. For example, the “marine carbonate packstone, packstone-grainstone-grainstone class (L7)” includes rocks having a variety of principal grain types and grain size but were deposited in a variety of environments (e.g., fine-grained pellets - tidal flat and lagoon, peloid and oncoids - restricted shelf and shoals, bioclasts - open shelf and shoals). Relative proportions of the 11 lithofacies in 6756 ft of core described in this study are shown in Figure 4.1.5. Continental lithofacies comprising fine-grained sandstones (L0), coarse siltstones (L1), and fine or shaly siltstones (L2) represent 36% of the rock volume whereas marine carbonates and marine siliciclastics represents 49% and 15%, respectively. Lithofacies with the greatest storage and flow capacity in marine rocks include L6 through L10, consistent with the principal reservoir lithofacies defined in previous studies (Siemers and Ahr, 1990; Olson et al., 1996, 1997; Heyer, 1999). These lithofacies represent 37% of the rock volume (Figure 4.1.5) and include very fine crystalline dolomite (L6), fine-medium crystalline dolomite (L9) with grain-moldic porosity, and lithofacies with grain-supported texture including packstone-grainstone (L7), grainstone and marine sandstone (L10), and phylloid algal bafflestone (L8). Continental, fine-grained sandstones represent only 4% of the rock volume, but are important to flow and storage in the Council Grove, especially near the west updip margin of the field in Kansas. All 11 lithofacies are present in the Chase Group, but continental sandstones and very fine crystalline, sucrosic dolomites are less common than

in the Council Grove. Coarser crystalline dolomite with grain-moldic porosity, typically dolomitized-bioclastic or ooid grainstone or packstone, is absent and marine sandstone is rare in the Council Grove. The very fine crystalline dolomite is interpreted to have originally been mud-rich carbonate, for the most part.

References

Dubois, M. K., Byrnes, A. P., Bohling, G. C., Seals, S. C., and Doveton, J. H., 2003, Statistically-based lithofacies predictions for 3-D reservoir modeling: examples from the Panoma (Council Grove) field, Hugoton embayment, southwest Kansas (abs): Proceedings American Association of Petroleum Geologists 2003 Annual Convention, Salt Lake City, Utah, v. 12, p. A44, and Kansas Geological Survey, Open-file Report 2003-30, 3 panels, <http://www.kgs.ku.edu/PRS/publication/2003/ofr2003-30/index.html> (accessed August 23, 2006).

Dunham, R. J., 1962, Classification of carbonate rocks according to depositional texture, *in*, W. E. Ham, ed., Classification of Carbonate Rocks: Tulsa, American Association of Petroleum Geologists, Memoir 1, p. 108-121.

Folk, R. L., 1954, The distinction between grain size and mineral composition in sedimentary rock nomenclature: *Journal of Geology*, v. 62, p. 344-359.

Heyer, J. F., 1999, Reservoir characterization of the Council Grove Group, Texas County, Oklahoma, *in*, D. F. Merriam, ed., Geosciences for the 21st Century: Transactions of the American Association of Petroleum Geologists Midcontinent Section Meeting, Wichita, KS, p. 71-82.

Olson, T. M., Babcock, J. A. and Wagner, P. D. , 1996, Geologic controls on reservoir complexity, Hugoton giant gas field, Kansas: *in*, D. L. Swindler and C. P. Williams, compilers: Transactions of 1995 American Association of Petroleum Geologists Midcontinent Section Meeting, p.189-198.

Olson, T. M., Babcock, J. A., Prasad, K. V. K., Boughton, S. D., Wagner, P. D., Franklin, M. K., and Thompson, K. A., 1997, Reservoir characterization of the giant Hugoton Gas field, Kansas: American Association of Petroleum Geologists, Bulletin, v. 81, p. 1785-1803.

Siemers, W. T., and W. M. Ahr, 1990, Reservoir facies, pore characteristics, and flow units: Lower Permian Chase Group, Guymon-Hugoton field, Oklahoma: Society of Petroleum Engineers Proceedings, 65th Annual Technical Conference and Exhibition, New Orleans, LA, September 23-26, 1990, Paper SPE 20757, p. 417-428.

VARIABLES					
	1	2	3	4	5
CODE	Rock Type	Dunham/Folk Classification	Grain Size	Principal Pore Size	Argillaceous Content
9	Evaporite	cobble conglomerate	vcrs rudite/cobble congl (>64mm)	cavern vmf (>64mm)	Frac-fill 10-50%
8	Dolomite	sucrosic/pebble conglomerate	m-crs rudite/pebble congl (4-64mm)	med-lrg vmf (4-64mm)	Frac-fill 5-10%
7	Dolomite-Limestone	baffle-boundstone/vcra sandstone	fn rudite/vcra sand (1-4mm)	sm vmf (1-4mm)	Shale >90%
6	Dolomite-Siliciclastic	grainstone/crs sandstone	arenite/crs sand (500-1000um)	crs(500-1000um)	Shale 75-90%
5	Limestone	packstone-grainstone/med Ss	arenite/med sand (250-500um)	med(250-500um)	Shale 50-75%
4	Carbonate-Siliciclastic	packstone/fn sandstone	arenite/fn sand (125-250um)	fn (125-250um)	Shale 25-50%
3	Siliciclastic-Carbonate	wackestone-packstone/vfn Ss	arenite/vfn sand (62-125um)	pin-vf (62-125um)	Shale 10-25%
2	Marine Siliciclastic	wackestone/crs siltstone	crs lutite/crs silt (31-62um)	pinpoint (31-62um)	wispy 5-10%
1	Continental Siliciclastic	mudstone-wackestone/vf-m Silt	fn-med lutite/vf-m silt (4-31um)	microporous (<31um)	trace 1-5%
0	Shale	mudstone/shale/clay	clay (<4um)	nonporous	Clean <1%

Table 4.1.1. Digital lithofacies-description system (after Dubois et al, 2003). Five-digit classification system used for core descriptions at half-foot intervals, gathered by visual observation with the aid of binocular microscope. A total of seven other variables were recorded but were not used in determining lithofacies.

Digital Description	Lithofacies Code	Lithofacies Class
1/>2	0	NM Sandstone
1/2	1	NM Siltstone
1/0-1	2	NM Shaley Siltstone
0,2/<3	3	Mar Shale & Siltstone
3-8/0-1	4	Mdst/Mdst-Wkst
3-8/2-3	5	Wkst/Wkst-Pkst
6-8/8/<3	6	Vfxln Sucrosic (Dol)
3-8/4-5-6	7	Pkst/Pkst-Grnst/Grnst
3-8/7	8	Phyl. Agal Bafflestone
7-8/8/>2	9	F-Mxln Sucrosic Moldic Dol
2/>2	10	Marine Sandstone

Table 4.1.2. Digital code for 11 lithofacies. An example, 13323, is a continental siliciclastic, very fine-grained sandstone (62-125 um), with pinpoint porosity and wispy clay laminations (5-10% clay). Abbreviated are nonmarine (NM), marine (Mar), carbonate mudstone (Mdst), wackestone (Wkst), packstone, (Pkst), grainstone (Grnst), phylloid (PA), dolomite (Dol), very fine crystalline (Vxln), and fine to medium crystalline (F-Mxln).

CODE	1 Rock Type	2 Dunham/Folk Classification	3 Consolidation/Fracturing	4 Argillaceous Content	5 Grain Size	6 Principal Pore Type
9	Evaporite	cobble conglomerate	unconsolidated	Frac-fill 10-50%	vcrs rudite/cobble congl (>64mm)	cavern vmf (>64mm)
8	Dolomite	sucrosic/pebble conglomerate	poorly cemented, high porosity	Frac-fill 5-10%	med-crs rudite/pebble congl (4-64mm)	med-lrg vmf (4-64mm)
7	Dolomite-Limestone	buffle-bounds lme/vcrs sandstone	cemented, >10% porosity, highly fractured	Shale >90%	fn rudite/vcrs sand (1-4mm)	sm vmf (1-4mm)
6	Dolomite-Clastic	grainstone/crs sandstone	cemented, >10% porosity, fractured	Shale 75-90%	arenite/crs sand (500-1000um)	crs (500-1000um)
5	Limestone	packstone-grainstone/med sandstone	cemented, >10% porosity, unfractured	Shale 50-75%	arenite/med sand (250-500um)	med (250-500um)
4	Carbonate-Clastic	packstone/fin sandstone	well cemented, 3-10% porosity, highly fractured	Shale 25-50%	arenite/fin sand (125-250um)	fn (125-250um)
3	Clastic-Carbonate	wackestone-packstone/vfn sandstone	well cemented, >3-10% porosity, fractured	Shale 10-25%	arenite/vfn sand (62-125um)	pin-vf (62-125um)
2	Marine Clastic	wackestone/crs siltstone	highly cemented, >3-10% porosity, unfractured	wispy 5-10%	crs lutite/crs silt (31-62um)	pinpoint (31-62um)
1	Nonmarine Clastic	mudstone-wackestone/vf-m siltstone	highly cemented, fractured	trace 1-5%	fn-med lutite/vf-m silt (4-3 lum)	microporous (<31um)
0	Shale	mudstone/shale/clay	totally cemented, dense, unfractured	Clean <1%	clay (<4um)	nonporous

CODE	7 Subsidiary Pore Type	8 Cement/Pore-Filling Mineral	9 Bedding	10 Water Depth	11 Faunal Assemblages	12 Color
9	cavern vmf (>64mm)	sulfide $\rho=3.85-5.0$	massive/structureless	Bathyal	Normal, one dominant (<3)	black
8	med-lrg vmf (4-64mm)	siderite $\rho=3.89$	planar, low angle X-bed	Slope	Normal, not diverse (2-4)	dark gray
7	sm vmf (1-4mm)	phosphate $\rho=3.13-3.21$	lrg X-bed (>4mm), trough	Outer Shelf	Normal, diverse (4+)	gray
6	crs (500-1000um)	anhydrite $\rho=2.35-2.98$	sm X-bed (<4mm), ripple	Mid-shelf	Mixed, diverse (5+)	light gray
5	med (250-500um)	dolomite $\rho=2.87$	flaser	L. Upper Shelf	Mixed, not diverse (<4)	shades of green
4	fn (125-250um)	calcite $\rho=2.71$	wavy bedded/cont. layers	U. Upper Shelf	Restricted, diverse (5+)	white
3	pin-vf (62-125um)	quartz $\rho=2.65$	lenticular/discont. layers	Intertidal	Restrict., not diverse (2-4)	tan
2	pinpoint (31-62um)	clay $\rho=2.0-2.7$	convolute/lrg burrows	Supratidal Carb.	Restrict., one dom. +2-4	brown
1	microporous (<31um)	carbonaceous $\rho=2.0$	churned/bioturbated	Supratidal Clastic	Restrict., one dom. +0-1	red-brown
0	nonporous	uncemented $\rho=1.0$	vertical k barriers	Nonmarine	Absent	red

Table 4.1.3. Digital lithofacies-description system (after Dubois et al, 2003). Twelve-digit classification system used for core descriptions at half-foot intervals, gathered by visual observation with the aid of binocular microscope. Five of these variables were considered when determining lithofacies (Tables 4.1.1 and 4.1.2).

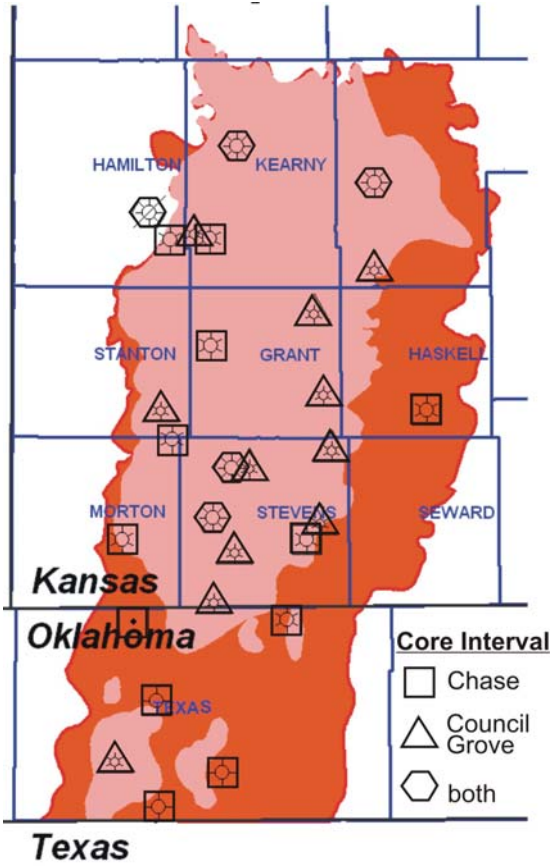


Figure 4.1.1. Distribution of Hugoton cores (continuous) for which lithofacies were defined at half-foot (0.15 m) intervals. Twenty-eight cores in all were described, 12 – Chase only, 11 – Council Grove only, and 5 – both intervals.

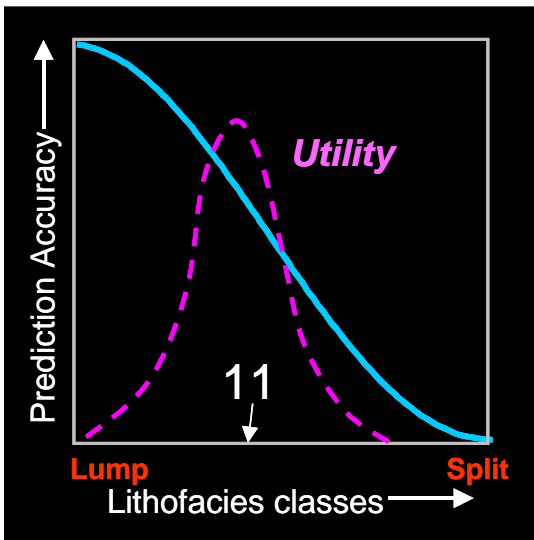


Figure 4.1.2. Diagrammatic illustration of the optimization process in achieving a balance between the number of lithofacies and prediction accuracy of neural network models.

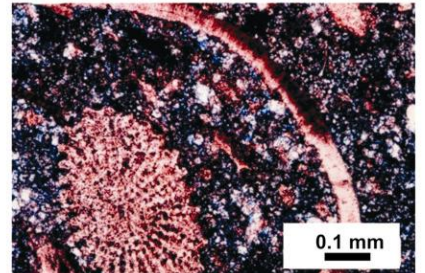
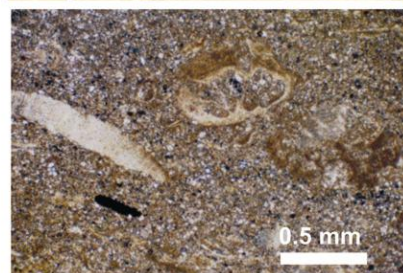
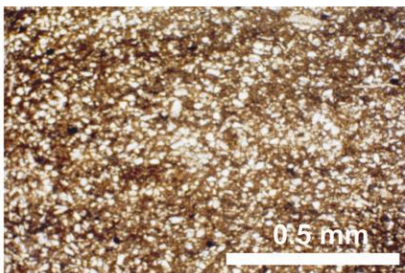
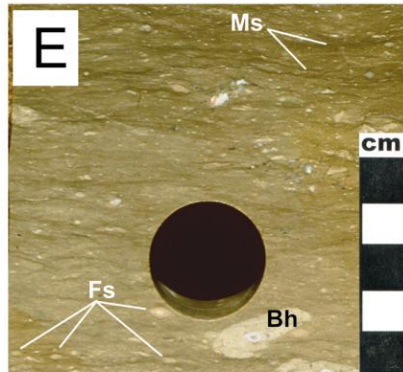
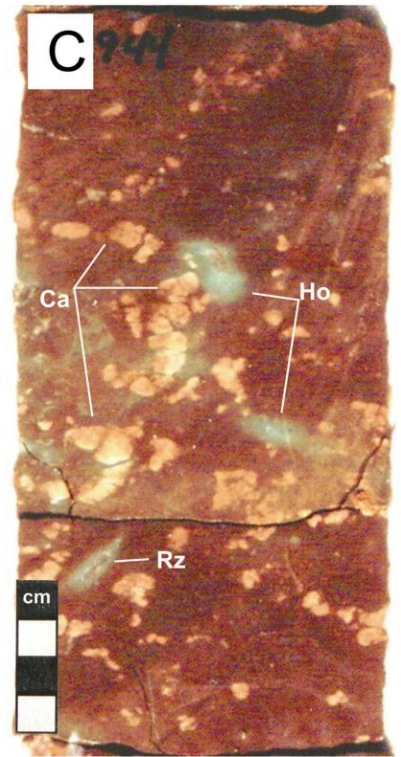
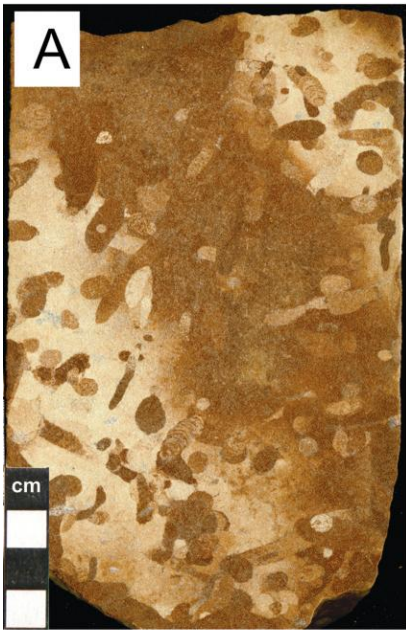


Figure 4.1.3. Major lithofacies in Chase and Council Grove, lithofacies code 0-5.

(A) Continental sandstone (L0) - Example: Blue Rapids (Council Grove, B1_SH), Cross H Cattle 1-6, 2652' (808 m). Coarse silt to very fine-grained sandstone, mostly quartz, massive bedded, adhesive meniscate burrows (S. Hasiotis, 2005, personal communication). Low-relief migrating eolian system. Digital classification: 13322.

(B) Continental coarse siltstone (L1) - Example: Stearns (Council Grove, B4_SH), Newby 2-28R, 2963' (903 m). Coarse quartz silt, rhizolith (Rz) and root traces with reduction haloes (Ho). Savannah, slow accumulation of silt by airfall, stabilized by vegetation and soil processes. Digital classification: 12213.

(C) Continental shaly siltstone (L2) - Example: Hooser (Council Grove, B3_SH), Newby 2-28R, 2944' (897 m). Fine to medium-grained quartz silt and clay, caliche (Ca), rhizolith (Rz), and root traces with reduction haloes (Ho). Coastal plain, slow accumulation of silt by airfall, stabilized by vegetation and soil processes. Digital classification: 11114.

(D) Marine siltstone and shale (L3) - Example: Funston (Council Grove, A1_LM), Newby 2-28R, 2872' (875 m). Very fine-grained shaly siltstone. Siliciclastic-dominated shelf during maximum flooding. Plug = 4.6%, $k = 0.0001$ md. Digital classification: 21104.

(E) Mudstone and mudstone-wackestone (L4) - Example: Crouse (Council Grove, B1_LM), Alexander D-2, 2962' (903 m). Silty mudstone-wackestone, wispy laminations and mini-stylolites (Ms), burrowed in part (Bh), sparse normal marine fauna including fusulinids (Fs). Low-energy shelf at a time close to maximum flooding. Plug = 3.1%, $k = 0.00239$ md. Digital classification: 41113

(F) Wackestone and wackestone-packstone (L5) - Example: Fort Riley (Chase), Flower A-1, 2700' (823 m). Slightly dolomitized wackestone, normal marine faunal assemblage includes echinoids, brachiopods, bryozoan, and fusulinids. Intercrystalline micropores (blue in thin section) in dolomitized mud matrix is dominant porosity (core slab and thin section stained with alizarin red). Low-energy normal-marine shelf. Full-diameter porosity= 15.2%, $k = 0.413$ md. Digital classification: 52111.

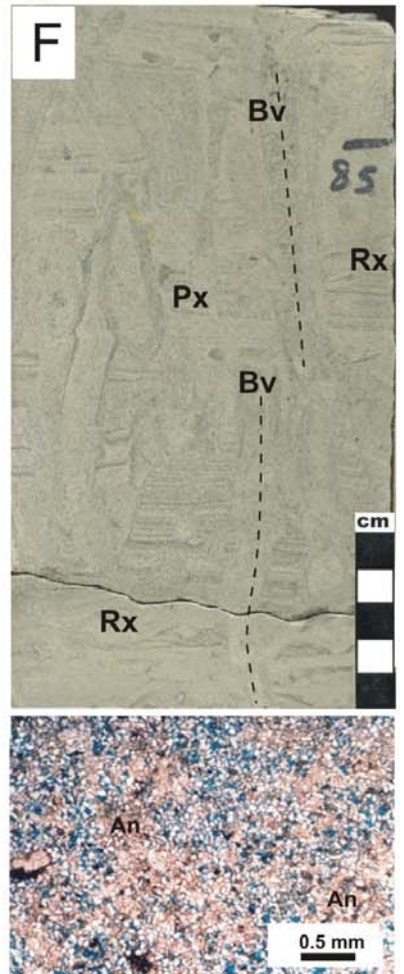
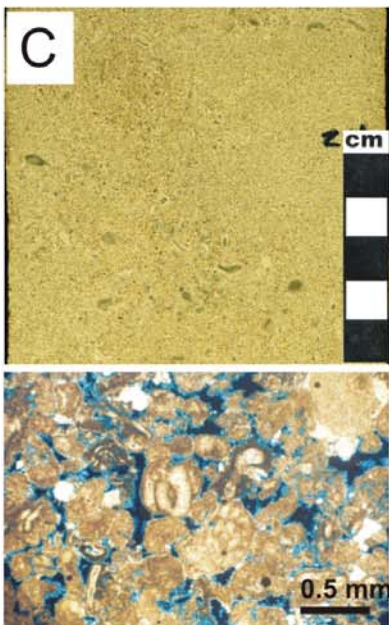
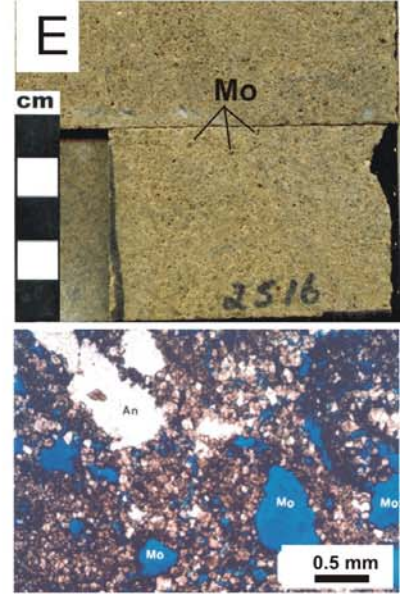
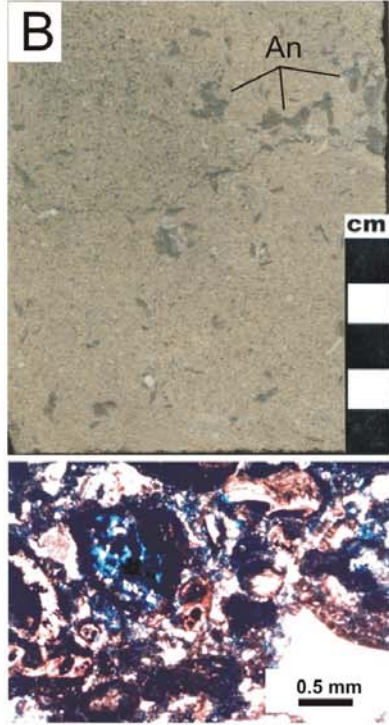
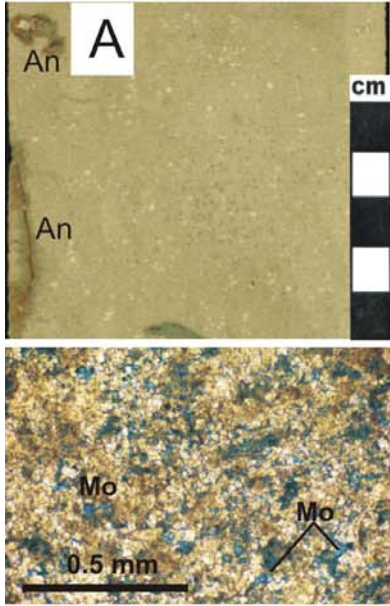


Figure 4.1.4. Major lithofacies in Chase and Council Grove, lithofacies code 6-10.

(A) Very fine crystalline sucrosic dolomite (L6) - Example: Cottonwood (Council Grove, B5_LM), Beatty E-2, 2800' (853 m). Finely crystalline, sucrosic dolomitized mudstone, locally with anhydrite cement and replacement in nodules and along fracture (An). Porosity (blue in thin section) is microporous (intercrystalline) and pinpoint (molds – Mo). Restricted, protected lagoon. Plug porosity = 13.9%, $k = 1.37$ md. Digital classification: 88120.

(B) Packstone and packstone-grainstone (L7) - Example: Winfield (Chase), Flower A-1, 2579' (768 m). Medium- to coarse-grained bioclastic-oncoid packstone, patchy anhydrite cement (An). Most porosity (blue in thin section) is intergranular. Carbonate sand shoal on open shelf. Full-diameter porosity = 16.4%, $k = 5.98$ md. Digital classification: 54520.

(C) Grainstone (L7) - Example: Cottonwood (Council Grove, B5_LM), Alexander D-2, 3024' (922 m). Medium- to coarse-grained oncoid-peloid grainstone. Well-connected intergranular porosity is blue in thin section. Carbonate sand shoal on restricted shelf. Full-diameter porosity = 18.8%, $k = 39.0$ md. Digital classification: 56540.

(D) Phylloid algal bafflestone (L8)- Example: Cottonwood (Council Grove, B5_LM), Newby 2-28R, 2992' (912 m). Phylloid algal bafflestone. Phylloid algal blade molds (Pm) partially filled with anhydrite cement (An). Matrix is largely peloid-pellet packstone (Pp). Phylloid algal mound on slightly restricted shelf. Full-diameter porosity = 20.6, $k = 1141$ md. Digital classification: 57770.

(E) Fine to medium crystalline moldic dolomite (L9) - Example: Krider (Chase), Flower A-1, 2516' (767 m). Fine-medium crystalline moldic dolomite. Large molds (Mo), possibly ooids and bioclasts, dominate the well-connected pore system in a dolomitized medium- to coarse-grained grainstone. Patchy anhydrite cement (An) occludes some porosity. Carbonate sand shoal on an open shelf. Full-diameter porosity = 22.3%, $k = 275$ md. Digital classification: 88550.

(F) Marine sandstone (L10) - Example: Herington (Chase), Flower A-1, 2485' (757 m). Planar (Px) and ripple (Rx) crossbedding and vertical burrows (Bv). Tidal flat. Very coarse silt to very fine-grained sandstone, well sorted, sub-arkose (83% of detrital fraction is quartz, by X-ray diffraction), well-connected intergranular porosity (blue), patchy anhydrite cement (An). Full-diameter porosity = 20.8%, $k = 48.2$ md. Digital classification: 23321.

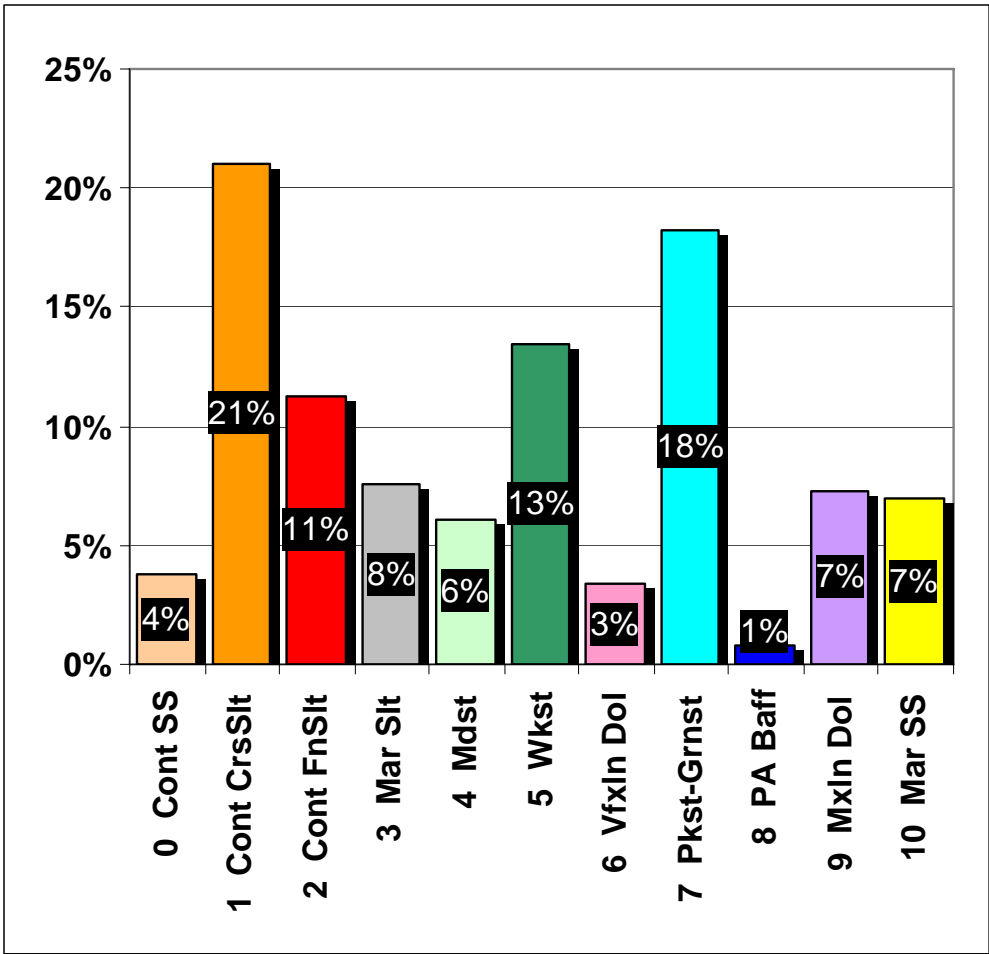


Figure 4.1.5. Relative proportions of 11 lithofacies in 6756 ft core (2060 m) from Chase and Council Grove Groups, Hugoton field.

4.2. CORE PETROPHYSICS

Alan P. Byrnes

Introduction

Previous petrophysical studies of the Hugoton and Panoma fields have generally utilized average properties assigned to formations (e.g., Siemers and Ahr, 1990; Olson et al., 1997). Siemers and Ahr (1990) characterized porosity in the Guymon-Hugoton Chase Group. They reported that within the Winfield, Krider, and Herington formations porosity is a function of lithofacies and degree of solution enhancement and dolomitization. Solution enhancement is associated with 2-15% porosity. Porosity can be characterized as initially intergranular but with diagenesis becomes variably moldic and vuggy and with dolomitization, intercrystalline porosity fraction increases. Porosity in the Gage, Odell, and Paddock dark-reddish-brown terrigenous siltstones, mudstones and shales was characterized as plugged with clay but porosity values were not reported.

Porosity and permeability characteristics of reservoir-quality wackestone, packstone, and grainstone lithofacies in the Council Grove Group, Texas County, Oklahoma, were reported by Heyer (1999). Byrnes et al (2001) and Dubois et al. (2003a) presented lithofacies-specific petrophysical properties for the Council Grove in Panoma field and illustrated the similarities between low-permeability carbonates and low-permeability sandstone. Fundamental to construction of the reservoir geomodel is the population of cells with the basic lithofacies and their associated petrophysical properties- porosity, permeability, and fluid saturation. Petrophysical properties vary among the 11 major lithofacies. Principal lithofacies-specific petrophysical properties analyzed and discussed here include grain density, routine helium and *in situ* porosity, routine air and *in situ* Klinkenberg gas permeability, capillary pressure, and gas-water drainage relative permeability.

Core Petrophysical Data

Data for routine porosity, permeability, and grain density were compiled for over 8,200 full-diameter and plug core samples from measurements performed by commercial laboratories and the Kansas Geological Survey. Data for these are presented in Table 4.2.1 (CORE_DATA&DESCRIPTIONS_DATABASE_Appendix 4.2.1). Data are reported for cores from 34 wells geographically distributed across the Hugoton field area (Figure 4.2.1). For the 8,200 core samples, 3,700 (45%) are Chase Group and 4,500 (55%) are Council Grove Group samples. Of the 8,200 core samples, 5,300 (65%) are full-diameter and 2,900 (35%) are core plugs.

Lithofacies were determined from core examination for over 5,700 samples. In addition, to investigate some statistical distributions, a general lithofacies class was estimated for an additional 2,100 samples from routine core description where the description was considered to have little ambiguity (e.g., a Gage sample described as “rdbd slty tr sdy shly sl calc” with a grain density = 2.69 g/cc was assigned a lithofacies of L1.1). The

lithofacies that were characterized using indirect evidence were assigned fractional lithofacies codes (e.g., L1.1) to separate them from directly measured lithofacies (e.g., L1). Figure 4.2.2 illustrates the relative distribution of lithofacies in the cores, core analysis data, and in the full geomodel. Comparison of these relative lithofacies distributions indicates that although the core-analysis lithofacies distribution is generally similar to distributions for the described core and the full 108-million cell geomodel, there are sufficient differences that some sampling bias may be present in the core-analysis data. The absence of core analysis for all L0-3 cores illustrates a core-analysis sampling bias away from analyzing siltstones. The possible sampling bias evident in the difference in lithofacies distribution precludes using core analysis data to characterize the Hugoton stratigraphic interval properties without potentially significant restrictions on accuracy. For this reason only grain density information were used to characterize stratigraphic interval properties. Though stratigraphic characterization is restricted, the wide well distribution supports the use of core properties to characterize general lithofacies properties and to develop property correlations (e.g. lithofacies-specific permeability versus porosity correlation).

Because a significant fraction of the rocks in the Hugoton have low porosity ($\phi < 8\%$) and low permeability ($k < 1$ md) core-analysis properties measured using routine laboratory methods do not necessarily reflect reservoir conditions. Properties representing reservoir conditions are referred to in this document as *in situ*. In general, *in situ* here refers to properties measured with the sample under a confining stress (in pounds per square inch, psi) near that in the reservoir, which in psi is equal to approximately 0.3-0.5 times the sample depth (in feet; e.g., confining pressure for 3,000 ft is 900-1,500 psi).

Grain Density

Grain densities of Hugoton rocks are generally consistent with the mineralogy of constituent lithofacies. Tables 4.2.2 and 4.2.3 present summary statistics by stratigraphic member and lithofacies, respectively. Figure 4.2.3 illustrates the frequency distribution of grain density for major lithofacies groups. Of particular note are the high grain densities of all marine and continental clastic units and associated lithofacies. Mean density of all siltstone and shale intervals average 2.70 g/cc.

For clastic stratigraphic intervals there is a weak trend of decreasing grain density with increasing depth. The shallow Paddock and Odell intervals exhibit mean grain densities of 2.79 and 2.73 g/cc, respectively, whereas the deep E-SH and F-SH intervals exhibit mean grain densities of 2.67 g/cc. High grain densities in these clastic intervals can generally be attributed to dolomite, anhydrite, and calcite cements. Minimum values average 2.59 ± 0.06 g/cc and maximum values average 2.82 ± 0.11 g/cc (error bars represent 2 s.d.).

For carbonate stratigraphic intervals, the shallow Herington, Krider, and Winfield intervals exhibit higher mean grain densities (2.78-2.82 g/cc) with the underlying Towanda and Ft. Riley exhibiting mean grain densities of 2.73 and 2.72 g/cc,

respectively. Basal Chase and many of the Council Grove limestone members exhibit mean densities of 2.71 ± 0.01 g/cc with the exception that the B3-LM, B4-LM, and B5-LM have mean densities of 2.73-2.74 g/cc. Minimum density for all intervals averages 2.60 ± 0.10 g/cc (1 s.d.), and maximum densities average 2.88 ± 0.15 g/cc (1 s.d.).

Higher grain densities in Chase units compared to Council Grove units are also evident in grain-density differences for lithofacies within the groups (Table 4.2.3). For all lithofacies, Chase grain densities average 0.02 ± 0.01 g/cc higher than similar Council Grove lithofacies.

Grain densities of the continental clastics (L0-2) average 2.70 ± 0.01 g/cc (Figure 4.2.4) and marine clastics average 2.71 ± 0.01 g/cc (Figure 4.2.6). The difference between continental and marine is dominated by the influence of the large population of marine clastics in the Chase. Chase marine clastics average 0.02 g/cc higher density than continental lithofacies, but Council Grove marine clastics average 0.01 g/cc lower grain density than continental lithofacies. Comparing grain-density distributions of the Chase and Council Grove, Chase clastic lithofacies exhibit a greater fraction of samples with densities of 2.70-2.78 g/cc and Council Grove have a greater fraction containing densities of 2.62-2.70 (Figure 4.2.5, 4.2.7).

Limestone lithofacies (L4, L5, L7, L8; Figure 4.2.8) average 2.72 ± 0.01 g/cc with Chase units averaging 2.74 ± 0.02 g/cc and Council Grove units averaging 2.71 ± 0.01 g/cc. Council Grove mudstone/mud-wackestone lithofacies (L4) exhibit slightly lower grain density (2.70 g/cc), possibly reflecting the influence of greater siliciclastic components (Figure 4.2.9). Conversely, Chase mudstone/mud-wackestone exhibit slightly higher grain density (2.75 g/cc), possibly reflecting greater dolomitization or anhydrite cement in lagoonal to tidal flat deposits.

Dolomite lithofacies (L6 and L9) average 2.83 ± 0.03 g/cc (Figure 4.2.10) with fine-crystalline sucrosic dolomites exhibiting a skewness to lower grain density, reflecting the presence of siliciclastic silt. Chase L6 dolomites exhibit an average grain density of 2.83 ± 0.02 g/cc and Council Grove L6 dolomites average 2.81 ± 0.04 g/cc. The high average for all L6 dolomites reflects the significantly larger population of Chase L6 dolomites (n=630) compared to the Council Grove (n=107).

Porosity

Routine (unconfined) helium porosity (ϕ_{He}) values range from 1% to 34% (Figure 4.2.11), averaging $9.2 \pm 5.1\%$ (1 s.d.) but with a median of 8.7% and mode of 7.0% (Figure 4.2.12). Routine helium porosity data are important, but in lower-porosity rocks can differ from reservoir values sufficiently to affect reservoir characterization. Accurate reservoir porosity is especially important when other petrophysical properties are tied to porosity and to wireline-log porosity. To develop an equation relating routine-helium porosity to *in situ*-total porosity, data were correlated for 405 cores representing all lithofacies in the Hugoton except medium-crystalline sucrosic moldic dolomites (L9);

Table 4.2.1). Correlations of routine-helium porosity values measured under no confining stress and at 800-psi confining stress with *in situ* porosity values measured under a confining stresses of ~1,300-1,800 psi (Figure 4.2.13) exhibit similar correlations within error (excluding five outlier samples in the unconfined-porosity sample population). *In situ* porosity (ϕ_i) can be predicted from routine-helium porosity (ϕ_{He}) using:

$$\phi_i = 1.02\phi_{He} - 0.68 \quad (4.2.1)$$

For over 93% of Hugoton rocks, which exhibit porosity less than 16%, the average *in situ* porosity is 0.54 porosity units (p.u., porosity %) less than routine core-analysis measured values (e.g., $\phi_i = 9.5\%$ for a core where $\phi_{He} = 10\%$). Equation 4.2.1 predicts that returning a core to *in situ* confining stress conditions has increasing influence with decreasing porosity. This can be interpreted to result from an increasing fraction of porosity that is involved in pore-throats and is subject to both expansion with core decompression (from being brought to surface) and compression with application of confining stress. Using equation 4.2.1, *in situ* porosity (ϕ_i) values were calculated for all samples with only routine helium-porosity data. All petrophysical analysis utilizes the *in situ* porosity values because these correspond more closely to reservoir conditions and are likely to provide better correlation with wireline-log-measured porosity values. *In situ* porosity data were not available for full-diameter cores. It was assumed that equation 4.2.1 could be applied to correct full-diameter routine data, though full-diameter core data might exhibit a slightly different correction to *in situ*-stress conditions.

Lithofacies-porosity summary statistics are presented in Table 4.2.4. Comparing porosity among lithofacies, average porosity decreases with decreasing grain size (i.e., very fine sandstone to siltstone) in the continental siliciclastics and from grainstone to mudstone in the carbonates. Where some continental very fine-grained sandstones (L0) exhibit porosities similar to coarse-grained siltstones, a significant fraction of the sandstone lithofacies population exhibits porosities greater than 14% (Figure 4.2.14). Although it might be anticipated that coarse siltstones (L1) would exhibit higher porosity than shaly siltstones (L2), there is little difference in the relative distribution of porosity classes between the two lithofacies. Mean porosity of the L2 lithofacies ($9.3 \pm 3.7\%$) is greater than L1 ($8.4 \pm 3.9\%$), though with the standard deviation of both lithofacies the difference is not significant. Comparison of Chase and Council Grove continental clastics (Figure 4.2.15) indicates that Chase very fine-grained sandstones (L0) exhibit significantly greater porosity and Chase coarse-grained siltstones exhibit higher porosity, however, Chase shaly siltstones (L2) are similar to Council Grove though the Chase contains a slightly greater fraction of low-porosity ($\phi < 6\%$) shaly siltstones.

Marine clastic sandstones (L10) exhibit significantly greater porosity than marine siltstones (L3; Figure 4.2.16). Chase marine siltstones have a larger fraction of rocks with porosity greater than 10% (Figure 4.2.17). Differences in the relative fraction of porosity classes between Chase and Council Grove marine sandstones vary with porosity class but the Chase has a greater fraction of the best-porosity ($\phi > 20\%$) sandstones.

Hugoton limestones exhibit increasing porosity with increasing grain size and decreasing mud-fraction texture. Mean porosities increase with lithofacies class: L4-6.3±3.5%, L5-8.0±4.5%, L7-9.8±4.5%, and L8-10.4±4.4% (error 1 s.d.; Figure 4.2.18). This porosity increase is both a function of increasing interparticle porosity and increasing moldic porosity development, identified in core as pinpoint porosity. Phylloid algal bafflestones (L8) are not present in the Chase cores sampled. All other limestone lithofacies in the Chase (L4, L5, L7) exhibit higher fractions of rocks with porosity greater than 8% (Figure 4.2.19).

Although the medium-crystalline sucrosic moldic dolomite lithofacies (L9) represents a major reservoir lithofacies because of high permeability, in the cores sampled this lithofacies exhibits an mean porosity (11.7±5.4%) slightly lower than the fine-crystalline sucrosic dolomite lithofacies (L6; 12.5±6.3%; Figure 4.2.20). The L9 lithofacies is not present in the Council Grove, but comparison of Chase and Council Grove L6 lithofacies porosity-class distribution indicates that the relative fractions of porosity classes vary with class though the Chase exhibits slightly better L6 mean porosity (14.0±5.5%) than the Council Grove L6 lithofacies (12.8±6.1%; Figure 4.2.21).

Permeability

Full-diameter and core plug measured routine air permeabilities range from 0.0001 md to 2690 md ($n = 7,650$; Figure 4.2.22). Though the database of full-diameter air permeability measurements is large ($n = 5,300$), a significant fraction (25%) are described or annotated as fractured and an unknown number of samples may contain unidentified hairline fractures that can significantly affect permeability in samples with matrix permeability less than 0.5 md. Full-diameter analyses, generally performed at confining pressures less than 400 psi (2.8 MPa), often exhibit significant difference from plug values for $k < 0.5$ md ($0.0005 \mu\text{m}^2$), even for samples where fractures were not identified but microfractures may have been present. A crossplot of routine air permeability versus porosity for full-diameter and core-plug values shows that cores with identified macrofracturing exhibit no change in air permeability with decreasing matrix permeability below approximately 0.2-0.5 md ($0.0005 \mu\text{m}^2$; Figure 2.2.23). The permeability of the fractured cores with matrix $k < 0.5$ md ($0.0005 \mu\text{m}^2$) can be attributed to the core-permeability measurement reflecting the permeability of a fracture(s) in the sample with the matrix contribution being small or negligible. Comparison of the frequency distribution of routine air permeability for full-diameter and plug samples (Figure 4.2.22) indicates that plugs exhibit a similar distribution in routine air permeability to full-diameter but shifted to lower permeability by approximately an order of magnitude. Both sample sets have a 14±1% fraction of their total that are below their minimum measurement threshold (evident as the 0.001 md and 0.01 md peaks). Both also exhibit greater fractions in the 0.03-0.1 md range, reflecting the influence of unconfined microfractures. Whether these microfractures are present in the subsurface is addressed by comparison of core-measured permeability and drill stem test or well test measured permeability, discussed below.

Influence of Confining Stress and Klinkenberg Effect

In most low-permeability rocks, routine air permeability values range from 10 to 1,000 times greater than *in situ* gas and liquid permeability values. Most previous studies of low-permeability rocks are on sandstones and have shown that the absolute difference between gas permeabilities measured at routine conditions and those measured under confining stress, both with and without correction for the Klinkenberg gas slippage effect, increases progressively with decreasing permeability and increasing confining stress (Vairogs et al., 1971; Thomas and Ward, 1972; Byrnes et al., 1979; Jones and Owens, 1980; Sampath and Keighin, 1981; Walls et al., 1982; Ostensen, 1983; Wei et al., 1986; Luffel et al., 1991; Byrnes, 1997; Castle and Byrnes, 1998; Byrnes et al., 2001; Byrnes, 2005). This relationship can be attributed primarily to the closing of thin, tabular pore-throats as confining stress is applied which; 1) is associated with an increase in the Klinkenberg gas slippage factor and a decrease in the Klinkenberg gas permeability, and 2) decreases permeability due to decreasing flow cross-sectional area.

Klinkenberg (1941) gas permeability is equivalent to single-phase inert liquid or high-pressure gas absolute permeability. Reported Klinkenberg gas permeabilities represent gas permeabilities corrected to reservoir gas pressure using Equation 4.2.2. Klinkenberg gas permeability is determined by measuring gas permeability at several different pore pressures and extrapolating to reservoir pore pressure or to infinite pore pressure (equivalent to liquid conditions). The Klinkenberg gas slippage effect results from greater gas movement due to decreased molecule-molecule and molecule-pore wall interactions at lower gas pressure which was characterized by Klinkenberg (1941) as:

$$k_{\text{gas}} = k_{\text{liquid}} (1 + 4cL/r) = k_{\text{liquid}} (1 + b/P) \quad (4.2.2)$$

where k_{gas} = gas permeability at pore pressure, k_{liquid} is liquid permeability, c = proportionality constant (approximately = 1), L = mean free path of gas molecule at pore pressure, r = pore radius, b = proportionality constant (= $f(c, L, r)$, atm), and P = pore pressure (atm). Equation 4.2.2 shows that as the pore diameter, r , decreases, the Klinkenberg term increases and the absolute difference between k_{gas} and k_{liquid} increases. Because b is a function of pore-radius distribution, it can vary between rock samples. However, general values for b can be estimated from the empirical correlation for air presented by (Heid et al., 1950):

$$b = 0.777 k_{\text{liquid}}^{-0.39} \quad (4.2.3)$$

and Jones and Owens (1980):

$$b = 0.867 k_{\text{liquid}}^{-0.33} \quad (4.2.4)$$

where k_{liquid} is in millidarcies (md) and b is in units of atmosphere (atm). In low-permeability reservoirs, very small sheetlike, tabular pore-throats connect significantly larger interparticle, and in many low-permeability sandstones, intraparticle pore bodies. For Hugoton carbonates, comparison of *in situ* air and *in situ* Klinkenberg permeabilities

(Figure 4.2.24) illustrates how the Klinkenberg effect increases with decreasing absolute permeability. Regression provides the following equation for predicting *in situ* Klinkenberg permeability (k_{ik}) from *in situ* air permeability (k_{ia}):

$$k_{ik} = 0.66 k_{ia}^{1.09} \quad (4.2.5)$$

In addition to Klinkenberg correction, routine air permeability data for Hugoton low-permeability rocks require correction for the effect of confining stress. When rocks are restored to reservoir confining stress, pore-throat size decreases and permeability decreases. Figure 4.2.25 shows a crossplot of *in situ* Klinkenberg permeability (k_{ik}) versus *routine* Klinkenberg permeability (k_{ak} ; the ak subscript represents ambient confining stress and k represents Klinkenberg), where the later measurement represents a permeability measured at routine air permeability conditions (e.g., 400-800 psi confining stress) but with Klinkenberg correction for gas slippage. This relationship indicates that the effect of confining stress for rocks with $k < 10$ md can be expressed:

$$\log_{10}k_{ik} = -0.129 (\log_{10}k_{ak})^2 + 1.236 \log_{10}k_{ak} - 0.12 \quad (4.2.6)$$

It is important to note that this equation is only valid for rocks with permeability $k_{ak} < 10$ md. This equation shows that confining stress exerts a progressively greater effect on permeability as permeability decreases.

Correction for both Klinkenberg gas-slippage effect and confining-stress effect on permeability provides an equation for conversion of routine-air permeability data to *in situ* Klinkenberg values, and by comparison with permeability values that would be obtained using Equations 4.2.5 and 4.2.6, provides some understanding of the relative role of gas slippage and confining stress. Values of *in situ* Klinkenberg-gas permeability (k_{ik}) were correlated with routine-air permeability (k_{air}) values (Figure 4.2.26) and can be predicted approximately from routine-air permeability using:

$$\log_{10}k_{ik} = 0.059 (\log_{10}k_{air})^3 - 0.187 (\log_{10}k_{air})^2 + 1.154 \log_{10}k_{air} - 0.159 \quad (4.2.7)$$

where permeabilities are in millidarcies (md). This equation can only be applied for rocks with permeability $k < 100$ md. Permeabilities in low-permeability sandstones exhibit similar response to confining stress (Vairogs et al., 1971; Thomas and Ward, 1972; Byrnes et al., 1979; Jones and Owens, 1980; Sampath and Keighin, 1981; Walls et al., 1982; Ostensen, 1983; Wei et al., 1986; Luffel et al., 1991; Byrnes, 1997; Castle and Byrnes, 1998; Byrnes et al., 2001; Byrnes, 2005; Figure 4.2.27). The trend is due both to the increase in effect of confining stress on pore-throat size with decreasing permeability and to the increase in gas slippage (i.e., Klinkenberg effect) with decreasing pore-throat size and decreasing permeability. Variance is due to several factors including differing rock response to confining stress and differences in mean pore pressure of air-permeability measurements.

Permeability and Pore-Throat Size

Permeability is conventionally shown crossplotted with porosity because porosity is an easy and inexpensive variable to measure and is often correlated with other variables that influence or control permeability. The principal variable that exerts greatest influence on permeability in low-permeability rocks is the pore-throat size (and pore-throat size distribution). Correlation between permeability and different measures of the pore-throat size is continuous for all lithofacies including both carbonates and siliciclastics. Different measures or statistics can be used to represent the rock pore-throat size distribution. Here a measure of the principal pore-throat diameter (PPTD) is used and is defined as the largest pore-throat diameter at which the change in nonwetting-phase saturation on a drainage capillary-pressure curve exceeds 25% of the total injection volume after reaching the threshold-entry pressure. This saturation also generally corresponds to the pore-throat diameter associated with the first standard deviation above the mean pore-throat diameter defined over the saturation-weighted pore-throat sizes associated with nonwetting-phase saturation from 10% to “ S_{wi} ”. This size generally is intermediate in size between the pore-throat diameter associated with the threshold-entry pressure and twice the r_{35} pore-throat aperture radius derived using the Winland equation (Coalson et al., 1985). Figure 4.2.28 illustrates the correlation between *in situ* Klinkenberg permeability (k_{ik}) and PPTD. Variance in this figure can be attributed to the influence of other variables including porosity, pore-size distribution, and pore architecture. The correlation between k_{ik} and PPTD can be expressed:

$$\text{PPTD} = 2.2 k_{ik}^{0.42} \quad (4.2.8)$$

where k_{ik} is the *in situ* Klinkenberg permeability (md) and PPTD is the principal pore entry throat diameter (micron, μm). Standard error of prediction for this correlation is a factor of 1.7x. It is important to note that the PPTD values shown in Figure 4.2.28 were obtained from capillary-pressure curves that were not measured under confining stress. Byrnes and Keighin (1993) showed that under confining stress the *in situ* PPTD values range from 15% to 84% of unconfined PPTD values and thus, more accurately represent reservoir pore-throat sizes, Equation 4.2.8 would have to be modified to represent *in situ* PPTD. The observed decrease in permeability with increasing confining stress discussed above is consistent with observed decreases in PPTD with confining stress and calculated flow through cracks. For a decrease in crack width of 30% to 70%, a change in permeability of approximately 3 to 40 times would be predicted and is observed in low-permeability rocks.

Permeability Distribution

Measured core-plug *in situ* Klinkenberg permeability values either measured or calculated from routine air-permeability values using equation 4.2.7 for samples that had only routine air permeability data are shown in Table 4.2.1. *In situ* Klinkenberg values were not calculated for full-diameter cores because of the potential for microfractures influencing the measured permeabilities (though values consistent with plug-matrix

trends might be used with restriction). *In situ* Klinkenberg permeability values range from 8×10^{-12} to 820 md (Figure 4.2.29).

Nearly 80% of Hugoton rocks exhibit an *in situ* Klinkenberg permeability less than 1 md, 56% less than 0.1 md, and 35% less than 0.01 md. Lithofacies-permeability summary statistics are presented in Table 4.2.5. Comparing permeability among lithofacies, average permeability decreases with decreasing grain size (i.e., very fine sandstone to siltstone) in the continental siliciclastics, from grainstone to mudstone in the limestones, and from medium-crystalline sucrosic moldic dolomite to very fine- fine-grained sucrosic texture in dolomites. Continental very fine-grained sandstones (L0) exhibit permeabilities ranging from 2 to 5 times those of coarse-grained siltstones (Figure 4.2.30). Although coarse siltstones (L1) exhibit a similar permeability distribution to shaly siltstones (L2), mean permeability of the L2 lithofacies (0.0025md) is half that of the L1 lithofacies (0.0052 md), though given the standard deviation of both lithofacies ($\pm 70X$ at 1 s.d.) the difference is not significant. Comparison of Chase and Council Grove continental clastics (Figure 4.2.31) indicates that Chase very fine-grained sandstones (L0) and shaly siltstones exhibit variable differences in permeability populations. Chase and Council Grove coarse-grained siltstones permeability distributions are similar.

Marine clastic sandstones (L10) exhibit significantly greater permeability than marine siltstones (L3; Figure 4.2.32A) primarily because the sandstones exhibit a high fraction of high-porosity rocks. Chase marine siltstones have a larger fraction of rocks with porosity greater than 10% (Figure 4.2.17). Differences in the relative fraction of permeability classes between Chase and Council Grove marine sandstones vary with permeability and porosity class, but the Chase has a greater fraction of the best porosity ($\phi > 20\%$) and permeability ($k > 0.1$ md) sandstones (Figure 4.2.32B).

Hugoton limestones exhibit increasing permeability with increasing grain size and decreasing mud-fraction texture. Mean permeabilities increase with lithofacies class: L4- 0.00011 md, L5-0.0016 md, L7-0.091 md, and L8- 3.6 md (Figure 4.2.33). This permeability increase is both a function of increasing interparticle porosity and increasing moldic-porosity development, identified in core as pinpoint porosity. Phylloid algal bafflestones (L8) are not present in the Chase cores sampled. All other limestone lithofacies in the Chase (L4, L5, L7) exhibit higher fractions of rocks with permeability greater than 0.001 md with the exception of lithofacies L7 for $k > 3$ md for which the Council Grove has a greater fraction of its total L7 population (Figure 4.2.34).

The medium-crystalline sucrosic moldic-dolomite lithofacies (L9) represents a major reservoir lithofacies because a significant fraction of these rocks exhibit $k > 3$ md (Figure 4.2.35). Though the fine-crystalline sucrosic dolomite lithofacies (L6) exhibits porosities slightly higher than the L9 lithofacies, permeabilities for this finer-grained facies are generally lower. The L9 lithofacies is not present in the Council Grove but comparison of Chase and Council Grove L6 lithofacies permeability class distribution indicates that permeabilities are lower in the Chase (Figure 4.2.36).

Relationship of Permeability to Porosity

Permeability is a function of several variables including grain size, shale bed architecture, pore-throat size, porosity, and pore architecture. The most easily measured independent variable for prediction of permeability is porosity. A simple crossplot of permeability versus porosity shows that permeability varies by over three orders of magnitude at any given porosity for Hugoton rocks undifferentiated. Using regression analysis a standard error of prediction for a power-law relationship between ϕ_i and k_{ik} is $\sim 20X$ (1 s.d., e.g. a predicted k_{ik} of 1 md might be 20 md or 0.05 md at 1 s.d.). For useful reservoir characterization this error in permeability prediction needs to be reduced. The good correlation between permeability and pore-throat size (Figure 4.2.28) indicates that the ability to provide information concerning pore-throat size can reduce permeability – porosity correlation variance. Two common approaches are applied to provide additional variables that improve the permeability-porosity correlation by accounting for remaining variance not associated with porosity: 1) identify wireline-log response signatures that correlate with permeability independent of porosity, and 2) identify rock types that exhibit unique permeability-porosity trends because of continuity of rock/pore texture changes with porosity that differ from other rock types.

The first method is often empirical and can provide equations with good predictive accuracy but provides little information about the variables defined that can be correlated to other meaningful variables for validation that the relationship developed is robust and has physical meaning. An exception to this is the common use of porosity and gamma ray to predict permeability where gamma ray is associated with argillaceousness or shale bedding. Lithofacies information, discriminating between matrix grain size and grain support has been demonstrated to improve permeability prediction. Limitations on this approach are the ability to accurately identify lithofacies from wireline-log response, consistency of depositional patterns, and the amount of difference between lithofacies permeability-porosity trends. The selection and optimization of lithofacies identification employed in this study is discussed above.

As with many sedimentary rocks, the relationship between permeability and porosity can be characterized using a power-law function though the relationship changes slightly in some lithofacies at porosities below $\sim 6\%$. For the major lithofacies characterized in the Hugoton, each defined lithofacies exhibits a relatively unique k_{ik} - ϕ_i correlation that can be represented using a power-law equation of the form:

$$k_{ik} = A \phi_i^B \quad (4.2.9)$$

where k_{ik} is in millidarcies (md), porosity is in percent (%), and values for A and B are shown in Table 4.2.6.

The equation parameters, A and B, were determined using reduced major axis analysis (RMA) of datasets for each of the 11 lithofacies. For the range of values of $\log_{10}k_{ik}$ and $\log_{10}\phi_i$ linear regression analysis (LRA) provided good correlation but, by minimizing variance in the “dependent” variable (k_{ik}) only, tended to predict slightly high

permeabilities at low porosity and low permeabilities at high porosity. RMA provided equations that are more balanced within the data sets. Statistical analysis of RMA results appear to give poorer predictive accuracy than LRA for a complete dataset but provide better accuracy for subsets of the dataset.

Outliers can exert significant influence on equations developed using regression analysis. Though equations developed with data sets that include outliers are statistically accurate for the entire population of samples as defined, the weighted influence of a single significant outlier can decrease the accuracy of the developed equation for prediction of the principal population of interest. Often in large core-analysis datasets outliers represent cores that exhibit properties that would not be considered appropriate for the lithofacies population or exhibit heterogeneity that should reject them from analysis. It was prohibitive or not possible to physically examine the outlier cores to determine the cause of the anomalous values. To avoid having these data influence the final equations, the outlier data were eliminated from the analysis. To develop equations that were optimally accurate for the primary population of each lithofacies, samples lying more than 2 standard deviations outside the general lithofacies trend were eliminated from analysis for the final equation development. Table 4.2.6 lists standard errors of prediction for each lithofacies. These errors represent the standard error (error at 1 s.d.) for 95% of the total population since outliers were eliminated. These errors also did not include comparison of predicted and measured values for permeability data that were designated as being less than a measurable threshold (e.g., “ $k < 0.01$ md”).

Standard errors of prediction are provided as factors, or multipliers, since error in the power-law equation is error of the logarithm of the permeability. For the entire Hugoton database of plug-permeability data, the standard error of prediction (SE) for a linear regression equation of all samples is 120X ($n=2317$) and for a sample population that excludes significant outliers and samples with $k < a$ measurement limit, SE=23X ($n=1980$). Using the lithofacies-specific equations developed using RMA, standard errors of prediction range from SE=2.9X to 16X ($n=1980$). For the principal reservoir rock lithofacies (L0, L5, L6, L7, L8, L9, L10), standard errors of prediction range from 2.9X to 7.5X and average 5.1X. This represents an improvement in predictive accuracy of 4.5X better than a single predictive equation. Predictive accuracy is low (15.6X-16.0X) in the low permeability continental shaly siltstone (L0) and lime mudstone/mud-wackestone (L4) lithofacies.

Variance in the permeability-porosity correlation can result from several sources including principally:

- 1) Error in core-plug permeability including laboratory measurement error, core heterogeneity (e.g. multiple lithofacies present in sample, patchy cement, bedding perpendicular to flow) or microfracturing.
- 2) Error in core porosity including laboratory measurement error, core heterogeneity (e.g. multiple lithofacies present in sample, patchy cement, bedding perpendicular to flow).

- 3) Error in conversion of routine-air permeability to *in situ* Klinkenberg permeability or routine-helium porosity to *in situ* porosity.
- 4) Misidentification of core lithofacies, e.g. sample lithofacies miscoded (e.g. L1 typed as L2).
- 5) Misidentification of lithofacies, half-foot core description does not accurately represent actual plug lithofacies.
- 6) Broad lithofacies classification – the inclusion of lithologically similar rocks with petrophysically different characteristics, e.g., a moldic porosity-rich wacke-packstone (L5) is included in the same lithofacies class as a wacke-packstone with no moldic porosity.

All these error sources either independently or cumulatively act to increase variance.

Figures 4.2.38-4.2.48 show the *in situ* Klinkenberg permeability versus *in situ* porosity trends from each lithofacies. Composite crossplots for each group of lithofacies display sub-parallel trends for the continental siliciclastics (Figure 4.2.49), marine siliciclastics (4.2.50), limestones (4.2.51), and dolomites (4.2.52). At $\phi_i > 6\%$, permeability in a phylloid algal bafflestone (L8) can be 60-100X greater than mudstone/mud-wackestone (L4), and >100X greater than marine siltstone (L3) of similar porosity. Within their principal range of porosity overlap ($\phi_i=2-10\%$), packstone/grainstones (L7) can exhibit 10-50X greater permeability than mudstone/mud-wackestones (L4). These differences illustrate the importance of identifying lithofacies to more accurately predict permeability from wireline-log porosity.

Comparison of petrophysical properties among lithofacies indicates that permeability increases with increasing energy in the depositional environment and corresponding decrease in mud and silt matrix. Within both the continental and marine siliciclastics, permeability increases with increasing mean grain size at any given porosity.

For the general porosity range $\phi_i = 4-14\%$, where the continental very fine to fine-grained sandstones (L0) and coarse-grained siltstone (L1) both exhibit a significant fraction of their population of samples in common, permeabilities of the sandstones are 3-20X greater than coarse-grained siltstones with the same porosity (Figure 4.2.49). Though it is likely there is more difference between the shaly fine- to medium-grained siltstones (L2) and the coarse siltstones (L1), the significant scatter in the L2 data preclude good $k_{ik}-\phi_i$ trend analysis. The large scatter and comparatively high permeabilities of some shaly siltstones may represent core samples with fine-scale bedding of different properties or might have contained microfractures. The shaly siltstones are fairly fissile, particularly when oven-dried, and the development of microfractures, especially in the lower porosity samples is possible.

The marine very fine- to fine-grained sandstones and the continental very fine to fine-grained sandstones exhibit a similar $k_{ik}-\phi_i$ trend within 2X in the porosity range $12 < \phi_i < 20\%$. At lower porosity the marine sandstone exhibit significantly lower permeability possibly due to greater clay content. For $\phi_i > 12\%$, the marine very fine to fine-grained sandstones (L10) exhibit only approximately 1-3X times greater permeability than marine

siltstone (L3). Below $\phi_i < 12\%$ the sandstones may exhibit lower permeability; however, the siltstone trend is influenced by several samples at low porosity ($\phi_i < 8\%$) and comparatively high permeability ($k_{ik} > 0.1$ md) which, as with the continental siltstones, may represent samples with microfracturing.

The limestone lithofacies (L4, L5, L7, L8) exhibit subparallel permeability-porosity trends (Figure 4.2.51) with greater permeability at a given porosity, increasing mean porosity (Figure 4.2.18), increasing uppermost porosity range, and increasing mean permeability from mudstone/mud-wackestone (L4) through phylloid algal bafflestone (L8). High permeabilities in the phylloid algal bafflestones (L8) result from dissolution of the phylloid algae frequently leaving a connected moldic porosity network. This pore system can exhibit permeabilities of $k_{ik} > 10$ -100 md. However, where moldic porosity is developed but the molds are not touching, the permeability is reduced to the low values of commonly infilling mudstone matrix. The difference in permeability between lithofacies L8 and the next most permeable lithofacies, the packstone/grainstones (L7) ranges from 10-30X at any given porosity. The differences between the wackestone/wacke-packstones (L5) and the packstones/grainstones (L7) is not as great, ranging from 6-3X for $4\% < \phi_i < 20\%$.

The medium-crystalline sucrosic moldic dolomite lithofacies represents one of the most important reservoir rocks in the upper Chase and in the Grant and Stevens County areas. Comparing the medium- (L9) and very fine to fine-crystalline sucrosic dolomite (L6), the decrease in crystal size results in a decrease in permeability of a factor of 10X.

Some lithofacies in some stratigraphic intervals exhibit k_{ik} - ϕ_i trends that are sufficiently different from the general lithofacies k_{ik} - ϕ_i trend that a unique k_{ik} - ϕ_i equation is warranted to improve permeability prediction. Notably the wackestone/wacke-packstone lithofacies (L5) in the Krider, Winfield and Ft. Riley exhibit better permeability, and marine sandstones (L10) in the Herington, Krider, Towanda, and Florence (basal Ft. Riley) exhibit permeabilities at a given porosity sufficiently different from the general trend that separate equations were constructed. Table 4.2.7 shows the equation parameters for the intervals and lithofacies for which unique equations were developed.

Water Saturation and Capillary Pressure

It is important to take into account the presence of water in the pore space of low-permeability reservoirs both for accurate volumetric calculations and because water occupies critical pore-throat space and can greatly diminish gas permeability, even in rocks at “irreducible” water saturation (S_{wi}). In the Hugoton, determination of formation water saturation from electric wireline-log response is problematic because of deep mud filtrate invasion with conventional mud programs due to the low reservoir pressure (Olsen et al., 1997; George et al., 2004). Because water saturations can not be reliably determined for most wells using logs, saturations were estimated based on matrix capillary-pressure properties and determination of the free-water level (level at which gas-brine capillary pressure is zero). Air-mercury capillary pressure data were compiled

and measured for 252 samples ranging in porosity, permeability, and lithofacies, and relationships were developed that allowed the prediction of a capillary-pressure curve for any given lithofacies and porosity (data are presented in Table 4.2.9; CORE_DATA&DESCRIPTIONS_DATABASE_Appendix 4.2.2).

To examine the lithofacies dependence of threshold-entry pressure, gas-column height, and pore-throat size, laboratory capillary pressure data were converted to reservoir gas-brine capillary pressure data using the standard equation (Purcell, 1949; Berg, 1975):

$$P_{C_{res}} = P_{C_{lab}} (\sigma \cos \theta_{res} / \sigma \cos \theta_{lab}) \quad (4.2.10)$$

where $P_{C_{res}}$ is the gas-brine capillary pressure (psia) at reservoir conditions, $P_{C_{lab}}$ is the laboratory-measured capillary pressure (psia), and $\sigma \cos \theta_{res}$ and $\sigma \cos \theta_{lab}$ is the interfacial tension (σ , dyne/cm) times the cosine of the contact angle (θ , degrees) at reservoir and laboratory conditions, respectively. For the Hugoton and Panoma fields, the gas-brine interfacial tension is ~63-65 dyne/cm for the initial reservoir gas pressures of ~400-450 psi (2.8-3.1 MPa) and temperatures of 90-100 °F (32-38 °C; Hough et al., 1951; Jennings and Newman, 1971)). Conversion of capillary pressure to height above free-water level to determine the water saturation in any given rock type as a function of height above the free-water level requires conversion of capillary-pressure data to height above free-water level. This conversion was performed using the standard relation (Hubbert, 1953; Berg, 1975):

$$H = P_{C_{res}} / (C(\rho_{brine} - \rho_{gas})) \quad (4.2.11)$$

where H is the height (ft) above free-water level, $P_{C_{res}}$ is the capillary pressure (psia) at reservoir conditions, ρ_{brine} and ρ_{gas} are the density of brine and gas at reservoir conditions ($\rho_{brine} = 1.16-1.19$ g/cc and $\rho_{gas} = 0.025-0.035$ g/cc, which are reasonable intermediate values for these fields, and C is a constant (0.433(psia/ft)/(g/cc)) for converting density to pressure gradient in psia/ft.

Ignoring the small uncertainty in laboratory air-mercury interfacial tension and contact angle, from equation 4.2.11, height calculations are sensitive to uncertainty in reservoir gas-brine interfacial tension (IFT, which controls $P_{C_{res}}$), gas density, and brine density. For the Hugoton system the estimated range for each of these variables is

$$\begin{array}{ll} 57 \text{ dyne/cm} < \text{IFT} < 67 \text{ dyne/cm}; & \text{for } P = 1,500 \text{ psi} - 115 \text{ psi}; T=90-100^\circ\text{F} \\ 0.008 \text{ g/cc} < \rho_{gas} < 0.11 \text{ g/cc}; & \text{for } P = 1,500 \text{ psi} - 115 \text{ psi}; T=90-100^\circ\text{F} \\ 1.10 \text{ g/cc} < \rho_{brine} < 1.19 \text{ g/cc}; & \text{for } P = 1,500 \text{ psi} - 115 \text{ psi}; T=90-100^\circ\text{F} \end{array}$$

For this range in uncertainty, the height above free-water level conversions exhibit an average error of 4.5%. For this uncertainty a calculated height of 1,000 ft might be 955 feet or 1,045 feet or a height of 100 ft might be 95.5 feet or 104.5 feet.

From the air-mercury capillary pressure data, pore-throat diameter was calculated using the modified Washburn (1921) relation:

$$d = 4C\sigma\cos\theta/Pc \quad (4.2.12)$$

where Pc = capillary pressure (psia), $C = 0.145$ ((psia·cm·μm)/dyne), θ = contact angle (140 degrees), σ = interfacial tension (484 dyne/cm), and d = pore-throat diameter (μm, microns). This relation assumes that the nonwetting phase (i.e., gas) enters the pores through circular pore-throats.

For the purpose of converting air-mercury capillary pressure data to gas-brine capillary pressure data and gas-brine height above free-water level at reservoir conditions, the following properties were assumed: $\rho_{\text{gas}} = 0.031$ g/cc, $\rho_{\text{brine}} = 1.16$ g/cc, CH₄-brine IFT = 64 dyne/cm, air-mercury IFT = 484 dyne/cm, air-mercury contact angle = 140 degrees, CH₄-brine contact angle = 0 degrees. These values are appropriate for the saturated brine present in the Hugoton and for the natural gas in the Hugoton at 400-450 psi.

Figure 4.2.53 illustrates selected capillary pressure curves for samples of different permeability. Differences among capillary pressure curves for the various lithofacies correspond to variations in threshold-entry pressure, pore-throat diameter, and water saturation for various gas-column heights above the free-water level, including the thickness of the transition zone from $S_w = 100\%$ to approximately “ S_{wi} ”.

Capillary pressures and corresponding water saturations (S_w) vary among lithofacies, and with porosity/permeability and gas-column height. Threshold-entry pressures and corresponding heights above free-water level are well correlated with permeability (Figure 4.2.54) where RMA and LRA provide the following equations:

$$H_{te} = 21.22 k_{ik}^{-0.433} \quad : \text{LRA (SE = 2.3X)} \quad (4.2.13)$$

$$H_{te} = 20.13 k_{ik}^{-0.486} \quad : \text{RMA (Se = 2.4X)} \quad (4.2.14)$$

Where H_{te} = threshold-entry height (feet) and k_{ik} is the *in situ* Klinkenberg permeability (md). This correlation is consistent with, and derivative from, the relationship between pore-throat size and permeability (Figure 4.2.28). Figure 4.2.54 shows that given an approximate maximum gas column height in the Hugoton of 550 feet, for rocks with *in situ* Klinkenberg gas permeability below approximately $k_{ik} < 0.0001$ - 0.003 md (0.1 - 3×10^{-6} μm²), threshold-entry heights are greater than the gas-column heights available in the Hugoton and therefore the samples have $S_w=100\%$. As gas column heights decrease from west to east across the field, the required permeability for gas entry increases.

Although the H_{te} - k_{ik} correlation is good, permeability data are not widely available for prediction and a model that utilizes porosity as the independent variable is more applicable. For this reason H_{te} - ϕ_i correlations were developed for geomodel construction.

Capillary-pressure properties differ between lithofacies in the Hugoton and differ within lithofacies between rocks of different porosity/permeability. With the significant fraction of Hugoton rocks exhibiting low permeability ($k_{ik} < 1$ md, 80%; $k_{ik} < 0.1$ md, 56%; $k_{ik} < 0.01$ md, 35%), it is important to precisely model the exact capillary-pressure

relationships to accurately model water saturation in the field. Utilizing the 252 air-mercury drainage capillary-pressure curves, measured on a range of lithofacies, equation parameters to construct generalized capillary-pressure curves were developed using: 1) capillary threshold-entry pressure, and 2) the slope of the $\log P_c$ - $\log S_w$ curve, reflecting pore-size distribution, using a modification of the Brooks and Corey (1966) lambda-function method. Converting capillary pressures to height above free-water level using the fluid properties discussed above, a synthetic capillary-pressure curve (expressed as height above free-water level, H_{afwl} , and water saturation, S_w) can be modeled using two parameters: Gas-water threshold-entry height (feet), H_{te} , and a dimensionless measure of the pore-size heterogeneity fractal dimension, H_f , represented by the slope of the $\log H_{afwl}$ - $\log S_w$ curve:

$$H_{te} = C \phi_i + D \quad (4.2.15)$$

$$\log_{10} H_f = A \phi_i + B \quad (4.2.16)$$

Where A, B, C and D are constants for each lithofacies. Using the capillary pressure parameters calculated for any given porosity using equations 4.2.15-4.2.16, water saturation can be calculated for any given porosity sample at any given gas column height using:

$$S_w = E h^F \quad (4.2.17)$$

where:

$$E = \left[\frac{1}{\frac{H_{te}}{100^{H_f}}} \right]^{1/H_f} \quad (4.2.18)$$

$$F = 1/H_f \quad (4.2.19)$$

where h is the gas column height above free-water level (ft), H_{te} is the gas-water threshold-entry height (ft), H_f is the dimensionless measure of pore-size heterogeneity, and S_w is the water saturation (%) at height, h .

Figure 4.2.55 illustrates the relationship between H_{te} and ϕ_i for all lithofacies. This relationship for all lithofacies is poorer than the H_{te} - k_{ik} relationship because the porosity – pore-throat size distribution correlation exhibits large variance, as evident in the k_{ik} - ϕ_i relationship for all rocks not separated by lithofacies. To be consistent with the power-law relationship between k_{ik} - ϕ_i , it is appropriate to also use a power-law relationship between H_{te} and ϕ_i . Such a relationship more accurately represents the correlation over the complete range of H_{te} but compromises the relationship at low porosity to accommodate the relationship at high porosity. It is apparent from Figure 4.2.55 that at $\phi_i > 18\%$, H_{te} is less than 20 ft and is generally less than 10 ft. These values of H_{te} are sufficiently small that accurate prediction would not change the geomodel saturations. That is, error in prediction of zero to 10 ft would not change predicted saturations in a

geomodel; and therefore, there is no significant difference in the resulting water saturation calculated from a modeled capillary-pressure curve for any prediction less than 10 ft except for the small volume of high-porosity reservoir rocks within 10 feet of the free-water level. Therefore, to improve accuracy in the range of porosity where accurate H_{te} values are most important, log-linear relationships between H_{te} and ϕ_i were developed (Figure 4.2.56). To improve the prediction of the H_{te} term, correlations of H_{te} versus ϕ_i were developed for each lithofacies or group of lithofacies. These correlations are shown in Figures 4.2.57-4.2.60. Table 4.2.8 presents the constants (A,B,C,D) for H_f and H_{te} for each lithofacies and the standard error of prediction for equations 4.2.15 and 4.2.16.

Average standard error of prediction for equation 4.2.15 for all lithofacies is a factor of 3X with a standard deviation of 0.8X. For error in predicted H_{te} , higher threshold-entry heights exhibit greater error. For example, for a predicted threshold-entry height, $H_{te} = 100$ ft, 67% of the population exhibits $33 \text{ ft} < H_{te} < 300 \text{ ft}$. For a predicted threshold-entry height, $H_{te} = 30$ ft, 67% of the population exhibits $10 \text{ ft} < H_{te} < 90 \text{ ft}$. For most lithofacies for $\phi_i > 10\text{-}13\%$, H_{te} is less than 50 ft and for lithofacies L7, L8 and L9, $H_{te} < 50$ ft for porosity approaching zero. For clastic rocks with porosity $\phi_i > 20\%$, equation 4.2.15 predicts $H_{te} < 10$ ft. As noted this error is negligible in saturation modeling of the Hugoton where basal Council Grove porosities are low.

Over 90% of all Hugoton rocks tested for capillary pressure exhibit a unimodal pore system or a significant fraction of the pore volume from $10\% < S_w < 100\%$ which can be modeled using a single $\log H_{afwl} - \log S_w$ function. Regression coefficients of correlation between $\log H_{afwl}$ and $\log S_w$ for over 90% of all samples exceeded $R^2 = 0.94$, and 65% exhibited R^2 between 0.98 and 1.00. Using linear regression analysis the dimensionless height fractal slope, H_f , of all 252 capillary pressure samples were determined and correlated with porosity (Figure 4.2.62). This correlation exhibits wide scatter for all lithofacies undifferentiated but gives improved correlation on a lithofacies-specific basis.

Figures 4.2.63 through 4.2.66 show the crossplot of the dimensionless height fractal slope, H_f , and *in situ* porosity for the continental clastic, marine clastic, limestone, and dolomite lithofacies groups. Figures 4.2.63 and 4.2.64 both show different relationships for the sandstones than for the siltstones with cross-over at approximately 15% porosity. For the sandstones, the increase in H_f with increasing porosity above 15% may be related to increasing sorting, decreasing clay content, and a resulting decrease in pore-size heterogeneity and consequent increase in H_f . It can be hypothesized that as the sandstones get “cleaner” and improve in porosity, they also become more uniform. The siltstones exhibit an opposite trend to the sandstones with increasing H_f with decreasing porosity. It can be proposed that this may reflect a progressive increase in clay content with decreasing porosity and a consequent shift to pores that are defined principally by the presence of clay particles. The pore-throat size distribution of shales is often lower than for siltstones and the trends for siltstones in both figures support the interpretation that at very low porosity the accessible pore-throat size distribution is narrow. The cross-over or “minimum” in the siltstone-sandstone system may be interpreted to reflect a region of maximum mixing of grain sizes and/or beds of varied lithofacies. Although the

mechanism to explain these trends is unproven, the utility of the parameters for use in equation 4.2.16 is still viable.

Each of the limestone lithofacies (Figure 4.2.65) exhibit slightly unique trends (Figure 4.2.65). The mudstone/mud-wackestone (L4), wackestone/wacke-packstone (L5) and phylloid algal bafflestone (L8) lithofacies exhibit decreasing H_f with increasing porosity. A clear trend was not evident for the packstone/grainstone lithofacies (L7) and the trend line shown effectively represents an average H_f with a standard error in predicting H_f of ± 0.55 (1 s.d.).

Using equations 4.2.15 through 4.2.19 and the values for the constants presented in Table 4.2.8, water saturations can be calculated for any given porosity for any lithofacies at any given height above free-water level. These equations form the basis for assigning unique water saturations to each of the 108-million cells in the geomodel depending on the lithofacies, porosity, and H_{afwl} of the cell.

Capillary-pressure curves, expressed as H_{afwl} versus S_w for each lithofacies (Figure 4.2.67-4.2.77) illustrate that with decreasing porosity (and associated permeability), threshold-entry heights and transition-zone heights increase. Although transition-zone heights increase with decreasing porosity, many lithofacies exhibit increasing H_f values with decreasing porosity. This would imply that the pore-throat size distribution is decreasing and therefore the transition zone height at a fixed threshold entry height would decrease. However, the transition-zone height is tied to the threshold-entry height (H_{te}), and so a decreased H_f is associated with increasing H_{te} giving a net result of increasing transition-zone height. The phylloid algal bafflestones (Figure 4.2.75) provide an example where the H_{te} does not increase sufficiently to offset decreasing H_f . The result is that the curves for high- and low-porosity rocks cross, and low-porosity rocks exhibit lower water saturation than high-porosity rocks at high values of H_{afwl} . This trend is based on only five capillary pressure samples and may be incorrect, but it can be postulated that as porosity decreases in bafflestones a larger fraction of the pore volume is moldic porosity, which exhibits lower water saturation. If this occurs, then low-porosity bafflestones could exhibit lower water saturation than high-porosity bafflestones because the water in the higher porosity rocks resides in the microporous matrix that would retain water even at high values of H_{afwl} .

Example capillary pressure curves, expressed as height, for all 11 lithofacies at 10% porosity (Figure 4.2.78) illustrate the significant differences in S_w that can exist among lithofacies at any given height above free-water level. Differences decrease with increasing height, and saturations for all lithofacies approximately approach a similar “irreducible” saturation at gas column heights above ~300 ft (90 m) except for low porosity rocks where saturation differences are still evident. Differences in the capillary pressure properties between lithofacies also decrease as porosity and permeability increase.

Relative Permeability

Limited work has been performed on the relative permeability of Hugoton rocks and even less has been published. As discussed, a significant fraction of Hugoton rocks exhibit low permeability with over 50% exhibiting $k_{ik} < 0.1$ md and over 75% exhibiting $k_{ik} < 1$ md. Little research has been reported on the relative permeability properties of low-permeability carbonate rocks though a significant amount of work has been published on low-permeability sandstones (Byrnes, 2005). Though they have different mineralogy, the petrophysics of thin, sheetlike tabular pore networks is similar. Comparison of “tight” gas sandstones and “tight” gas carbonates was presented by Byrnes et al. (2001). To provide relative permeability models for the geomodel construction, gas-water drainage relative permeability data were compiled for 32 samples representing a range of lithofacies. (CORE_DATA&DESCRIPTIONS_DATABASE_Appendix 4.2.3) These data did not test the relative permeability for rocks with absolute permeability $k_{ik} < 0.1$ md and did not include an adequate population of continental fine- to coarse-grained siltstones. To model the continental and marine clastics, equations developed for other low-permeability clastics, and summarized recently (Byrnes, 2005), were adopted and are discussed below.

In general, gas and water drainage relative permeability curves for the Hugoton samples reveal several characteristics similar to other low-permeability rocks. Water permeability, even at 100% S_w , is less than Klinkenberg gas permeability and decreases with decreasing permeability. Gas relative permeability is less than the absolute gas permeability at all water saturations greater than zero and gas relative permeability decreases significantly as S_w increases above 50%. Gas and water relative permeability was modeled in the carbonates and low-permeability siltstones and sandstones using the modified Corey (1954) equations: $k_{rg} = (1 - (S_w - S_{wc,g}) / (1 - S_{gc} - S_{wc,g}))^p (1 - ((S_w - S_{wc,g}) / (1 - S_{wc,g})))^q$ and $k_{rw} = ((S_w - S_{wc}) / (1 - S_{wc}))^r$, where S_w = water saturation, S_{gc} = critical gas saturation (expressed as fraction gas saturation), $S_{wc,g}$ = critical water saturation for gas equation (expressed as fraction water saturation), S_{wc} = critical water saturation, and p , q , and r are exponents reflecting pore-size distribution and architecture. The following text examines some aspects of water and gas relative permeability.

Water Permeability

Based on the lack of significant water production for many areas of the Hugoton, most of the rocks can be characterized as at or near “irreducible” water saturation (S_{wi}) or critical water saturation (S_{wc}). Critical water saturation can be defined as the saturation at which water is immobile or is nearly immobile on the time scale of importance for the evaluation of flow properties. Critical water saturation can also be defined as the saturation at which the ratio of water flow to nonwetting phase (i.e. gas or oil) flow is less than a specified value, such as 0.0001 (i.e. water flow represents less than 0.0001 of total flow). In high-permeability rocks S_{wc} is easily observed and defined in the field and laboratory, but in low-permeability rocks the extremely low flow rates of water even above S_{wc} make measurement of water relative permeability and definition of S_{wc} difficult.

Brine permeabilities in limestones of the Chase and Council Grove Groups in the Hugoton exhibit values significantly less than corresponding Klinkenberg permeabilities. The trend between *in situ* permeability to water (k_{iw}) and *in situ* Klinkenberg permeabilities can be characterized as

$$k_{iw} = 0.39 k_{ik}^{0.89} \quad (4.2.20)$$

The trend was defined by Jones and Owens (1980) for tight gas sandstones:

$$k_{iw} = k_{ik}^{1.32} \quad (\text{for } k_{ik} < 1 \text{ md}) \quad (4.2.21)$$

It is important to note that the Jones and Owens (1980) trend has $k_{iw} = k_{ik}$ at $k_{ik} = 1$ md, but the Hugoton rocks exhibit $k_{iw} < k_{ik}$ even at $k_{ik} > 1$ md. For the permeability range of comparison ($k_{ik} < 1$ md), the Hugoton carbonate rocks appear to exhibit lower permeability than sandstones. However, examining just the carbonate brine permeability values for $k_{ik} < 1$ md, the Hugoton samples might follow the Jones and Owen (1980) trend. If the samples with $k_{ik} < 1$ md are excluded from the trend analysis, the trend between brine and Klinkenberg permeability can be expressed:

$$k_{iw} = 0.32 k_{ik}^{0.98} \quad (4.2.22)$$

This trend indicates that cores with $k_{ik} > 1$ md exhibit brine permeabilities that are ~32% of Klinkenberg gas permeabilities.

Gas and Water Relative Permeability

Table 4.2.10 summarizes measured drainage gas-water relative permeability data for Hugoton rocks. The data primarily represent measurements on cores with absolute permeability greater than 0.5 md and half have permeability greater than 3 md.

Figure 4.2.80 shows a summary of all the drainage-gas relative permeability curves. These curves exhibit similar subparallel trends. To model the gas relative permeability, a modified Corey (1954) equation was used:

$$k_{rg} = (1 - (S_w - S_{wc,g}) / (1 - S_{gc} - S_{wc,g}))^p (1 - ((S_w - S_{wc,g}) / (1 - S_{wc,g}))^q) \quad (4.2.23)$$

where S_w is fractional water saturation, S_{gc} is the fractional critical gas saturation, $S_{wc,g}$ is the fractional critical water saturation with respect to gas drainage (discussed below), and p and q are empirical exponents expressing pore-size distribution influence. Corey (1954) derived his empirical equation from a synthesis of work by Burdine (1953) and assigned a value of 2 to p and q consistent with work by Carman (1937) on isotropic, homogeneous porous media and consistent with experimental data obtained on high-permeability sandpicks and consolidated sandstones. In this equation the first term, $((1 - (S_w - S_{wc,g}) / (1 - S_{gc} - S_{wc,g}))^p)$, and second term, $(1 - ((S_w - S_{wc,g}) / (1 - S_{wc,g}))^q)$, represent the influence of tortuosity and the mean hydraulic radius, respectively, on relative

permeability. Corey (1954) found for a large number of rock types, generally with $k > 10$ md, p and q were approximately 2 although it was recognized that p and q can change with pore structure. Brooks and Corey (1966) more thoroughly investigated the nature of pore-size distribution influence on relative permeability.

For the Hugoton rock samples studied, the gas relative permeability curves could be modeled using exponents of $p = 1.3 \pm 0.4$ (1 s.d.), $q = 2$, and $S_{wc,g} = 0$.

It is important to note that in Equation 4.2.23 critical water saturation is defined by $S_{wc,g}$ and not S_{wc} , and k_{rg} is not defined for water saturations less than the critical water saturation, S_{wc} . At water saturations below the critical water saturation it can be assumed the non-wetting phase (i.e., gas) relative permeability is effectively 1 and the wetting phase relative permeability is effectively zero. Gas-permeability measurements on tight-gas sandstone at water saturations below S_{wc} however, show that k_{rg} at $S_w < S_{wc}$ is less than 1. To model this property, the Corey equation has been modified to the form shown in Equation 4.2.23 by defining separate terms for critical water saturation with respect to gas flow ($S_{wc,g}$) and with respect to water flow (S_{wc}). The $S_{wc,g}$ term is used only in the Corey gas relative permeability equation (Equation 4.2.23), and the S_{wc} term is used in the Corey water relative permeability equation (Equation 4.2.24) discussed below. The $S_{wc,g}$ term defines the role of water with respect to gas flow and does not relate to water flow or water saturations that necessarily exist in reservoirs. For example, many low-permeability rocks exhibit measured $k_{rg} < 1$ at $S_w < S_{wi}$. For these measurements S_w was achieved by methods such as evaporation representing capillary forces that are not realized in nature. The fact that k_{rg} is less than 1 indicates that $S_{wc,g}$ must be less than the saturation at which the measurement was performed because, by definition in Equation 4.2.23, $k_{rg} = 1$ at $S_{wc,g}$.

To model gas relative permeability in the low-permeability sandstones and siltstones ($k_{ik} < 1$ md) trends developed for low-permeability rocks in other regions were used. Relative gas permeability data, representing k_{rg} values obtained at a single S_w , and complete k_{rg} curves with k_{rg} values obtained for single samples at several saturations, were previously compiled from published studies (Thomas and Ward, 1972; Byrnes et al., 1979; Jones and Owens, 1980; Sampath and Keighin, 1981; Walls, 1981; Ward and Morrow, 1987; Byrnes, 1997; Castle and Byrnes, 1998; Byrnes and Castle, 2000; Byrnes, 2005) and from unpublished data. Figure 4.2.81 illustrates gas relative permeability curves for 43 core plug samples from various western low-permeability formations from seven of the studies cited. For most of the studies, water saturations were achieved by both drainage gas displacement of water (i.e., water saturation successively decreasing) and by evaporation. The curves for all samples have been referenced to k_{ik} at $S_w = 0\%$. No trend with lithofacies or absolute permeability could be discerned that would improve gas relative permeability prediction, and average trend values were used.

The gas relative permeability curves shown in Figure 4.2.81 for low-permeability sandstones are defined by the Corey-type Equation 4.2.23 with the following empirical parameters:

$$S_{wc,g} = 0.16 + 0.053 \cdot \log_{10} k_{ik} \quad (\text{for } k_{ik} \geq 0.001 \text{ md}) \quad (4.2.24)$$

$$S_{wc,g} = 0 \quad (\text{for } k_{ik} < 0.001 \text{ md}) \quad (4.2.25)$$

$$S_{gc} = 0.15 - 0.05 \cdot \log_{10} k_{ik} \quad (4.2.26)$$

$$p = 1.7 \quad (4.2.27)$$

$$q = 2 \quad (4.2.28)$$

where $S_{wc,g}$ and S_{gc} are expressed in fractions and k_{ik} is expressed in md. It is important to note the difference in how $S_{wc,g}$ and S_{gc} are expressed; $S_{wc,g}$ is the critical water saturation expressed as fraction of pore volume occupied by water, S_{gc} is the critical gas saturation (saturation below which gas is immobile) expressed as fraction of pore volume occupied by gas. The bounding Corey-equation curves utilize values for $S_{wc,g}$ and S_{gc} for rocks with permeability of 0.001 md and 1 md, which approximate the range of permeabilities of the samples for which relative permeability data are shown. Using Equation 4.2.24, $S_{wc,g} = 0.21$ for $k_{ik} = 10$ md and approaches $S_{wc,g} = 0$ as k_{ik} approaches 0.001 md. Conversely, $S_{gc} = 0.10$ for $k_{ik} = 10$ md and approaches $S_{gc} = 0.30$ as k_{ik} approaches 0.001 md.

To model water relative permeability a modified Corey (1954) equation was used:

$$k_{rw} = ((S_w - S_{wc}) / (1 - S_{wc}))^q (k_w / k_{ik}) \quad (4.2.29)$$

Figure 4.2.82 illustrates the range of water relative permeability curves. The average curve (black) was defined using an exponent value of $q = 8.3$. The bounding gray curves represent values of $q = 11.3$ and $q = 5.3$.

Critical water saturations shown here are consistent with saturations obtained at high capillary pressures, reflecting small pore-throats and low permeability. In reality, water may be mobile at very low water saturations, but flow rates are extremely low. Though these rates may be less than those of concern for reservoir production, they are important in explaining the presence of low water saturations in some reservoirs, in integrating relative permeability critical water saturations with observed water saturations, and in modeling possible water movement in the reservoir over periods of decades.

Vertical Permeability

Vertical permeability in the Hugoton represents a critical variable because it controls migration of gas from higher pressure, low-permeability intervals to more depleted, low pressure, high permeability interval either above or below. Figures 4.2.83 through 4.2.90 show the frequency distribution of the ratio (K_{vert} / K_{havg}) of full-diameter routine vertical air permeability (K_{vert}) to the average horizontal air permeability (K_{havg}). K_{havg} was calculated as the arithmetic average of K_{max} and K_{90} . Where K_{max} was more than 5X greater than K_{90} , it was assumed that the core might contain a fracture and the K_{vert} / K_{havg} ratio was not calculated. Also where K_{vert} / K_{havg} was greater than 1, it was assumed that a fracture might be present. Summary statistics are presented in Table 4.2.11.

These figures show that the ratio of vertical to horizontal permeability can vary widely for each lithofacies. With such wide distributions averages must be used with caution especially with the presence of a large fraction with very low values where the presence of a few high values can significantly influence the average. If a population is uniformly distributed an arithmetic average can be considered representative though it exhibits large variance. Where the population is heavily skewed to low values, as the Hugoton rocks are, the arithmetic average is biased to high values and the arithmetic mean may not be considered an appropriate description of the population. It is also important to note that the K_{vert}/K_{havg} values used were measured under routine air permeability conditions that involve lower confining stress. Increased confining stress affects lower permeability rocks more than higher permeability rocks and generally decreases vertical permeability more than horizontal permeability. To represent the population a logarithmic distribution was analyzed.

For the continental sandstones, K_{vert}/K_{havg} averages 14%. Limited data for the very fine to fine-grained sandstones indicate a higher average for the L0 lithofacies near 17%. Marine siltstones and sandstones exhibit a average of 18%. Within the limestone lithofacies the mudstone/mud-wackestone exhibits low K_{vert}/K_{havg} (17%), with the remaining lithofacies exhibiting significantly higher K_{vert}/K_{havg} : L5-30%, L7-38%, and L8-25%. The dolomite lithofacies exhibit the highest K_{vert}/K_{havg} with L6-37% and L9 – 33%. Average K_{vert}/K_{havg} for the basic lithofacies groups are: continental siliciclastics-14%, marine siliciclastics – 18%, limestones-32%, and dolomites-34%.

Permeability At Different Scales

Fundamental to modeling the permeability distribution in the Hugoton is the need to understand the relative role of matrix and fracture flow and the possible scale dependence of permeability. Figure 4.2.23 showed that for rocks below approximately 8% porosity, or approximately 0.5 md ($0.0005 \mu\text{m}^2$), microfractures in core significantly increased permeability. A fundamental question for these data is are the microfractures present in the subsurface or are they a stress release or coring-induced phenomenon? This question can only be answered by comparing upscaled matrix permeabilities with unfractured full-diameter permeabilities and with drill stem test (DST) or well test calculated permeabilities. Comparing carefully examined unfractured full-diameter porosity and permeability values with core plug values measured on plugs taken from the full-diameter cores (Figures 4.2.91 and 4.2.92) indicates that for homogenous samples, matrix properties apply to the full-diameter core scale. Permeability-porosity trends for core plugs compared to full-diameter core in a study well indicates that the full-diameter trend is similar to the core plug with the exception of a portion of the low-porosity cores that may have had permeability influenced by microfractures (Figure 4.2.93)

The ability to compare well-scale permeability with matrix permeability is limited because so few wells have DST or well test data for thin intervals for which core data are available and which were tested prior to hydraulic fracturing, which complicates artificial fracture-enhanced permeability with reservoir permeability. In four key research wells,

permeability was measured using DST for multiple intervals for which core analysis was also performed. To compare with core permeabilities, full-diameter and plug permeabilities were arithmetically averaged (representing parallel flow contribution from each depth interval) to determine average interval permeabilities. Correlation between DST, and upscaled full-diameter and plug core permeabilities (Figure 4.2.94) shows good correlation for intervals with permeability greater than ~ 0.5 md ($0.0005 \mu\text{m}^2$). For interval permeabilities below 0.5 md ($0.0005 \mu\text{m}^2$), full-diameter permeabilities exhibit nearly constant permeability between 0.5 and 3 md (0.0005 - $0.000033 \mu\text{m}^2$), characteristic of microfracture-influenced permeability. Matrix-scale plug permeabilities can be either higher or lower than DST permeabilities.

Variance in the DST-matrix permeability correlation is partially or predominantly related to the limited vertical sampling of the core plugs and difficulty in representing some pore properties that are larger in scale than core plugs. The single phylloid algal bafflestone interval exhibits significantly lower matrix permeability because core plugs did not sample the larger-scale vuggy nature of this lithofacies, which exhibits high permeability. Because microfractures do not contribute significantly to measured permeability for rocks with permeability greater than 0.5 md ($0.0005 \mu\text{m}^2$), both full-diameter and plug data reflect matrix properties and the good correlation with DST permeabilities indicates that the reservoir is not fractured at the scale of investigation of the DST test. The better correlation of plug and DST permeabilities for intervals with permeability below 0.5 md, and the fact that upscaled permeabilities from plug data are greater than or equal to DST permeabilities for three of four intervals can be interpreted to indicate that these intervals are also unfractured. These data, and less precise data from other wells, indicate that the production characteristics of many wells in the Hugoton are consistent with matrix properties control of flow, without significant natural fracture contribution. Data and statistics on the fraction of wells that exhibit production greater than what would be predicted from matrix properties have not yet been compiled and calculated.

Electrical Properties

As noted above, in the Hugoton, determination of formation water saturation from electric wireline-log response is problematic because of deep mud filtrate invasion with conventional mud programs due to the low reservoir pressure (Olsen et al., 1997; George et al., 2004). Although wireline logs cannot be easily interpreted in the low-pressure gas zones, invasion is more limited in water saturated intervals and wireline-log analysis is feasible in these intervals. This possibility is important for determining water-saturated intervals and the free-water level. It is also important to define rock electrical properties in the event that some log analysis is attempted.

To evaluate electrical log properties Archie cementation exponent data were compiled and measured on 239 core samples, representing the range of lithofacies from 15 wells. In addition, Archie saturation exponent data were obtained for 126 samples. All cementation exponent data were measured under *in situ* confining stress (i.e., confining stress greater than $1,000$ psi). These data are tabulated in Table 4.2.1 (Appendix 4.2.1). Figure 4.2.95 illustrates the range of cementation exponents (where the Archie intercept $a = 1$) for the

range in porosity. Though some rocks can exhibit a decrease in m with decreasing porosity, all lithofacies except L7 exhibit no significant correlation with porosity. The packstone/pack-grainstone lithofacies (L7) exhibits a weak decrease in m with decreasing porosity. It is also evident in Figure 4.2.95 that some lithofacies exhibit cementation exponent values below the “standard” value exhibited by interparticle porosity rocks of $m=2$. Lithofacies exhibiting low mean cementation exponent values include the lower-porosity continental shaly siltstone (L2), marine siltstones (L3), and lime mudstone/wackestone (L4). Values greater than ~ 2.5 represent cores with moldic porosity. Within this group the very-fine crystalline sucrosic dolomite lithofacies frequently displays high cementation exponents. Figure 4.2.96 shows that, exclusive of the moldic rocks, the distribution of cementation exponents for all rocks are approximately normally distributed about the mean value of $m = 1.96 \pm 0.15$ (1 s.d.). Mean Archie saturation exponents for all lithofacies average $n = 1.83 \pm 0.31$ (1 s.d.) but mean values are greater and less for different lithofacies (Figure 4.2.97). The frequency distribution for these saturation exponents is not normally distributed, exhibiting a mode near $n = 1.7$ with a slight skewness to values of $1.9 < n < 2.3$. There is no correlation of saturation exponents with porosity for any lithofacies (Figure 4.2.98).

References

- Berg, R. R., 1975, Capillary pressures in stratigraphic traps: American Assoc. Petroleum Geologists Bulletin, v. 59, p. 939-956.
- Brooks, R. H., and Corey, A. T., 1966, Properties of porous media affecting fluid flow: J. Irrig. Drainage Div., v. 6 (June 1966), p. 61-88.
- Burdine, N. T., 1953, Relative permeability calculations from pore-size distribution data, Petroleum Transactions Am. Inst. Mechanical Engineers, v. 198, p. 71-77.
- Byrnes, A. P., 1997, Reservoir characteristics of low-permeability sandstones in the Rocky Mountains: The Mountain Geologist v. 43, no. 1, p. 39-51.
- Byrnes, A. P., and Castle, J. W., 2001, Comparison of core petrophysical properties between low-permeability sandstone reservoirs: Eastern U.S. Medina Group and Western U.S. Mesaverde Group and Frontier Formation: SPE 60304 Proceedings of the 2000 SPE Rocky Mountain Regional/Low Permeability Reservoirs Symposium, Denver, CO, March 12–15, 2000, p. 10.
- Byrnes, A. P., and Keighin, C. W., 1993, Effect of confining stress on pore-throats and capillary pressure measurements, selected sandstone reservoir rocks, American Association of Petroleum Geologists Annual Convention Program Abstracts, April 25-28, New Orleans, p. 82.
- Byrnes, A. P., Sampath, K., and Randolph, P. L., 1979, Effect of pressure and water saturation on the permeability of western tight sandstones: Proceedings of the 5th Annual U.S. Dept. Energy Symposium on Enhanced Oil and Gas Recovery, Tulsa, Oklahoma, August 22-26, 1979, p. 247-263.

Byrnes, A. P., Dubois, M. K., and Magnuson, M., 2001, Western tight gas carbonates: comparison of Council Grove Group, Panoma Field, southwest Kansas and western low permeability sandstones: 2001 American Assoc. Petroleum Geologists Annual Convention Official Program, Denver, CO, p. A31.

Byrnes, A. P., 2003, "Aspects of Permeability, Capillary Pressure, and Relative Permeability Properties and Distribution in Low-Permeability Rocks Important to Evaluation, Damage, and Stimulation", Proceedings Rocky Mountain Association of Geologists – Petroleum Systems and Reservoirs of Southwest Wyoming Symposium, Denver, Colorado, September 19, 2003, 12 p.

Byrnes, A. P., 2005, "Permeability, capillary pressure, and relative permeability properties in low-permeability reservoirs and the influence of thin, high-permeability beds on production", in *"Gas in Low Permeability Reservoirs of the Rocky Mountain Region"*, Rocky Mountain Assoc. of Geologists 2005 Guidebook CD, M.G. Bishop, S.P. Cumella, J.W. Robinson, and M.R. Silverman eds., p. 69-108.

Carman, P. C., 1937, Fluid flow through granular bed: Transactions of the Institution of Chemical Engineers, v. 15, p. 150-156.

Castle, J. W., and Byrnes, A. P., 1998, Petrophysics of low-permeability Medina Sandstone, northwestern Pennsylvania, Appalachian Basin: The Log Analyst, v. 39, no. 4, p. 36-46.

Castle, J. W., and Byrnes, A. P., 2005, Petrophysics of Lower Silurian sandstones and integration with the tectonic-stratigraphic framework, Appalachian basin, United States, American Assoc. Petroleum Geologists Bulletin, v. 89, no. 1 (January 2005), pp. 41-60.

Coalson, E.B., Hartmann, D. J., and Thomas, J. B., 1985, Productive characteristics of common reservoir pore types: Bull. O the South Texas Geological Society, v. 15, no. 6, (February 1985), p. 35-51.

Corey, A. T., 1954, The interrelations between gas and oil relative permeabilities, Producers Monthly, v. 19 (Nov 1954), p 38-41.

Corey, A. T., and Rathjens, C. H., 1956, Effect of stratification on relative permeability, Journal of Petroleum Technology Technical Note 393, December 1956, pp. 69-71.

Dubois, M. K., Byrnes, A. P., Bohling, G. C., Seals, S. C., and Doveton, J. H., 2003a, Statistically-based lithofacies predictions for 3-D reservoir modeling: examples from the Panoma (Council Grove) Field, Hugoton Embayment, Southwest Kansas, Kansas Geological Survey Open File Report #2003-30, 3 panels.

Dubois, M. K., Bohling, G. C., Byrnes, A. P., and Seals, S. C., 2003b, "Extracting lithofacies from digital well logs using artificial intelligence", Kansas Geological Survey

Open-file Report # 2003-68. www.kgs.ku.edu/PRS/publication/2003/ofr2003-68/index.html

George, B. K., Torres-Verdin, C., Delshad, M., Sigal, R., Zouioueche, R., and Anderson, B., 2004, Assessment of in-situ hydrocarbon saturation in the presence of deep invasion and highly saline connate water: *Petrophysics*, v. 45, no. 2, p. 141-156.

Heid, J. G., McMahon, J. J., Nielsen, R.F., and Yuster, S. T., 1950, Study of the permeability of rocks to homogeneous fluids, *Am Petroleum Institute Drilling and Production Practices*, p. 230-246.

Hough, E. W., Rzasa, M. J., and Wood, B. B., 1951, Interfacial tensions at reservoir pressures and temperatures; apparatus and the water-methane system: *Petroleum Transaction American Institute of Mechanical Engineering*, Tech. Pub. 3019, v. 192, p. 57-60.

Hubbert, M. K., 1953, Entrapment of petroleum under hydrodynamic conditions: *American Assoc. Petroleum Geologists Bulletin*, v. 37, p. 1954-2026.

Heyer, J. F., 1999, Reservoir characterization of the Council Grove Group, Texas County, Oklahoma, in D.F. Merriam, ed., *Transactions of the American Association of Petroleum Geologists Midcontinent Section Meeting*, Wichita, KS., p. 71-82.

Jennings, H. Y., Jr, and Newman, G. H., 1971, The effect of temperature and pressure on the interfacial tension of water against methane-normal decane mixtures, *Am. Inst. Mech. Eng. (AIME)*, v. 251, p. 171-175.

Jones, F. O., and Owens, W. W., 1980, A laboratory study of low-permeability gas sands: *Journal of Petroleum Technology*, v. 32, no. 9, p.1631-1640.

Klinkenberg, L. J., 1941, The permeability of porous media to liquids and gases, *Drilling and Production Practice*, American Petroleum Inst., pp. 200–213.

Luffel, D. L., Howard, W. E., and Hunt, E. R., 1991, Travis Peak core permeability and porosity relationships at reservoir stress, *Society of Petroleum Engineers Formation Evaluation*, (Sept 1991) p. 310-318.

Newman, G. H., 1973, Pore-volume compressibility of consolidated, friable, and unconsolidated reservoir rocks under hydrostatic loading: *Journal of Petroleum Technology* (Feb.1973), p. 129-134.

Newman, G. H., and J. C. Martin, 1977, Equipment and experimental methods for obtaining laboratory compression characteristics of reservoir rocks under various stress and pressure conditions: *SPE 6855*, 52nd Annual Tech. Conf. of SPE, Denver, CO., Oct. 9-12, (1977) 16 p.

Olson, T. M., Babcock, J. A., Prasad, K.V. K., Boughton, S. D., Wagner, P. D., Franklin,

M. K., and Thompson, K. A., 1997, Reservoir characterization of the giant Hugoton Gas Field, Kansas, American Association of Petroleum Geologists Bulletin, v. 81, p. 1785-1803.

Ostensen, R. W., 1983, Microcrack permeability in tight gas sandstone: Society of Petroleum Engineering Journal, v. 23, no. 6, p. 919-927.

Purcell, W. R., 1949, Capillary pressure – their measurements using mercury and the calculation of permeability therefrom: American Institute of Mechanical Engineers Petroleum Transactions, v. 186, p. 39-48.

Sampath, K., and Keighin, C. W., 1981, Factors affecting gas slippage in tight sandstones, paper SPE 9872, Proceedings of the 1981 SPE/DOE Symposium on Low Permeability Gas Reservoirs, Denver, CO, May 27-29 (1981) p. 409-416.

Siemers, W. T., and W. M. Ahr, 1990, Reservoir facies, pore characteristics, and flow units: Lower Permian Chase Group, Guymon-Hugoton Field, Oklahoma, Society of Petroleum Engineers proceedings 65th Annual Technical Conference and Exhibition, New Orleans, LA, September 23-26, 1990, p. 417-428, SPE #20757.

Thomas, R. D., and Ward, D. C., 1972, Effect of overburden pressure and water saturation on gas permeability of tight sandstone cores: Journal of Petroleum Technology, v. 25, no. 2, p.120-124.

Vairogs, J., Hearn, C. L., Dareing, D. W., and Rhoades, V. W., 1971, Effect of rock stress on gas production for low-permeability rocks: Journal of Petroleum Technology, v. 24, no. 9, p. 1161-1167.

Walls, J. D., 1981, Tight gas sands: permeability, pore structure and clay, SPE 9871, Proceedings of the 1981 SPE/DOE Symposium on Low Permeability Gas Reservoirs, Denver, CO, May 27-29 (1981) p. 399-409.

Walls, J. D., Nur, A. M., and Bourbie, T., 1982, Effects of pressure and partial water saturation on gas permeability in tight sands: experimental results: Journal of Petroleum Technology, April 1982 p. 930-936.

Ward, J. S., and Morrow, N. R., 1987, Capillary pressure and gas relative permeabilities of low permeability sandstone: Society of Petroleum Engineers, Formation Evaluation, Sept. 1987, p. 345-356.

Washburn, E. W., 1921, A method of determining the distribution of pore sizes in a porous material: Proceedings of the National Academy of Sciences, v. 7, p. 115-116.

Wei, K. K., Morrow, N. R., and Brower, K. R., 1986, Effect of fluid, confining pressure, and temperature on absolute permeabilities of low permeability sandstones,: Society of Petroleum Engineers, Formation Evaluation, Aug. 1986, p. 413-423.

Stratigraphic Interval	Mean Grain Density (g/cc)	Maximum Grain Density (g/cc)	Minimum Grain Density (g/cc)	Median Grain Density (g/cc)	Mode Grain Density (g/cc)	Deviation Grain Density (g/cc)	Skewness Grain Density (g/cc)	Kurtosis Grain Density (g/cc)	Sum Grain Density (g/cc)	Count Grain Density
Sumner Group	2.79	2.95	2.60	2.81	2.83	0.08	-0.29	-0.02	123	44
Herington Limestone Member	2.78	3.00	2.64	2.78	2.75	0.07	0.11	-0.71	896	322
Paddock Shale Member	2.79	2.89	2.64	2.79	2.83	0.05	-0.36	-0.18	287	103
Krider Limestone Member	2.82	2.95	2.63	2.84	2.85	0.05	-1.30	0.83	1503	533
Odell Shale Member	2.73	2.87	2.50	2.73	2.69	0.05	-0.20	1.57	472	173
Winfield Limestone Member	2.77	2.90	2.58	2.77	2.84	0.07	-0.14	-1.31	1395	504
Gage Shale Member	2.71	2.84	2.62	2.71	2.69	0.04	0.64	0.96	602	222
Towanda Limestone Member	2.73	2.88	2.50	2.71	2.70	0.06	0.32	1.46	1570	575
Holmesville Shale Member	2.70	2.75	2.65	2.71	2.71	0.03	-0.10	-0.51	95	35
Fort Riley Limestone Member	2.72	2.88	2.57	2.72	2.71	0.04	0.59	1.73	1778	653
Florence Limestone Member	2.70	2.76	2.65	2.70	2.70	0.02	0.60	-0.15	178	66
Matfield Shale Member	2.70	2.82	2.50	2.70	2.69	0.05	-1.06	3.90	491	182
Wreford Limestone	2.71	2.80	2.56	2.71	2.70	0.03	-0.47	1.96	889	328
Speiser Shale Member (A1-SH)	2.70	2.97	2.54	2.70	2.68	0.05	0.62	3.47	867	321
Funston Limestone Member (A1-LM)	2.70	2.88	2.57	2.70	2.70	0.04	0.53	1.05	1750	647
Blue Rapids Shale Member (B1-SH)	2.70	2.93	2.56	2.70	2.72	0.05	0.24	1.27	948	351
Crouse Limestone Member (B1-LM)	2.72	2.87	2.65	2.71	2.71	0.03	1.14	1.62	863	317
Easley Creek Shale Member (B2-SH)	2.71	2.81	2.63	2.70	2.70	0.04	0.54	0.57	400	148
Middleburg Limestone Member (B2-LM)	2.71	2.83	2.52	2.71	2.71	0.04	-1.37	11.49	537	198
Hooser Shale Member (B3-SH)	2.71	2.79	2.58	2.71	2.71	0.03	-0.35	0.29	631	233
Eiss Limestone Member (B3-LM)	2.74	2.87	2.65	2.72	2.72	0.05	0.89	-0.12	291	106
Stearns Shale Member (B4-SH)	2.69	2.81	2.59	2.69	2.68	0.03	0.48	1.77	439	163
Morrill Limestone Member (B4-LM)	2.73	2.85	2.68	2.72	2.72	0.04	1.07	0.71	410	150
Florena Shale Member (B5-SH)	2.73	2.87	2.64	2.73	2.77	0.05	0.15	-0.10	161	59
Cottonwood Limestone Member (B5-LM)	2.74	2.90	2.60	2.73	2.71	0.04	1.25	1.98	1038	379
Eskridge Shale (C-SH)	2.73	2.80	2.58	2.74	2.75	0.04	-0.92	1.10	338	124
Grenola Limestone (C-LM)	2.71	2.97	2.56	2.71	2.71	0.03	0.55	7.09	1496	553
Roca Shale (D-SH)	2.70	2.78	2.60	2.70	2.70	0.04	0.03	-0.30	213	79
Red Eagle Limestone (D-LM)	2.71	3.00	2.60	2.71	2.72	0.05	1.95	10.95	385	142
Johnson Shale (E-SH)	2.67	2.75	2.59	2.67	2.66	0.03	0.11	1.43	96	36
Foraker Limestone (E-LM)	2.70	2.79	2.61	2.70	2.74	0.04	-0.64	0.89	135	50
Janesville Shale (F-SH)	2.67	2.69	2.64	2.69	#N/A	0.03	-1.78	3.16	11	4
Falls City Limestone (F-LM)	2.71	2.76	2.67	2.71	2.71	0.02	0.53	1.21	84	31

Table 4.2.2. Summary statistics of grain density for Chase and Council Grove stratigraphic members

Chase and Council Grove

Lithofacies Code	Mean Grain Density (g/cc)	Maximum Grain Density (g/cc)	Minimum Grain Density (g/cc)	Median Grain Density (g/cc)	Mode Grain Density (g/cc)	Deviation Grain Density (g/cc)	Skewness Grain Density (g/cc)	Kurtosis Grain Density (g/cc)	Sum Grain Density (g/cc)	Count Grain Density
0	2.70	2.81	2.63	2.70	2.70	0.03	0.65	1.72	208	77
1	2.70	2.87	2.50	2.70	2.71	0.05	-0.21	1.22	2304	853
1.1	2.69	3.00	2.58	2.69	2.70	0.04	1.41	7.66	1361	505
1.X	2.70	3.00	2.50	2.70	2.70	0.05	0.18	2.44	3665	1358
2	2.72	2.87	2.50	2.72	2.71	0.04	-0.18	2.17	862	317
2.1	2.69	2.78	2.63	2.68	2.68	0.02	0.47	1.41	290	108
2.X	2.71	2.87	2.50	2.71	2.68	0.04	0.15	1.70	1152	425
3	2.71	2.88	2.50	2.70	2.68	0.06	0.32	0.57	1162	429
4	2.72	2.89	2.56	2.71	2.70	0.06	0.47	-0.27	1038	381
5	2.73	2.97	2.60	2.72	2.70	0.05	0.96	1.03	2244	822
5.1	2.72	2.89	2.60	2.71	2.70	0.04	0.88	2.29	3666	1348
5.X	2.72	2.97	2.60	2.72	2.70	0.04	1.07	2.13	5910	2170
6	2.82	2.90	2.67	2.83	2.84	0.04	-1.04	0.57	515	183
6.1	2.79	2.87	2.68	2.79	2.80	0.04	-0.41	-0.26	245	88
6.X	2.81	2.90	2.67	2.82	2.84	0.05	-0.74	-0.09	761	271
7	2.73	3.00	2.52	2.72	2.71	0.05	1.34	2.37	3506	1282
8	2.71	2.83	2.52	2.71	2.71	0.06	-1.54	5.34	146	54
9	2.84	2.91	2.66	2.85	2.85	0.03	-2.52	9.21	1254	441
10	2.71	2.88	2.59	2.70	2.69	0.05	0.73	0.38	1334	492

Chase

Lithofacies Code	Mean Grain Density (g/cc)	Maximum Grain Density (g/cc)	Minimum Grain Density (g/cc)	Median Grain Density (g/cc)	Mode Grain Density (g/cc)	Deviation Grain Density (g/cc)	Skewness Grain Density (g/cc)	Kurtosis Grain Density (g/cc)	Sum Grain Density (g/cc)	Count Grain Density
0	2.71	2.81	2.63	2.71	2.71	0.03	0.83	2.60	84	31
1	2.72	2.87	2.50	2.72	2.69	0.05	-0.23	2.64	1141	420
1.1	2.67	2.81	2.50	2.67	2.67	0.05	-0.42	1.12	261	98
1.X	2.71	2.87	2.50	2.71	2.69	0.05	-0.42	2.01	1400	517
2	2.71	2.81	2.50	2.71	2.69	0.05	-1.04	4.14	187	69
2.1										
2.X										
3	2.73	2.88	2.50	2.72	2.71	0.06	-0.05	0.64	728	267
4	2.75	2.89	2.56	2.76	2.66	0.07	-0.14	-1.00	462	168
5	2.75	2.91	2.61	2.73	2.70	0.06	0.51	-0.41	1157	421
5.1	2.72	2.83	2.62	2.71	2.70	0.03	0.86	1.77	380	140
5.X	2.74	2.91	2.61	2.72	2.70	0.05	0.73	0.01	1534	560
6	2.81	2.89	2.67	2.82	2.83	0.04	-0.76	0.50	295	105
6.1	2.85	2.90	2.80	2.85	2.85	0.02	0.26	1.32	174	61
6.X	2.82	2.90	2.67	2.83	2.84	0.04	-1.17	1.58	466	165
7	2.75	3.00	2.52	2.73	2.71	0.06	0.92	0.83	2076	756
8										
9	2.84	2.91	2.66	2.85	2.85	0.03	-2.52	9.21	1254	441
10	2.72	2.88	2.59	2.71	2.69	0.05	0.68	-0.27	1350	496

Council Grove

Lithofacies Code	Mean Grain Density (g/cc)	Maximum Grain Density (g/cc)	Minimum Grain Density (g/cc)	Median Grain Density (g/cc)	Mode Grain Density (g/cc)	Deviation Grain Density (g/cc)	Skewness Grain Density (g/cc)	Kurtosis Grain Density (g/cc)	Sum Grain Density (g/cc)	Count Grain Density
0	2.69	2.76	2.63	2.70	2.70	0.03	0.11	-0.10	127	47
1	2.70	2.93	2.54	2.70	2.70	0.05	0.16	1.05	1162	431
1.1	2.69	3.00	2.58	2.69	2.68	0.04	1.67	11.91	1106	411
1.X	2.69	3.00	2.54	2.69	2.70	0.05	0.60	3.56	2267	842
2	2.72	2.87	2.58	2.72	2.71	0.04	0.15	0.86	678	249
2.1	2.69	2.78	2.63	2.68	2.68	0.02	0.47	1.41	290	108
2.X	2.71	2.87	2.58	2.71	2.68	0.04	0.47	0.77	968	357
3	2.68	2.82	2.56	2.68	2.68	0.04	-0.04	1.48	436	163
4	2.70	2.80	2.58	2.70	2.70	0.04	-0.08	0.30	578	214
5	2.71	2.97	2.60	2.71	2.71	0.04	1.33	5.09	1072	395
5.1	2.72	2.88	2.60	2.71	2.70	0.04	0.82	2.08	3307	1216
5.X	2.72	2.97	2.60	2.71	2.71	0.04	0.98	3.29	4379	1611
6	2.78	2.86	2.68	2.78	2.80	0.04	-0.27	-0.66	269	97
6.1	2.84	2.87	2.79	2.84	2.84	0.03	-0.40	-0.64	28	10
6.X	2.78	2.87	2.68	2.79	2.80	0.05	-0.28	-0.64	298	107
7	2.72	2.87	2.57	2.71	2.71	0.03	1.07	4.56	1433	527
8	2.71	2.83	2.52	2.71	2.71	0.06	-1.54	5.34	146	54
9										
10	2.69	2.72	2.68	2.69	2.69	0.01	1.12	1.55	92	34

Table 4.2.3. Summary statistics for Chase and Council Grove grain density. Lithofacies codes with decimal extensions were estimated from routine core description but are not confirmed by direct measurement.

Chase and Council Grove

Lithofacies Code	Mean <i>in situ</i> Porosity (%)	Maximum <i>in situ</i> Porosity (%)	Minimum <i>in situ</i> Porosity (%)	Median <i>in situ</i> Porosity (%)	Standard Deviation <i>in situ</i> Porosity (%)	Skewness <i>in situ</i> Porosity (%)	Kurtosis <i>in situ</i> Porosity (%)	Sum <i>in situ</i> Porosity (%)	Count <i>in situ</i> Porosity
0	12.1	19.6	1.9	13.2	4.4	-0.3	-0.9	1007	83
1	8.2	20.2	0.1	7.9	3.8	0.5	0.2	6944	843
1.1	8.6	20.2	0.1	8.2	3.9	0.2	-0.5	4366	509
1.X	8.4	20.2	0.1	8.0	3.9	0.4	-0.1	11310	1352
2	9.7	22.5	1.1	9.6	3.8	0.2	-0.1	3118	323
2.1	8.3	22.2	2.5	7.7	3.0	1.4	3.7	898	108
2.X	9.3	22.5	1.1	9.1	3.7	0.4	0.2	4016	431
3	8.4	23.5	0.1	7.7	4.0	0.8	0.8	3685	440
4	6.3	19.6	0.1	5.5	3.5	0.9	0.7	2446	390
5	8.5	34.3	0.1	7.2	5.8	1.6	4.0	7361	868
5.1	7.3	25.4	0.1	6.3	5.0	0.8	0.1	9908	1354
5.X	7.8	34.3	0.1	6.7	5.4	1.2	2.4	17269	2222
6	11.6	29.9	0.6	11.1	5.8	0.5	0.1	2212	191
6.1	15.1	25.0	6.3	15.3	4.7	-0.1	-0.6	1417	94
6.X	12.7	29.9	0.6	12.8	5.7	0.2	-0.4	3629	285
7	9.8	30.7	0.1	10.1	4.5	0.0	0.0	13124	1346
8	10.4	20.3	0.9	10.3	4.4	-0.1	-0.7	594	57
9	11.7	28.0	0.1	11.2	5.4	0.4	-0.3	5813	496
10	14.6	30.3	0.6	14.7	4.8	0.0	0.0	7166	490

Chase

Lithofacies Code	Mean <i>in situ</i> Porosity (%)	Maximum <i>in situ</i> Porosity (%)	Minimum <i>in situ</i> Porosity (%)	Median <i>in situ</i> Porosity (%)	Standard Deviation <i>in situ</i> Porosity (%)	Skewness <i>in situ</i> Porosity (%)	Kurtosis <i>in situ</i> Porosity (%)	Sum <i>in situ</i> Porosity (%)	Count <i>in situ</i> Porosity
0	15.2	19.6	1.9	15.5	3.6	-1.9	5.0	470	31
1	9.9	20.2	0.3	10.0	4.1	0.1	-0.4	4033	406
1.1	6.2	19.5	0.1	5.9	3.8	1.1	2.2	612	98
1.X	9.2	20.2	0.1	9.0	4.2	0.2	-0.4	4645	503
2	9.7	18.5	1.6	10.0	3.9	0.0	-0.7	589	61
2.1									
2.X									
3	9.4	23.5	0.1	8.9	4.3	0.6	0.2	2571	273
4	7.1	19.6	0.1	6.8	3.7	0.7	0.8	1246	175
5	9.3	28.4	0.1	9.0	4.6	1.0	2.0	4294	463
5.1	13.9	34.3	0.1	12.6	7.9	1.0	0.7	1948	140
5.X	10.4	34.3	0.1	9.4	5.9	1.5	3.4	6242	602
6	14.0	29.9	1.8	13.9	5.5	0.5	0.1	1583	113
6.1	9.1	17.4	0.6	9.1	4.3	0.0	-1.1	558	61
6.X	12.3	29.9	0.6	12.1	5.5	0.5	0.3	2136	173
7	10.4	30.7	0.1	10.8	4.1	-0.2	0.8	8290	797
8									
9	11.7	28.0	0.1	11.2	5.4	0.4	-0.3	5813	496
10	15.1	30.3	0.6	15.0	4.9	0.1	-0.1	7312	485

Council Grove

Lithofacies Code	Mean <i>in situ</i> Porosity (%)	Maximum <i>in situ</i> Porosity (%)	Minimum <i>in situ</i> Porosity (%)	Median <i>in situ</i> Porosity (%)	Standard Deviation <i>in situ</i> Porosity (%)	Skewness <i>in situ</i> Porosity (%)	Kurtosis <i>in situ</i> Porosity (%)	Sum <i>in situ</i> Porosity (%)	Count <i>in situ</i> Porosity
0	10.2	16.5	1.9	10.3	4.0	0.0	-1.0	539	53
1	8.1	18.2	0.1	7.9	3.5	0.2	-0.2	3563	438
1.1	7.5	20.2	0.1	7.2	3.6	0.6	0.6	3102	412
1.X	7.8	20.2	0.1	7.5	3.5	0.4	0.1	6665	850
2	9.6	22.5	1.1	9.5	3.8	0.2	0.1	2537	263
2.1	8.3	22.2	2.5	7.7	3.0	1.4	3.7	898	108
2.X	9.3	22.5	1.1	8.9	3.6	0.5	0.5	3435	371
3	6.7	14.3	1.8	6.7	2.6	0.3	-0.3	1118	168
4	5.6	15.7	0.2	4.9	3.1	1.0	0.4	1205	216
5	6.5	18.3	0.2	5.9	3.9	0.7	0.0	2646	406
5.1	6.9	25.4	0.1	5.5	5.1	1.0	0.4	8381	1215
5.X	6.8	25.4	0.1	5.6	4.8	1.0	0.6	11027	1621
6	12.8	25.0	0.6	14.1	6.1	-0.1	-0.9	1322	103
6.1	17.1	21.4	8.5	17.6	3.6	-1.5	3.3	171	10
6.X	13.2	25.0	0.6	14.3	6.0	-0.2	-0.9	1493	113
7	8.8	22.2	0.1	8.7	4.9	0.4	-0.4	4834	550
8	10.4	20.3	0.9	10.3	4.4	-0.1	-0.7	594	57
9									
10	14.2	18.7	1.0	15.8	4.4	-1.3	1.2	484	34

Table 4.2.4. Summary statistics for Chase and Council Grove *in situ* porosity. Porosity values were either measured or calculated from routine values using equations in text. Lithofacies codes with decimal extensions were estimated from routine core description but are not confirmed by direct measurement.

Chase and Council Grove

Lithofacies Code	Mean log10 <i>in situ</i> Klinkenberg Permeability (log md)	Maximum log10 <i>in situ</i> Klinkenberg Permeability (log md)	Minimum log10 <i>in situ</i> Klinkenberg Permeability (log md)	Median log10 <i>in situ</i> Klinkenberg Permeability (log md)	Standard Deviation log10 <i>in situ</i> Klinkenberg Permeability (log md)	Skewness log10 <i>in situ</i> Klinkenberg Permeability (log md)	Kurtosis log10 <i>in situ</i> Klinkenberg Permeability (log md)	Sum log10 <i>in situ</i> Klinkenberg Permeability (log md)	Count log10 <i>in situ</i> Klinkenberg Permeability
0	-0.59	0.81	-2.42	-0.53	0.84	-0.47	-0.01	-17.0	29
1	-2.29	2.74	-8.13	-2.30	1.85	-0.43	1.32	-574.0	251
1.1	-4.08	0.98	-8.13	-2.54	3.26	-0.26	-1.66	-783.1	192
1.X	-3.06	2.74	-8.13	-2.40	2.70	-0.77	-0.35	-1357.1	443
2	-2.61	1.95	-8.13	-1.56	3.05	-0.83	-0.55	-229.3	88
2.1	-3.34	0.72	-8.13	-3.58	2.28	-0.41	0.97	-63.5	19
2.X	-2.74	1.95	-8.13	-1.67	2.93	-0.73	-0.52	-292.9	107
3	-2.09	1.23	-8.72	-2.30	1.98	-0.43	0.29	-256.8	123
4	-3.95	0.67	-9.64	-3.69	2.51	-0.36	-0.78	-335.4	85
5	-2.80	0.93	-8.00	-2.63	2.00	-0.34	-0.63	-727.2	260
5.1	-3.29	2.20	-11.08	-2.05	3.42	-0.43	-1.37	-1595.9	485
5.X	-3.12	2.20	-11.08	-2.42	3.01	-0.54	-0.97	-2323.1	745
6	-1.84	0.39	-8.13	-1.32	1.73	-1.71	4.59	-55.2	30
6.1	-0.21	1.28	-3.69	0.14	1.12	-1.14	1.09	-9.7	46
6.X	-0.85	1.28	-8.13	-0.46	1.60	-1.59	4.40	-64.9	76
7	-1.04	2.39	-6.90	-0.77	1.55	-0.94	1.14	-514.8	495
8	0.56	2.92	-3.69	0.94	1.58	-1.06	0.86	21.7	39
9	0.02	1.40	-2.73	0.57	1.26	-1.08	0.32	0.4	19
10	-0.25	1.97	-4.08	-0.19	1.30	-0.36	-0.24	-36.5	148

Chase

Lithofacies Code	Mean log10 <i>in situ</i> Klinkenberg Permeability (log md)	Maximum log10 <i>in situ</i> Klinkenberg Permeability (log md)	Minimum log10 <i>in situ</i> Klinkenberg Permeability (log md)	Median log10 <i>in situ</i> Klinkenberg Permeability (log md)	Standard Deviation log10 <i>in situ</i> Klinkenberg Permeability (log md)	Skewness log10 <i>in situ</i> Klinkenberg Permeability (log md)	Kurtosis log10 <i>in situ</i> Klinkenberg Permeability (log md)	Sum log10 <i>in situ</i> Klinkenberg Permeability (log md)	Count log10 <i>in situ</i> Klinkenberg Permeability
0	-0.48	0.60	-1.64	-0.59	0.74	0.12	-1.27	-5.8	12
1	-1.85	2.74	-6.48	-1.86	1.84	-0.06	-0.04	-223.8	121
1.1	-2.07	-0.24	-2.95	-2.30	0.99	1.22	0.94	-14.5	7
1.X	-1.86	2.74	-6.48	-1.93	1.81	-0.04	0.05	-238.3	128
2	-1.22	1.95	-3.69	-1.56	1.82	0.28	-0.82	-13.5	11
2.1									
2.X									
3	-0.80	1.23	-4.46	-0.52	1.40	-0.69	-0.12	-44.3	55
4	-2.78	0.67	-7.72	-2.15	2.59	-1.00	0.80	-33.4	12
5	-2.24	0.93	-8.00	-1.65	2.13	-0.86	-0.09	-324.2	145
5.1									
5.X	-2.24	0.93	-8.00	-1.65	2.13	-0.86	-0.09	-324.2	145
6	-1.39	0.39	-3.66	-1.03	1.14	-0.60	-0.82	-36.2	26
6.1									1
6.X	-1.48	0.39	-3.69	-1.05	1.21	-0.55	-0.97	-39.9	27
7	-1.06	0.91	-6.16	-0.85	1.08	-1.35	3.21	-209.1	198
8									
9	0.02	1.40	-2.73	0.57	1.26	-1.08	0.32	0.4	19
10	0.01	2.44	-4.08	0.15	1.34	-0.46	-0.17	2.3	178

Council Grove

Lithofacies Code	Mean log10 <i>in situ</i> Klinkenberg Permeability (log md)	Maximum log10 <i>in situ</i> Klinkenberg Permeability (log md)	Minimum log10 <i>in situ</i> Klinkenberg Permeability (log md)	Median log10 <i>in situ</i> Klinkenberg Permeability (log md)	Standard Deviation log10 <i>in situ</i> Klinkenberg Permeability (log md)	Skewness log10 <i>in situ</i> Klinkenberg Permeability (log md)	Kurtosis log10 <i>in situ</i> Klinkenberg Permeability (log md)	Sum log10 <i>in situ</i> Klinkenberg Permeability (log md)	Count log10 <i>in situ</i> Klinkenberg Permeability
0	-0.66	0.81	-2.42	-0.53	0.93	-0.59	0.07	-11.2	17
1	-2.30	1.28	-8.13	-2.03	1.80	-1.15	2.31	-422.5	184
1.1	-5.32	0.63	-8.13	-8.13	3.12	0.38	-1.59	-696.4	131
1.X	-3.55	1.28	-8.13	-2.56	2.85	-0.63	-0.98	-1118.8	315
2	-2.79	1.24	-8.13	-1.56	3.13	-0.77	-0.80	-217.4	78
2.1	-3.34	0.72	-8.13	-3.58	2.28	-0.41	0.97	-63.5	19
2.X	-2.90	1.24	-8.13	-1.68	2.98	-0.69	-0.71	-281.0	97
3	-3.12	0.81	-8.72	-3.26	1.74	-0.32	1.80	-215.2	69
4	-4.14	-0.25	-9.64	-4.00	2.46	-0.32	-0.83	-302.1	73
5	-2.79	0.70	-6.90	-2.71	1.81	-0.25	-0.71	-457.2	164
5.1	-3.54	2.20	-11.08	-2.61	3.51	-0.28	-1.51	-1541.7	436
5.X	-3.33	2.20	-11.08	-2.65	3.15	-0.42	-1.17	-1998.9	600
6	-0.51	1.28	-8.13	0.06	1.69	-2.32	7.61	-25.0	49
6.1									
6.X	-0.51	1.28	-8.13	0.06	1.69	-2.32	7.61	-25.0	49
7	-1.03	2.39	-6.90	-0.63	1.80	-0.83	0.31	-305.6	297
8	0.56	2.92	-3.69	0.94	1.58	-1.06	0.86	21.7	39
9									
10									

Table 4.2.5. Summary statistics for Chase and Council Grove *in situ* Klinkenberg permeability. Values were either measured or were converted from routine air permeability values using equations in text. Lithofacies codes with decimal extensions were estimated from routine core description but are not confirmed by direct measurement.

Lithofacies Code	General Lithology Lithologic Description	<i>In situ</i> Klinkenberg Permeability Equation Parameter A	<i>In situ</i> Klinkenberg Permeability Equation Parameter B	Permeability Standard Error of Prediction Factor (factor)
0	Continental vf-fn Sandstone	1.318E-08	6.65	2.9
1	Continental crs Siltstone	1.096E-10	8.00	9.3
2	Continental fn-med Siltstone	8.913E-11	8.00	15.6
3	Marine Shale/Siltstone	3.890E-10	7.74	9.2
4	Mudstone/Mud-wackestone Limestone	1.585E-11	9.20	16.0
5	Wackestone/Wacke-packstone Limestone	1.148E-09	7.61	7.5
6	vf-fn Sucrosic Dolomite	1.585E-12	9.70	5.3
7	Packstone/Grainstone Limestone	1.549E-08	7.09	4.0
8	Phylloid Algal Bafflestone	5.129E-09	8.65	5.4
9	med Sucrosic Moldic Dolomite	1.585E-11	9.70	6.7
10	Marine vf-fn Sandstone	2.399E-12	9.75	3.5

Table 4.2.6. Equation parameters for predicting *in situ* Klinkenberg permeability from *in situ* porosity for each lithofacies. Parameters are used in equation of form:

$$k_{ik} = A \phi_i^B$$

where k_{ik} is in millidarcies (md), porosity is in percent (%). Standard error of prediction factors are also presented (e.g. for a SE = 4X, predicted $k_{ik} = 1$ md has first standard deviation range of $k_{ik} = 4$ md or $k_{ik} = 0.25$ md).

Stratigraphic Interval	Lithofacies Code	General Lithology Lithologic Description	<i>In situ</i> Klinkenberg Permeability Equation Parameter A	<i>In situ</i> Klinkenberg Permeability Equation Parameter B
Herington	3	Marine Shale/Siltstone	1.755E-08	7.74
Krider	5	Wackestone/Wacke-packstone Limestone	2.309E-09	7.61
Krider	10	Marine vf-fn Sandstone	4.801E-13	9.75
Winfield	5	Wackestone/Wacke-packstone Limestone	1.924E-09	7.61
Towanda	10	Marine vf-fn Sandstone	4.801E-13	9.75
Ft Riley	5	Wackestone/Wacke-packstone Limestone	3.207E-10	7.61
Ft Riley	7	Packstone/Grainstone Limestone	6.473E-09	7.09
Florence	10	Marine vf-fn Sandstone	8.402E-12	9.75
CLm	7	Packstone/Grainstone Limestone	3.884E-08	7.09
B4Lm	7	Packstone/Grainstone Limestone	5.438E-08	7.09

Table 4.2.7. Equation parameters for predicting *in situ* Klinkenberg permeability from *in situ* porosity for specific lithofacies in specific stratigraphic intervals. These parameters provide improved prediction for the specified population to the general parameters in Table 4.2.6.

Lithofacies Code	Pc/Height Slope Hr Parameter A	Pc/Height Slope Hr Parameter B	Pc/Height Slope Standard Error	Threshold Entry Height H _{te} C	Threshold Entry Height H _{te} D	Threshold Entry Height standard Error (factor)
0	0.198	-5.319	0.58	-0.194	4.050	4.1
1	-0.153	0.099	0.52	-0.194	4.250	2.3
2	-0.153	0.099	0.41	-0.194	4.430	3.5
3	-0.153	0.099	0.50	-0.206	4.346	3.7
4	-0.066	-1.150	0.72	-0.122	3.300	4.2
5	-0.042	-1.000	0.39	-0.119	3.060	3.2
6	0.004	-1.219	0.28	-0.054	2.630	2.4
7	0.000	-1.670	0.55	-0.055	1.970	2.9
8	-0.110	-0.710	0.98	-0.031	1.520	2.8
9	0.128	-3.898	0.15	-0.054	1.700	2.4
10	0.198	-5.139	0.54	-0.080	2.517	1.4

Table 4.2.8. Parameters for use in capillary pressure equations:

$$H_{te} = C \phi_i + D$$

$$\log_{10} H_f = A \phi_i + B$$

Where A, B, C and D are constants for each lithofacies. Water saturation can be calculated for any given porosity sample at any given gas column height using:

$$S_w = E h^F$$

where:

$$E = \left[\frac{1}{\frac{H_{te}}{100^{H_f}}} \right]^{1/H_f}$$

$$F = 1/H_f$$

Where h is the gas column height above free-water level (ft), H_{te} is the gas-water threshold entry height (ft), H_f is the dimensionless measure of pore-size heterogeneity, and S_w is the water saturation (%) at height, h.

Lithofacies Code	Mean log ₁₀ <i>in situ</i> Klinkenberg Permeability (log md)	Maximum log ₁₀ <i>in situ</i> Klinkenberg Permeability (log md)	Minimum log ₁₀ <i>in situ</i> Klinkenberg Permeability (log md)	Median log ₁₀ <i>in situ</i> Klinkenberg Permeability (log md)	Standard Deviation log ₁₀ <i>in situ</i> Klinkenberg Permeability (log md)	Skewness log ₁₀ <i>in situ</i> Klinkenberg Permeability (log md)	Kurtosis log ₁₀ <i>in situ</i> Klinkenberg Permeability (log md)	Sum log ₁₀ <i>in situ</i> Klinkenberg Permeability (log md)	Count log ₁₀ <i>in situ</i> Klinkenberg Permeability
0	-0.77	-0.16	-2.19	-0.66	0.63	-1.56	3.09	-6.9	9
1	-0.87	0.00	-3.19	-0.59	0.81	-1.25	0.65	-151.0	174
1.1	-0.23	-0.01	-0.54	-0.19	0.21	-0.43	-1.53	-2.3	10
1.X	-0.83	0.00	-3.19	-0.57	0.81	-1.31	0.84	-153.2	184
2	-0.86	-0.01	-3.16	-0.61	0.73	-1.26	1.56	-29.2	34
2.1									
2.X	-0.86	-0.01	-3.16	-0.61	0.73	-1.26	1.56	-29.2	34
3	-0.74	0.00	-2.71	-0.53	0.64	-0.83	-0.22	-71.6	97
4	-0.76	0.00	-2.93	-0.48	0.71	-1.35	1.17	-80.0	105
5	-0.52	0.00	-3.39	-0.30	0.59	-2.13	5.03	-114.4	221
5.1	-0.31	0.00	-0.99	-0.24	0.25	-1.50	2.32	-5.9	19
5.X	-0.50	0.00	-3.39	-0.30	0.57	-2.21	5.56	-120.4	240
6	-0.43	0.00	-1.98	-0.26	0.44	-1.49	2.05	-39.2	91
6.1	-0.67	-0.02	-3.16	-0.48	0.87	-2.44	6.64	-8.0	12
6.X	-0.46	0.00	-3.16	-0.29	0.51	-2.26	7.45	-47.3	103
7	-0.41	0.00	-2.88	-0.24	0.47	-2.36	7.06	-115.0	278
8	-0.60	-0.18	-1.06	-0.61	0.34	-0.14	-1.59	-3.6	6
9	-0.48	0.00	-2.90	-0.33	0.48	-2.10	5.54	-115.8	242
10	-0.73	-0.02	-3.17	-0.61	0.60	-1.44	2.24	-93.5	129

Table 4.2.11. Summary statistics for Chase and Council Grove ratio of full-diameter vertical permeability over horizontal permeability. Ratio calculated using K_{vert} divided by $K_{avg} = (K_{max} + K_{90})/2$. Where $K_{max} > 5 * K_{90}$ sample was tentatively assumed to be possibly fractured and K_{vert}/K_{avg} was not calculated. Also where $K_{vert}/K_{avg} > 1$ the datum was not included in the statistics.

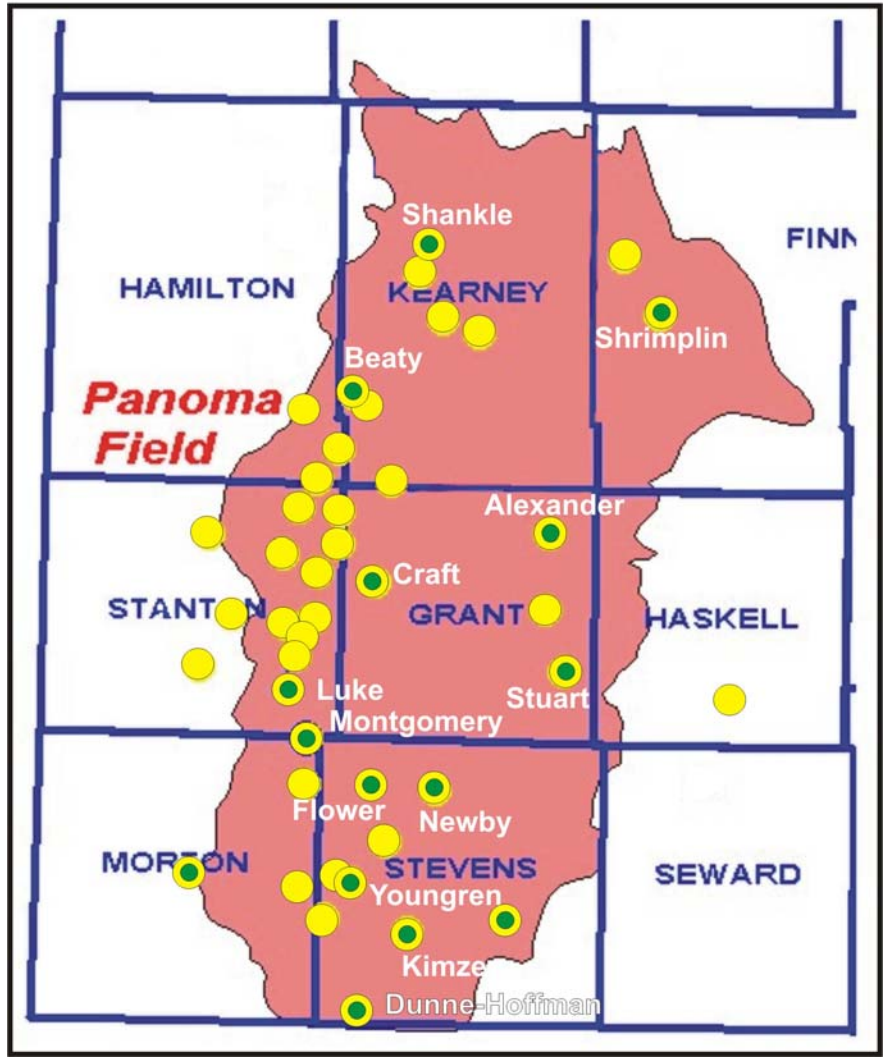


Figure 4.2.1. Location of wells for which core-analysis data are presented in Table 4.2.1. Green dots indicate important wells with advanced rock property data (e.g., capillary pressure, relative permeability).

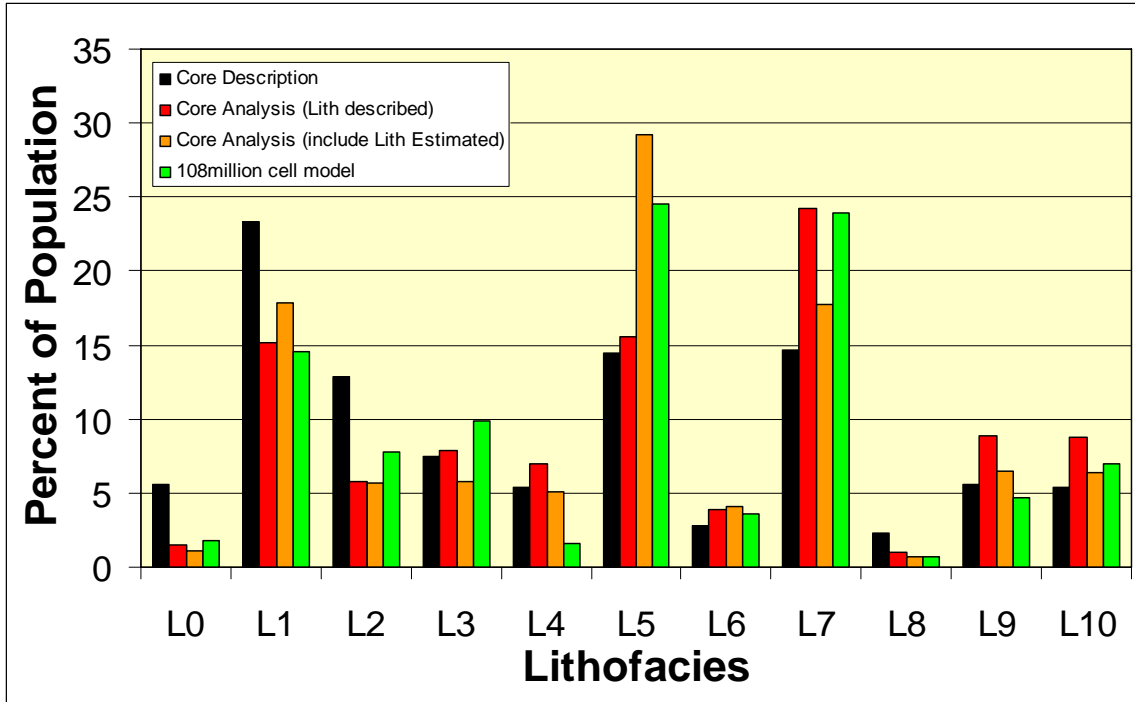


Figure 4.2.2. Frequency distribution of lithofacies for described core, for core analysis data where lithofacies was directly observed on the core, for core analysis where lithofacies were both directly observed in core and were estimated based on routine core description and rock properties, and for the full 108-million cell model based on node well training and prediction at well locations and between wells. Differences between core analysis relative percentages and the described core and full geomodel preclude unconditional statistical analysis of core analysis data on a stratigraphic basis.

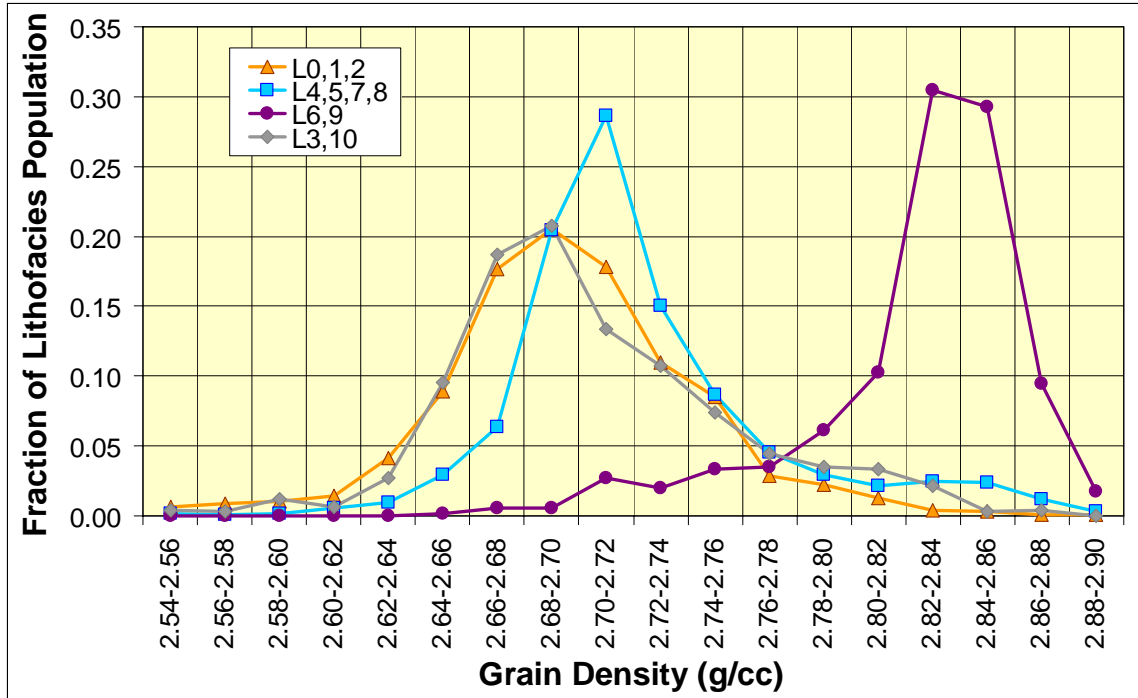


Figure 4.2.3. Frequency distribution of grain density for major lithofacies groups. Note high (2.70 g/cc) mean grain density for continental (L0,1,2) and marine (L3, 10) clastics. Not shown is that Chase grain densities average 0.02±0.01 g/cc greater than Council Grove densities for every lithofacies.

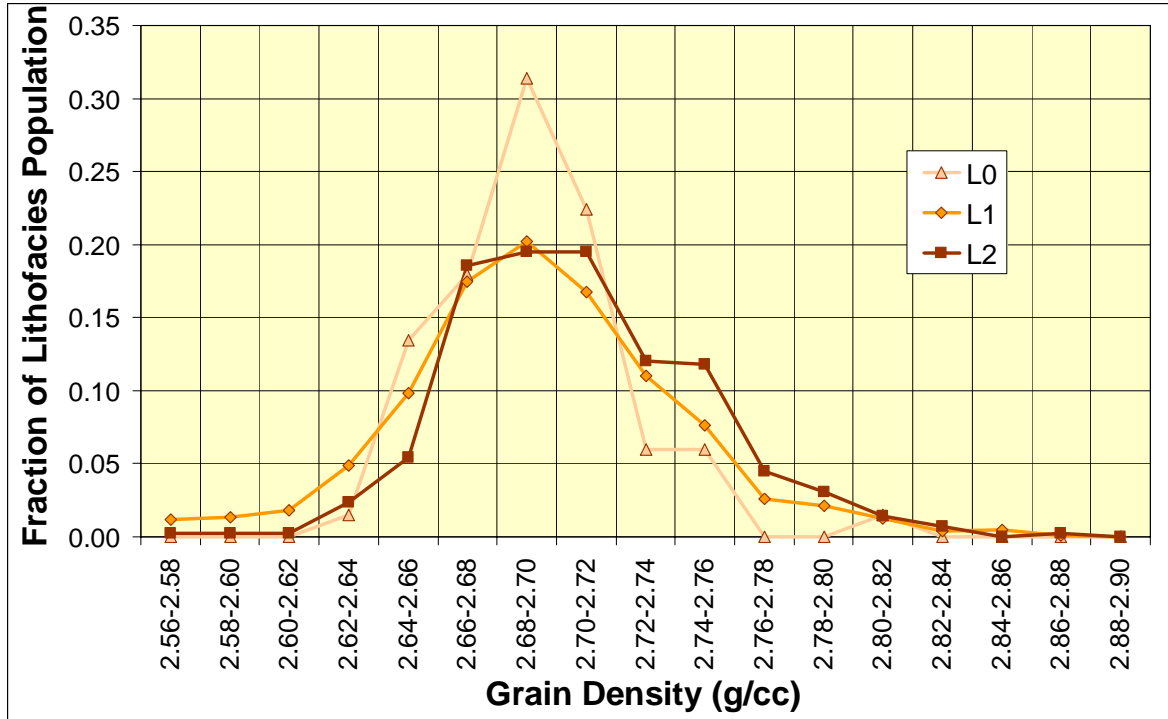


Figure 4.2.4. Frequency distribution of grain density for continental lithofacies L0, L1, and L2. Note high (2.70 g/cc) mean grain density and skew to higher densities.

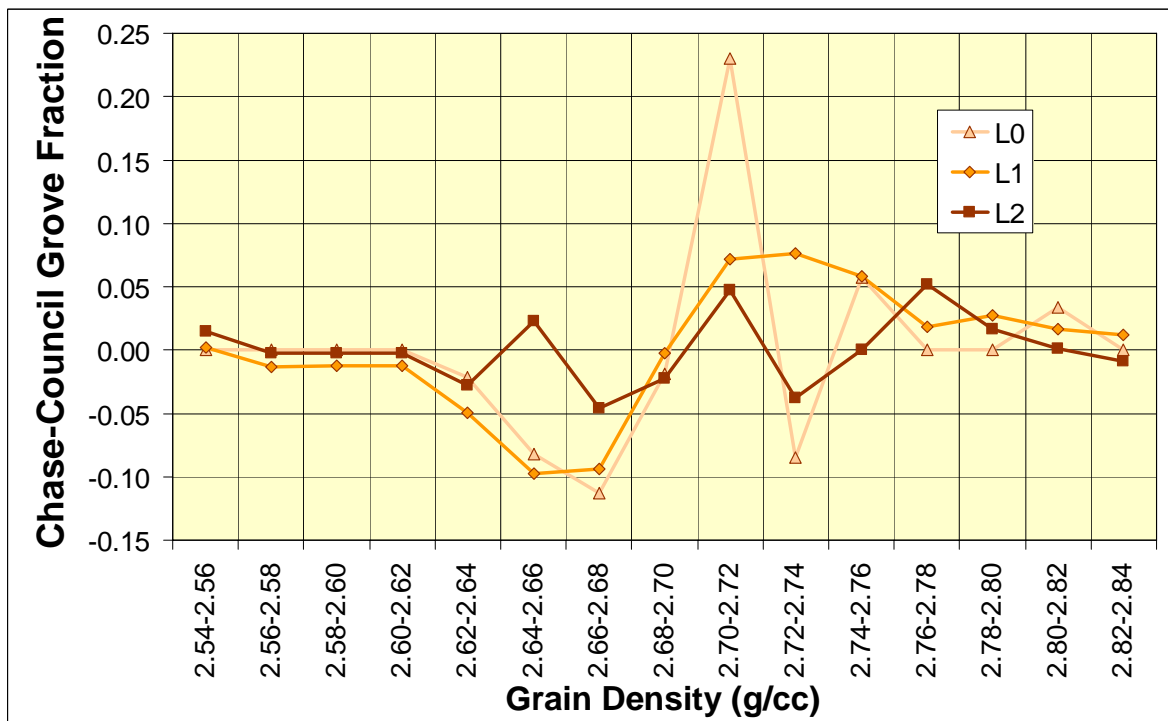


Figure 4.2.5. Difference between Chase and Council Grove fractions for each bin class of grain density for continental clastic facies showing higher densities of Chase. Zero indicates fraction of total populations for both groups are equal.

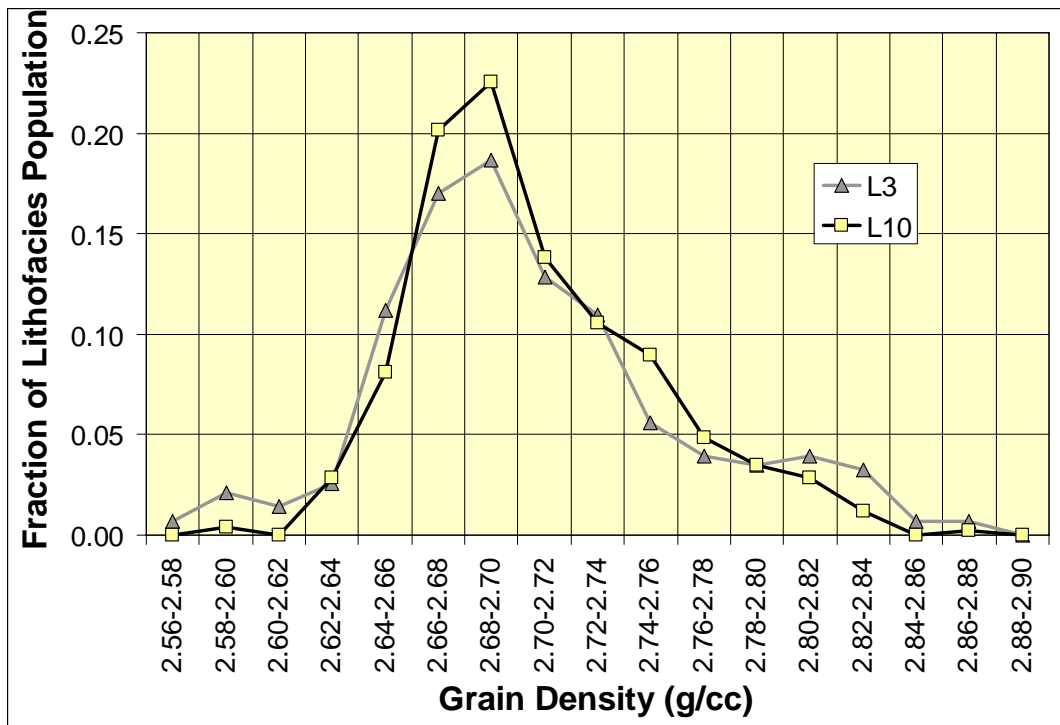


Figure 4.2.6. Frequency distribution of grain density for marine lithofacies L3, L10. Note high (2.70 g/cc) mean grain density and skew to higher densities.

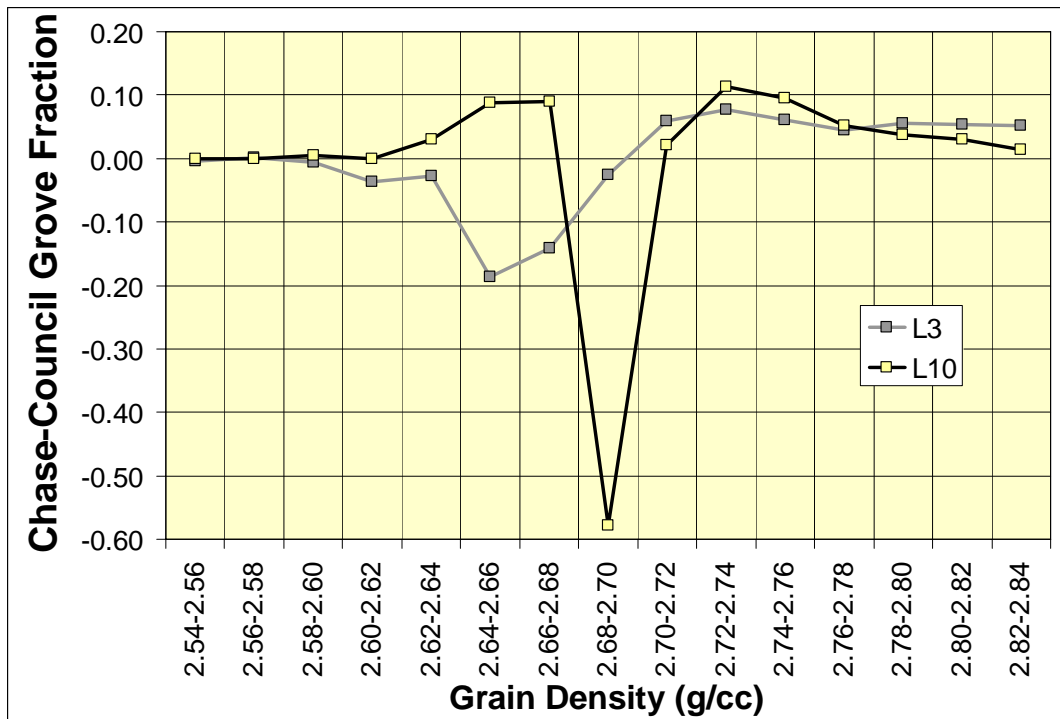


Figure 4.2.7. Difference between Chase and Council Grove fractions for each bin class of grain density for marine clastic facies showing variable differences in densities with higher densities of Chase.

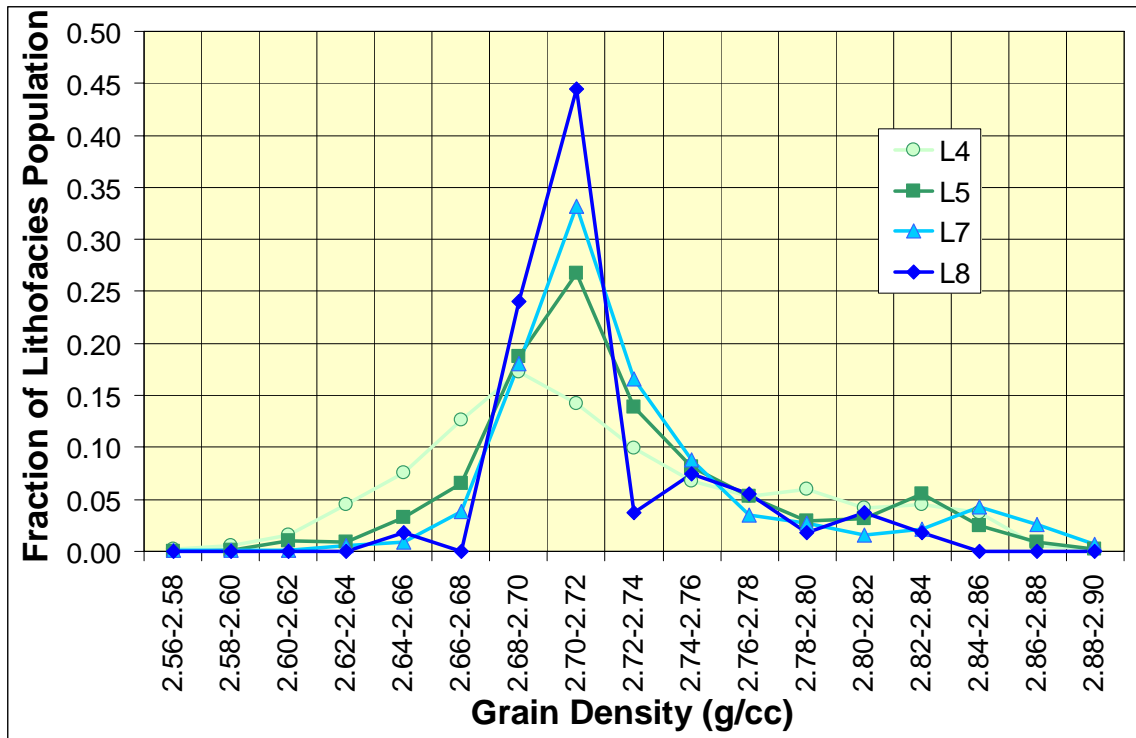


Figure 4.2.8. Frequency distribution of grain density for limestone lithofacies L4, L5, L7, and L8. Mudstone (L4) facies exhibits greater fraction of lower density rocks.

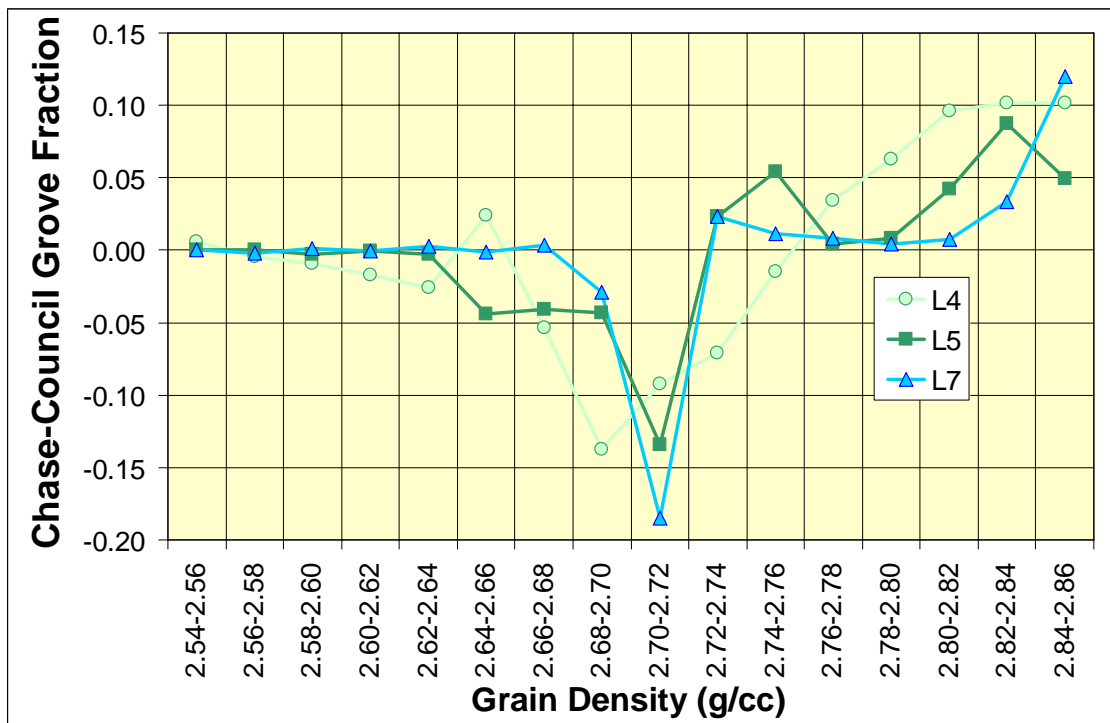


Figure 4.2.9. Difference between Chase and Council Grove fractions for each bin class of grain density for limestone facies showing higher densities of Chase for all facies and greater fraction of 2.64-2.71 g/cc rocks in Council Grove.

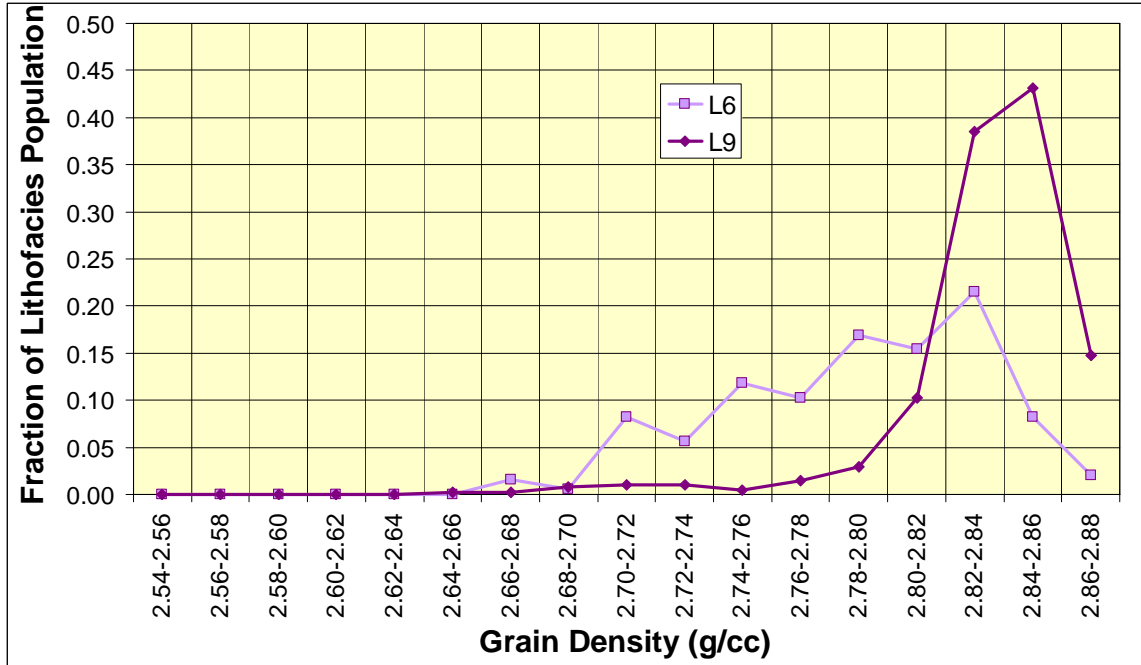


Figure 4.2.10. Frequency distribution of grain density for dolomite lithofacies L6 and L9. Skewness to lower density for fine-grained dolomites reflects greater siliciclastic silt/clay content.

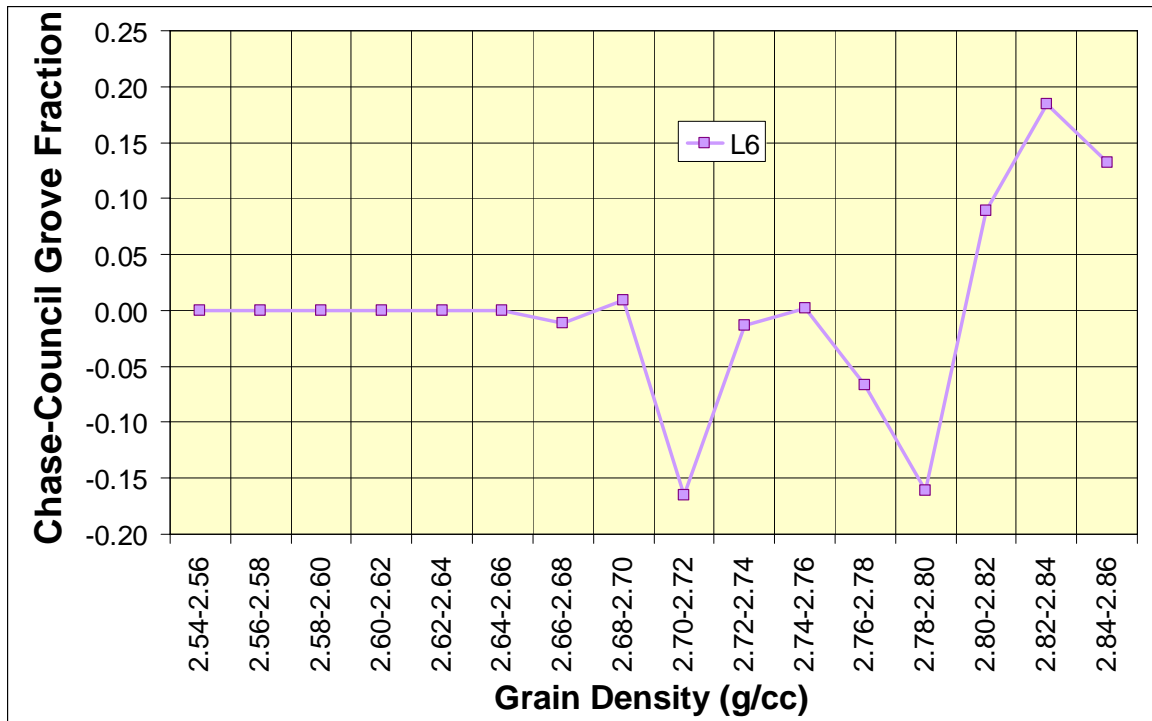


Figure 4.2.11. Difference between Chase and Council Grove fractions for each bin class of grain density for dolomite facies showing higher densities of Chase for L6. There are no identified coarse-grained dolomites (L9) in the Council Grove.

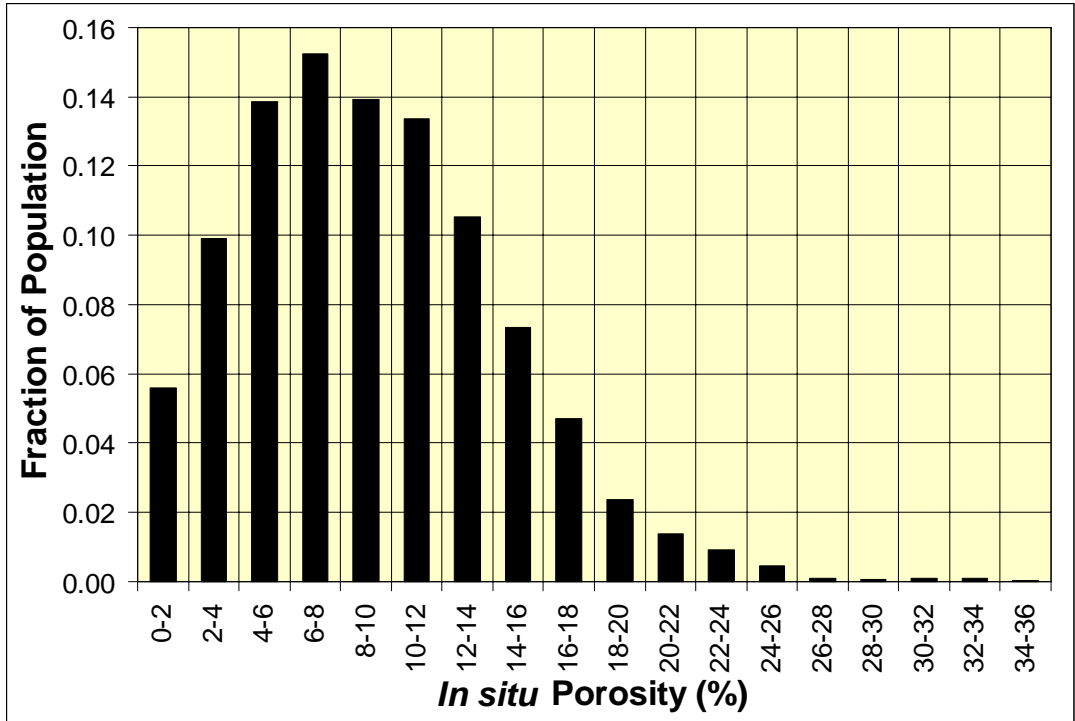


Figure 4.2.12. Frequency distribution of *in situ* helium porosity measured on core under confining stress to restore *in situ* stress or routine unconfined value corrected to *in situ* conditions for all 8,200 core samples in Table 4.2.1.

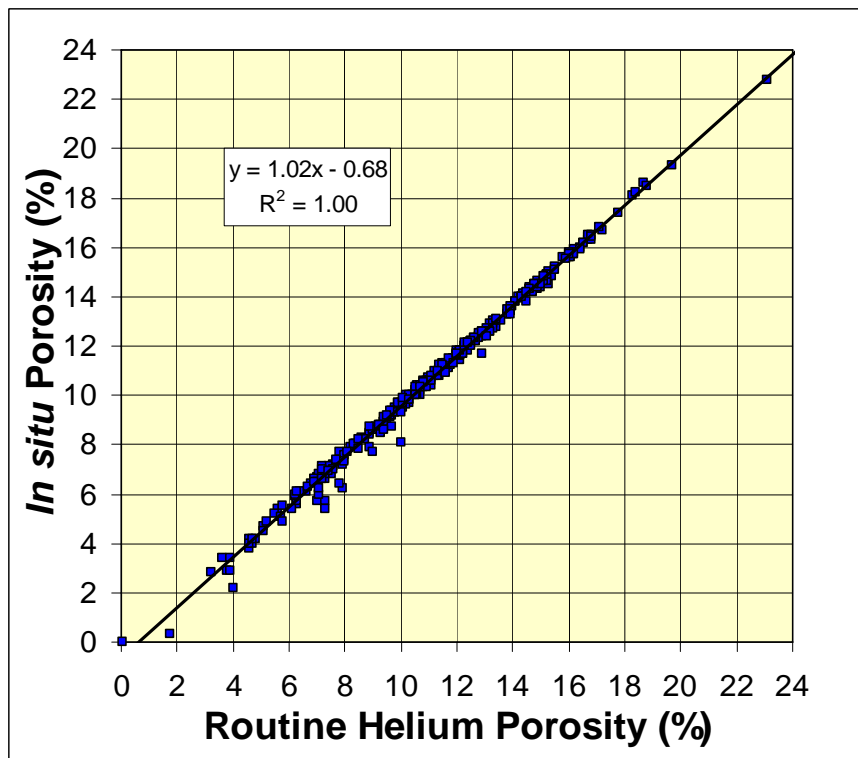


Figure 4.2.13. Crossplot of measured routine helium porosity and *in situ* porosity for Hugoton core plug samples of all lithofacies.

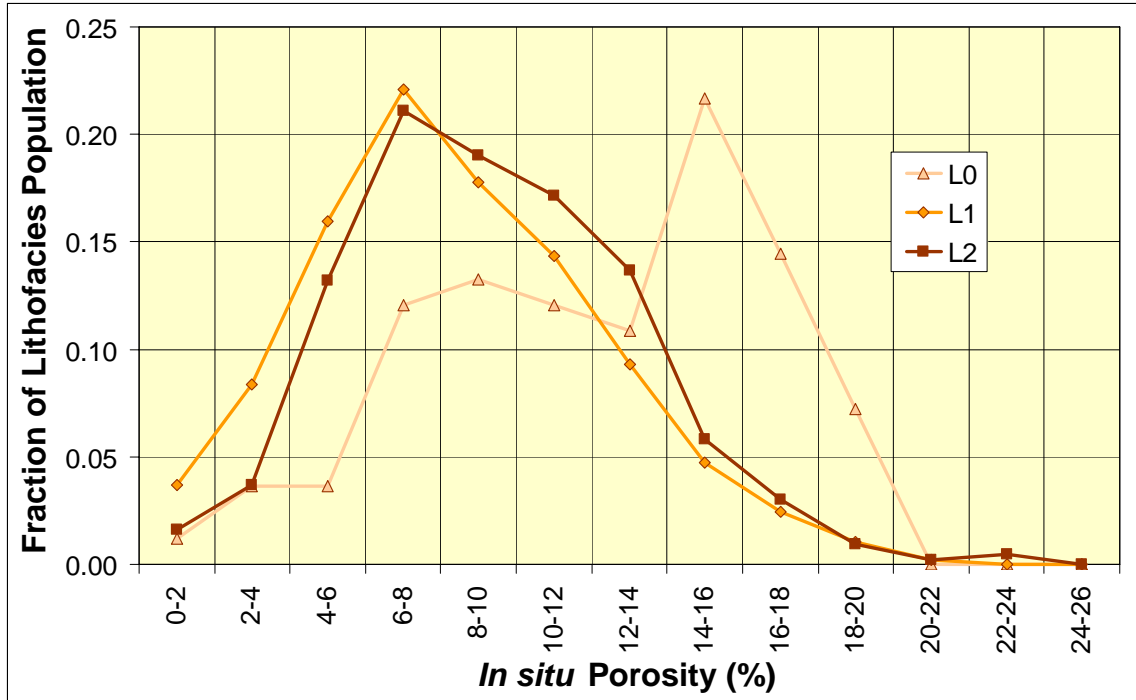


Figure 4.2.14. Frequency distribution of *in situ* porosity for continental lithofacies L0, L1, and L2. Bimodal distribution for very fine grained sandstones (L0) reflects presence of both clean very fine grained sandstones and marginal very coarse silt-very fine grained sandstone samples in same lithofacies class.

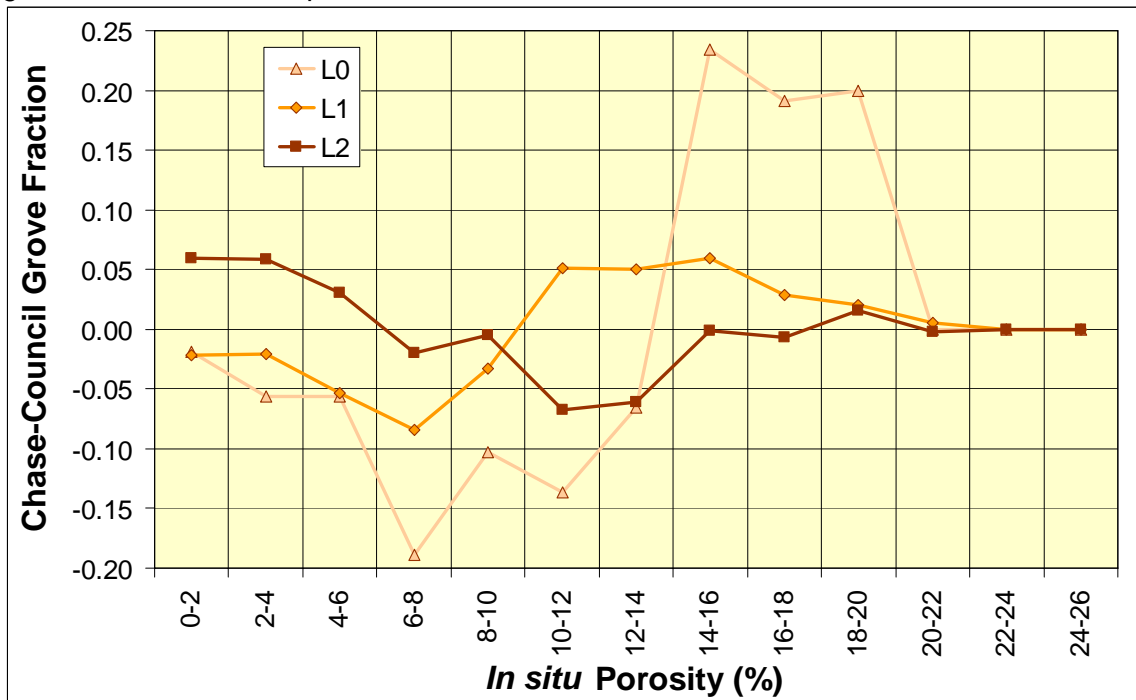


Figure 4.2.15. Difference between Chase and Council Grove fractions for each bin class of porosity for continental clastic facies showing higher porosities of Chase sandstones (L0) and coarse siltstones (L1) though Chase shaly siltstones exhibit lower porosity. Zero indicates fraction of total populations for both groups are equal.

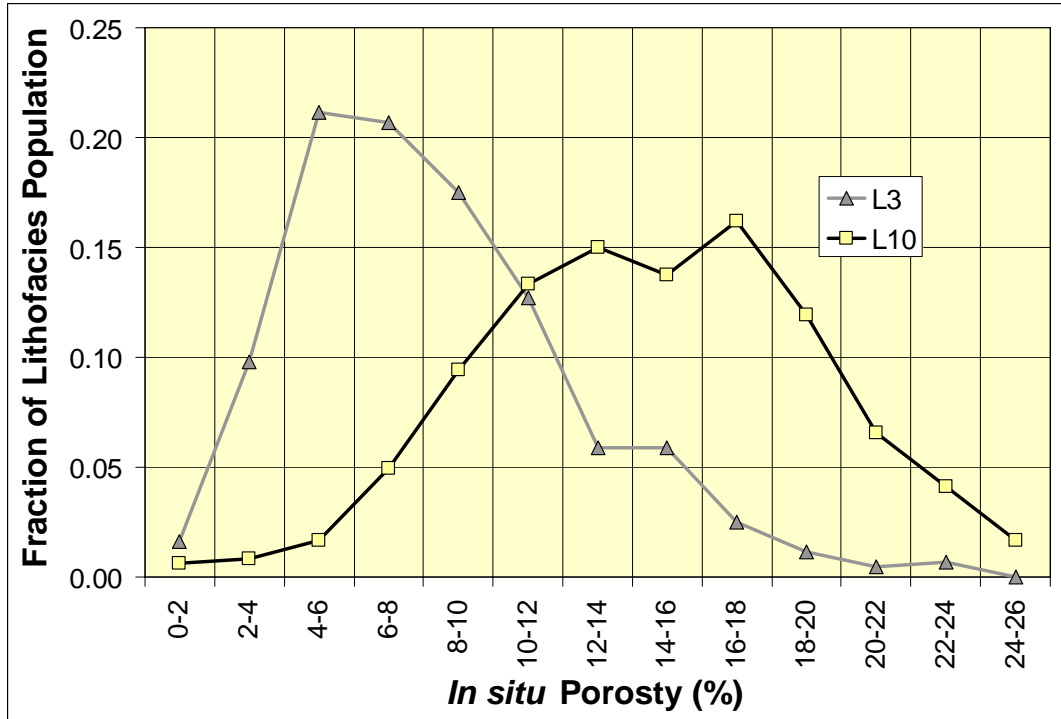


Figure 4.2.16. Frequency distribution of *in situ* porosity for marine clastic lithofacies L3 and L10. Fractions of higher porosity significantly greater for sandstones.

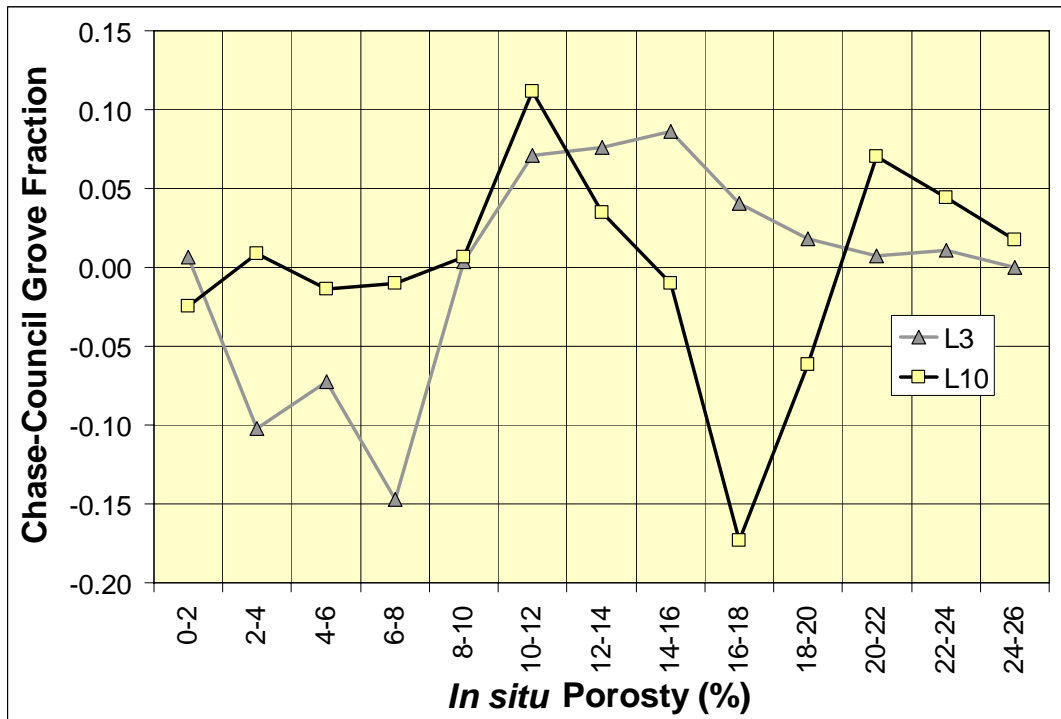


Figure 4.2.17. Difference between Chase and Council Grove fractions for each bin class of porosity for marine clastic lithofacies showing higher porosities of Chase lithofacies L3. Differences between sandstones vary with porosity, but Chase has larger fraction of highest porosity range.

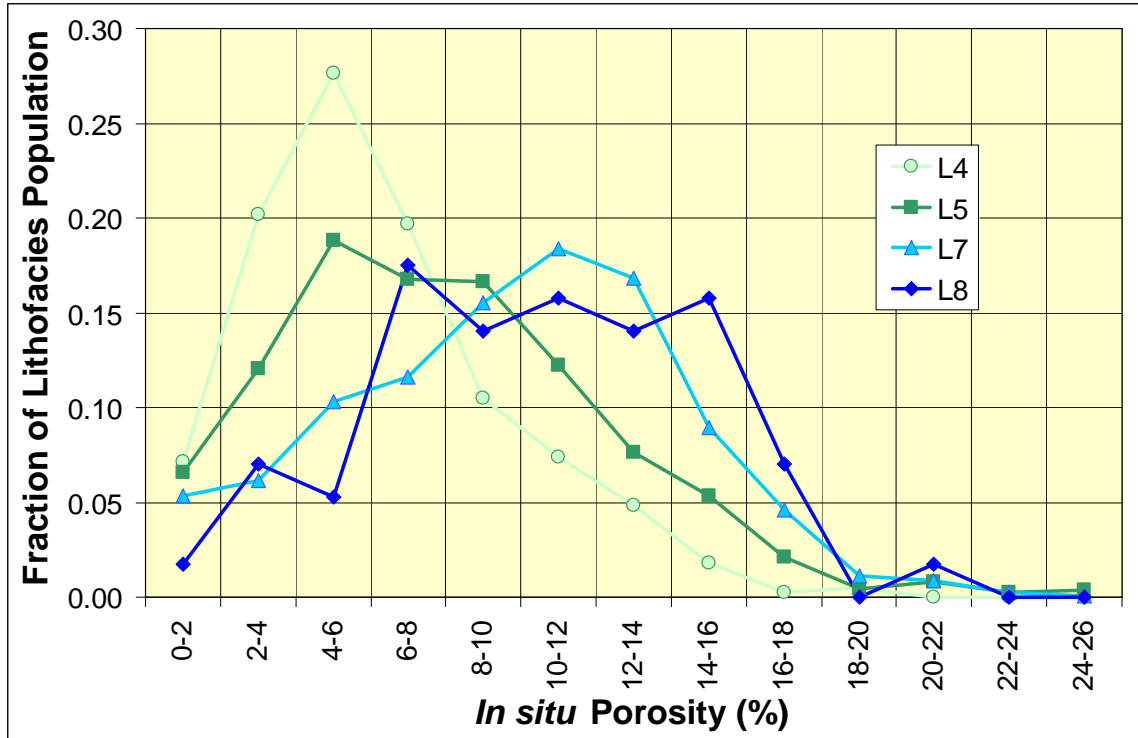


Figure 4.2.18. Frequency distribution of *in situ* porosity for limestone lithofacies L4, L5, L7, and L8. Fractions of higher porosity generally increase with increasing grain support texture.

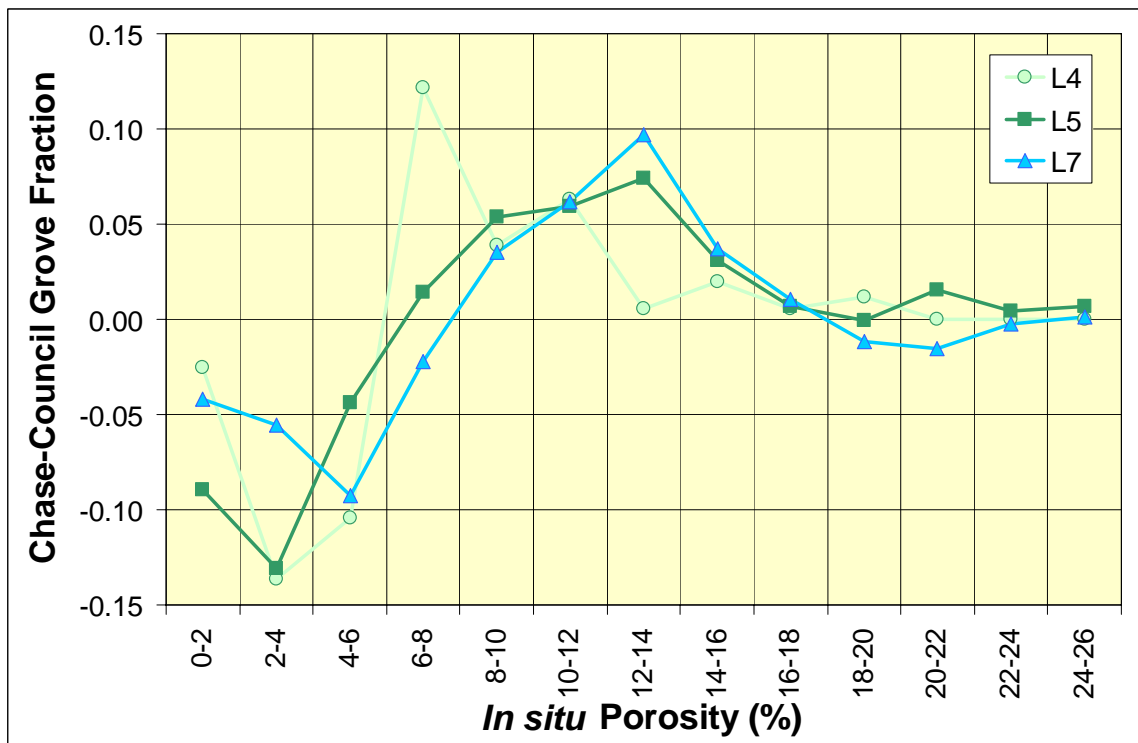


Figure 4.2.19. Difference between Chase and Council Grove fractions for each bin class of porosity for limestone lithofacies showing higher porosities of Chase. Phylloid algal bafflestones (L8) were not sampled in Chase cores.

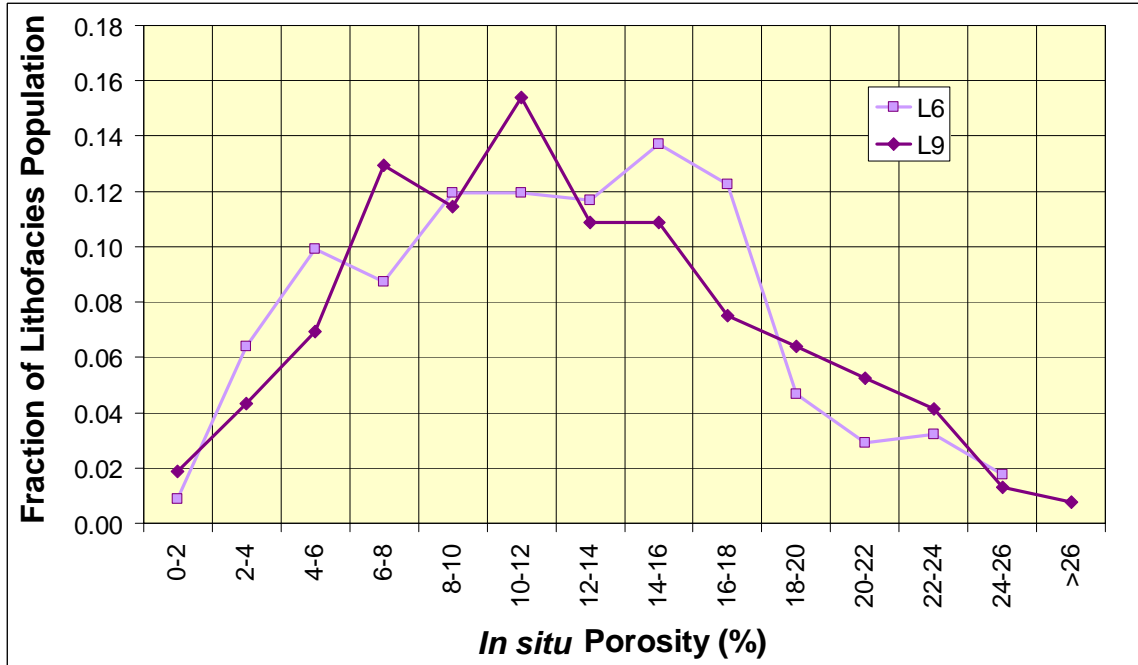


Figure 4.2.20. Frequency distribution of *in situ* porosity for dolomite lithofacies L6 and L9. Coarse-grained dolomites in cores sampled exhibit slightly lower porosity than fine-grained dolomites.

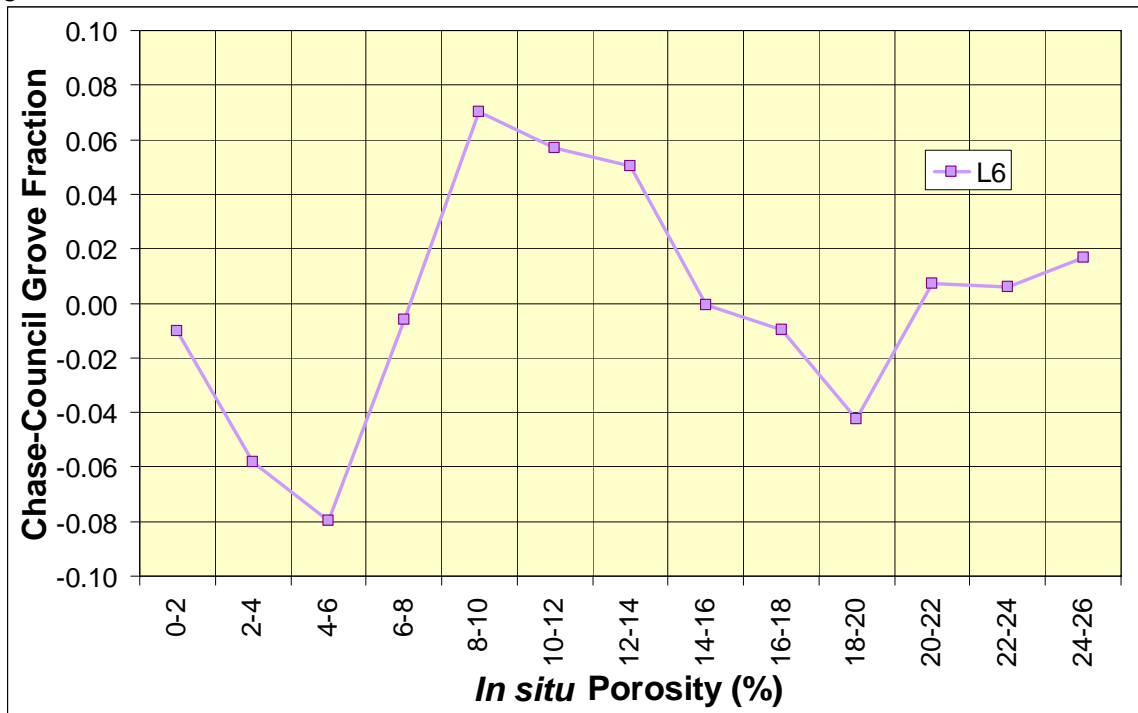


Figure 4.2.21. Difference between Chase and Council Grove fractions for each bin class of porosity for dolomite lithofacies showing Chase has larger fraction of mid-range porosities (8-14%) but has a smaller fraction of upper-middle range porosities (16-20%). Lithofacies L9, coarse-grained dolomite, is not present in the Council Grove core samples.

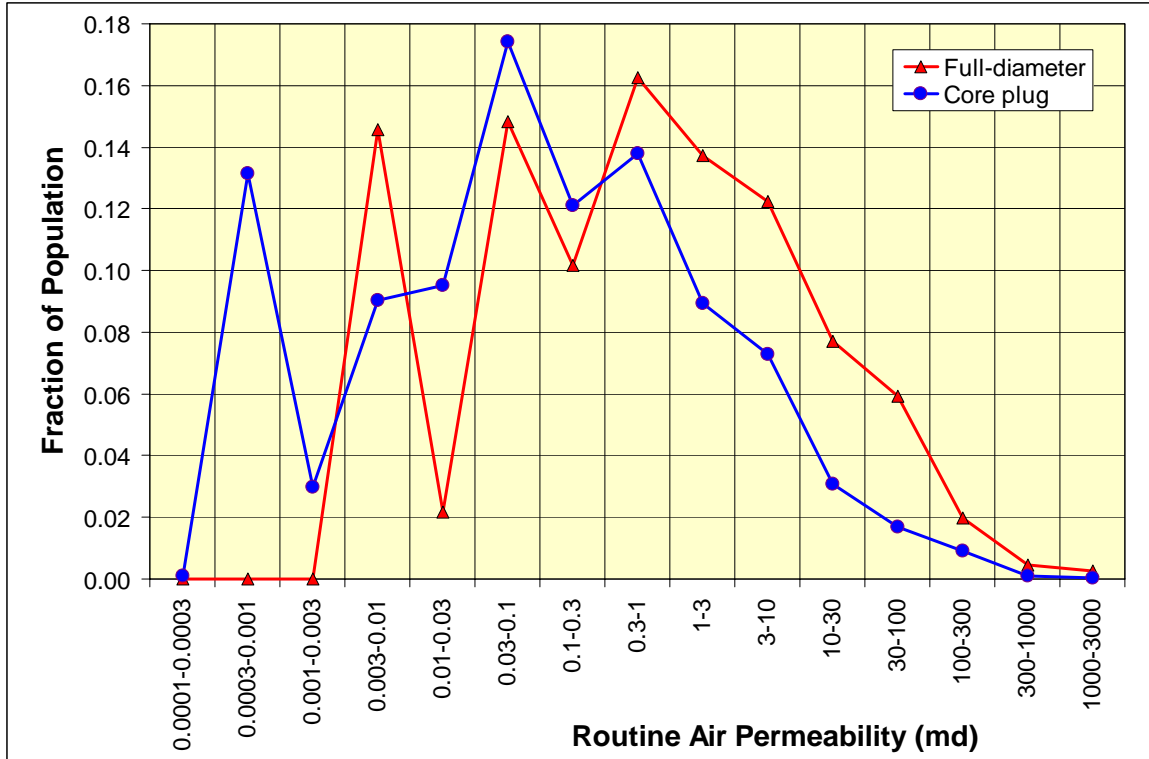


Figure 4.2.22. Frequency distribution of full-diameter and plug routine air permeability for Chase and Council Grove. This distribution does not exclude samples identified as fractured. Samples with permeability identified as “k<0.1 md” were assigned k=0.1 md and samples with permeability identified as “k< 0.01 md” were assigned a value of k=0.001 md.

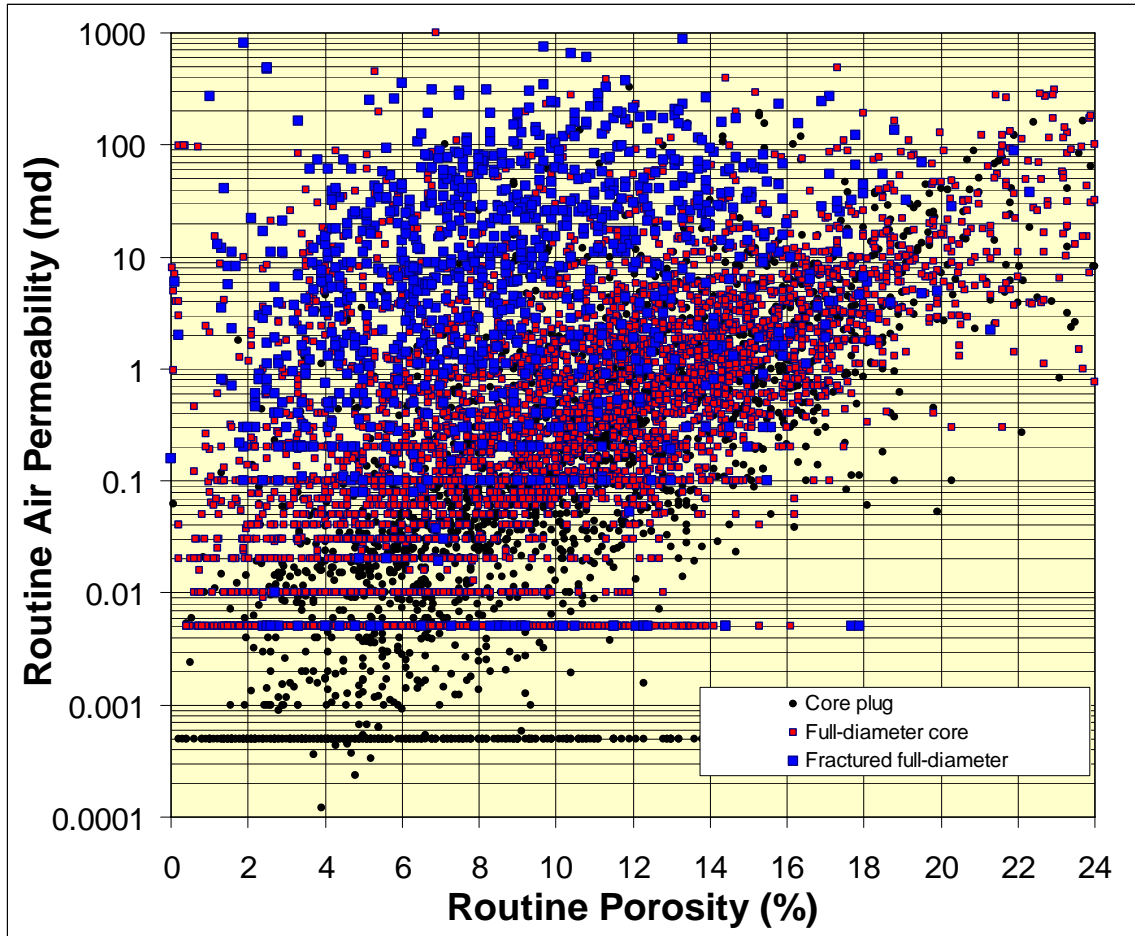


Figure 4.2.23. Crossplot of routine air permeability versus porosity for full-diameter cores where fractures were noted, for the remaining fraction of full-diameter cores in which fractures were not noted but may have been present, and core plugs. Samples with permeability identified as “ $k < 0.1$ md” were assigned $k = 0.05$ md and samples with permeability identified as “ $k < 0.01$ md” were assigned a value of $k = 0.005$ md. Full-diameter core values begin to diverge from matrix (plug) values at porosities less than $\sim 10\%$ and matrix permeability of ~ 0.5 md reflecting the influence of microfracture(s) on permeability in whole core samples with porosity $< 10\%$. Above 10% porosity influence of microfractures(s) is small.

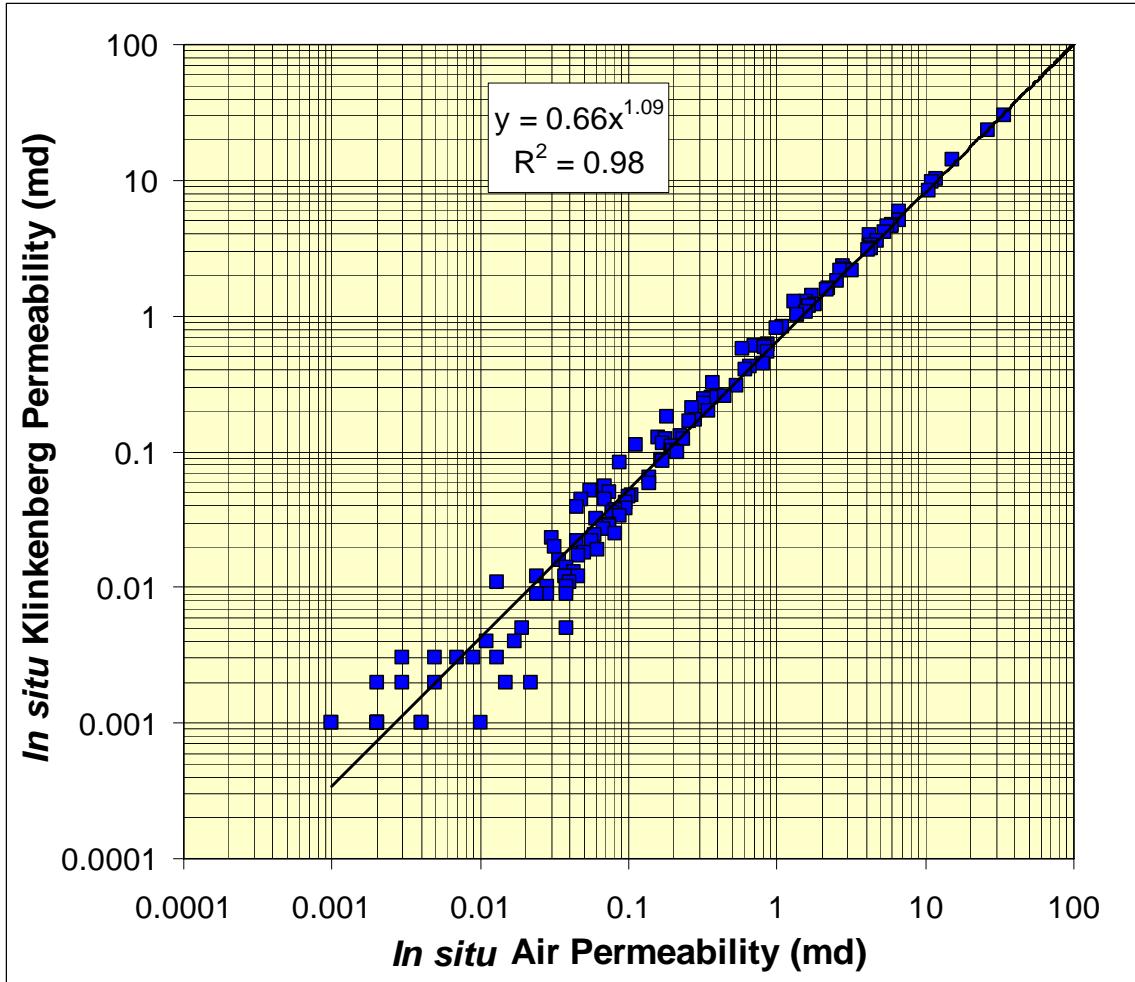


Figure 4.2.24. Crossplot of *in situ* Klinkenberg permeability versus *in situ* air permeability. This crossplot isolates the influence of Klinkenberg effect on permeability after confining stress influence is in effect. Klinkenberg effect is a function of the mean pore pressure which is not controlled in the crossplot and accounts for some of the variance exhibited. Routine confining stress and pore-pressure measurements also vary between laboratories which can influence the plot. However, the equation provides a means to predict Klinkenberg permeability within the error shown: $k_{ik} = 0.66 k_{ia}^{1.09}$.

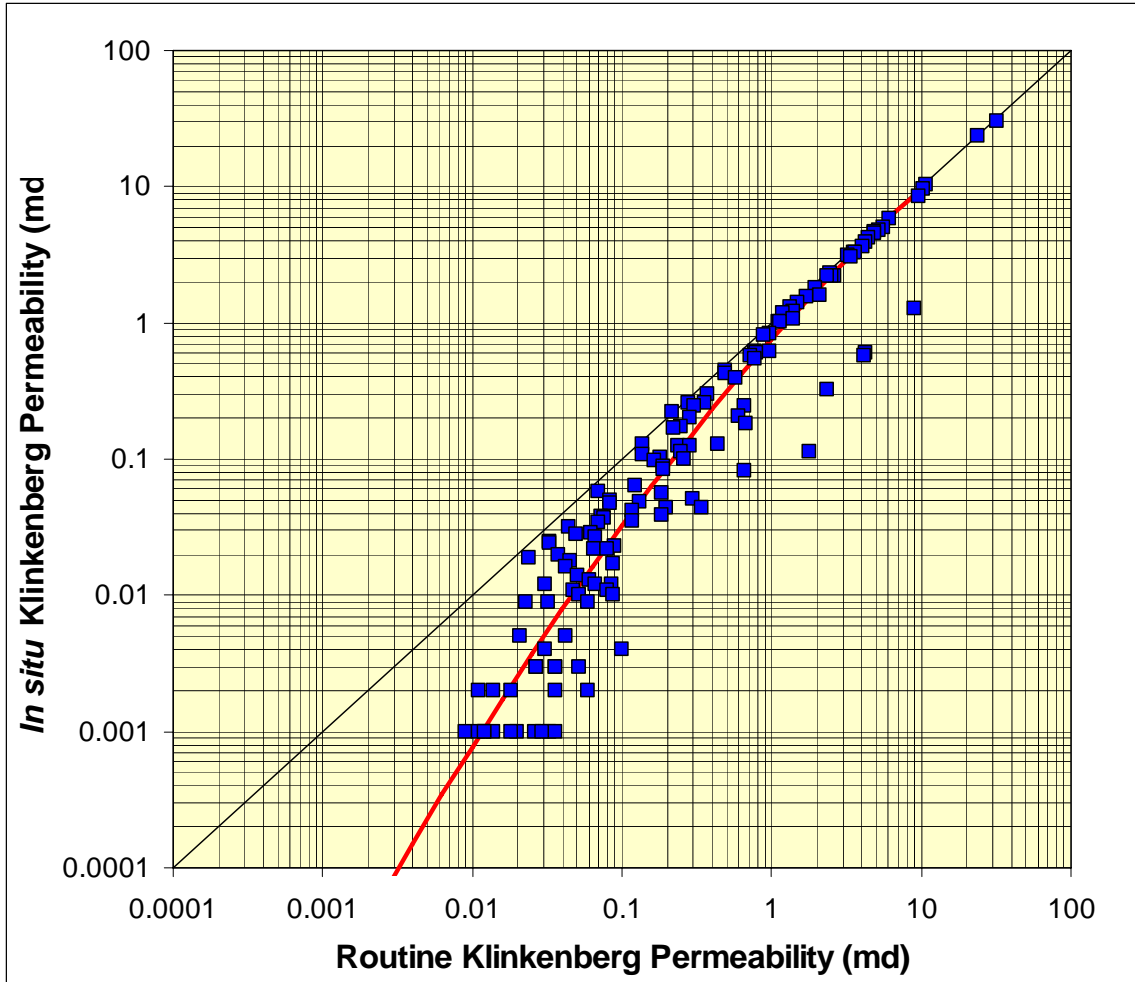


Figure 4.2.25. Crossplot of *in situ* Klinkenberg permeability versus routine Klinkenberg permeability where routine confining stress is generally 400-800 psi. This crossplot isolates the influence of confining stress effect on permeability. Routine confining stress measurements vary between laboratories which can influence the plot. However, the equation provides a means to predict *in situ* Klinkenberg permeability within the error shown: $\log_{10}k_{ik} = -0.129 (\log_{10}k_{ak})^2 + 1.236 \log_{10}k_{ak} - 0.12$. This equation can only be applied for samples with $k < 10$ md. The few low outliers probably represent samples with fractures.

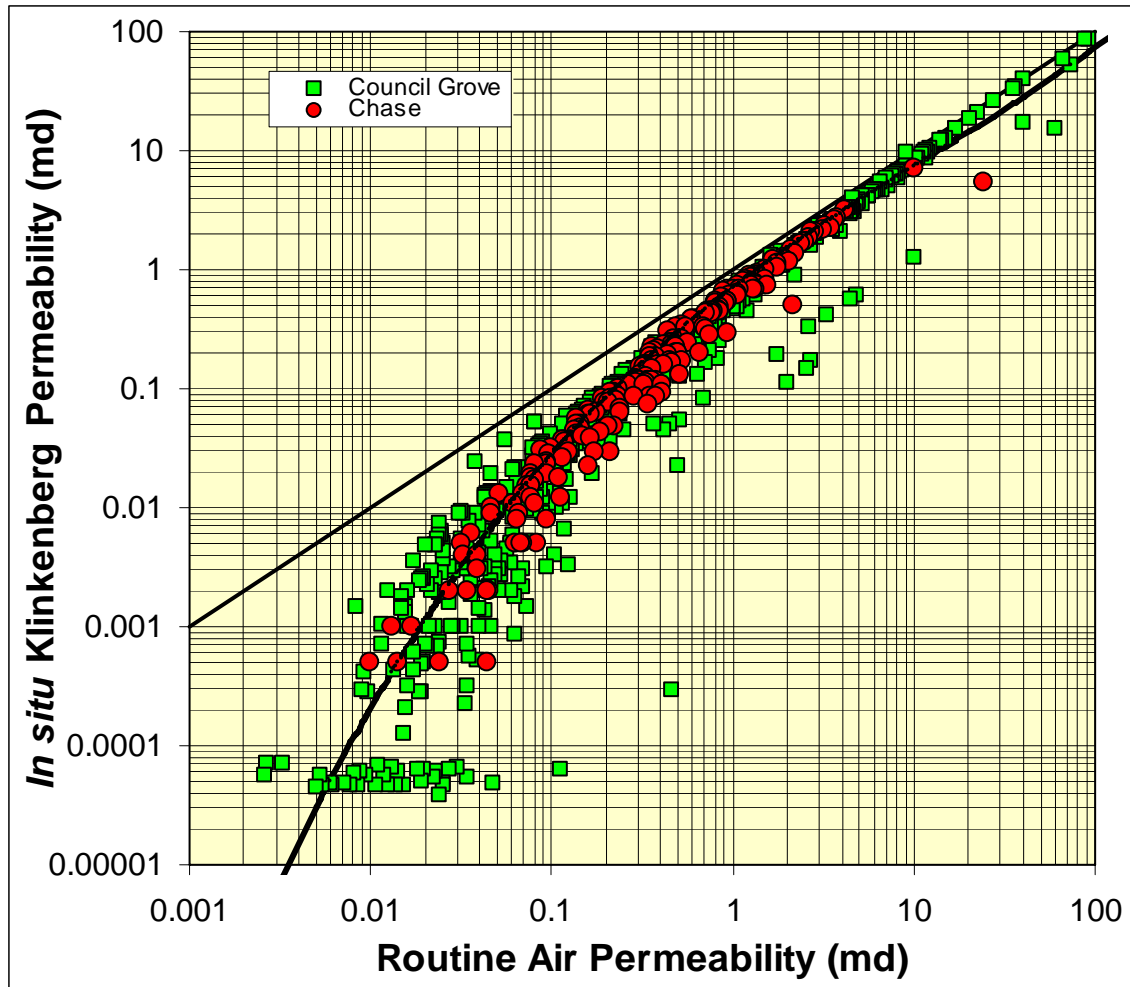


Figure 4.2.26. Crossplot of routine air permeability (k_{air}) versus *in situ* Klinkenberg gas permeability (k_{ik}) for Council Grove rocks (green squares) and Chase rocks (red circles). Influence of both confining stress and Klinkenberg correction increase with decreasing permeability. Values of k_{ik} can be predicted approximately from k_{air} using:

$$\log_{10}k_{ik} = 0.059 (\log_{10}k_{air})^3 - 0.187 (\log_{10}k_{air})^2 + 1.154 \log_{10}k_{air} - 0.159$$
where permeabilities are in millidarcies (md). Equation is only valid for $k < 10$ md. Variance is due to both differing routine conditions and rock response.

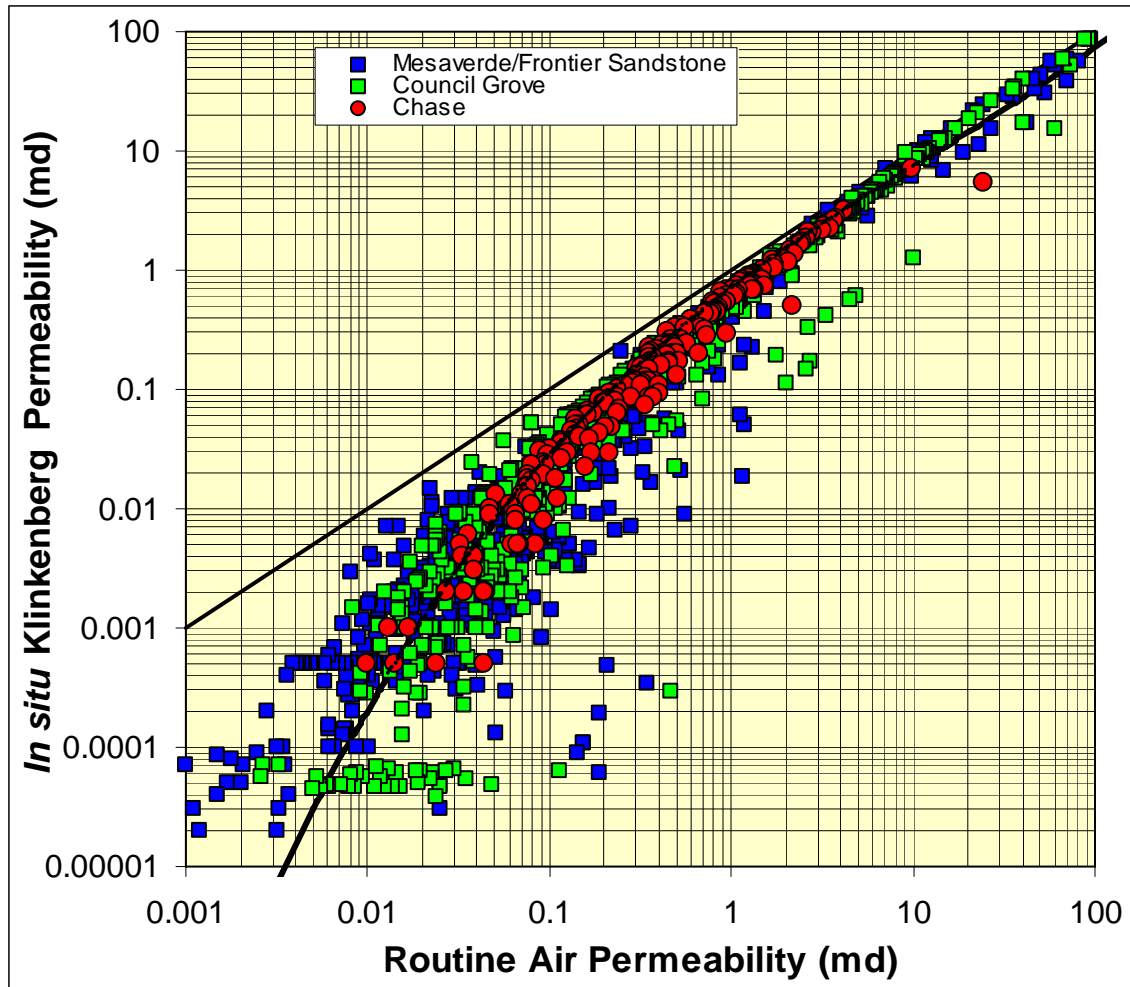


Figure 4.2.27. Crossplot of routine air permeability (k_{air}) versus *in situ* Klinkenberg gas permeability (k_{ik}) for Council Grove rocks (green squares) and Chase rocks (red circles) and for comparison with other low-permeability rocks Mesaverde-Frontier sandstones (blue squares). Influence of both confining stress and Klinkenberg correction increase with decreasing permeability. Values of k_{ik} can be predicted approximately from k_{air} using:

$$\log_{10}k_{ik} = 0.059 (\log_{10}k_{air})^3 - 0.187 (\log_{10}k_{air})^2 + 1.154 \log_{10}k_{air} - 0.159$$

where permeabilities are in millidarcies (md). Equation is only valid for $k < 10$ md. Variance is due to both differing routine conditions and rock response.

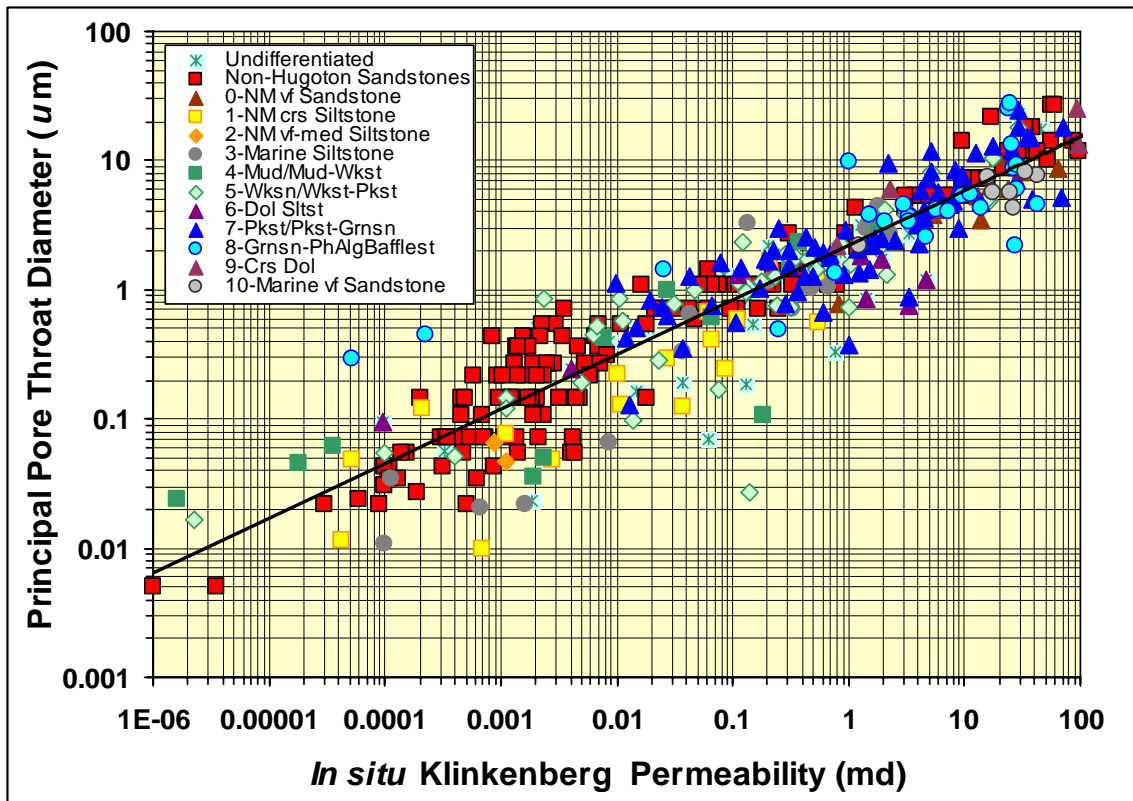


Figure 4.2.28. Crossplot of principal pore-throat diameter (PPTD, microns) versus *in situ* Klinkenberg permeability (k_{ik}) for lithofacies in Chase and Council Grove Groups and sandstones from outside the Hugoton Embayment for comparison. The good correlation over eight orders of magnitude shows the predominant influence that pore-throat size exerts on permeability and explains permeability changes with grain size and Dunham classification at a given porosity. Second Y-axis shows corresponding threshold entry heights necessary for gas column to enter sample for gas pressure and temperature conditions in Hugoton area and discussed in text. The correlation between k_{ik} and PPTD can be expressed: $PPTD = 2.2 k_{ik}^{0.42}$. Standard error of prediction for this correlation is a factor of 1.7x.

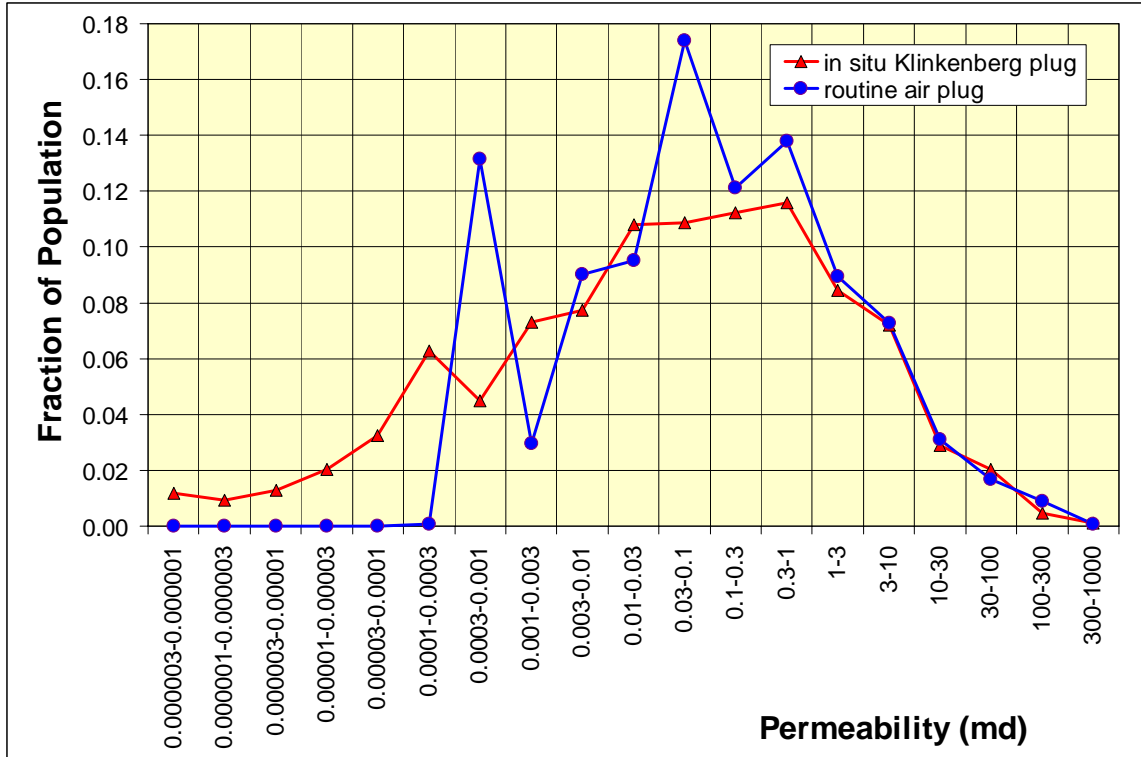


Figure 4.2.29. Frequency distribution of core plug routine air permeability and *in situ* Klinkenberg permeability for Chase and Council Grove.

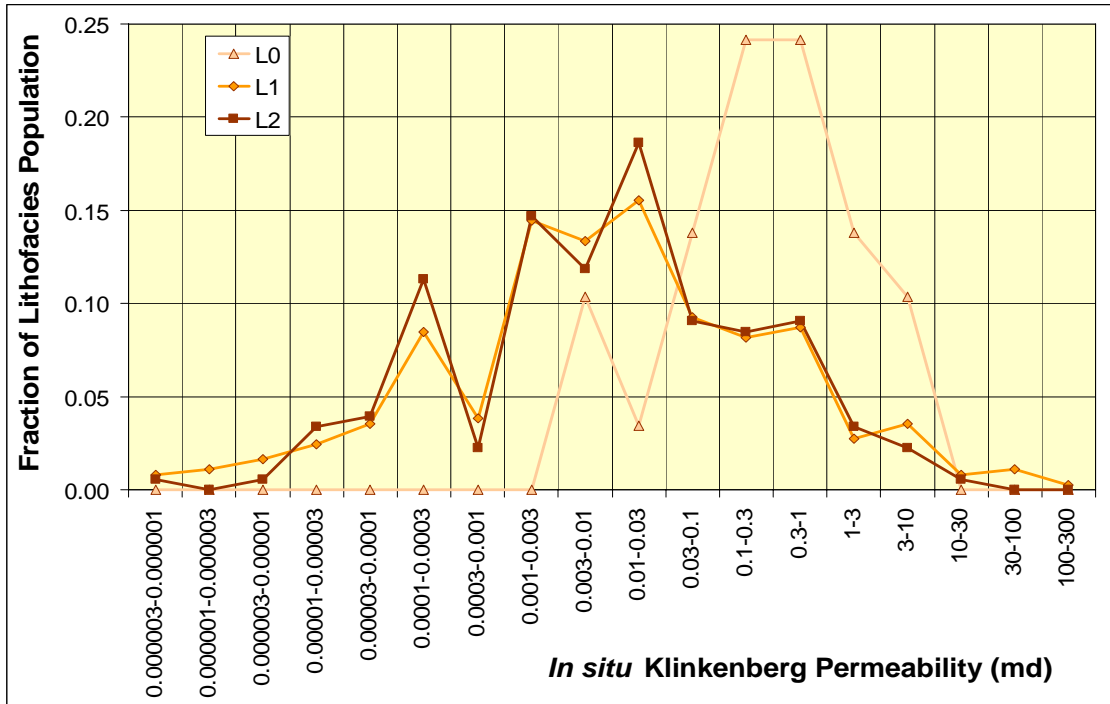


Figure 4.2.30. Frequency distribution of *in situ* Klinkenberg permeability for continental lithofacies L0, L1, and L2. Very fine to fine-grained sandstones (L0) exhibit permeabilities 2-5X greater than siltstones. Coarse siltstones (L1) and shaly fine-medium-grained siltstones (L2) are similar in distribution.

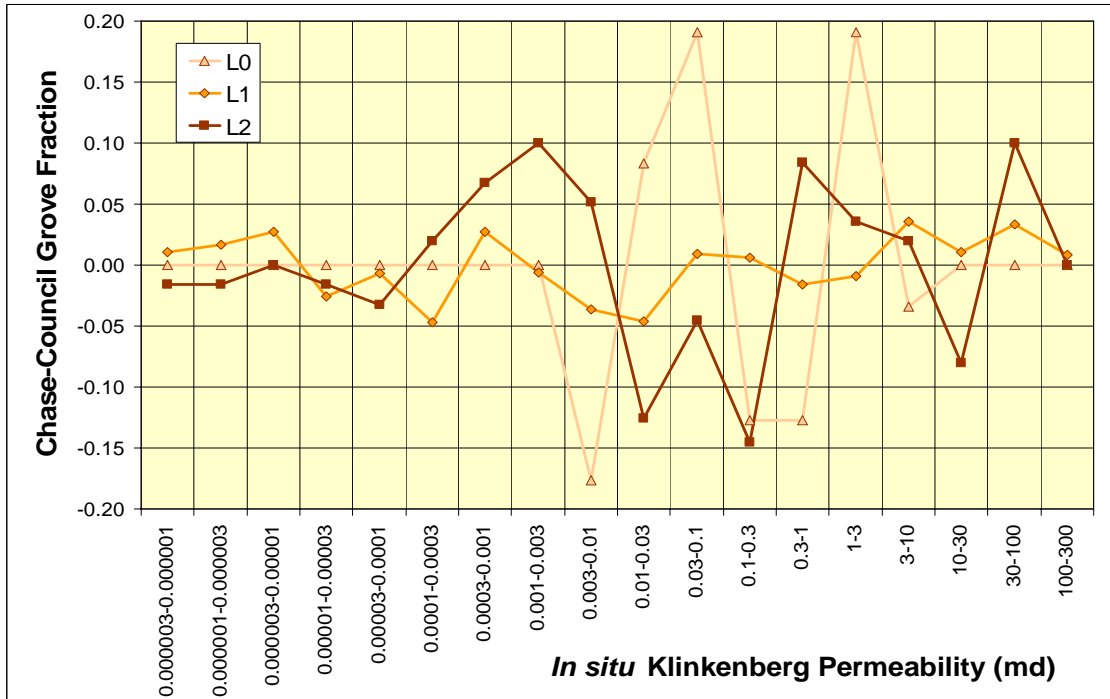


Figure 4.2.31. Difference between Chase and Council Grove fractions for each bin class of permeability for continental clastic facies showing similarities of L1 distributions and variability of L0 and L2 distribution differences.

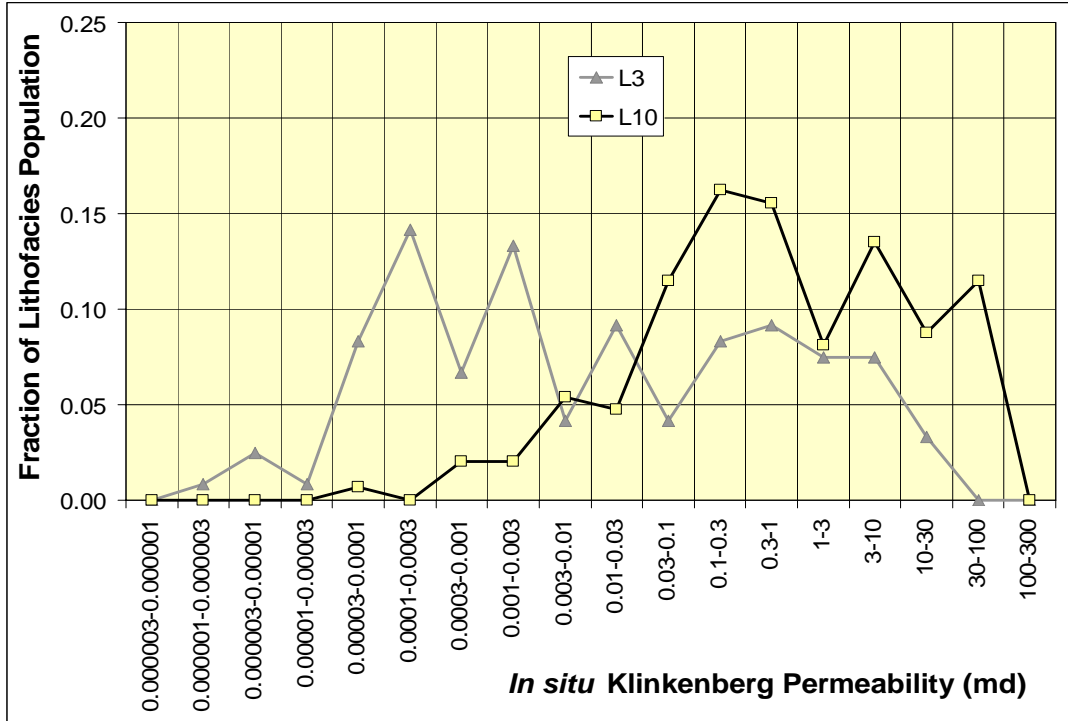


Figure 4.2.32A. Frequency distribution of *in situ* Klinkenberg permeability for marine clastic shale/siltstones (L3) and very fine to fine-grained sandstones (L10).

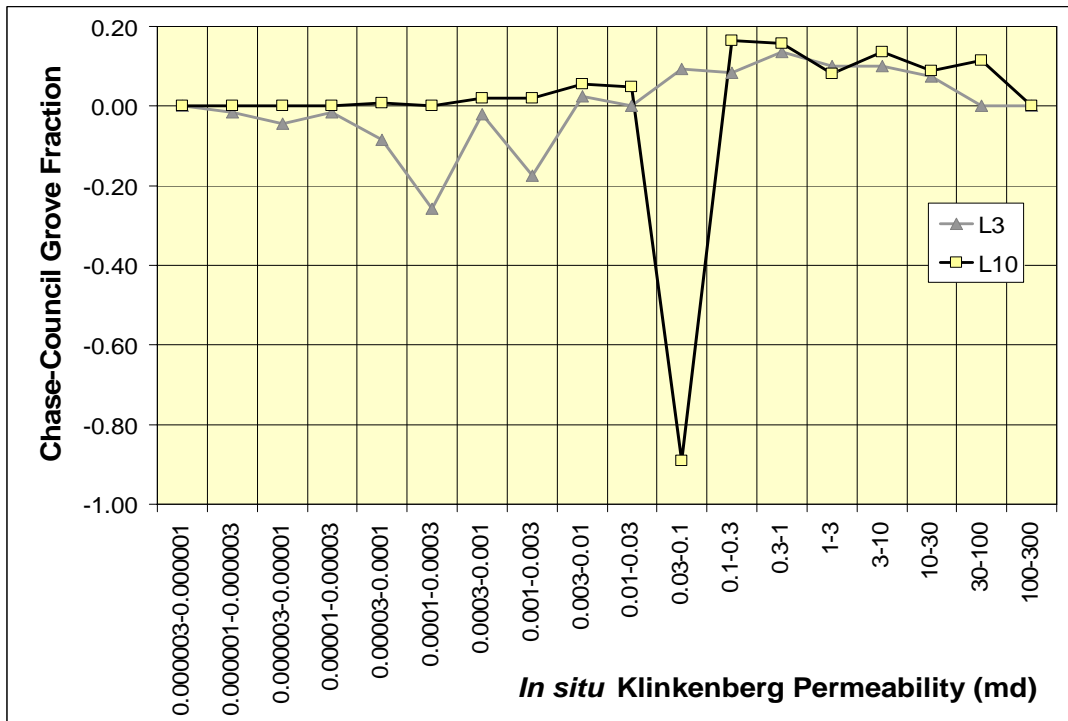


Figure 4.2.32B. Difference between Chase and Council Grove fractions for each bin class of permeability for marine clastic lithofacies (L3, L10) showing higher permeabilities of Chase very fine to fine-grained sandstones (L10) and siltstones (L3). Differences between sandstones vary with permeability and porosity, but Chase has larger fraction of highest porosity range.

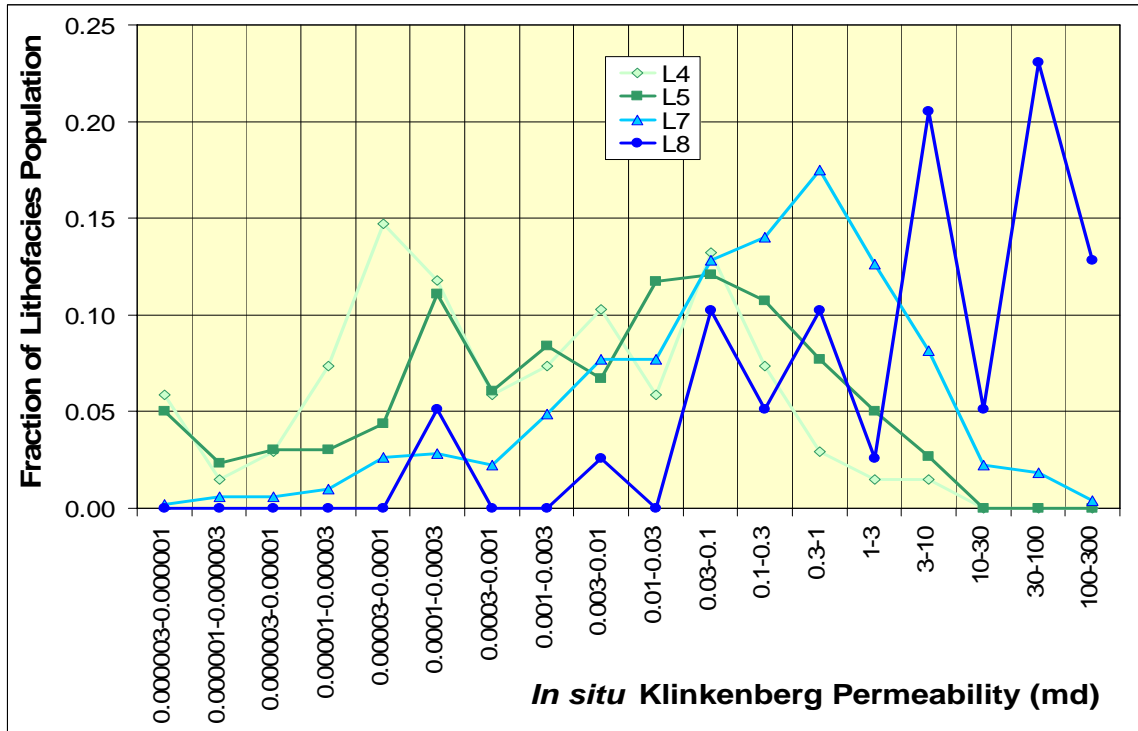


Figure 4.2.33. Frequency distribution of *in situ* Klinkenberg permeability for limestone lithofacies L4, L5, L7, and L8. Fractions of higher permeability generally increase with increasing grain support texture.

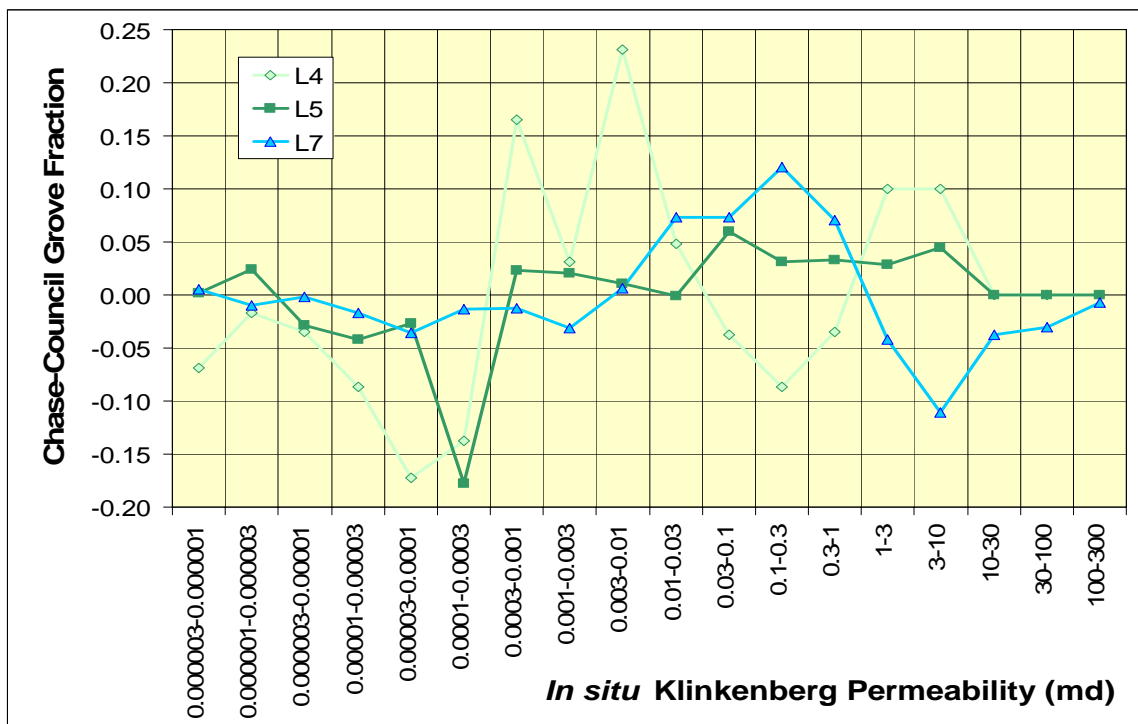


Figure 4.2.34. Difference between Chase and Council Grove fractions for each bin class of permeability for limestone lithofacies (L4, L5, L7) showing higher permeabilities of Chase rocks except L7 $K > 1$ md. Phylloid algal bafflestones, L8) not sampled in Chase.

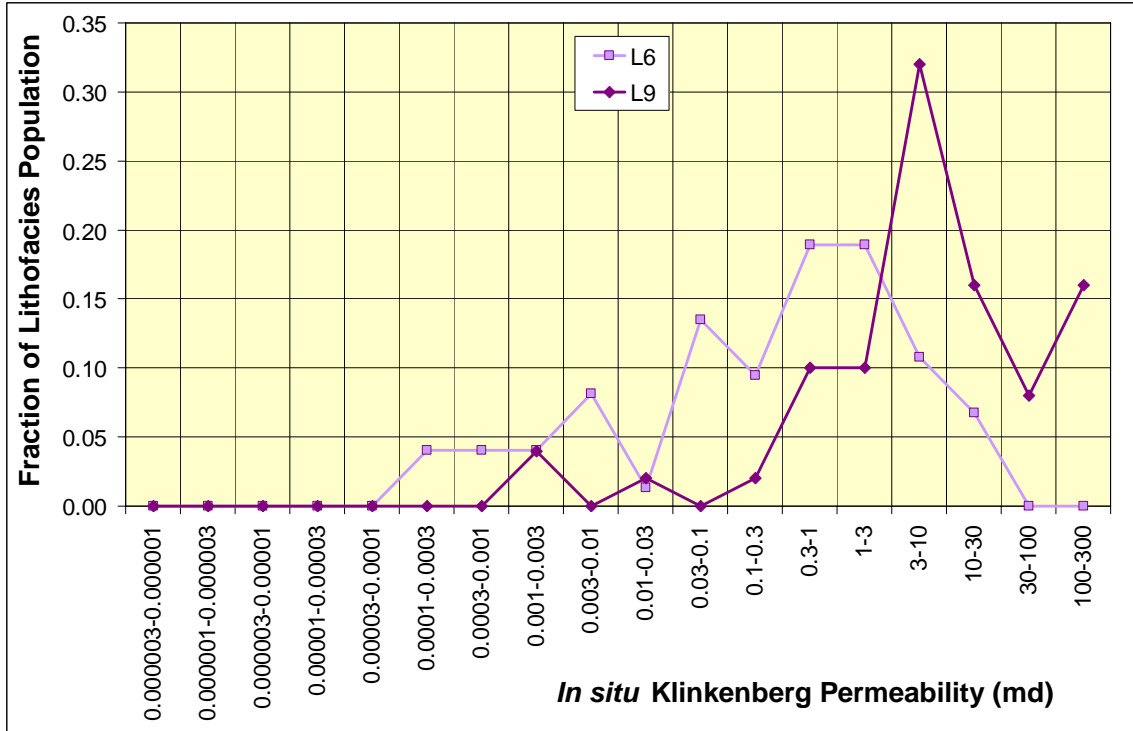


Figure 4.2.35. Frequency distribution of *in situ* Klinkenberg permeability for dolomite lithofacies L6 and L9. Medium-crystalline sucrosic moldic dolomites exhibit higher permeability than fine-grained dolomites.

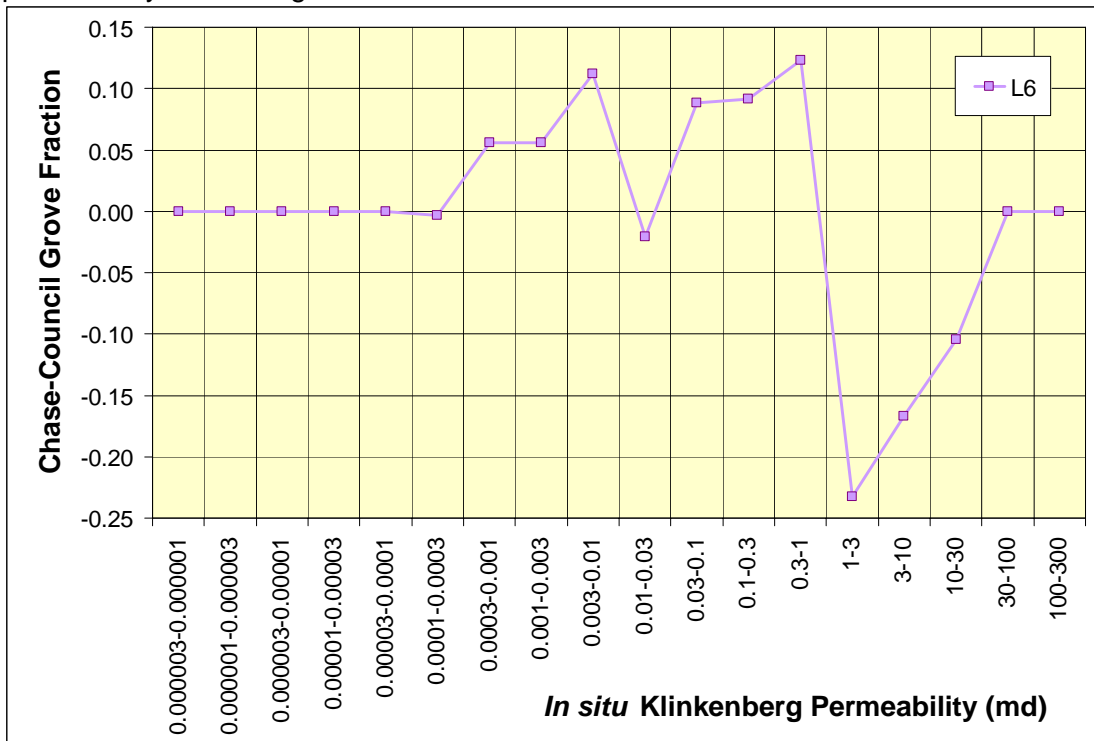


Figure 4.2.36. Difference between Chase and Council Grove fractions for each bin class of permeability for very fine to fine-crystalline sucrosic dolomites (L6) showing lower permeability of Chase. There are no identified medium-crystalline dolomites (L9) in the Council Grove.

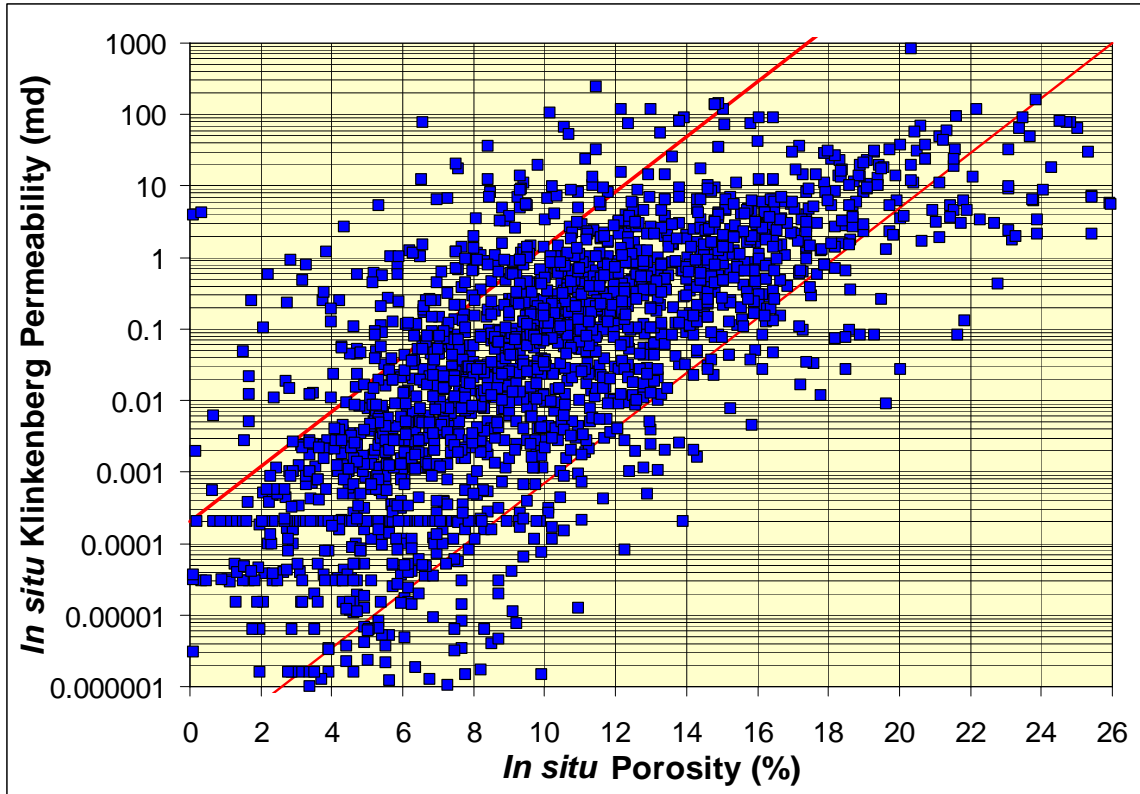


Figure 4.2.37. Crossplot of *in situ* porosity versus *in situ* Klinkenberg gas permeability (k_{ik}) for all Chase and Council Grove core plugs exhibits more than three orders of magnitude variance at any given porosity.

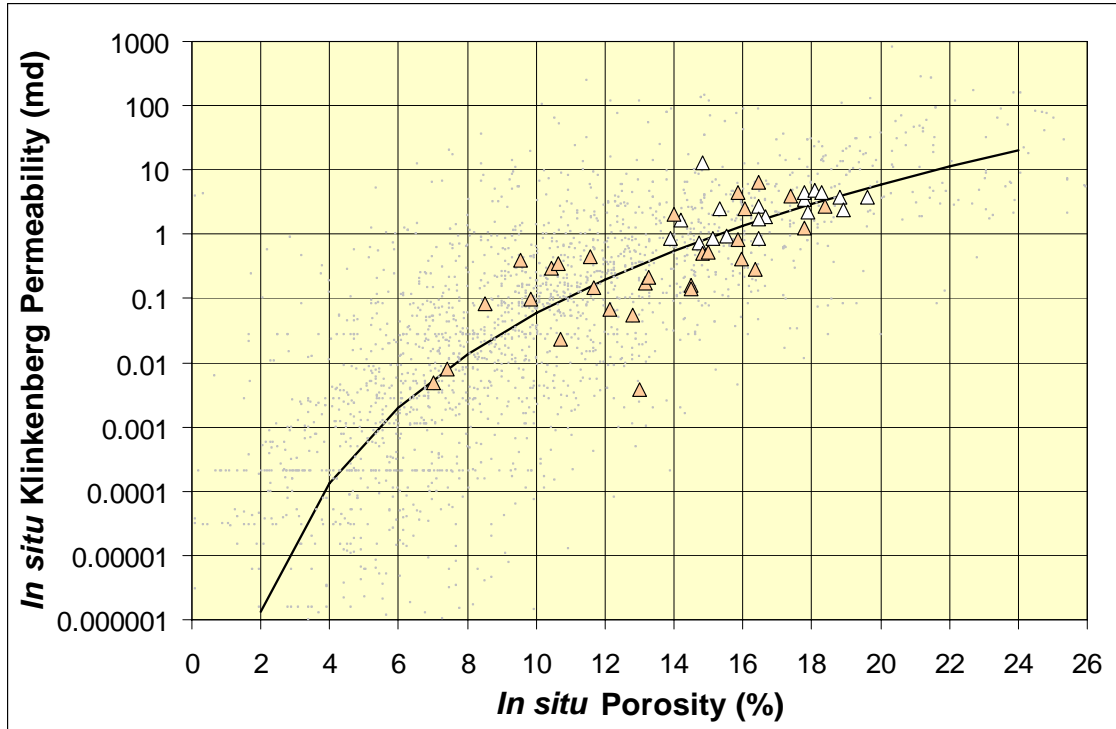


Figure 4.2.38. Crossplot of core plug *in situ* Klinkenberg permeability (k_{ik}) versus *in situ* porosity (ϕ_i) for the continental very fine to fine-grained sandstones (L0, tan triangles) including limited full-diameter data (open triangles) and all Hugoton (gray dot). For curve $k_{ik} = A \phi_i^B$, $A = 6.65$ and $B = -7.888$, $SE = 2.9X$.

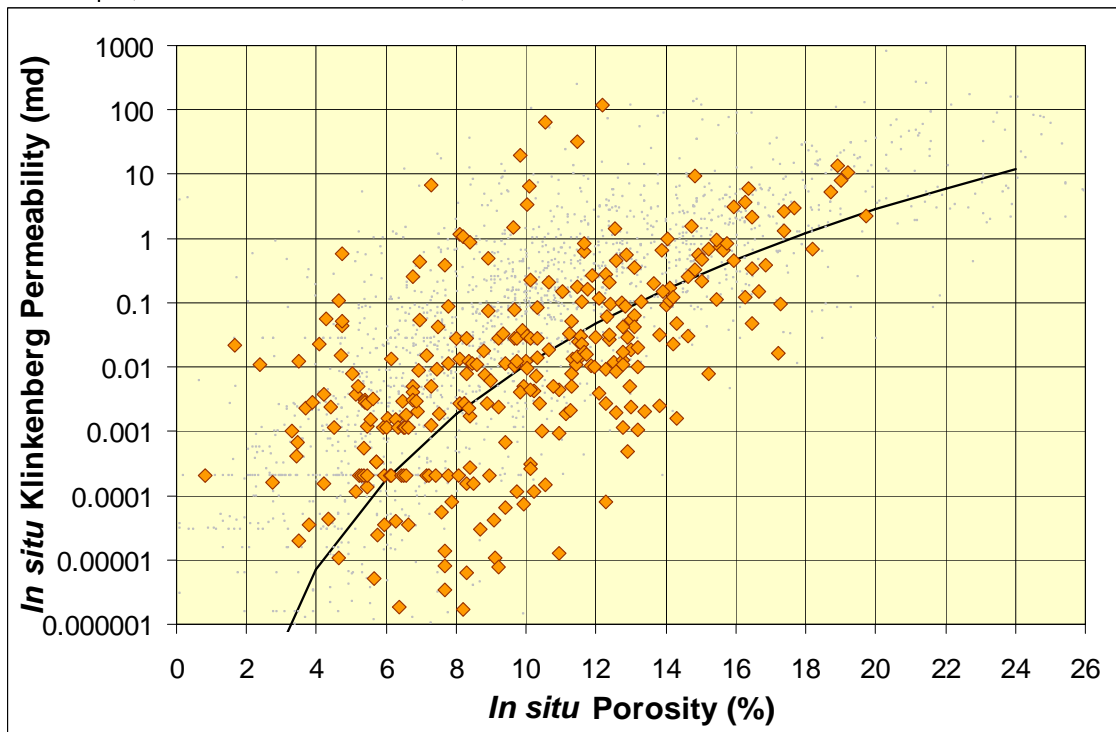


Figure 4.2.39. Crossplot of core plug *in situ* Klinkenberg permeability (k_{ik}) versus *in situ* porosity (ϕ_i) for the continental coarse-grained siltstones (L1, orange diamonds) and all Hugoton (gray dot). For curve $k_{ik} = A \phi_i^B$, $A = 8.00$ and $B = -9.96$, $SE = 9.3X$.

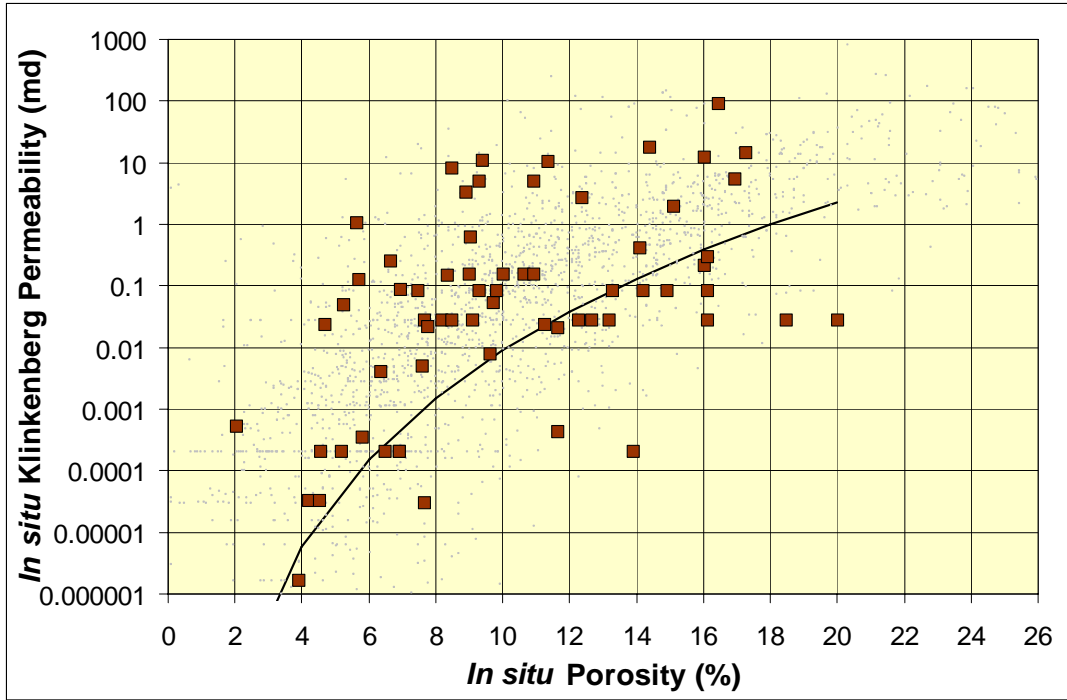


Figure 4.2.40. Crossplot of core plug *in situ* Klinkenberg permeability (k_{ik}) versus *in situ* porosity (ϕ_i) for the continental shaly fine to medium-grained siltstones (L2, brown square) and all Hugoton (gray dot). For curve $k_{ik} = A \phi_i^B$, $A = 8.00$ and $B = -10.05$, $SE = 15.6X$.

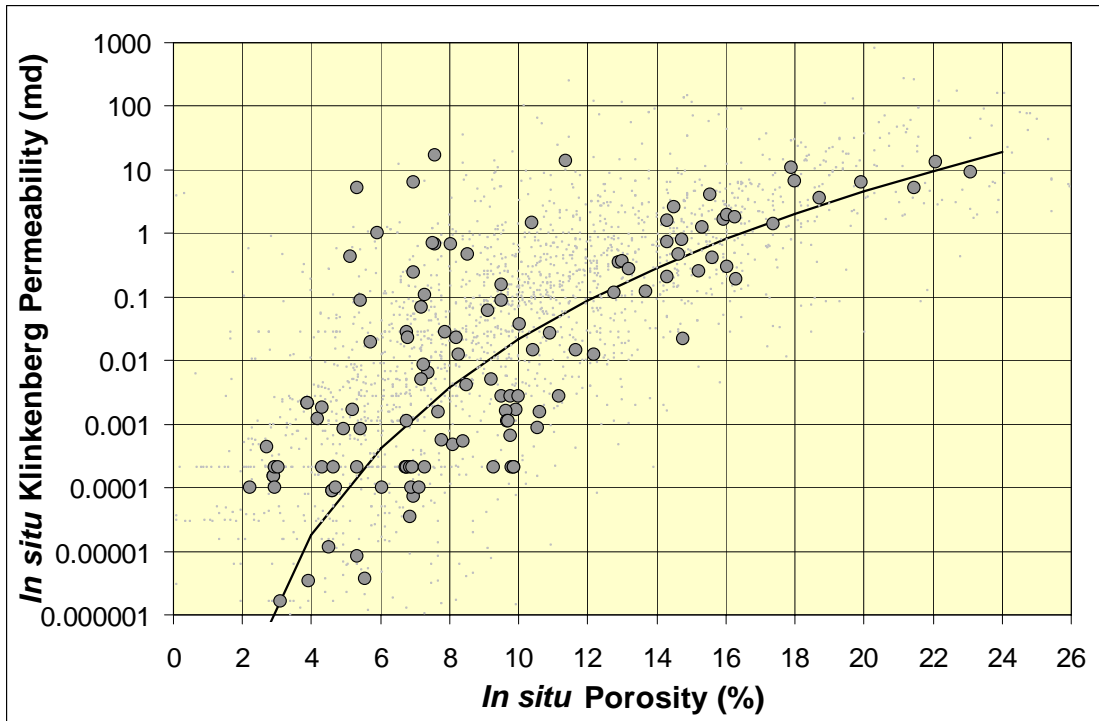


Figure 4.2.41. Crossplot of core plug *in situ* Klinkenberg permeability (k_{ik}) versus *in situ* porosity (ϕ_i) for the marine shale/siltstones (L3, gray circle) and all Hugoton (gray dot). For curve $k_{ik} = A \phi_i^B$, $A = 7.74$ and $B = -9.41$, $SE = 9.2X$.

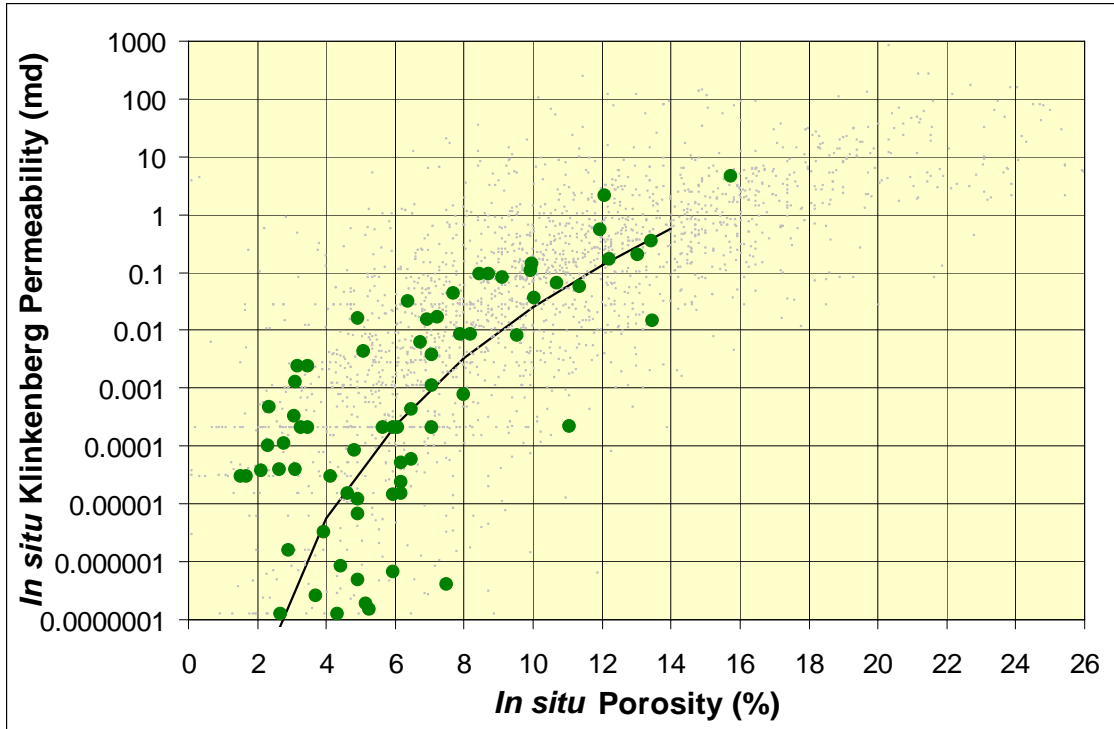


Figure 4.2.42. Crossplot of core plug *in situ* Klinkenberg permeability (k_{ik}) versus *in situ* porosity (ϕ_i) for the mudstone/mud-wackestone (L4, green circle) and all Hugoton (gray dot). For curve $k_{ik} = A \phi_i^B$, $A = 9.20$ and $B = -10.80$, $SE = 16.0X$.

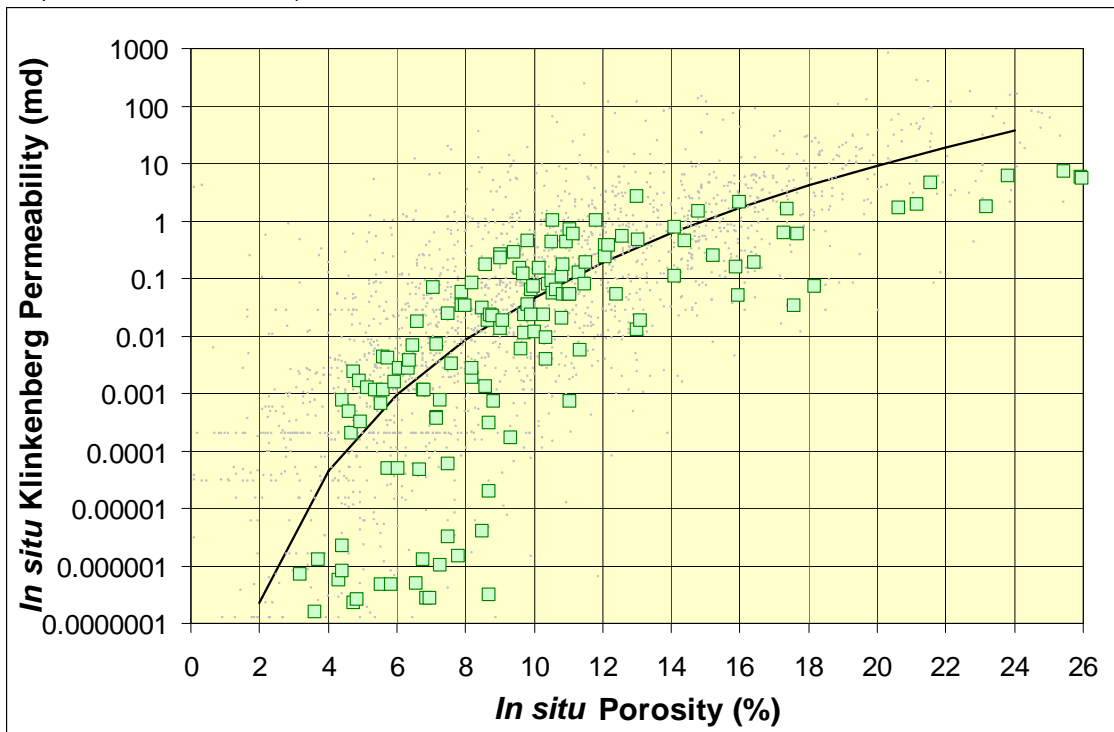


Figure 4.2.43. Crossplot of core plug *in situ* Klinkenberg permeability (k_{ik}) versus *in situ* porosity (ϕ_i) for the wackestone/wacke-packstone (L5, light-green diamond) and all Hugoton (gray dot). For curve $k_{ik} = A \phi_i^B$, $A = 7.74$ and $B = -9.41$, $SE = 9.2X$.

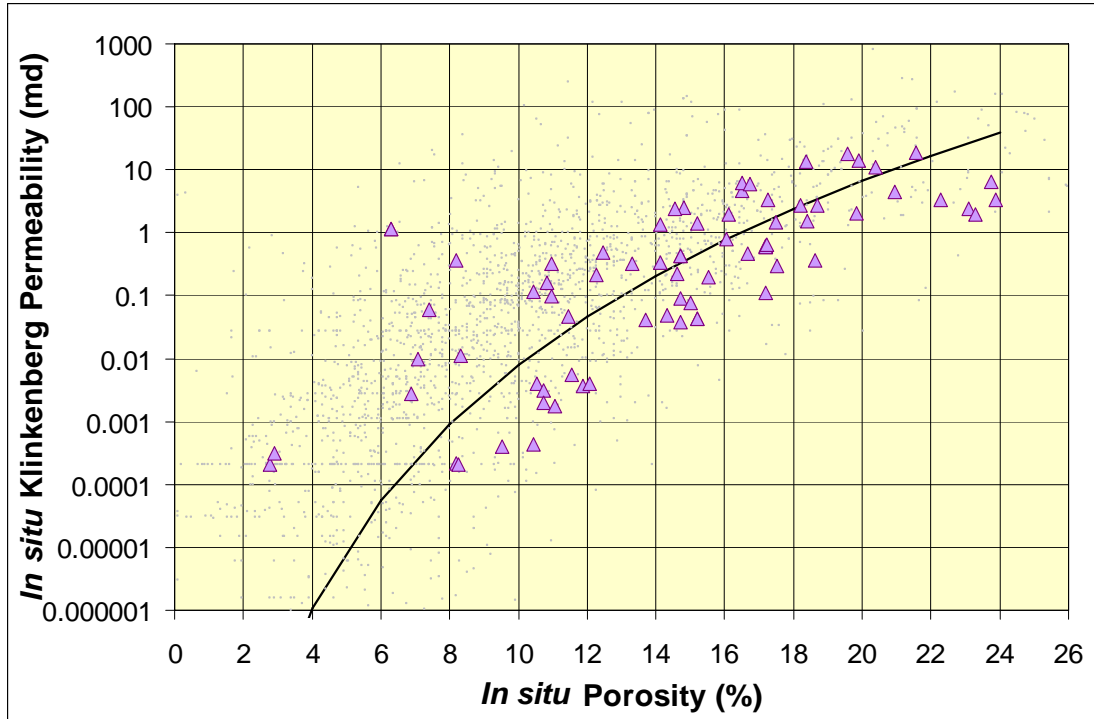


Figure 4.2.44. Crossplot of core plug *in situ* Klinkenberg permeability (k_{ik}) versus *in situ* porosity (ϕ_i) for the very fine to fine-crystalline sucrosic dolomite (L6, light purple triangle) and all Hugoton (gray dot). For curve $k_{ik} = A \phi_i^B$, $A = 9.70$ and $B = -11.80$, $SE = 5.3X$.

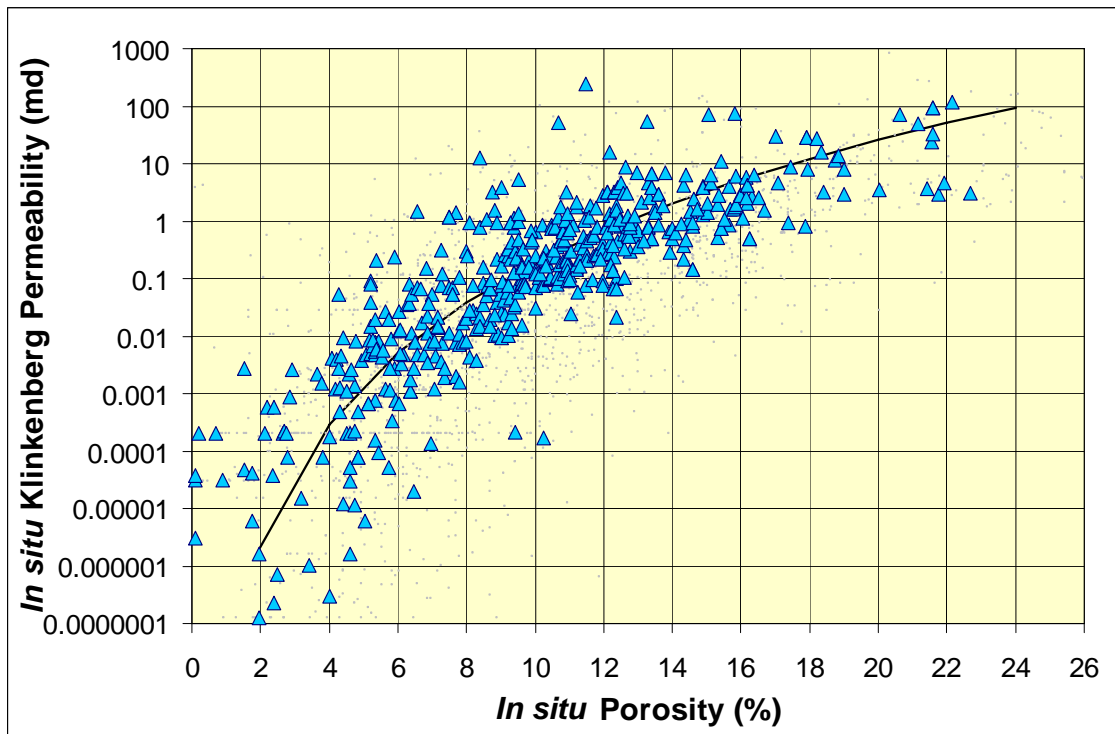


Figure 4.2.45. Crossplot of core plug *in situ* Klinkenberg permeability (k_{ik}) versus *in situ* porosity (ϕ_i) for the packstone/grainstone (L7, light-blue triangle) and all Hugoton (gray dot). For curve $k_{ik} = A \phi_i^B$, $A = 7.09$ and $B = -7.81$, $SE = 4.0X$.

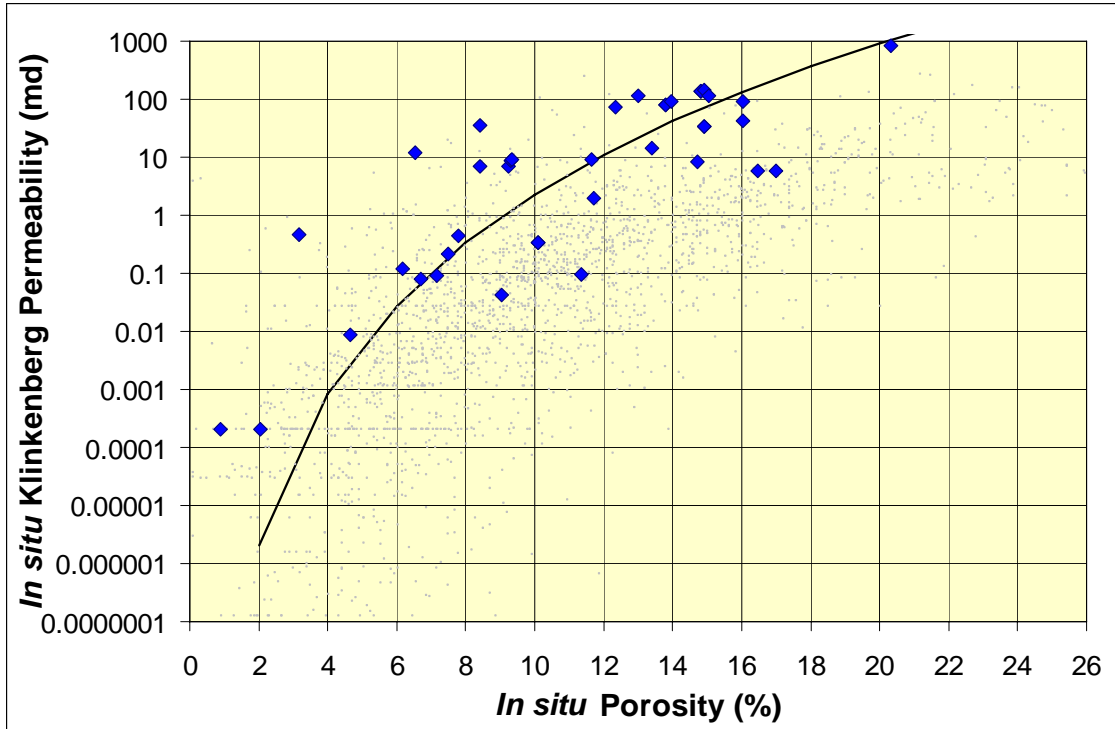


Figure 4.2.46. Crossplot of core plug *in situ* Klinkenberg permeability (k_{ik}) versus *in situ* porosity (ϕ_i) for the phylloid algal bafflestone (L8, blue diamond) and all Hugoton (gray dot). For curve $k_{ik} = A \phi_i^B$, $A = 8.65$ and $B = -8.29$, $SE = 5.4X$.

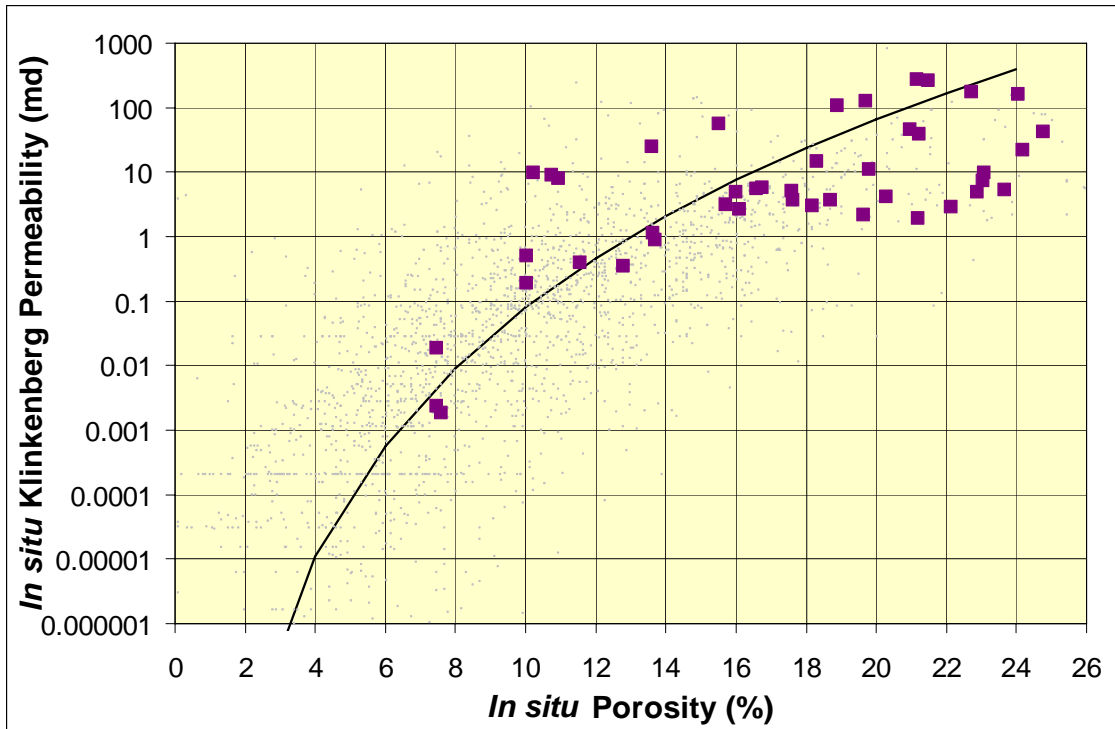


Figure 4.2.47. Crossplot of core plug *in situ* Klinkenberg permeability (k_{ik}) versus *in situ* porosity (ϕ_i) for the medium-crystalline sucrosic moldic dolomite (L9, purple square) and all Hugoton (gray dot). For curve $k_{ik} = A \phi_i^B$, $A = 9.70$ and $B = -10.80$, $SE = 6.7X$.

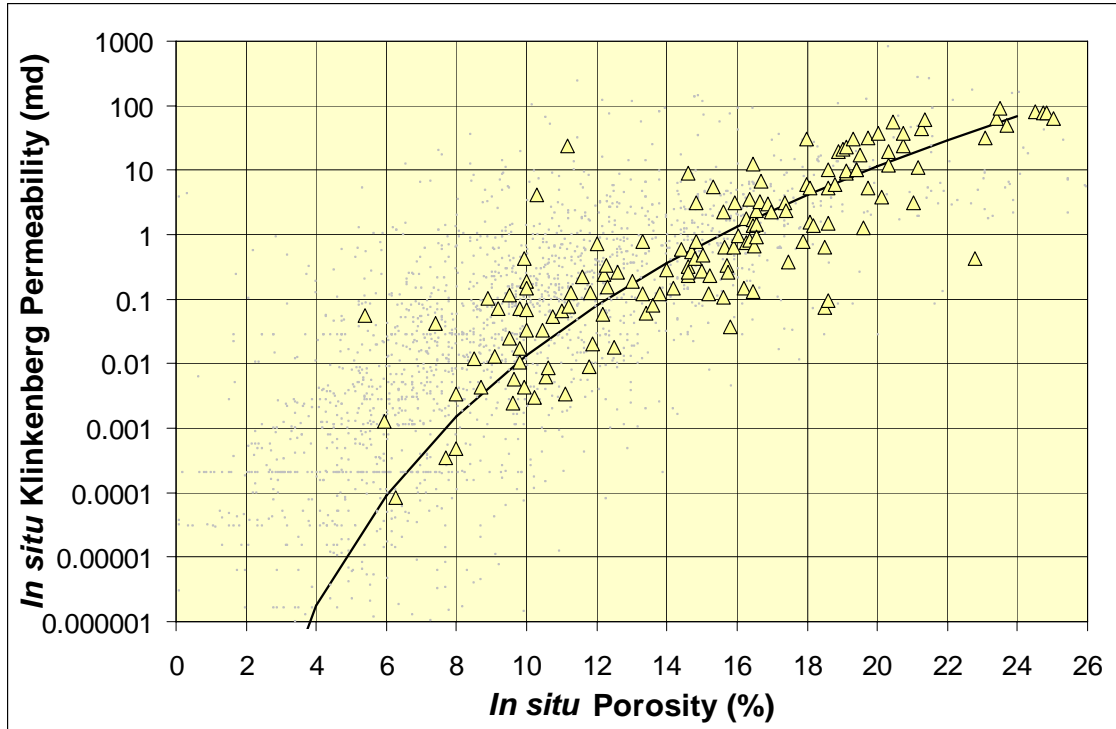


Figure 4.2.48. Crossplot of core plug *in situ* Klinkenberg permeability (k_{ik}) versus *in situ* porosity (ϕ_i) for the marine very fine to fine-grained sandstone (L10, light-yellow triangle) and all Hugoton (gray dot). For curve $k_{ik} = A \phi_i^B$, $A = 9.75$ and $B = -11.62$, $SE = 3.5X$.

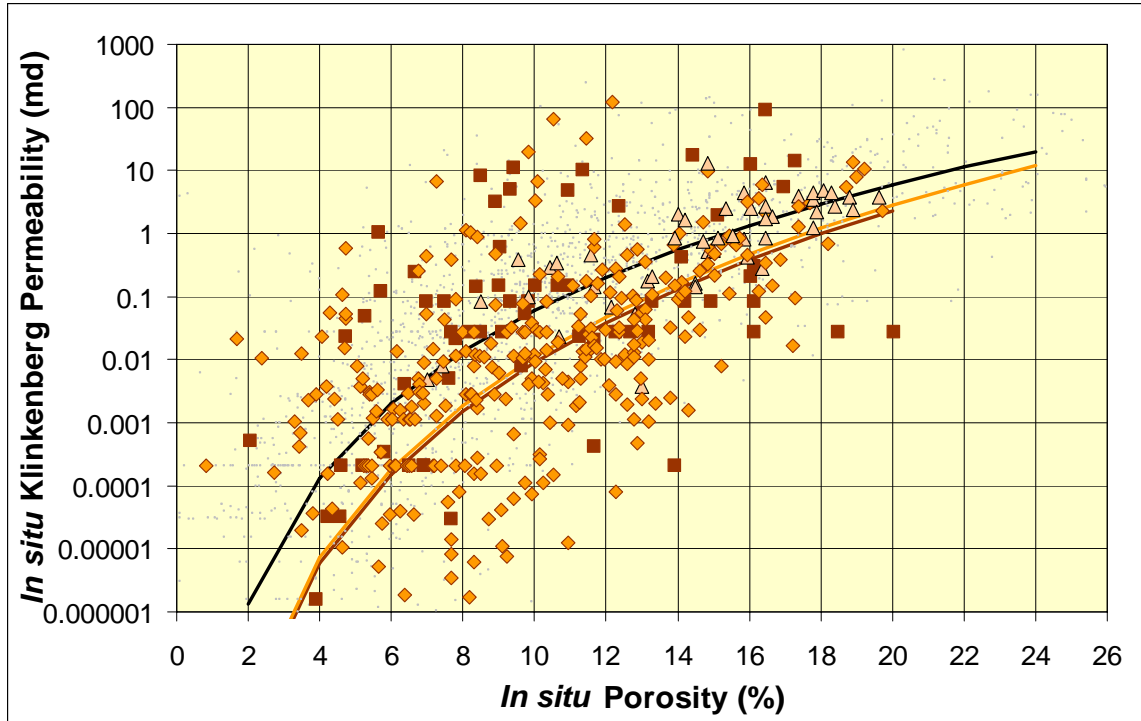


Figure 4.2.49. Crossplot of core plug *in situ* Klinkenberg permeability (k_{ik}) versus *in situ* porosity (ϕ_i) for the continental lithofacies including very fine to fine-grained sandstone (L0, tan triangle), coarse-grained siltstones (L1, orange diamonds), shaly fine- to medium-grained siltstones (L2, brown square) and all Hugoton (gray dot). For curves $k_{ik} = A \phi_i^B$, L0 (A = 9.75 and B = -11.62, SE = 3.5X), L1 (A = 8.00 and B = -9.96, SE = 9.3X), L2 (A = 8.00 and B = -10.05, SE = 15.6X).

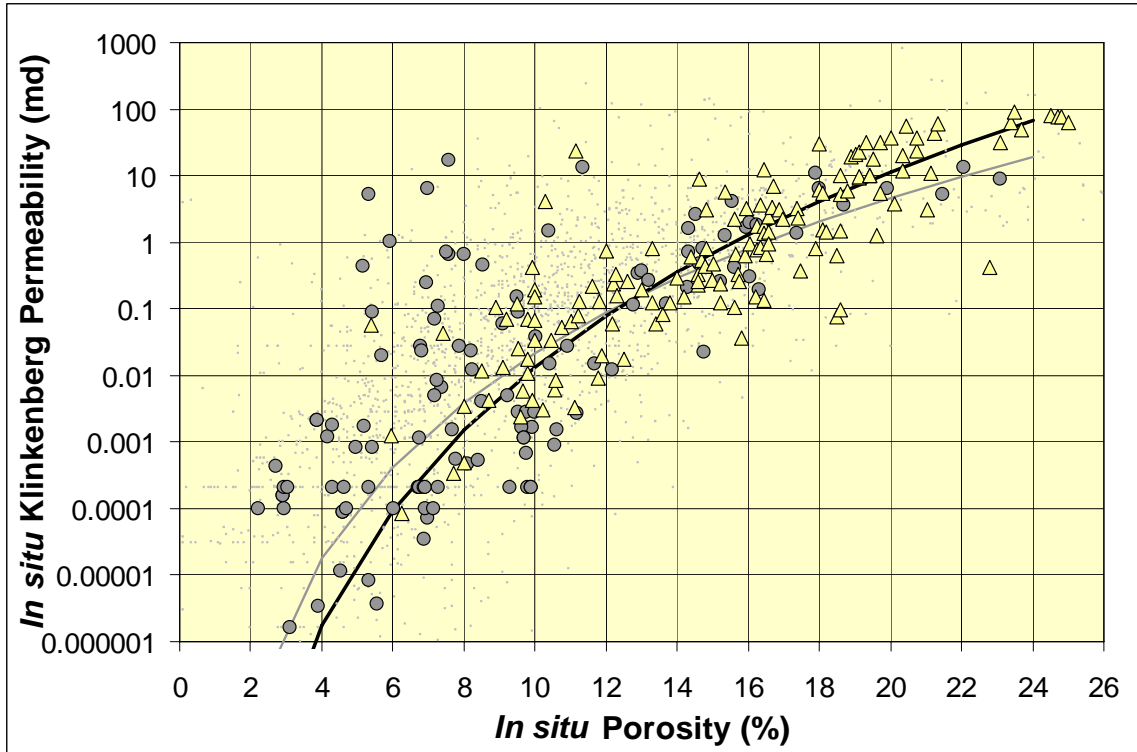


Figure 4.2.50. Crossplot of core plug *in situ* Klinkenberg permeability (k_{ik}) versus *in situ* porosity (ϕ_i) for the marine clastic lithofacies including shale/siltstone (L3, gray circle), very fine to fine-grained sandstone (L10, light yellow triangle), and all Hugoton (gray dot). For curves $k_{ik} = A \phi_i^B$, L3 ($A = 7.74$ and $B = -9.41$, $SE = 9.2X$), L10 ($A = 9.75$ and $B = -11.62$, $SE = 3.5X$).

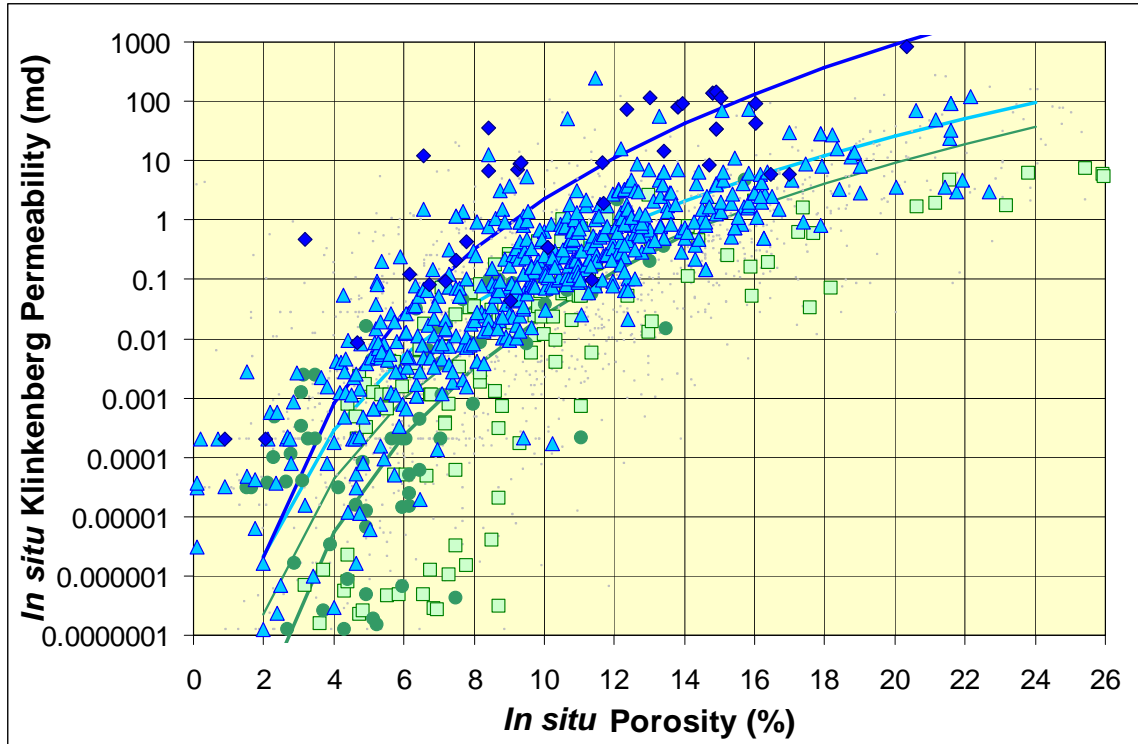


Figure 4.2.51. Crossplot of core plug *in situ* Klinkenberg permeability (k_{ik}) versus *in situ* porosity (ϕ_i) for the limestone lithofacies including mudstone/mud-wackestone (L4, green circle), wackestone/wacke-packstone (L5, light-green square), packstone/grainstone (L7, light blue triangle), phylloid algal bafflestone (L8, blue diamond) and all Hugoton (gray dot). For curves $k_{ik} = A \phi_i^B$, L4 ($A = 9.20$ and $B = -10.80$, $SE = 16.0X$), L5 ($A = 7.61$ and $B = -8.94$, $SE = 7.5X$), L7 ($A = 7.08$ and $B = -7.81$, $SE = 4.0X$), L8 ($A = 8.65$ and $B = -8.29$, $SE = 5.4X$).

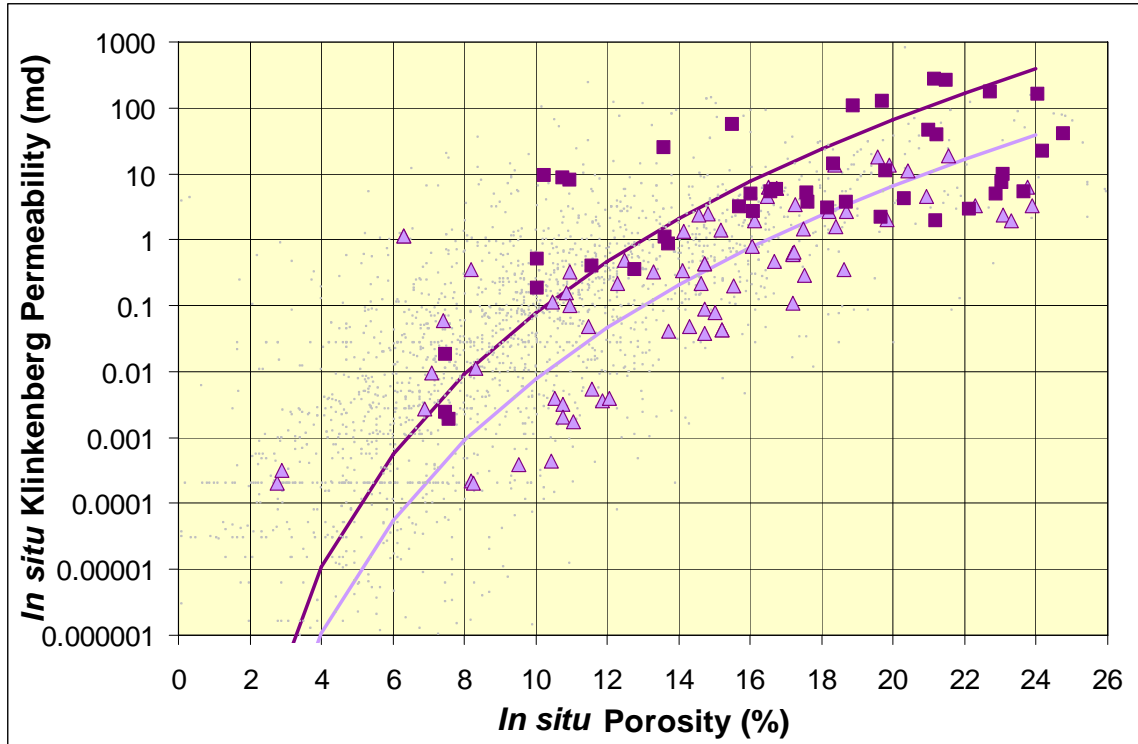


Figure 4.2.52. Crossplot of core plug *in situ* Klinkenberg permeability (k_{ik}) versus *in situ* porosity (ϕ_i) for the dolomite lithofacies including fine-crystalline sucrosic dolomite (L6, light purple triangle), medium-crystalline sucrosic moldic dolomite (L9, purple square), and all Hugoton (gray dot). For curves $k_{ik} = A \phi_i^B$, L6 ($A = 9.70$ and $B = -11.80$, $SE = 5.3X$), L9 ($A = 9.70$ and $B = -10.8$, $SE = 6.7X$).

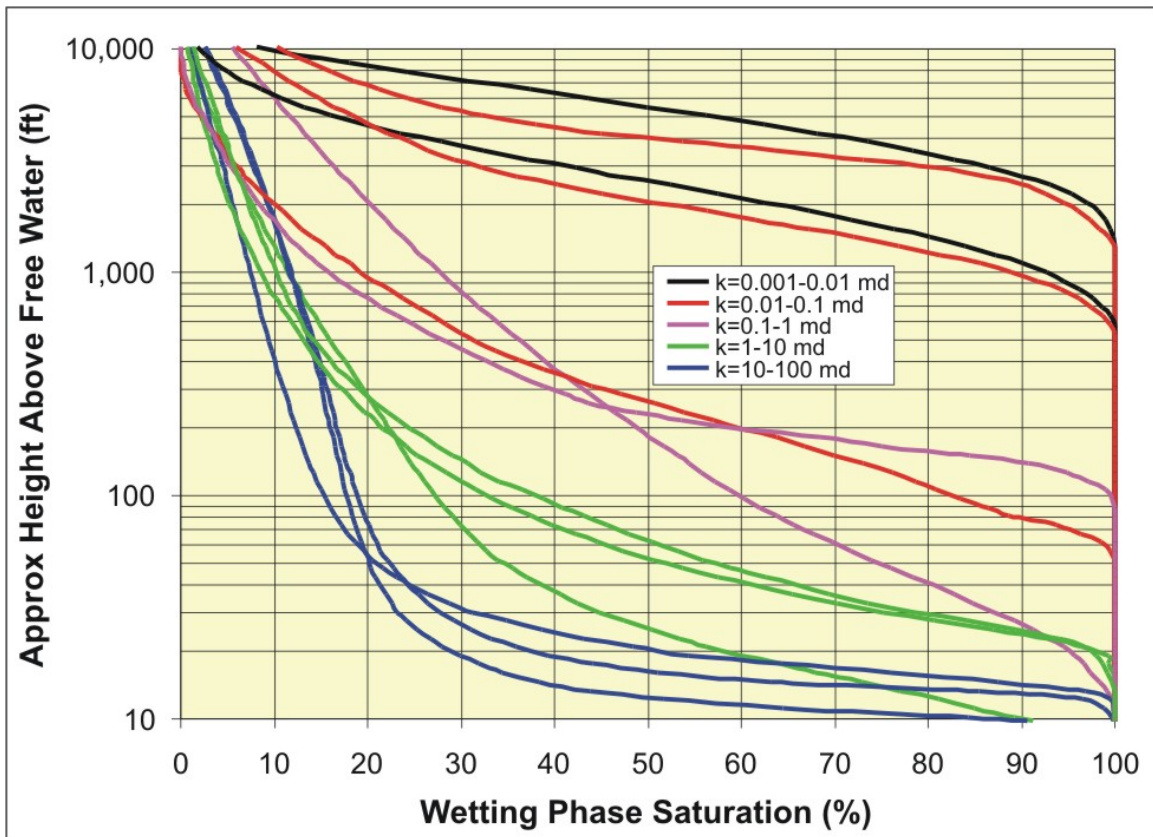


Figure 4.2.53. Selected capillary pressure curves for rocks of different permeability illustrating general curve characteristics. Capillary pressure has been converted to height above free-water level (at which $P_c = 0$) using equations in text. These curves illustrate how threshold entry height and transition zone height increase with decreasing permeability.

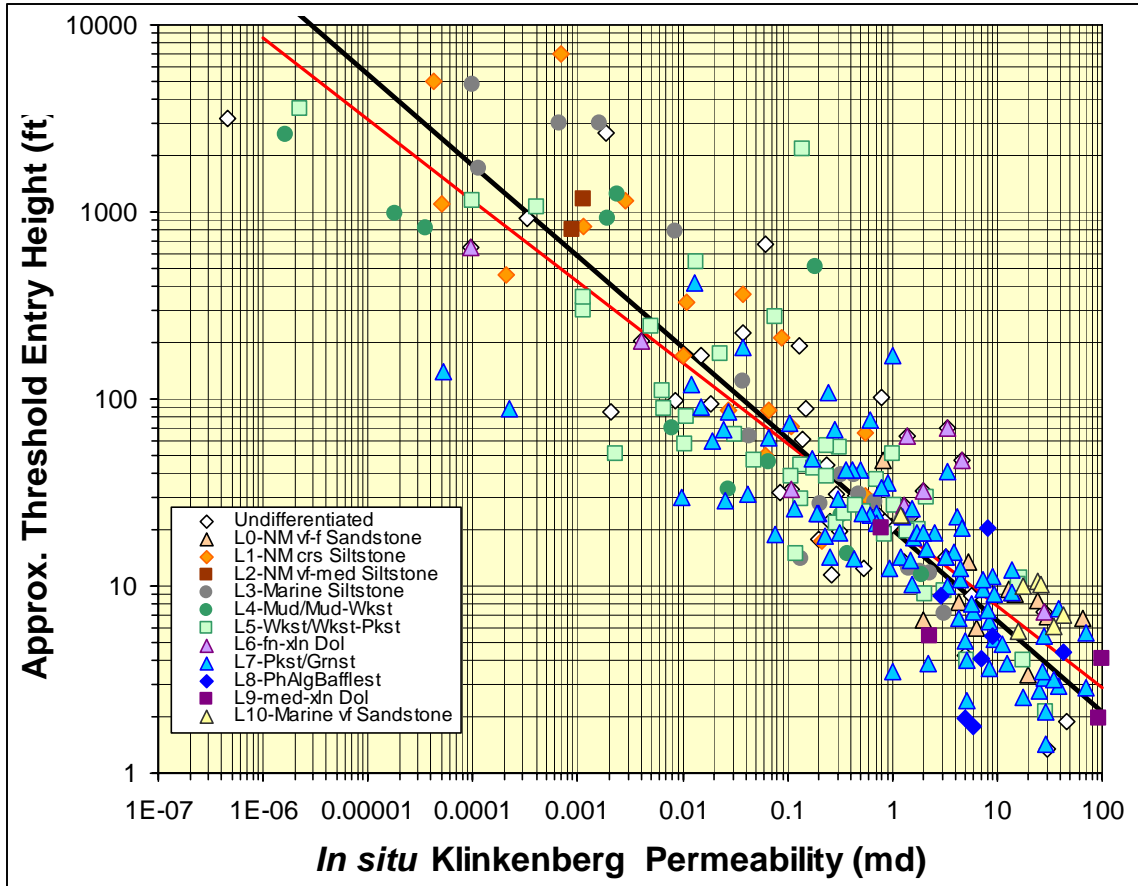


Figure 4.2.54. Crossplot of threshold-entry height (H_{te} , feet) versus *in situ* Klinkenberg permeability for 11 lithofacies in Hugoton. Lines represent relationship $H_{te} = A k_{ik}^B$ where linear regression (LRA, red line) provides $A = 21.22$, $B = -0.433$, reduced major axis (RMA, black line) provides $A = 20.13$, $B = -0.486$. Standard error of prediction for the LRA equation is $SE=2.3X$ and for the RMA equation $SE= 2.4X$. The good correlation results from the control of pore-throat size on both capillary threshold pressure and permeability.

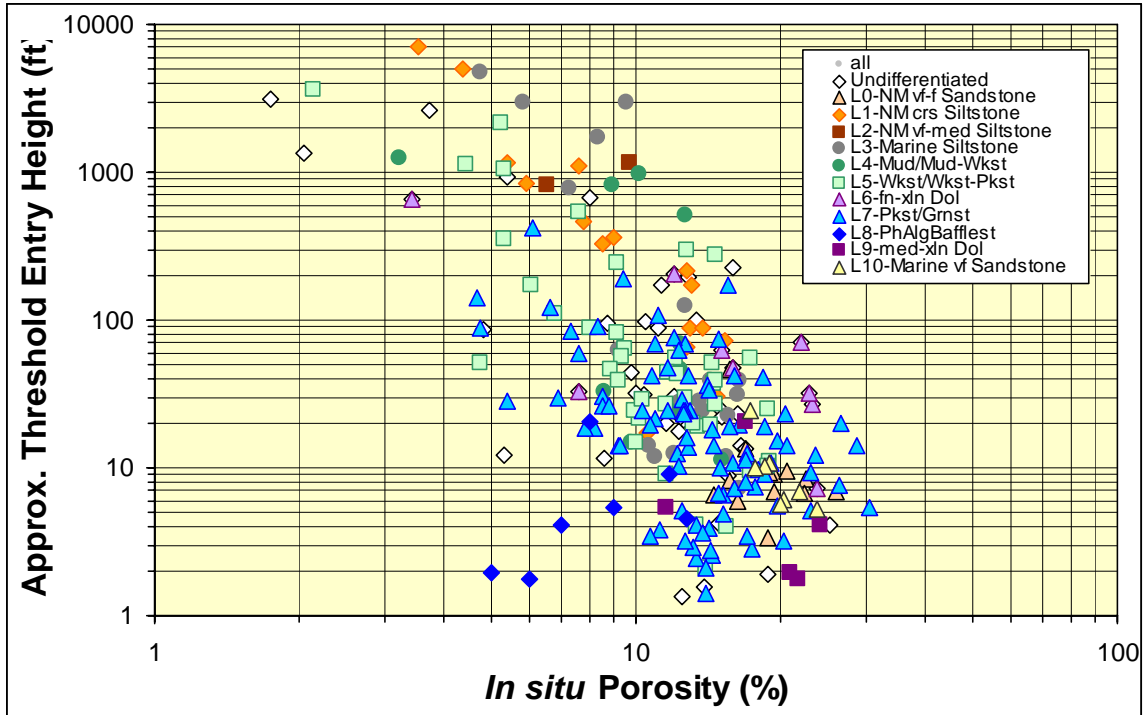


Figure 4.2.55. Crossplot (log-log) of threshold entry height (H_{te} , feet) versus *in situ* Porosity for 11 lithofacies in Hugoton. Variance in correlation corresponds to the variance in permeability-porosity correlation.

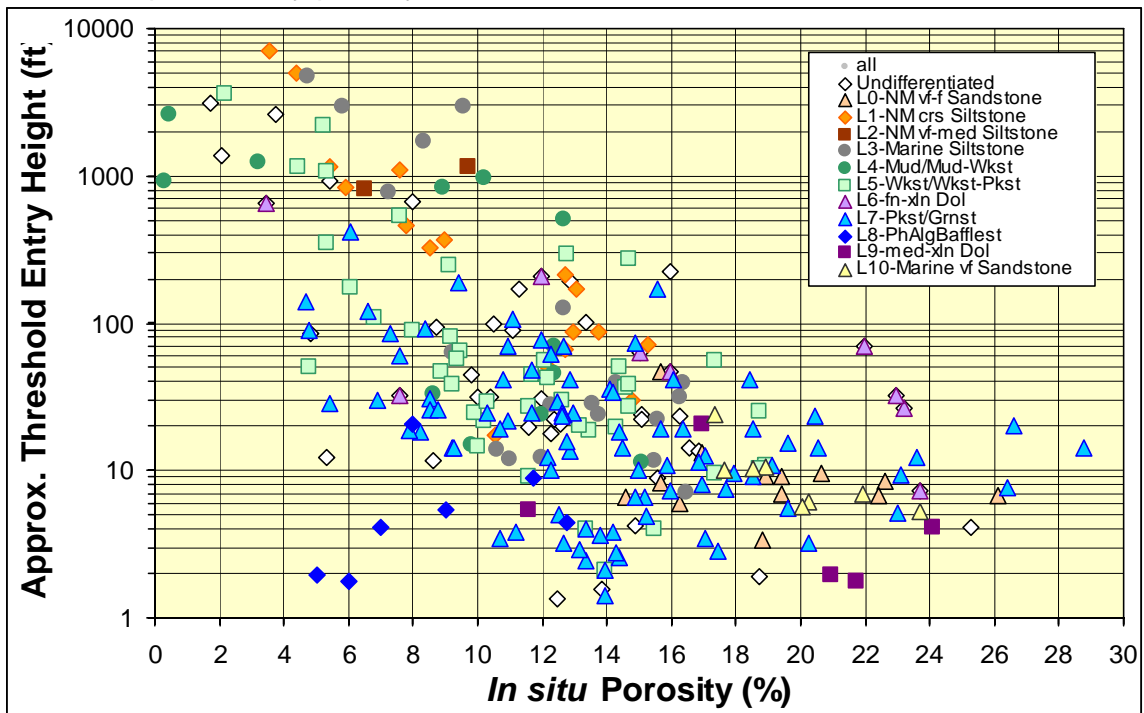


Figure 4.2.56. Crossplot (log-linear) of threshold entry height (H_{te} , feet) versus *in situ* Porosity for 11 lithofacies in Hugoton. Variance in correlation corresponds to the variance in permeability-porosity correlation.

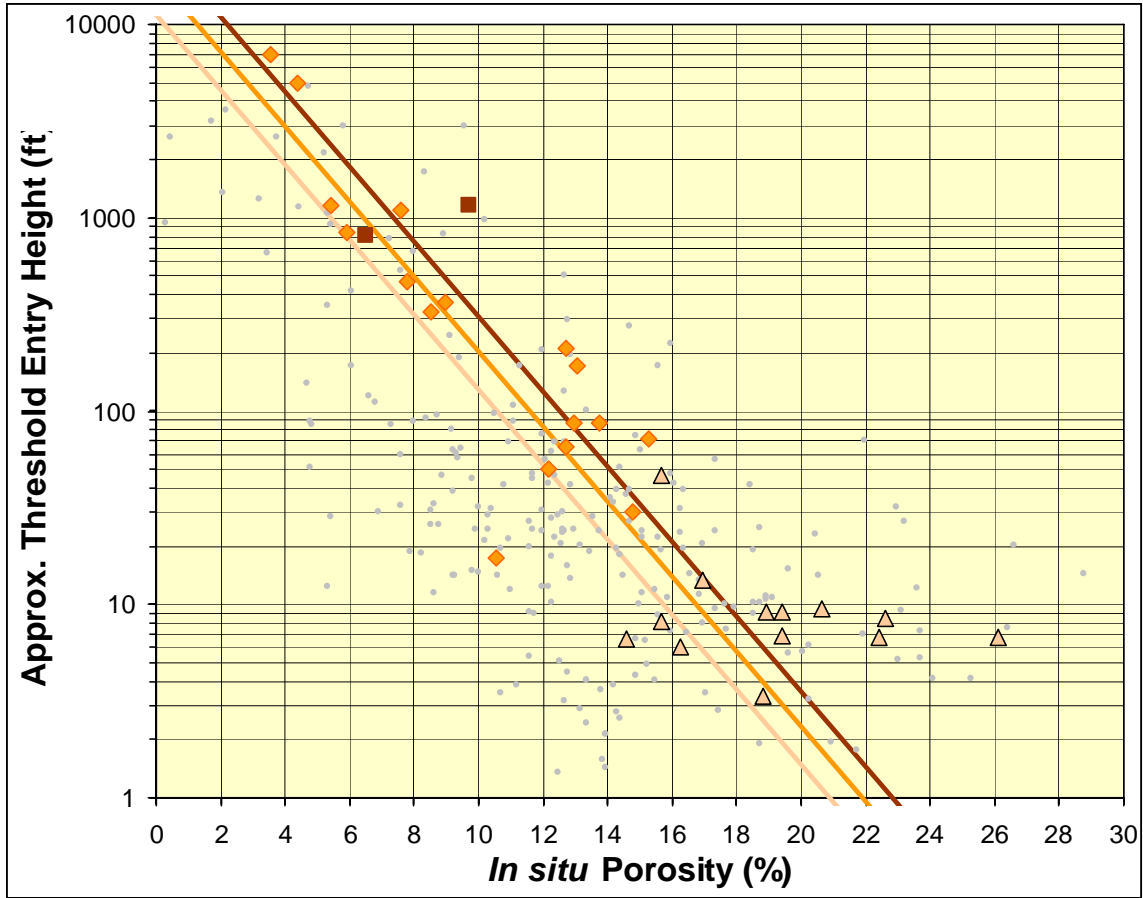


Figure 4.2.57. Crossplot of threshold entry height (H_{te} , feet) versus *in situ* porosity for continental lithofacies including very fine to fine-grained sandstone (L0, tan triangle), coarse-grained siltstones (L1, orange diamonds), shaly fine- to medium-grained siltstones (L2, brown square) and all Hugoton (gray dot). For curves $\log_{10} H_{te} = A \phi_i + B$, L0 ($A = -0.19$ and $B = 4.05$), L1 ($A = -0.19$ and $B = 4.25$), L2 ($A = -0.19$ and $B = 4.43$).

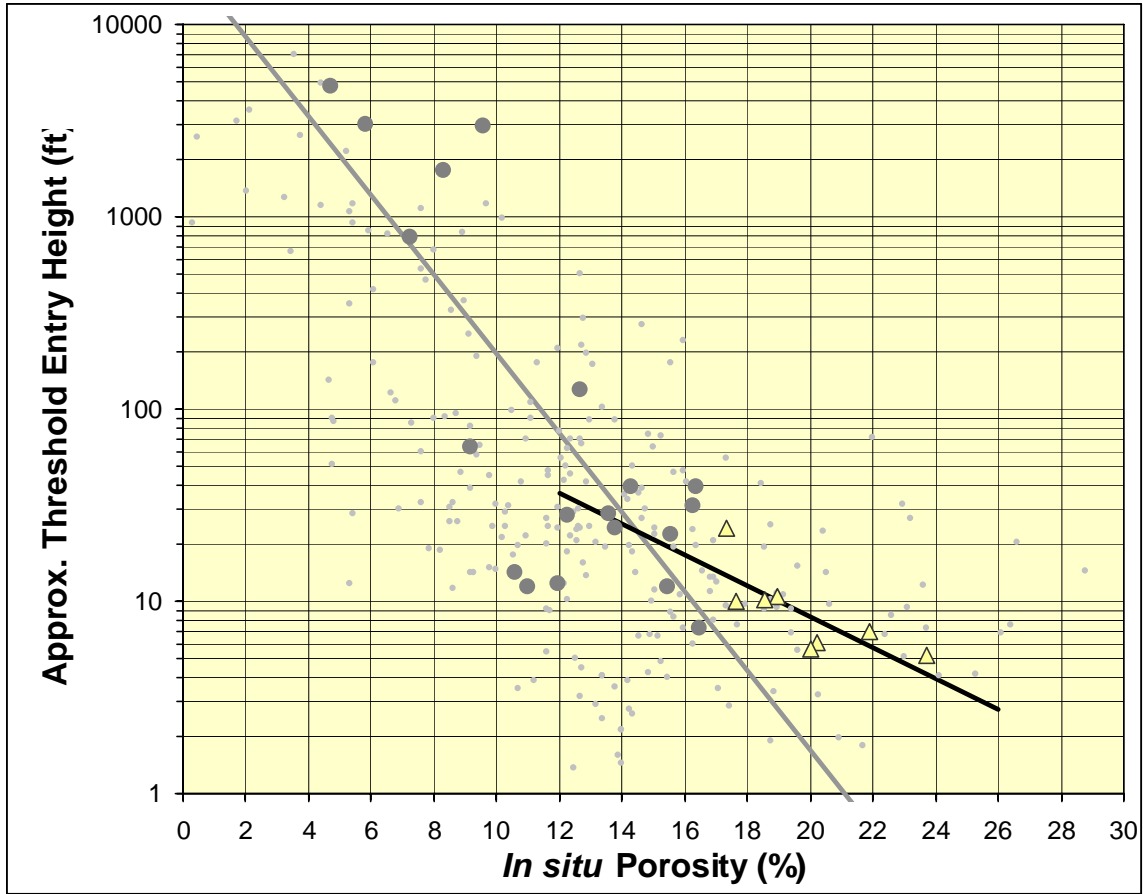


Figure 4.2.58. Crossplot of threshold entry height (H_{te} , feet) versus *in situ* Porosity for the marine clastic lithofacies including shale/siltstone (L3, gray circle), very fine-fine grained sandstone (L10, light yellow triangle), and all Hugoton (gray dot). For curves $\log_{10}H_{te} = A \phi_i + B$, L3 ($A = -0.21$ and $B = 4.35$), L10 ($A = -0.08$ and $B = 2.52$).

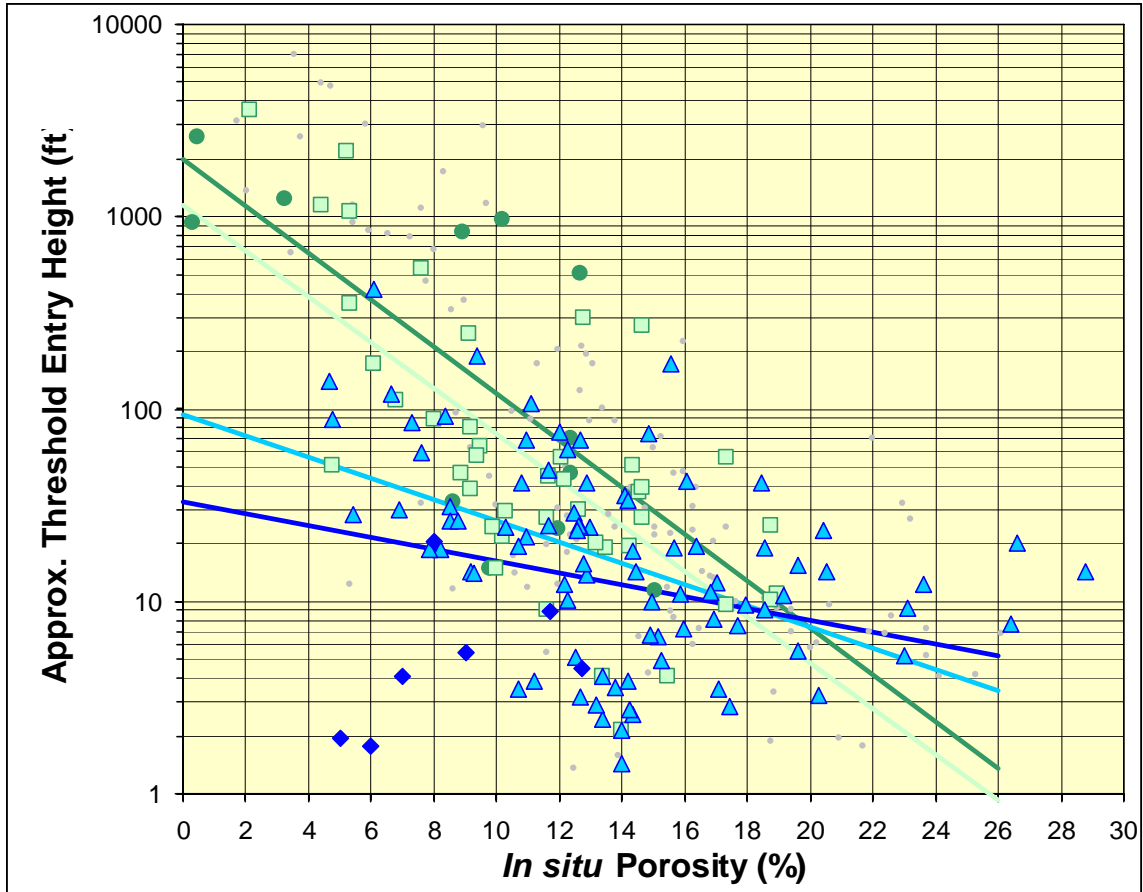


Figure 4.2.59. Crossplot of threshold entry height (H_{te} , feet) versus *in situ* porosity for the limestone lithofacies including mudstone/mud-wackestone (L4, green circle), wackestone/wacke-packstone (L5, light green square), packstone/grainstone (L7, light blue triangle), phylloid algal bafflestone (L8, blue diamond) and all Hugoton (gray dot). For curves $\log_{10}H_{te} = A \phi_i + B$, L4 ($A = -0.12$ and $B = 3.30$), L5 ($A = -0.12$ and $B = 3.06$), L7 ($A = -0.06$ and $B = 1.97$), L8 ($A = -0.03$ and $B = 1.52$).

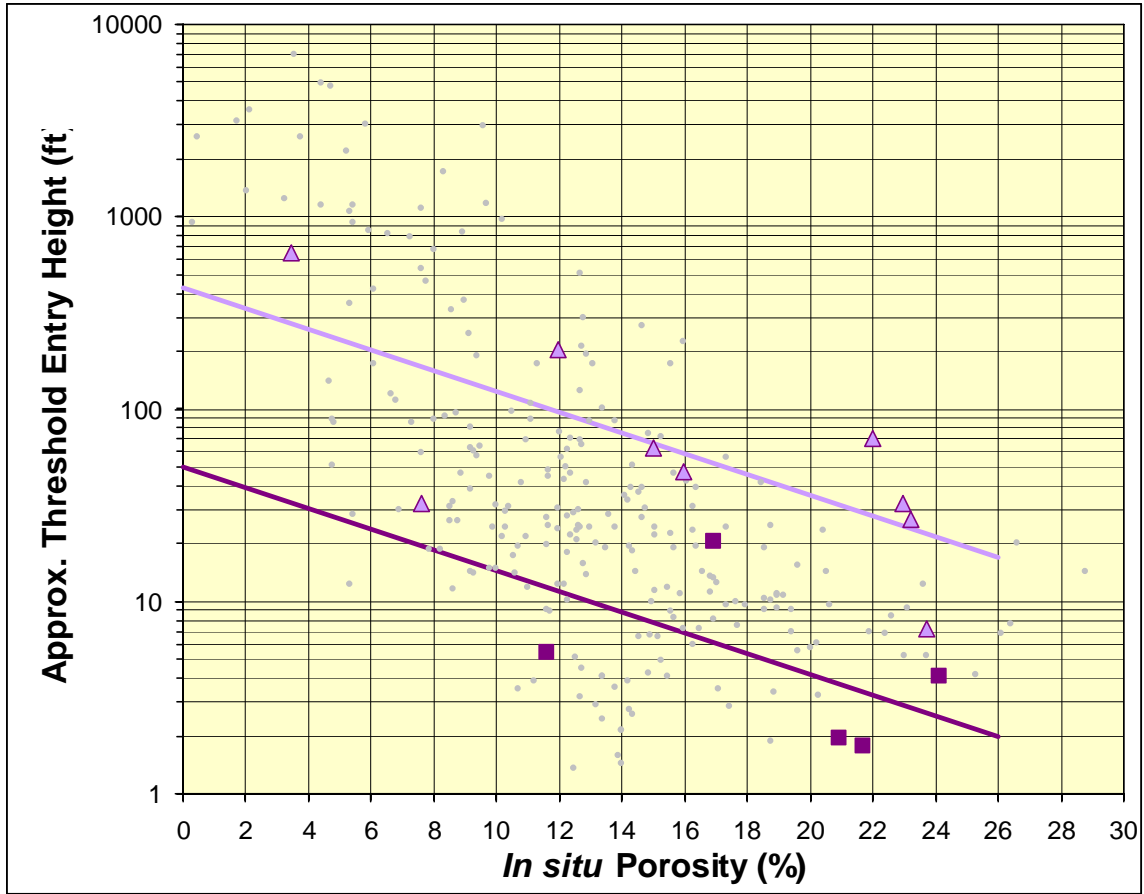


Figure 4.2.60. Crossplot of threshold entry height (H_{te} , feet) versus *in situ* porosity for the dolomite lithofacies including fine-crystalline sucrosic dolomite (L6, light purple triangle), medium-crystalline sucrosic moldic dolomite (L9, purple square), and all Hugoton (gray dot). For curves $\log_{10}H_{te} = A \phi_i + B$, L6 ($A = -0.05$ and $B = 2.63$), L10 ($A = -0.05$ and $B = 1.70$).

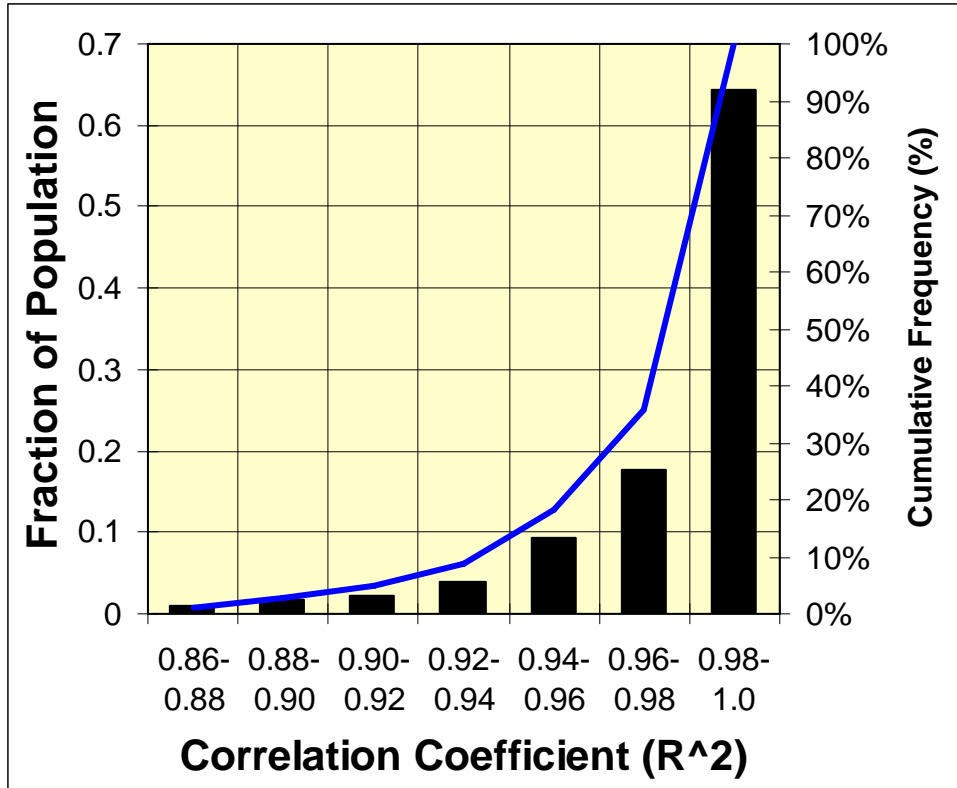


Figure 4.2.61. Histogram of correlation coefficients of dimensionless height fractal slope equations with capillary pressure data for the 252 air-mercury capillary pressure samples. A significant fraction of all samples exhibit fractal slopes.

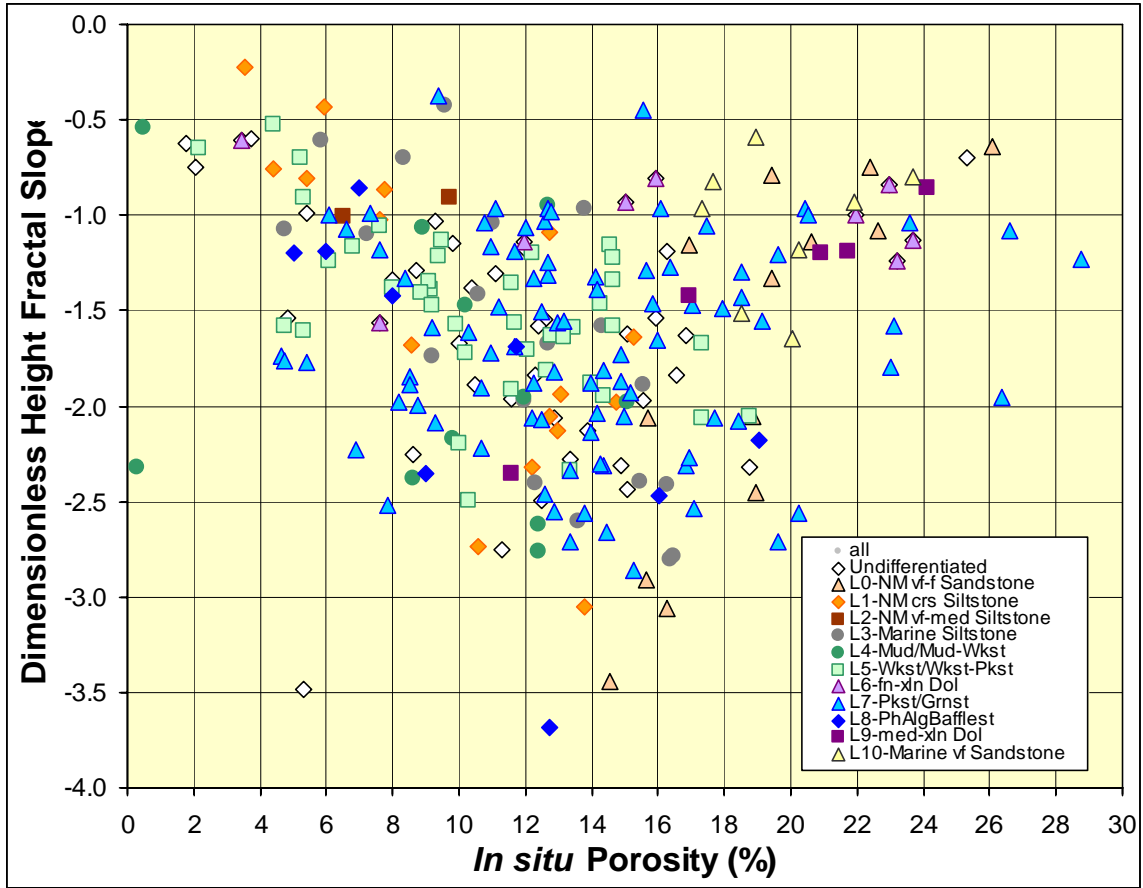


Figure 4.2.62. Crossplot of dimensionless height fractal slope (H_f) versus *in situ* Porosity for 11 lithofacies in Hugoton. Dimensionless slope represents slope of $\log_{10} S_w - \log_{10} H_{afw}$ relationship over saturation range of relevance to reservoir modeling prediction (e.g., $S_w=10-100\%$). H_f value of zero indicates complete desaturation at threshold entry height, H_{te} . More negative values of H_f imply greater pore-throat size heterogeneity and large range of height change to change saturation.

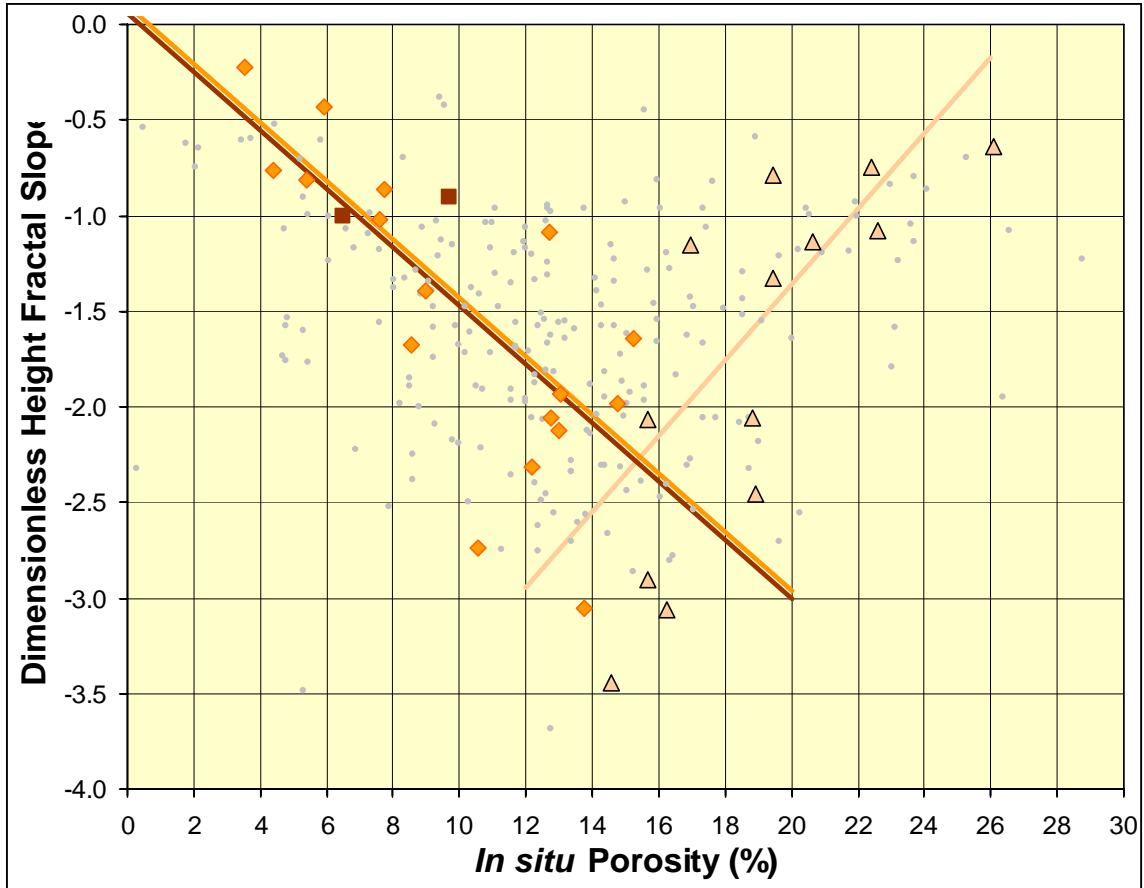


Figure 4.2.63. Crossplot of dimensionless height fractal slope (H_f) versus *in situ* porosity for continental lithofacies including very fine to fine-grained sandstone (L0, tan triangle), coarse-grained siltstones (L1, orange diamonds), shaly fine- to medium-grained siltstones (L2, brown square) and all Hugoton (gray dot). For curves $H_f = A \phi_i + B$, L0 ($A = 0.20$ and $B = -5.32$), L1 ($A = -0.15$ and $B = 0.10$), L2 ($A = -0.15$ and $B = 0.10$)

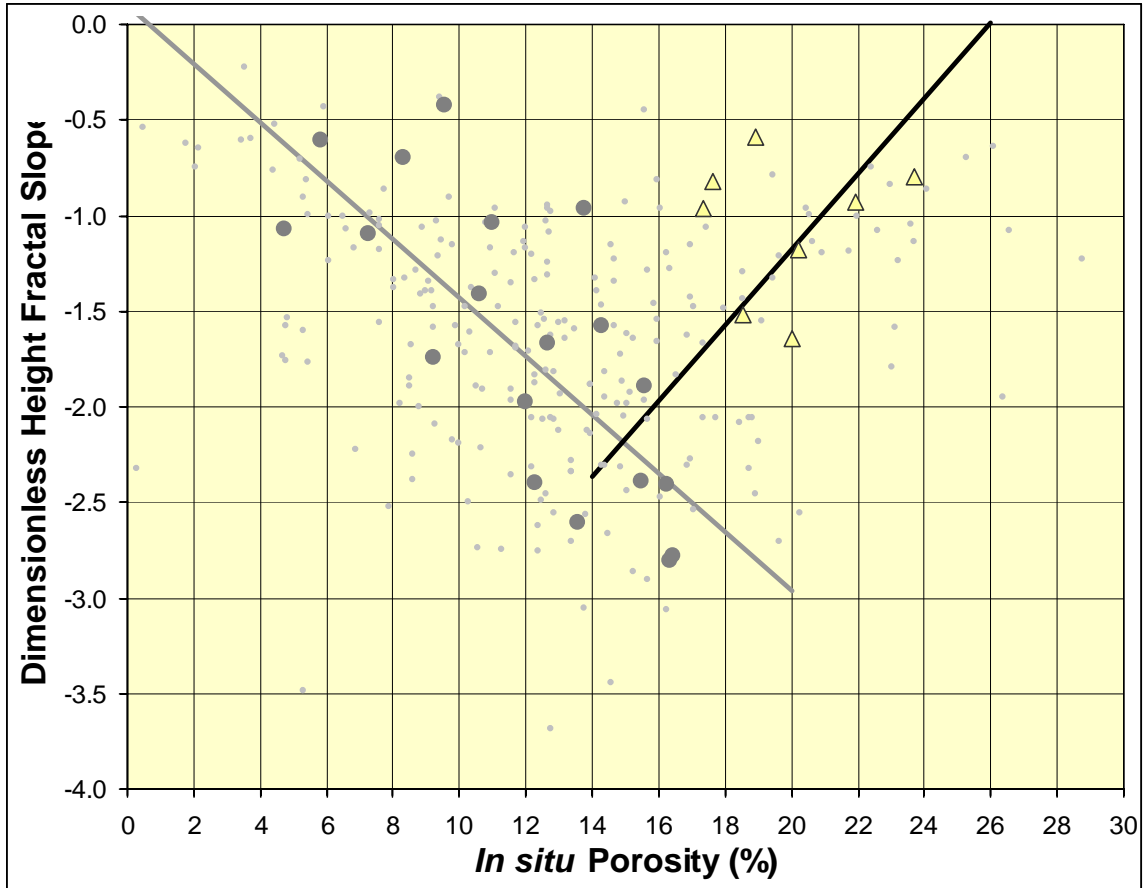


Figure 4.2.64. Crossplot of dimensionless height fractal slope (H_f) versus *in situ* porosity for the marine clastic lithofacies including shale/siltstone (L3, gray circle), very fine-grained sandstone (L10, light yellow triangle), and all Hugoton (gray dot). For curves $H_f = A \phi_i + B$, L3 ($A = -0.15$ and $B = 0.10$), L10 ($A = 0.20$ and $B = -5.14$).

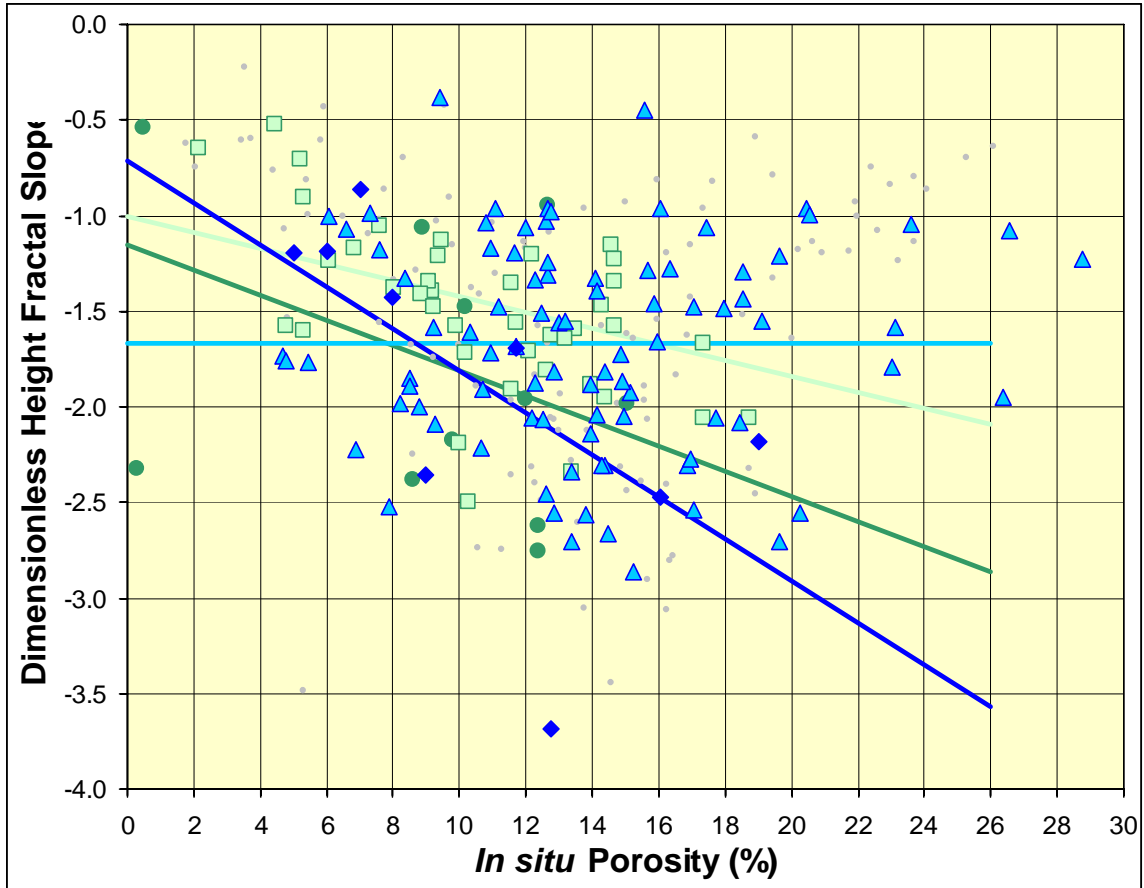


Figure 4.2.65. Crossplot of dimensionless height fractal slope (H_f) versus *in situ* porosity for the limestone lithofacies including mudstone/mud-wackestone (L4, green circle), wackestone/wacke-packstone (L5, light green square), packstone/grainstone (L7, light blue triangle), phylloid algal bafflestone (L8, blue diamond) and all Hugoton (gray dot). For curves $H_f = A \phi_i + B$, L4 ($A = -0.07$ and $B = -1.15$), L5 ($A = -0.04$ and $B = -1.00$), L7 ($A = 0.00$ and $B = -1.67$), L8 ($A = -0.11$ and $B = -0.71$).

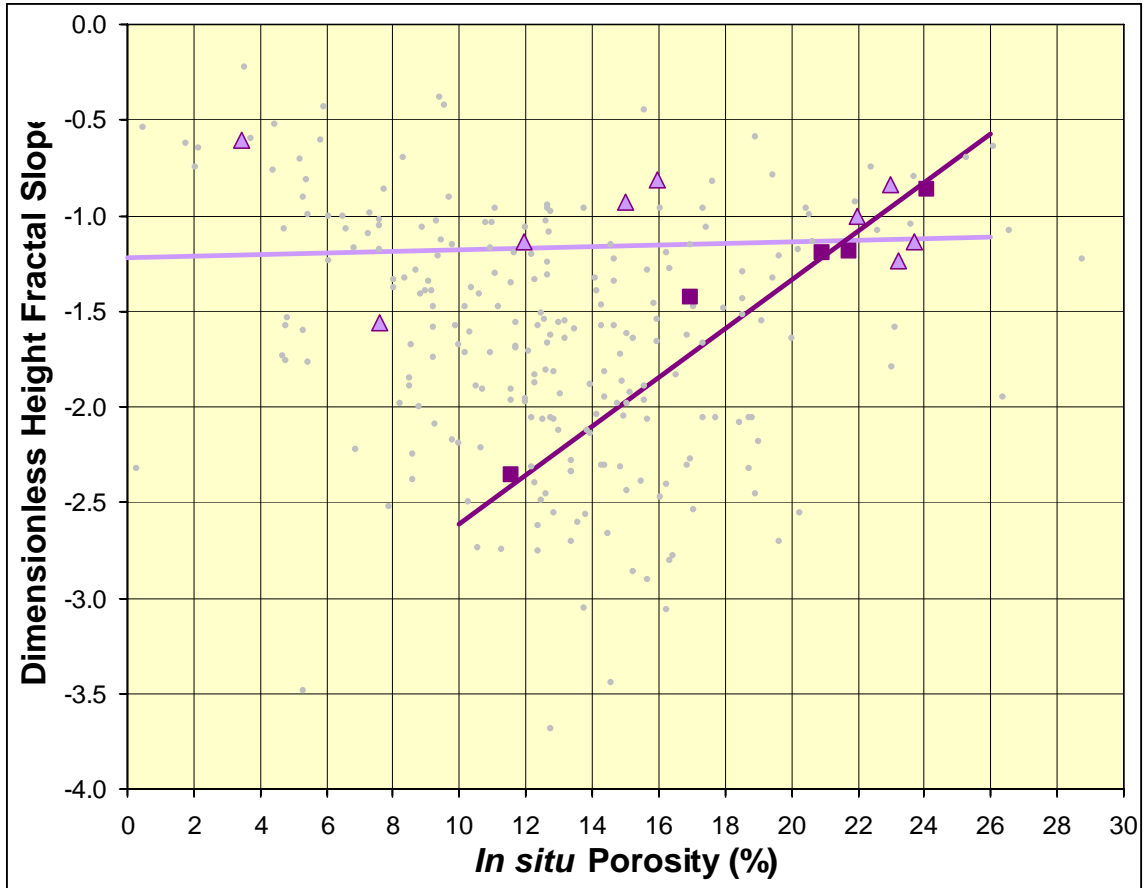


Figure 4.2.66. Crossplot of dimensionless Height fractal slope (H_f) versus *in situ* Porosity for the dolomite lithofacies including fine-crystalline sucrosic dolomite (L6, light purple triangle), medium-crystalline sucrosic moldic dolomite (L9, purple square), and all Hugoton (gray dot). For curves $H_f = A \phi_i + B$, L6 ($A = 0.00$ and $B = -1.22$), L9 ($A = 0.13$ and $B = -3.90$).

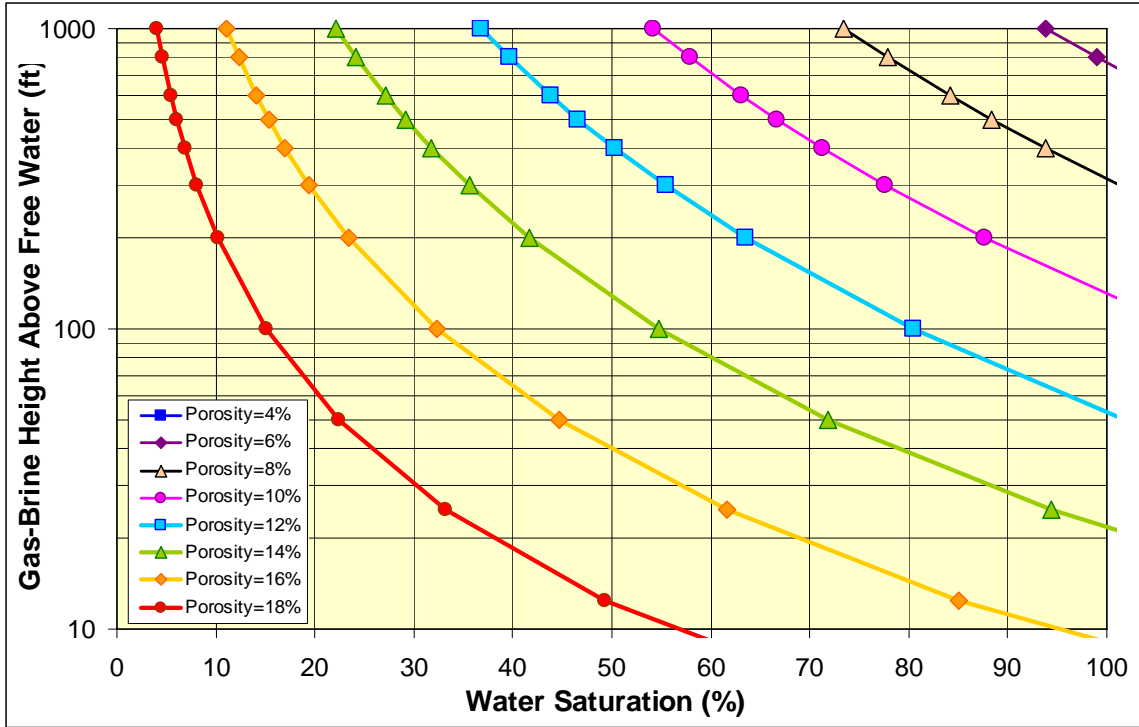


Figure 4.2.67. Model height above free-water level curves for continental very fine to fine-grained sandstones (L0) constructed using equations 4.2.15-4.2.19 in text.

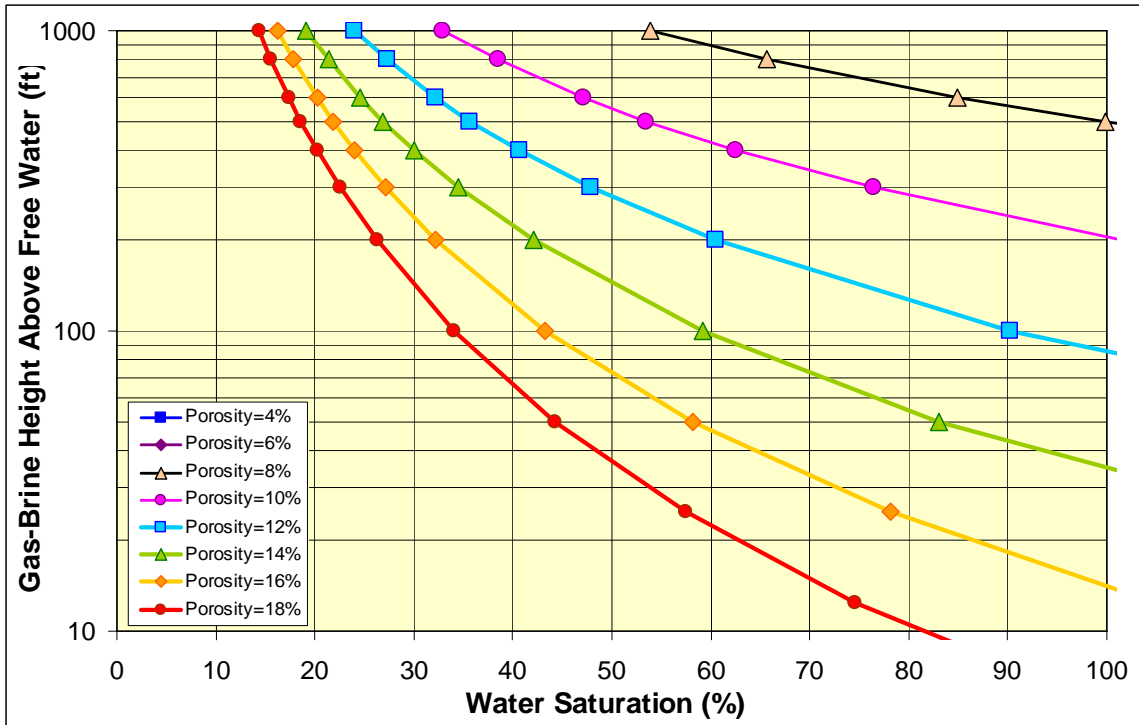


Figure 4.2.68. Model height above free-water level curves for continental coarse-grained siltstones (L1) constructed using equations 4.2.15-4.2.19 in text.

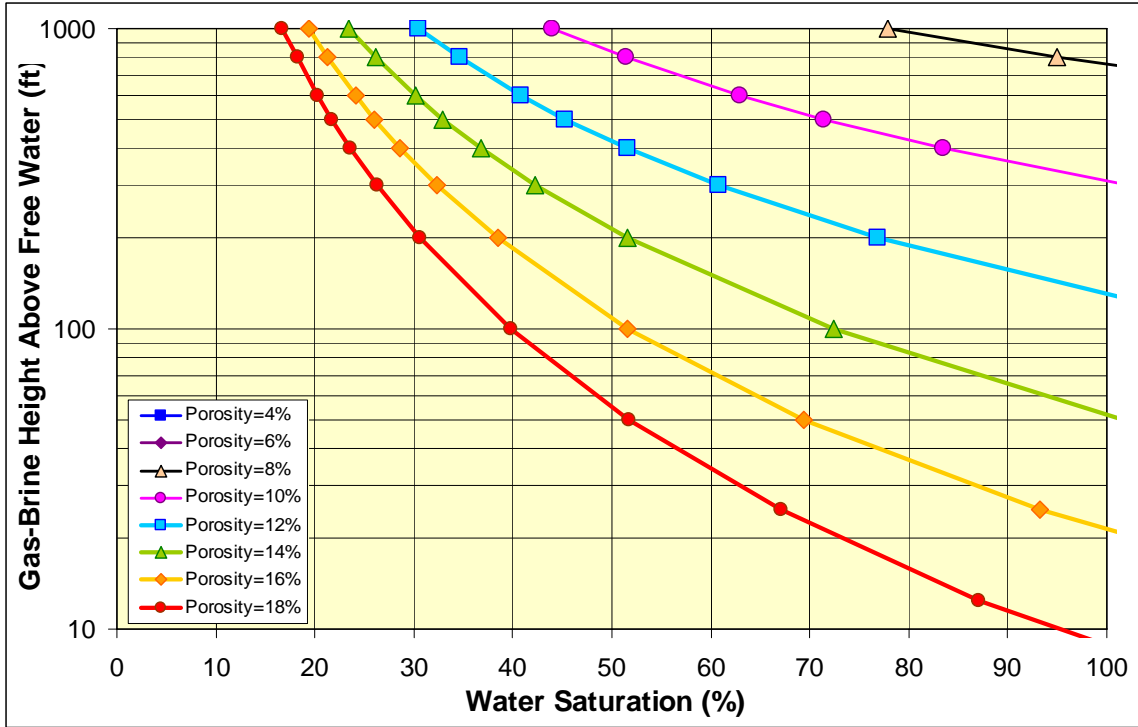


Figure 4.2.69. Model height above free-water level curves for continental fine to medium-grained siltstones (L2) constructed using equations 4.2.15-4.2.19 in text.

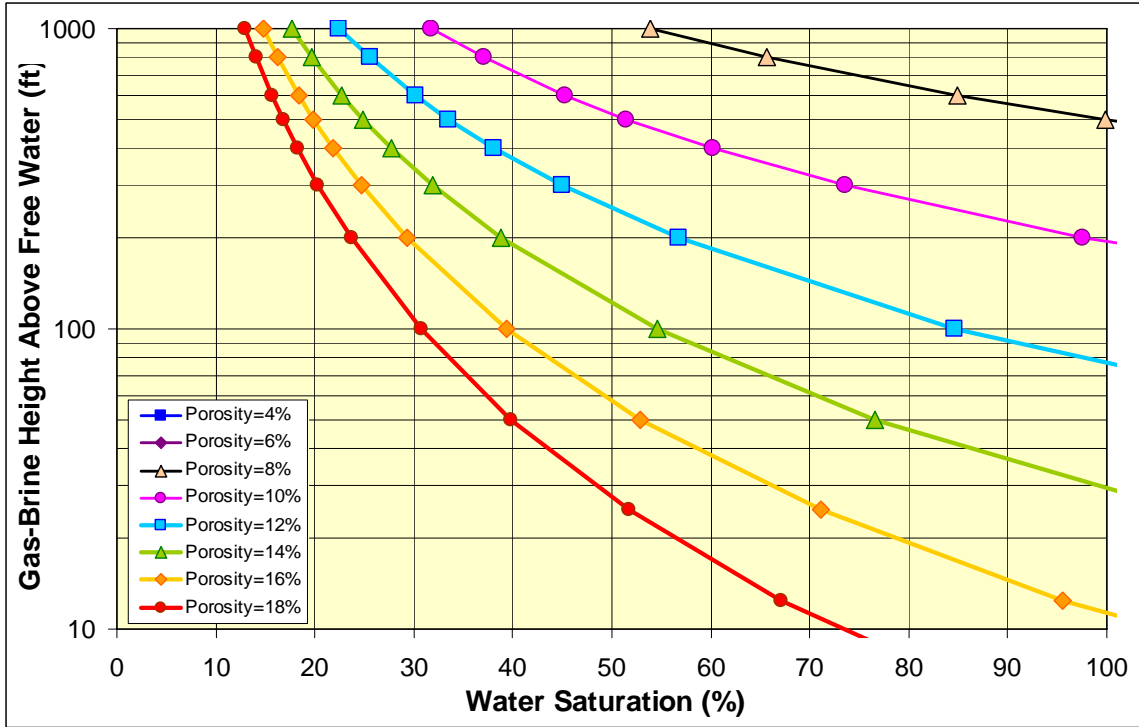


Figure 4.2.70. Model height above free-water level curves for marine shales and siltstones (L3) constructed using equations 4.2.15-4.2.19 in text.

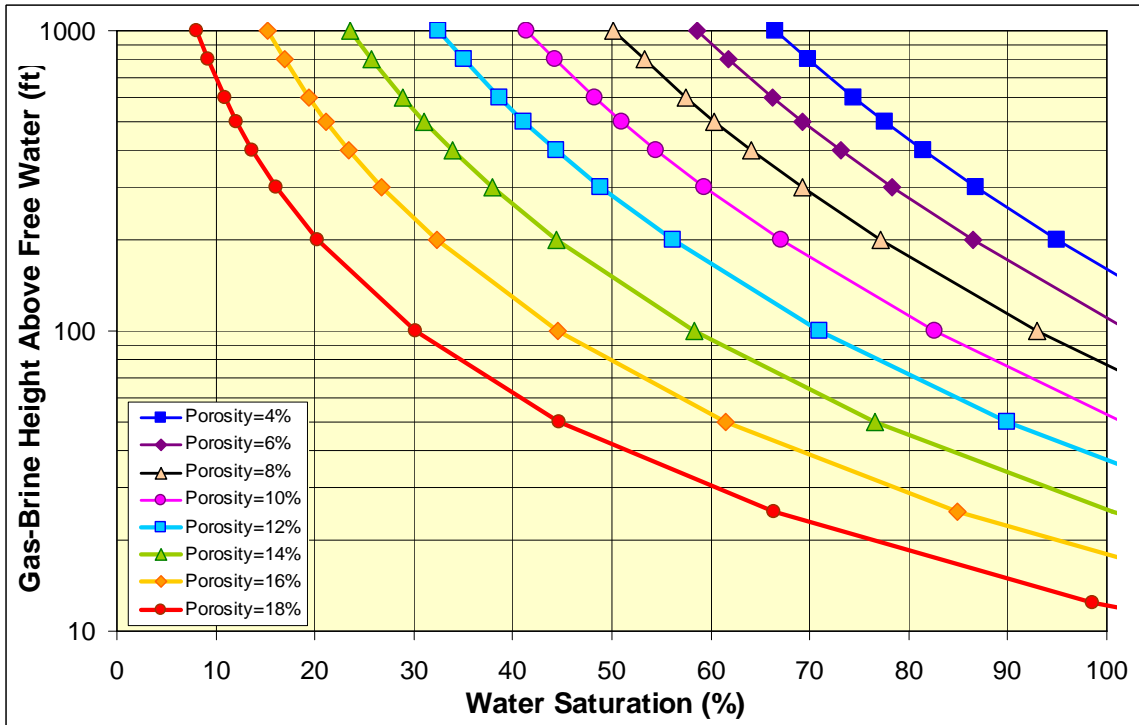


Figure 4.2.71. Model height above free-water level curves for marine very fine to fine-grained sandstones (L10) constructed using equations 4.2.15-4.2.19 in text.

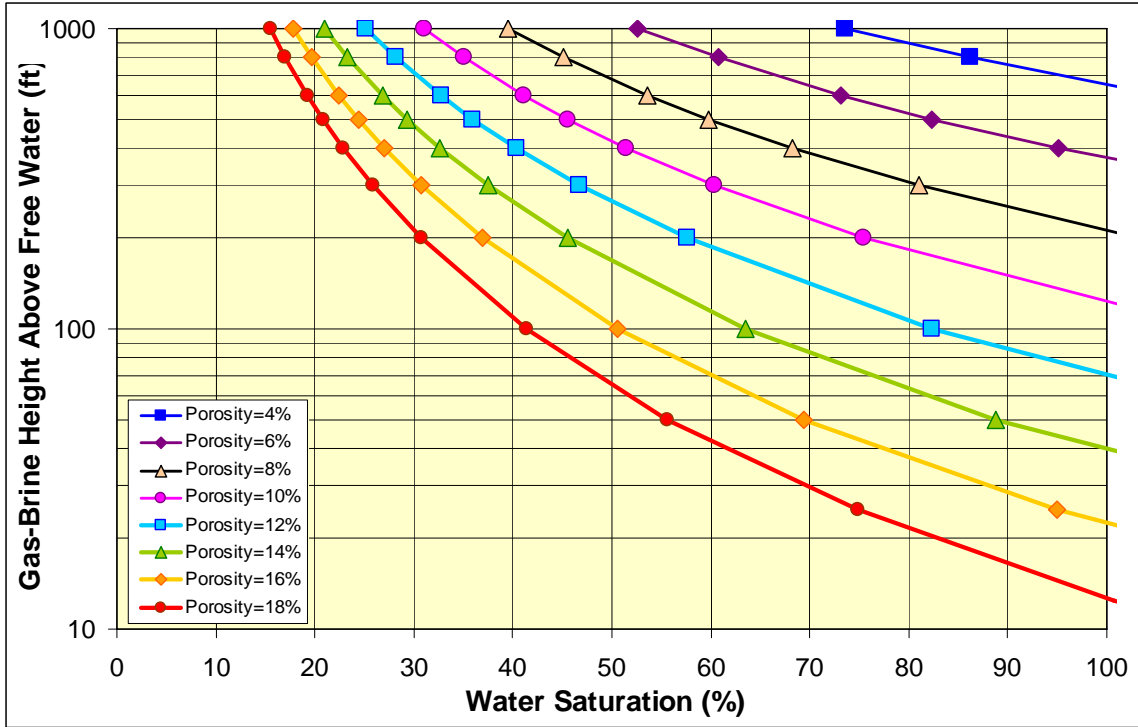


Figure 4.2.72. Model height above free-water level curves for mudstone/mud-wackestone (L4) constructed using equations 4.2.15-4.2.19 in text.

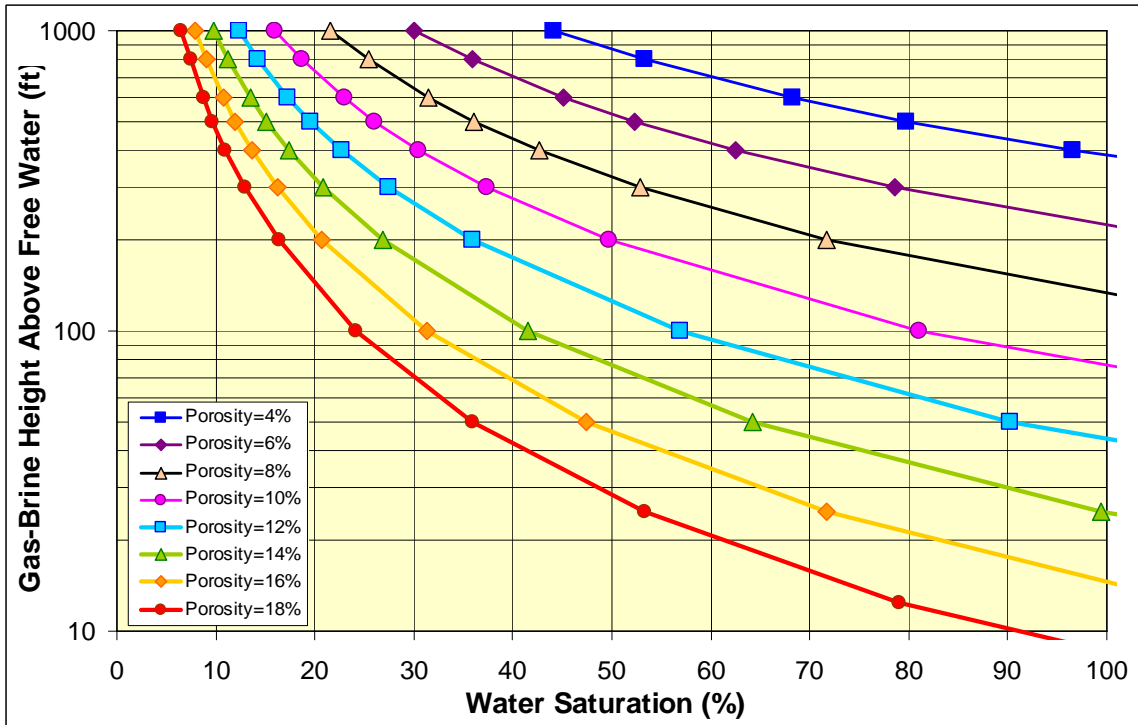


Figure 4.2.73. Model height above free-water level curves for wackestone/wackepackstone (L5) constructed using equations 4.2.15-4.2.19 in text.

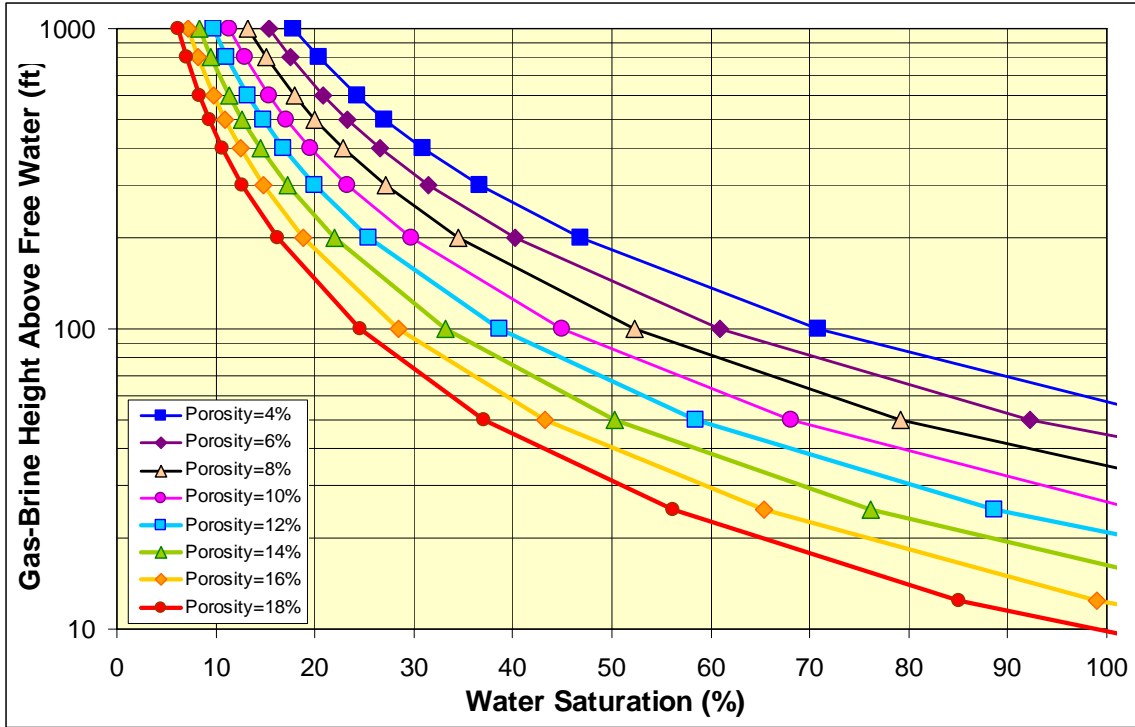


Figure 4.2.74. Model height above free-water level curves for packstone/grainstone (L7) constructed using equations 4.2.15-4.2.19 in text.

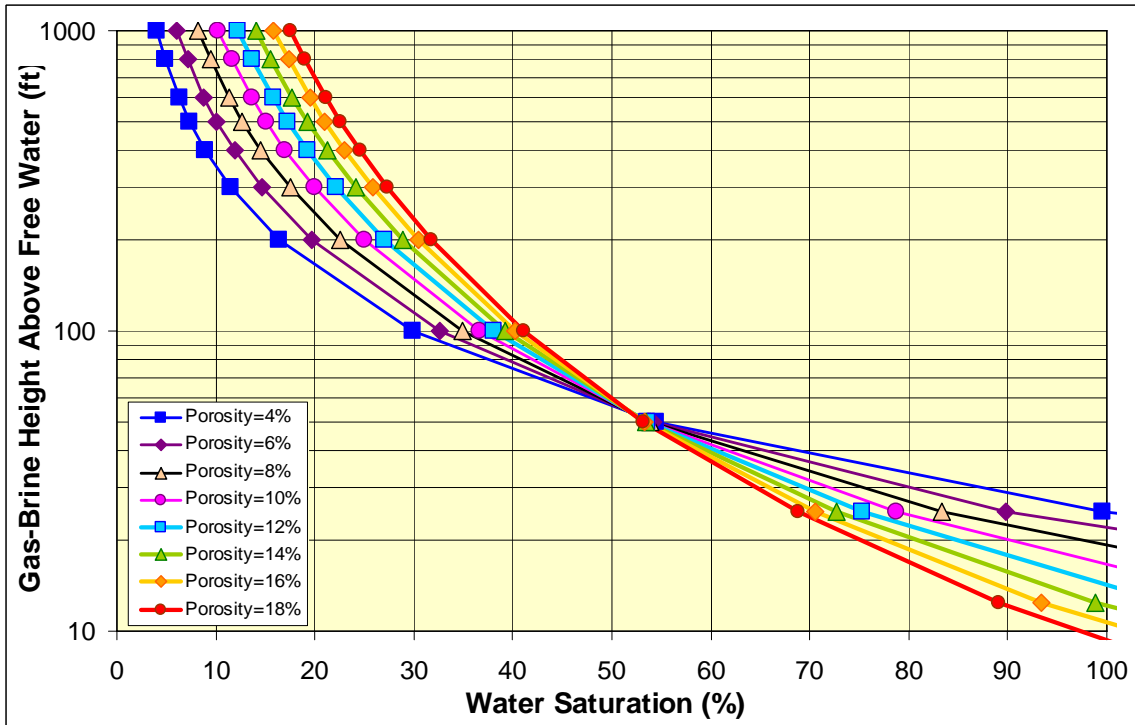


Figure 4.2.75. Model height above free-water level curves for phylloid algal bafflestone (L8) constructed using equations 4.2.15-4.2.19 in text.

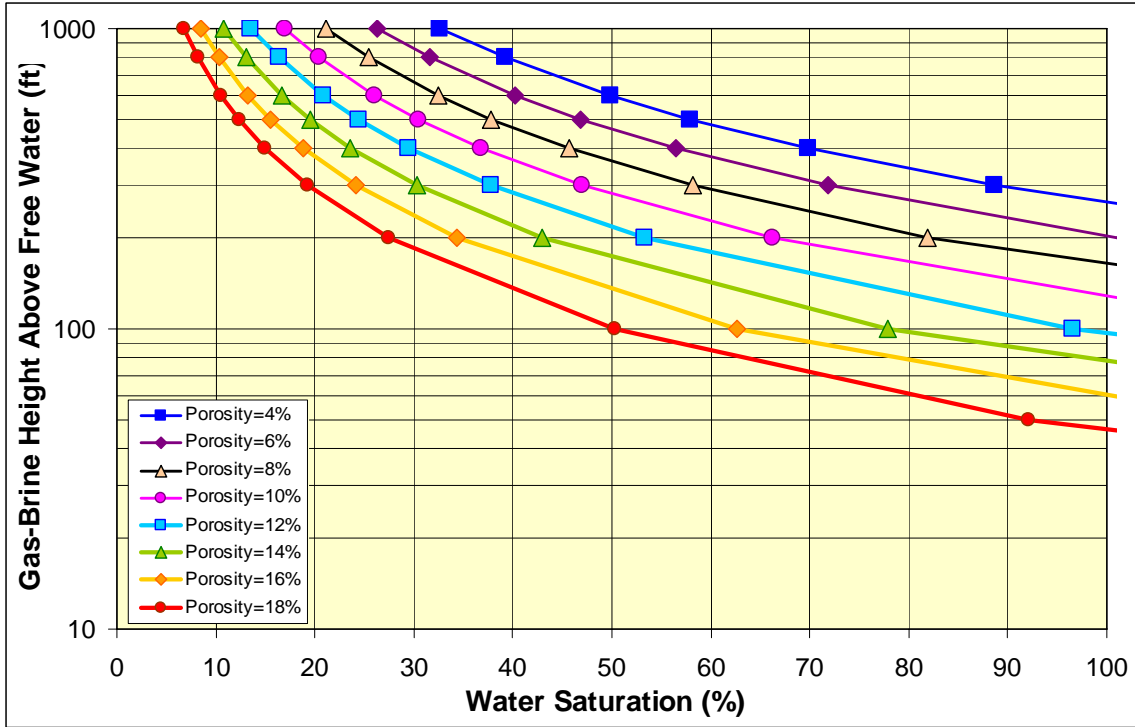


Figure 4.2.76. Model height above free-water level curves for very fine- to fine-crystalline sucrosic dolomite (L6) constructed using equations 4.2.15-4.2.19 in text.

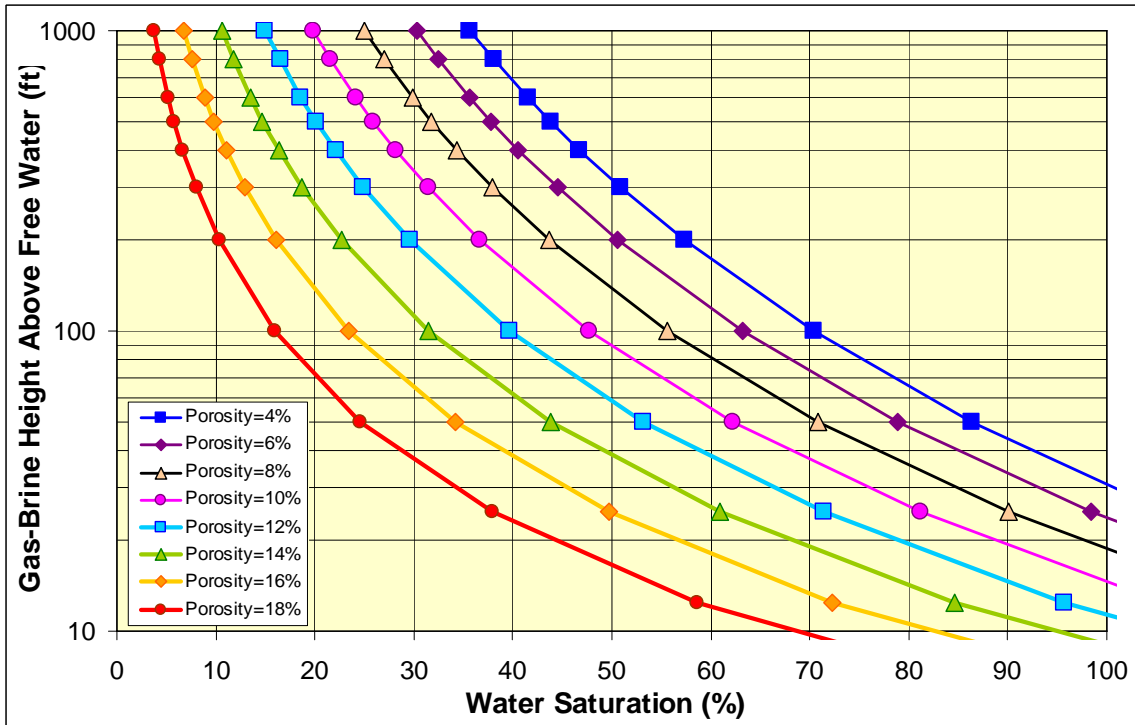


Figure 4.2.77. Model height above free-water level curves for medium-crystalline sucrosic moldic dolomite (L9) constructed using equations 4.2.15-4.2.19 in text.

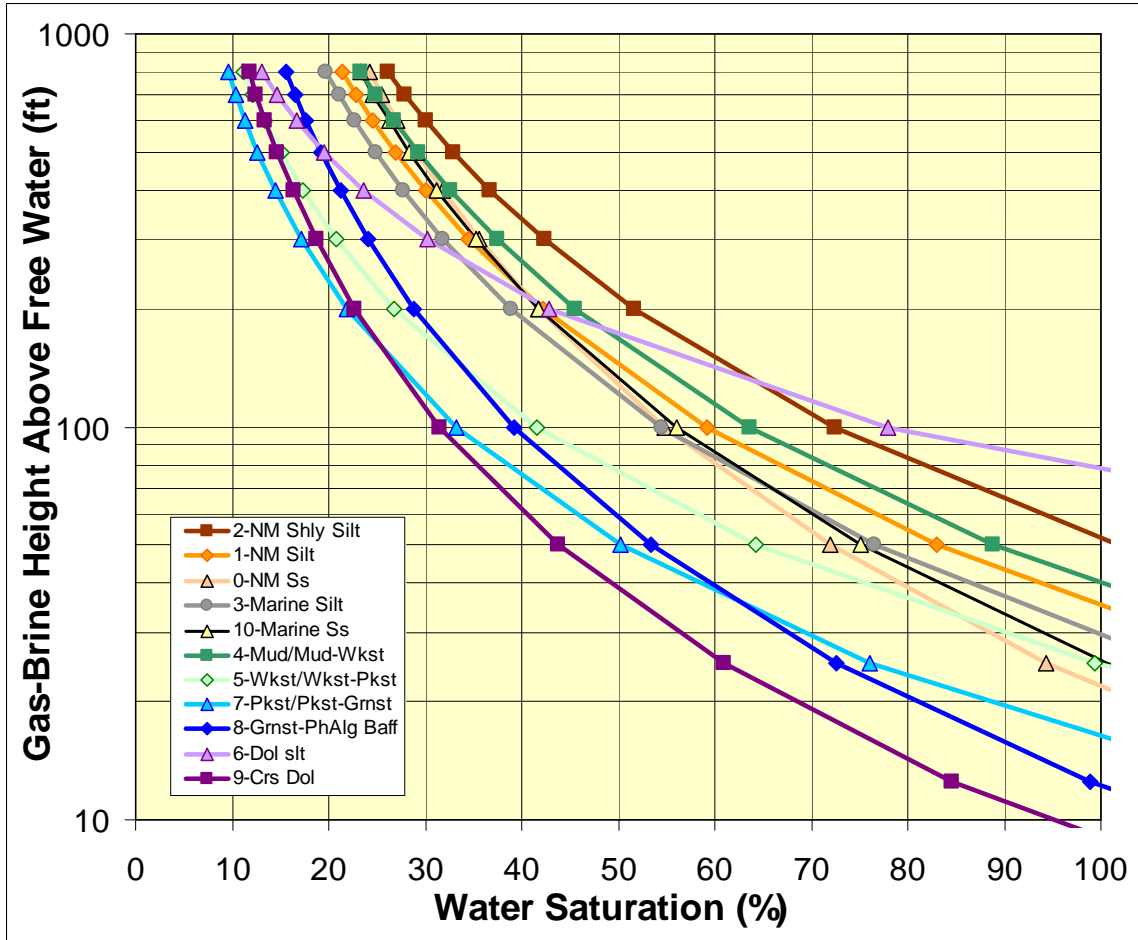


Figure 4.2.78. Model height above free-water level curves for all 11 lithofacies for a $f_i = 10\%$ rock. Water saturation can vary by up to 60% for the same porosity rock depending on the lithofacies. Curves were constructed using equations 4.2.15-4.2.19 in text. Differences in water saturation are greatest at lower heights and decrease with increasing height above free-water level.

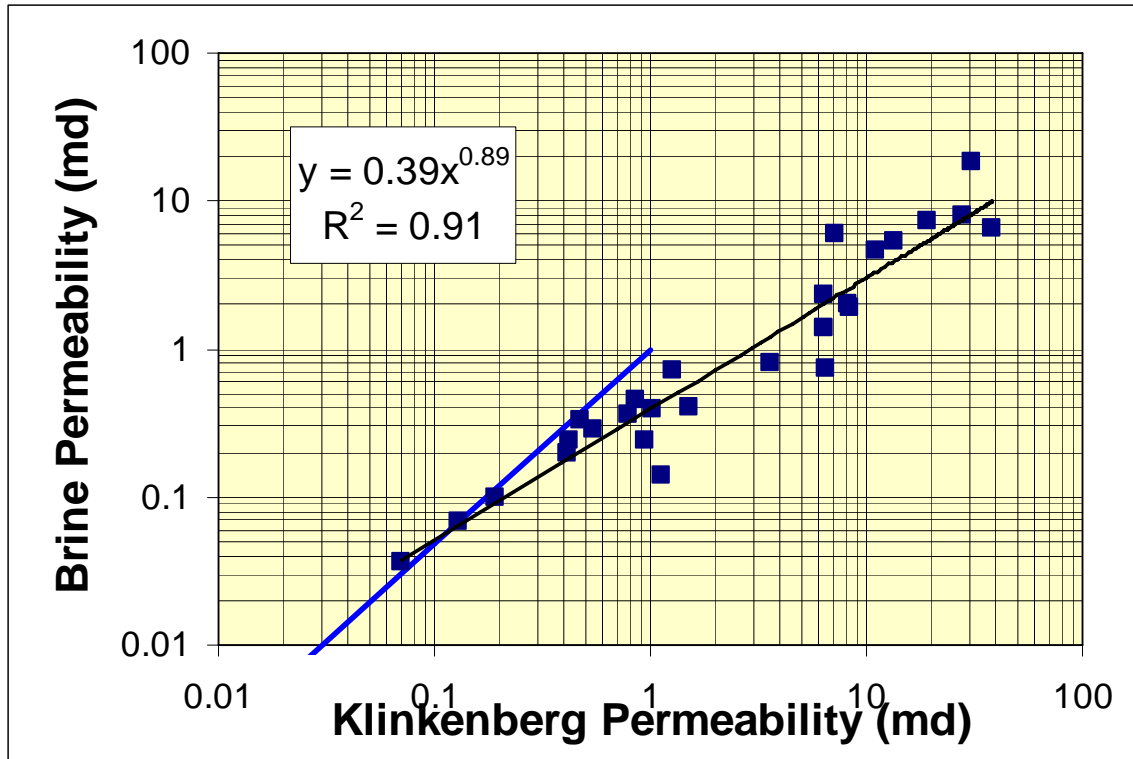


Figure 4.2.79. Crossplot of *in situ* permeability to brine versus *in situ* Klinkenberg gas permeability showing that water permeability is less than gas permeability can be characterized as: $k_{iw} = 0.39 k_{ik}^{0.89}$. The trend defined by Jones and Owens (1980) for tight gas sandstones: $k_{iw} = k_{ik}^{1.32}$ (for $k_{ik} < 1$ md) is also shown (blue line).

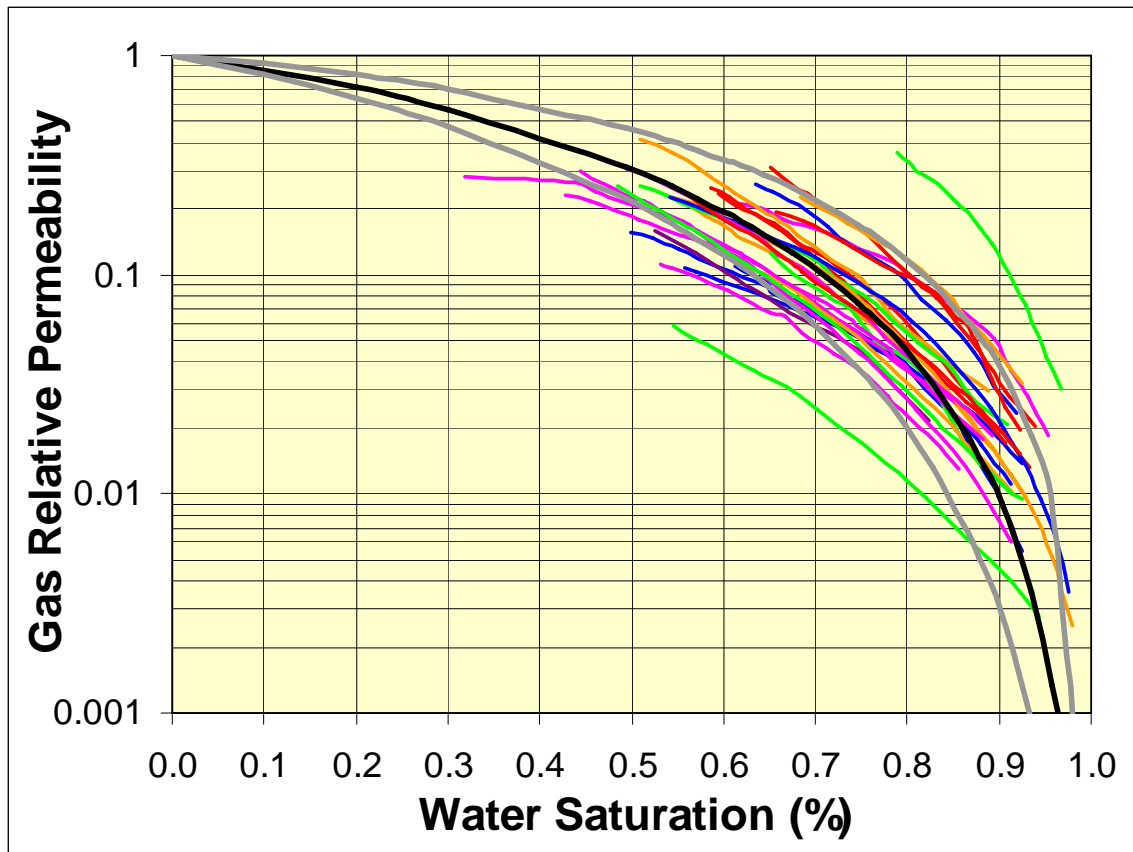


Figure 4.2.80. Relative gas permeability curves for 32 samples of various lithofacies. Black curves represent predicted values for the Corey-type equation model:

$$k_{rg} = (1 - (S_w - S_{wc,g}) / (1 - S_{gc} - S_{wc,g}))^p (1 - ((S_w - S_{wc,g}) / (1 - S_{wc,g}))^2)$$

where S_{wc} is the critical water saturation, $S_{wc,g}$ is the critical water saturation for gas flow, and all saturation terms are in fractions. Black curves represent mean values of exponents $p = 1.3$ for gas curve while gray bounding curves represent outer limits of curves using exponents $p = 1.3 \pm 0.4$, $S_{wc,g} = 0$, $S_{gc} = 0$ which represents the range exhibited by the sample set, which had $0.1 \text{ md} < k_{ik} < 50 \text{ md}$.

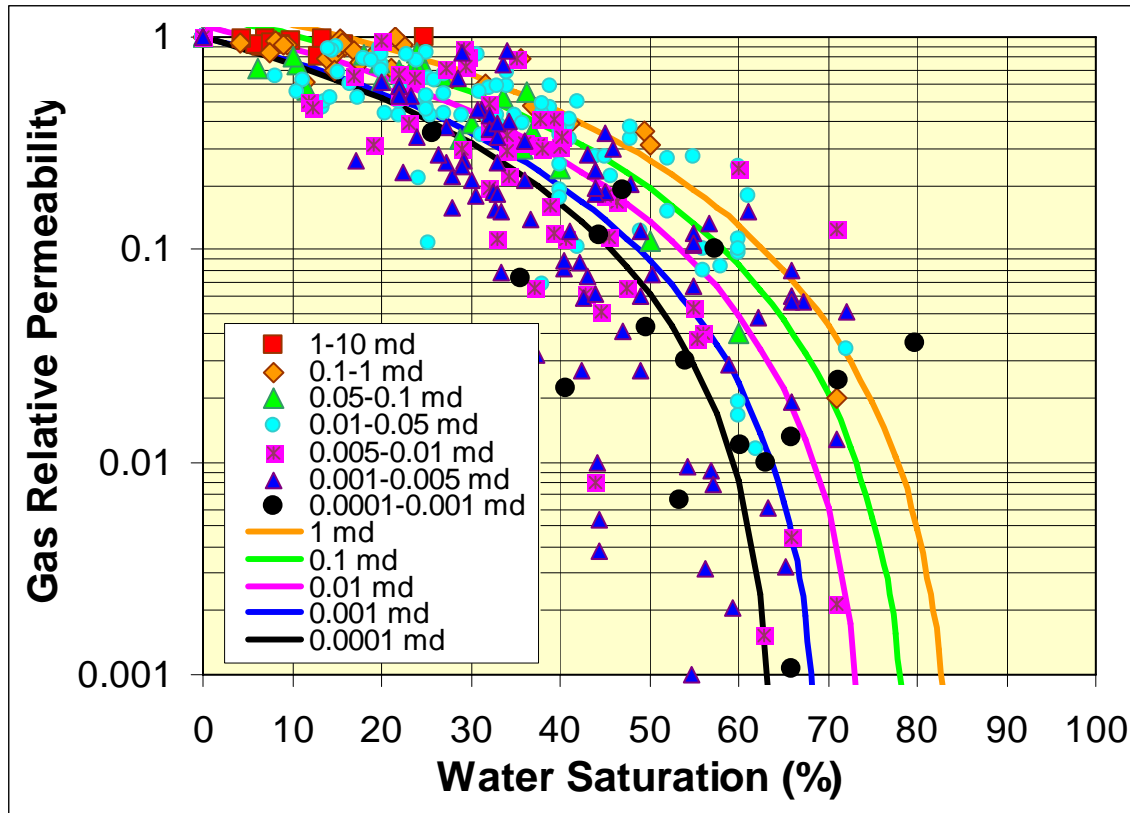


Figure 4.2.81. Gas relative permeabilities measured at single water saturations shown parametrically with sample k_{ik} . Curves show Corey-predicted $k_{rg,Sw}$ values for samples with $k_{ik}=0.0001$ md to $k_{ik}=1$ md using Equations 4.2.23-4.2.28 in text. Curves illustrate the abrupt decrease in relative permeability as water saturations increase above 50% and how critical gas saturation appears to increase with decreasing permeability (after Byrnes, 2003).

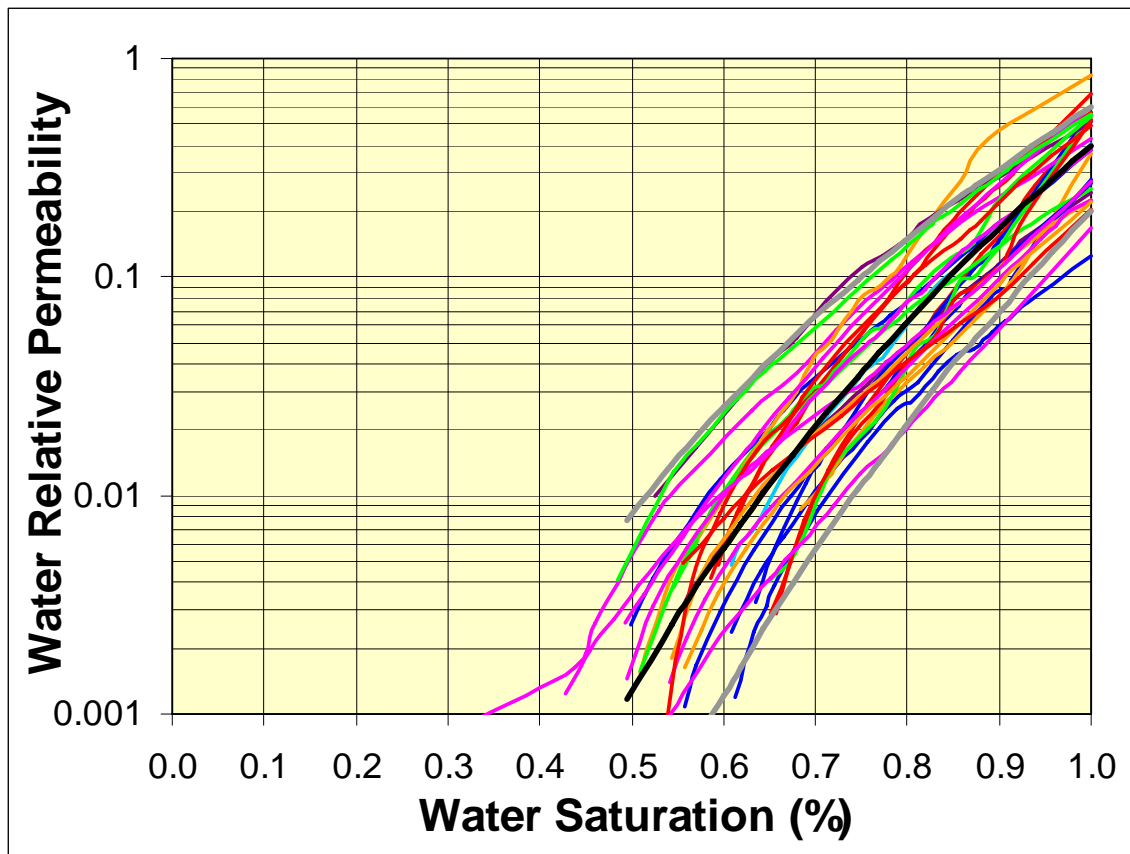


Figure 4.2.82. Drainage water relative permeability curves for 32 samples of various lithofacies. Black curves represent predicted values for the Corey-type equation model:

$$k_{rw} = ((S_w - S_{wc}) / (1 - S_{wc}))^q (k_w / k_{ik})$$

where S_{wc} is the critical water saturation and all saturation terms are in fractions. Black curves represent mean values of exponents $q = 8.3$ while gray bounding curves represent outer limits of curves using exponents $q = 8.3 \pm 3$ which represents the range exhibited by the sample set, which had $0.1 \text{ md} < k_{ik} < 50 \text{ md}$.

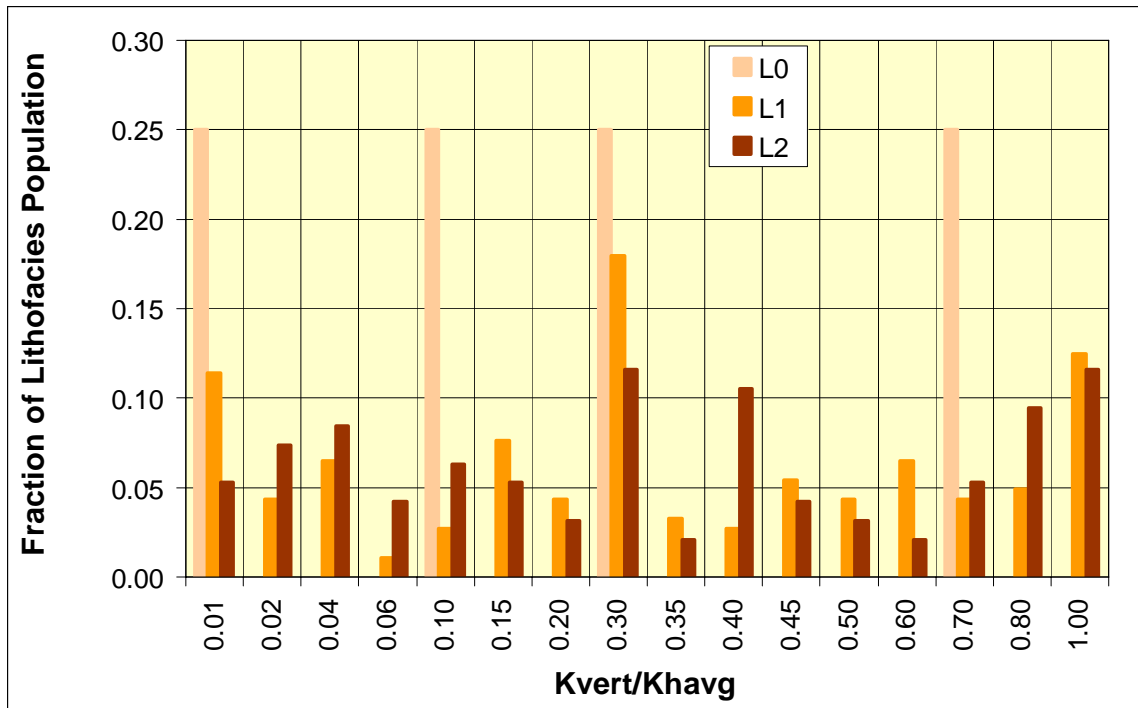


Figure 4.2.83. Frequency distribution of ratio of vertical/maximum horizontal full-diameter core permeability (K_{vert}/K_{max}) in the continental very fine sandstones and siltstones based on full-diameter core permeability data excluding fractured full-diameter cores and cores where $K_{max} > 5 * K_{90}$ (which might be fractured).

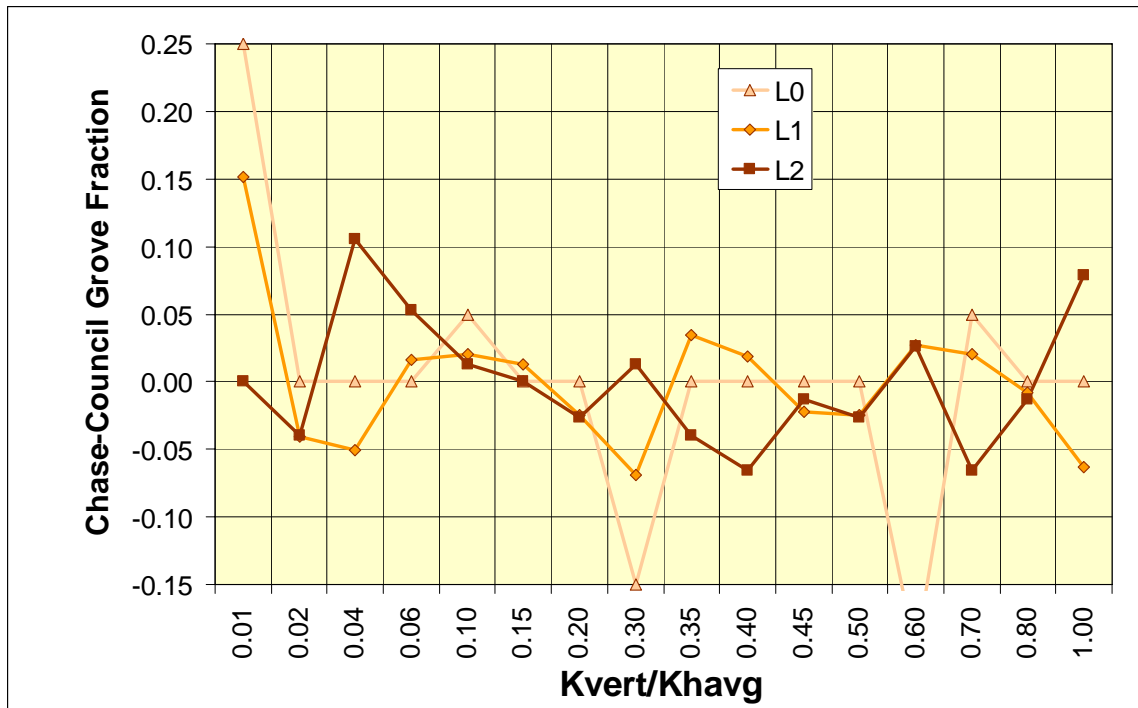


Figure 4.2.84. Difference between Chase and Council Grove fractions for each bin class of ratio K_{vert}/K_{max} for continental clastic facies. Zero indicates fraction of total populations for both groups are equal.

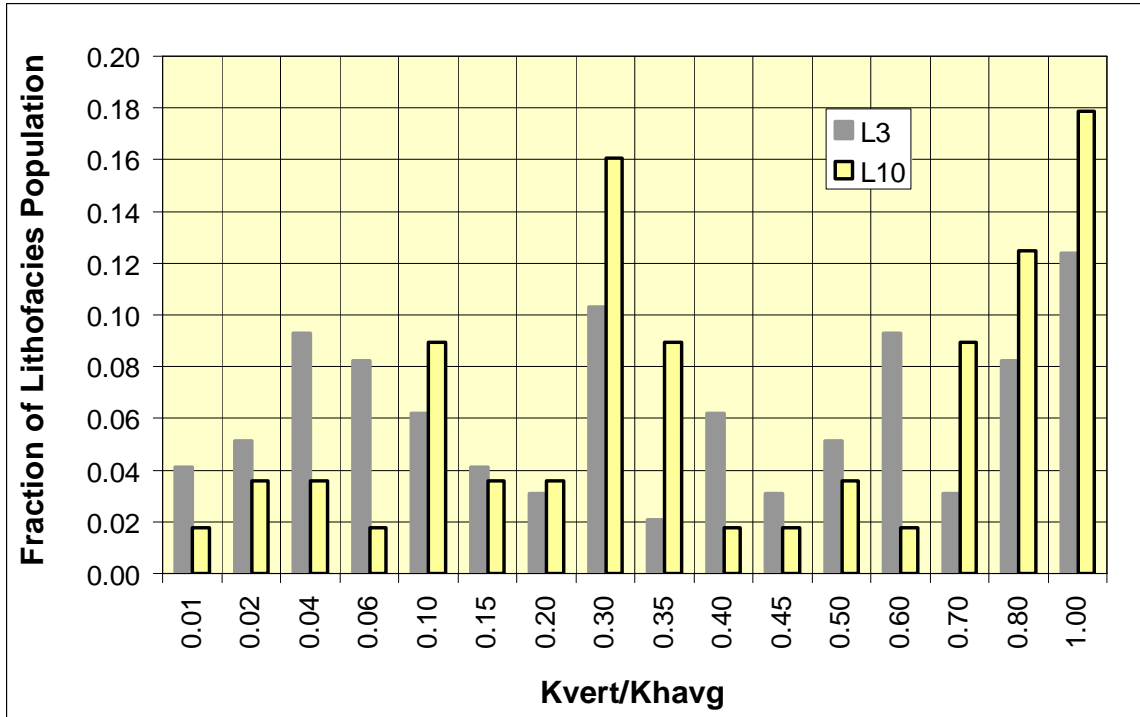


Figure 4.2.85. Frequency distribution of ratio of vertical/maximum horizontal full-diameter core permeability (K_{vert}/K_{max}) in the marine very fine sandstone (L10) and shale/siltstone (L3) lithofacies based on full-diameter core permeability data excluding fractured full-diameter cores and cores where $K_{max} > 5 \cdot K_{90}$ (which might be fractured).

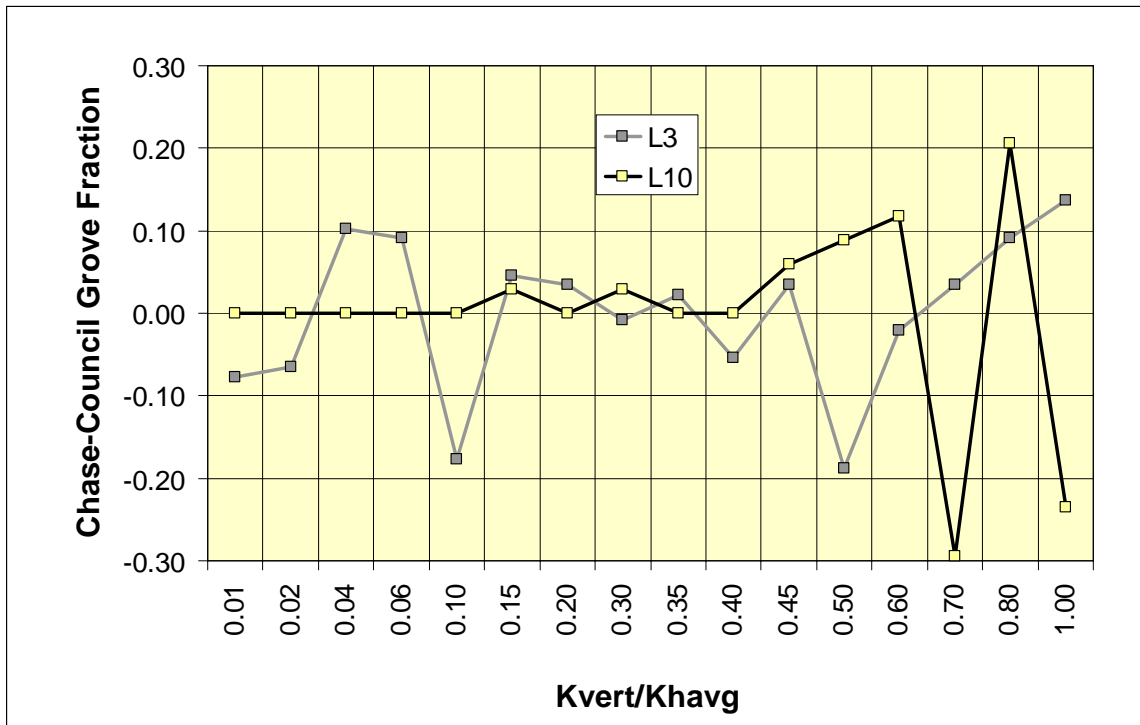


Figure 4.2.86. Difference between Chase and Council Grove fractions for each bin class of ratio K_{vert}/K_{max} for the marine very fine sandstone (L10) and shale/siltstone (L3) lithofacies. Zero indicates fraction of total populations for both groups are equal.

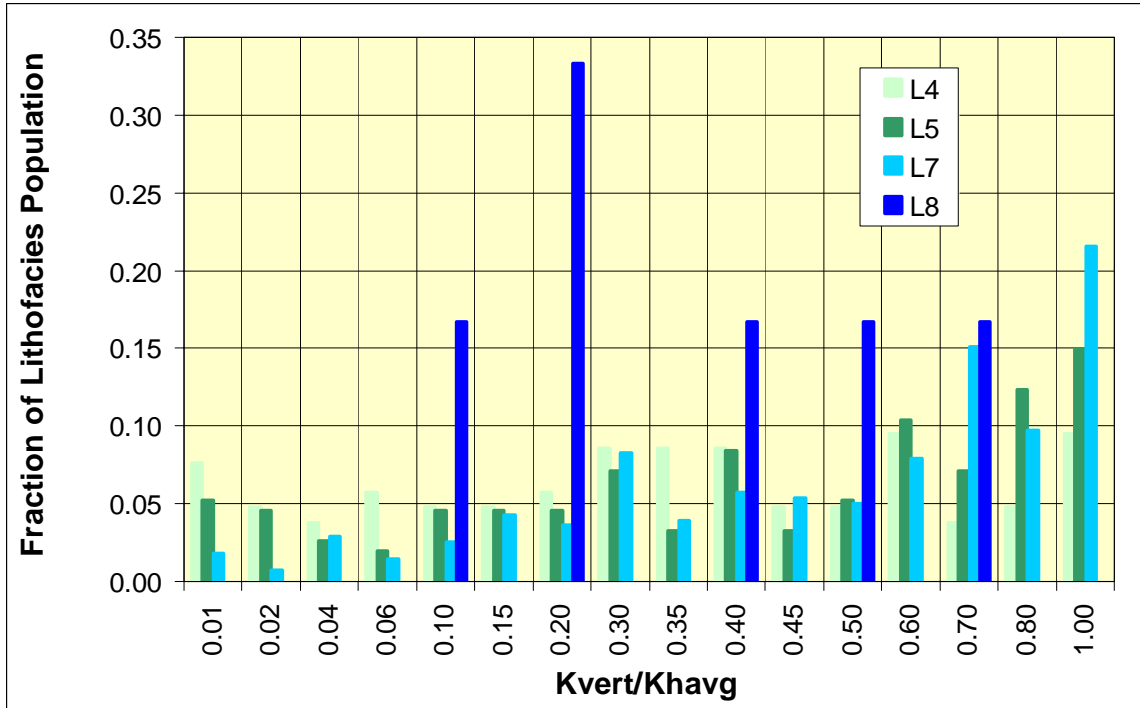


Figure 4.2.87. Frequency distribution of ratio of vertical/maximum horizontal full-diameter core permeability (K_{vert}/K_{max}) in the limestone lithofacies based on full-diameter core permeability data excluding fractured full-diameter cores and cores where $K_{max} > 5 \cdot K_{90}$ (which might be fractured).

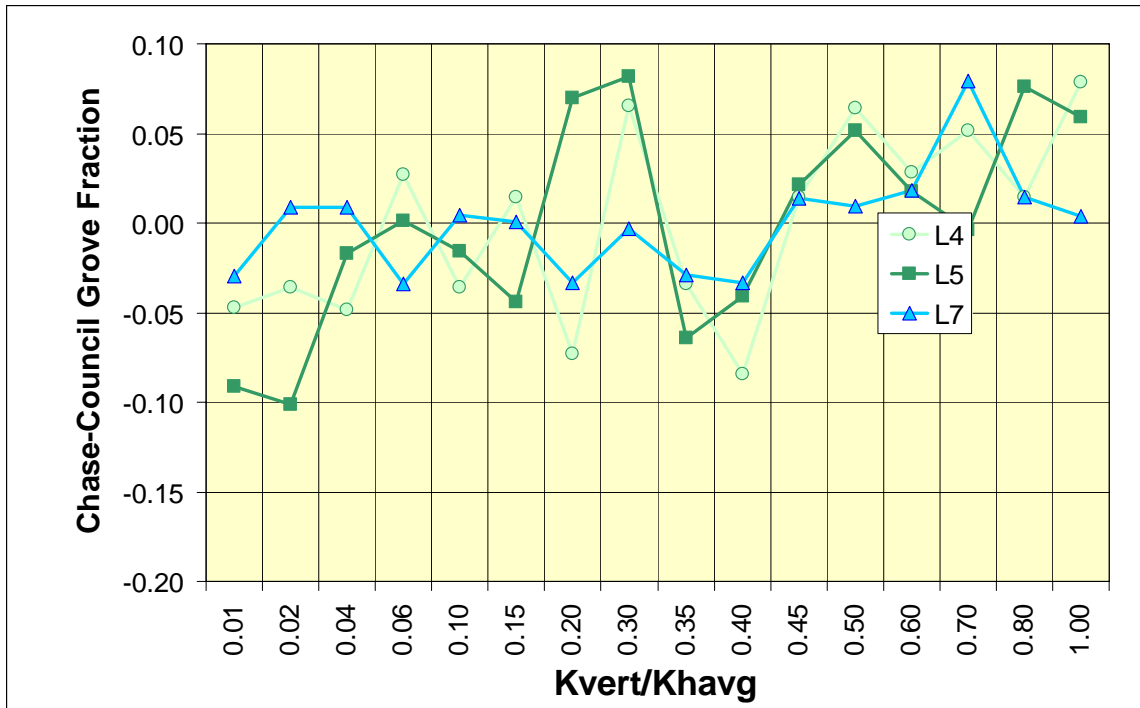


Figure 4.2.88. Difference between Chase and Council Grove fractions for each bin class of ratio K_{vert}/K_{max} for limestone lithofacies. Zero indicates fraction of total populations for both groups are equal.

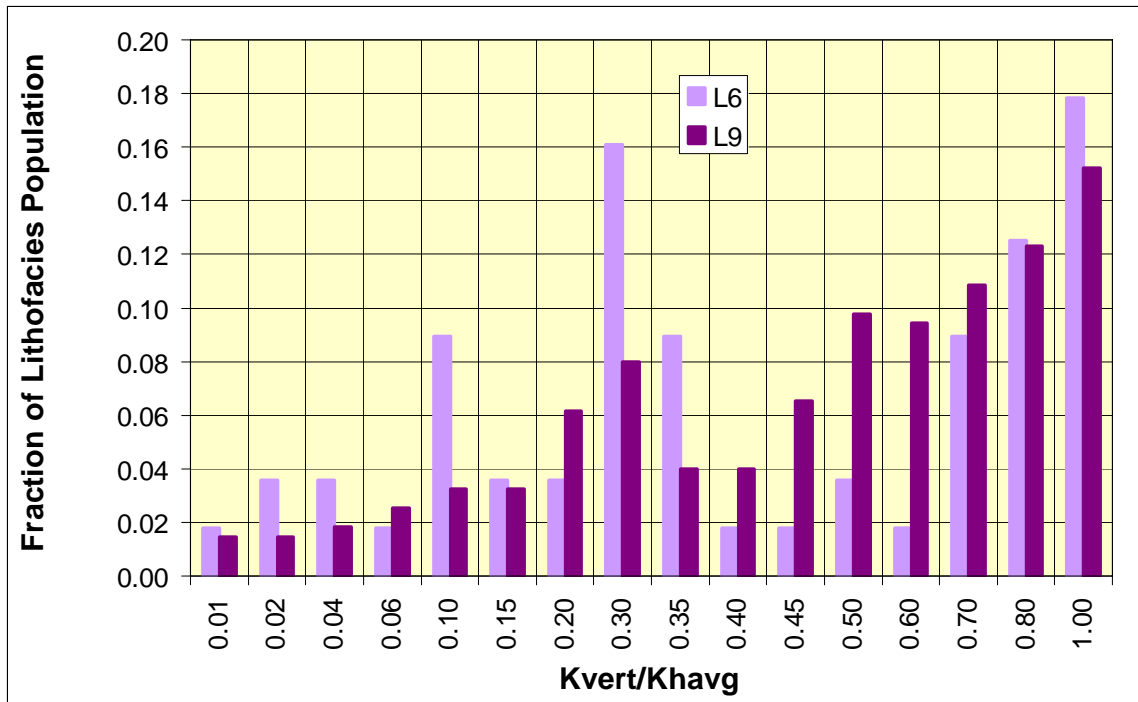


Figure 4.2.89. Frequency distribution of ratio of vertical/maximum horizontal full-diameter core permeability (K_{vert}/K_{max}) in the fine- and medium-crystalline sucrosic dolomite lithofacies based on full-diameter core permeability data excluding fractured full-diameter cores and cores where $K_{max} > 5 \cdot K_{90}$ (which might be fractured).

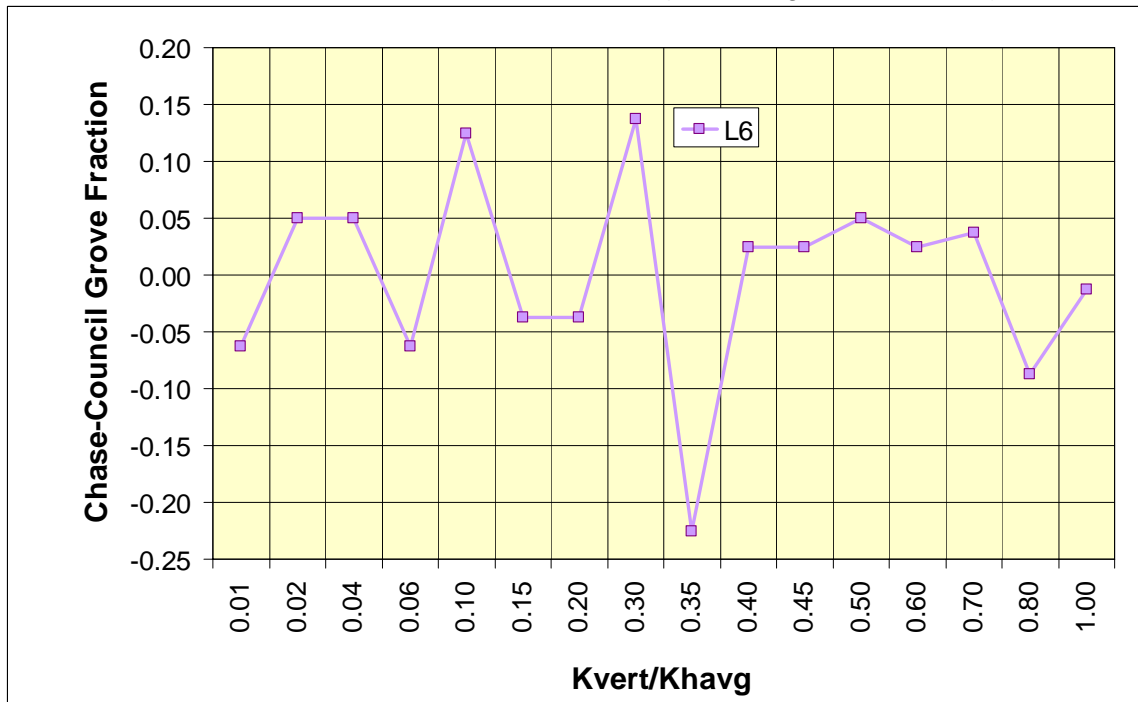


Figure 4.2.90. Difference between Chase and Council Grove fractions for each bin class of ratio K_{vert}/K_{max} for fine- and medium-crystalline sucrosic dolomite lithofacies. Zero indicates fraction of total populations for both groups are equal.

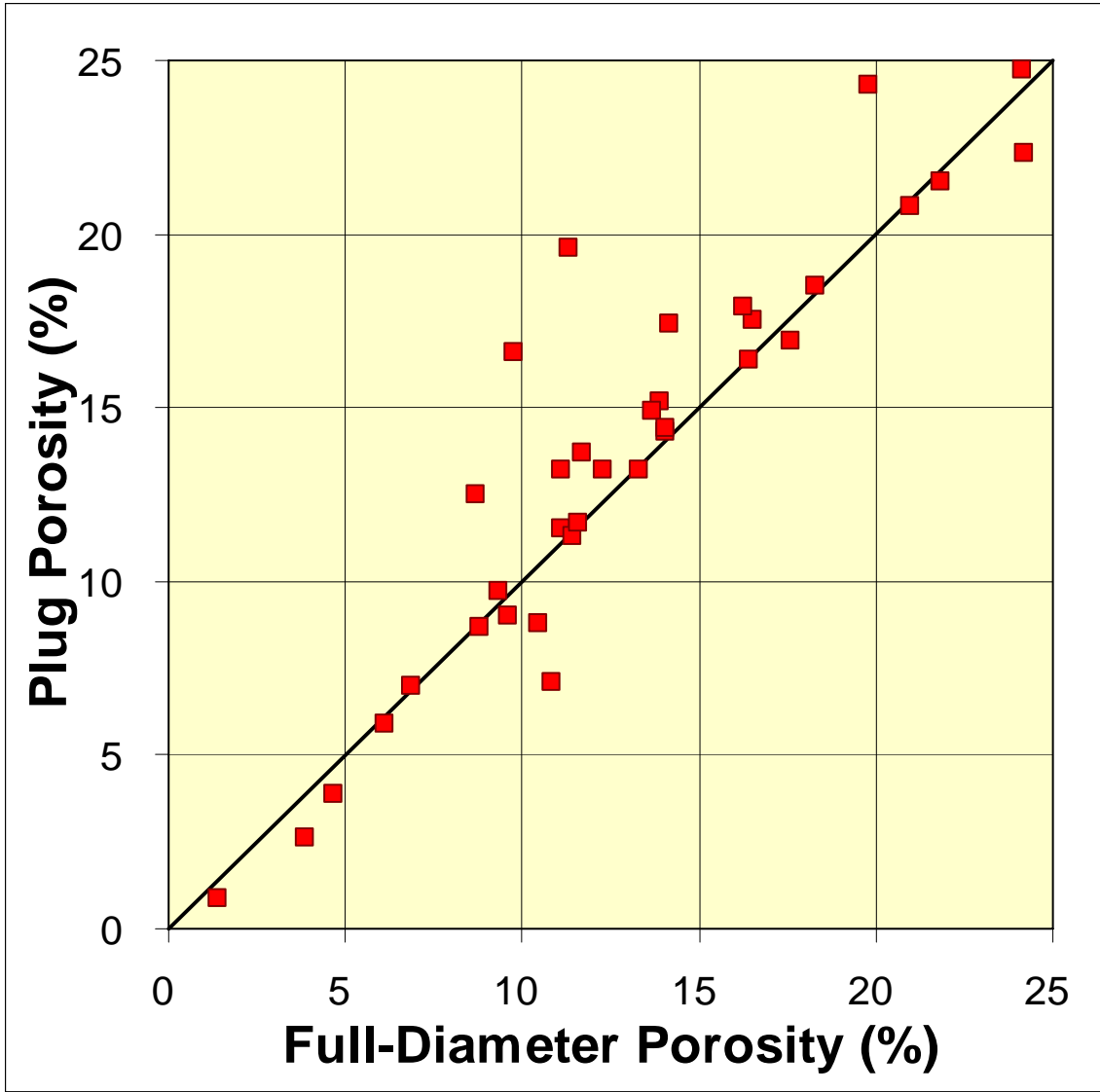


Figure 4.2.91. Crossplot of full-diameter core porosity versus plug porosity for Anadarko Flower A-1 well. Good correlation indicates that matrix-scale properties apply to full-diameter scale. Variance can be attributed to full-diameter core sampling multiple lithofacies or a range in porosity not sampled by the corresponding core plug.

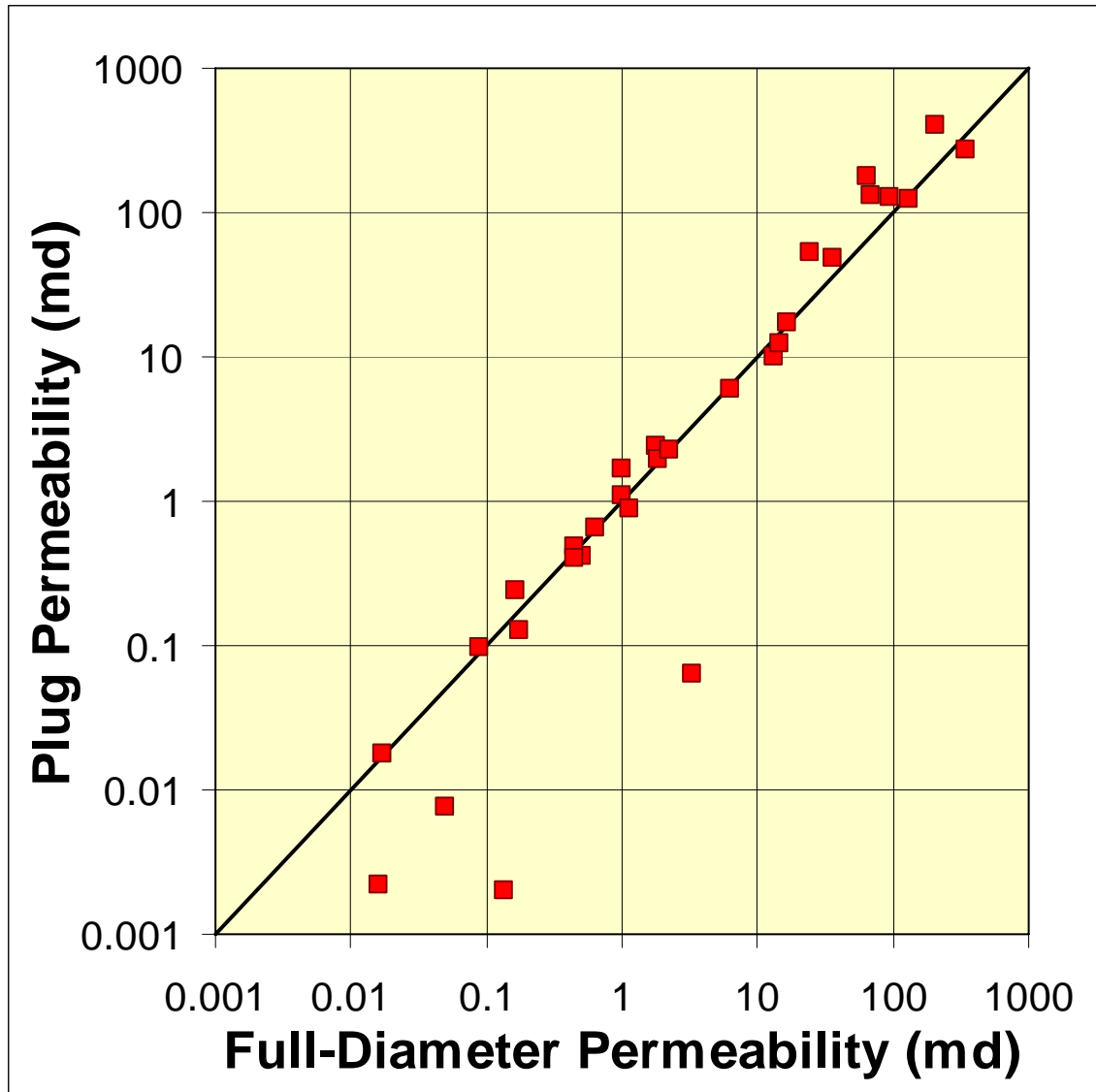


Figure 4.2.92. Crossplot of full-diameter core average horizontal permeability $((K_{max}+K_{90})/2)$ versus plug permeability for the Anadarko Flower A-1 well. Good correlation indicates that matrix-scale properties apply to full-diameter scale. Variance can be attributed to full-diameter core sampling multiple lithofacies or a range in porosity not sampled by the corresponding core plug.

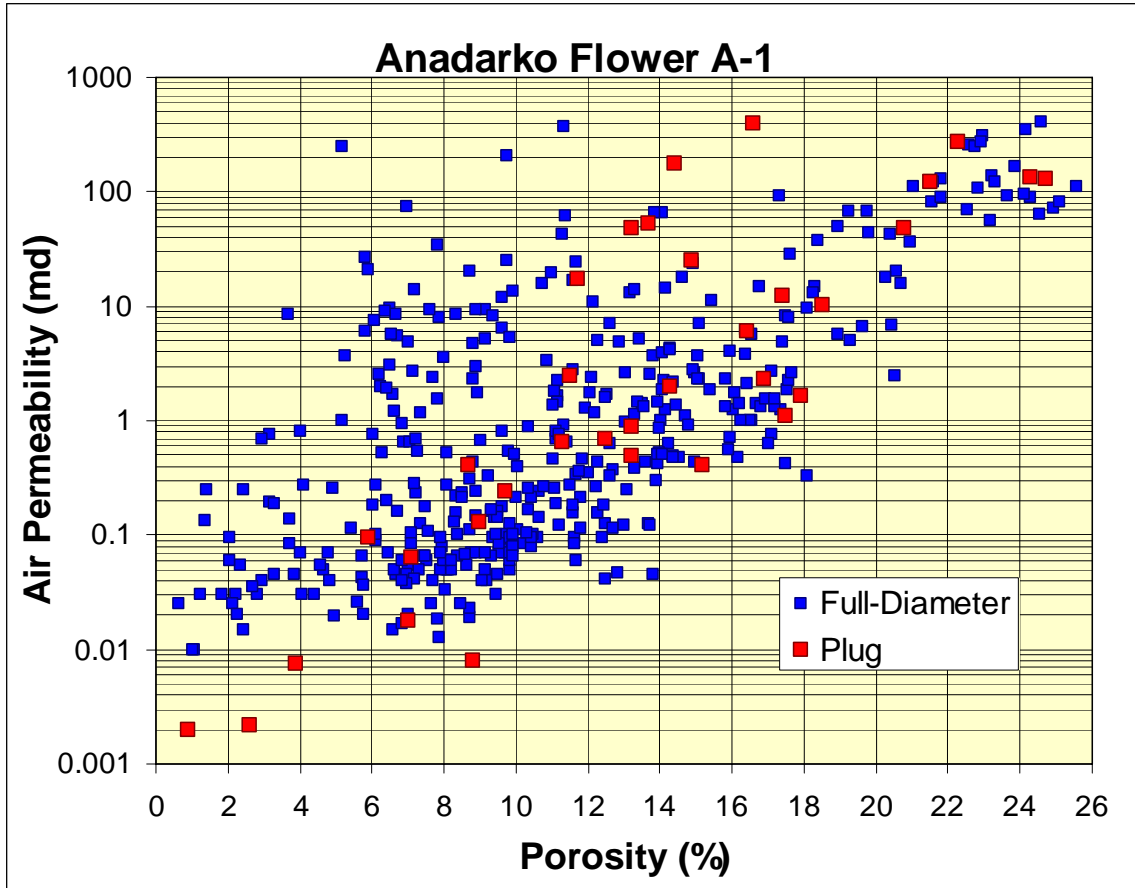


Figure 4.2.93. Comparison of full-diameter and core plug air permeability versus routine helium porosity correlation showing similarity of trends.

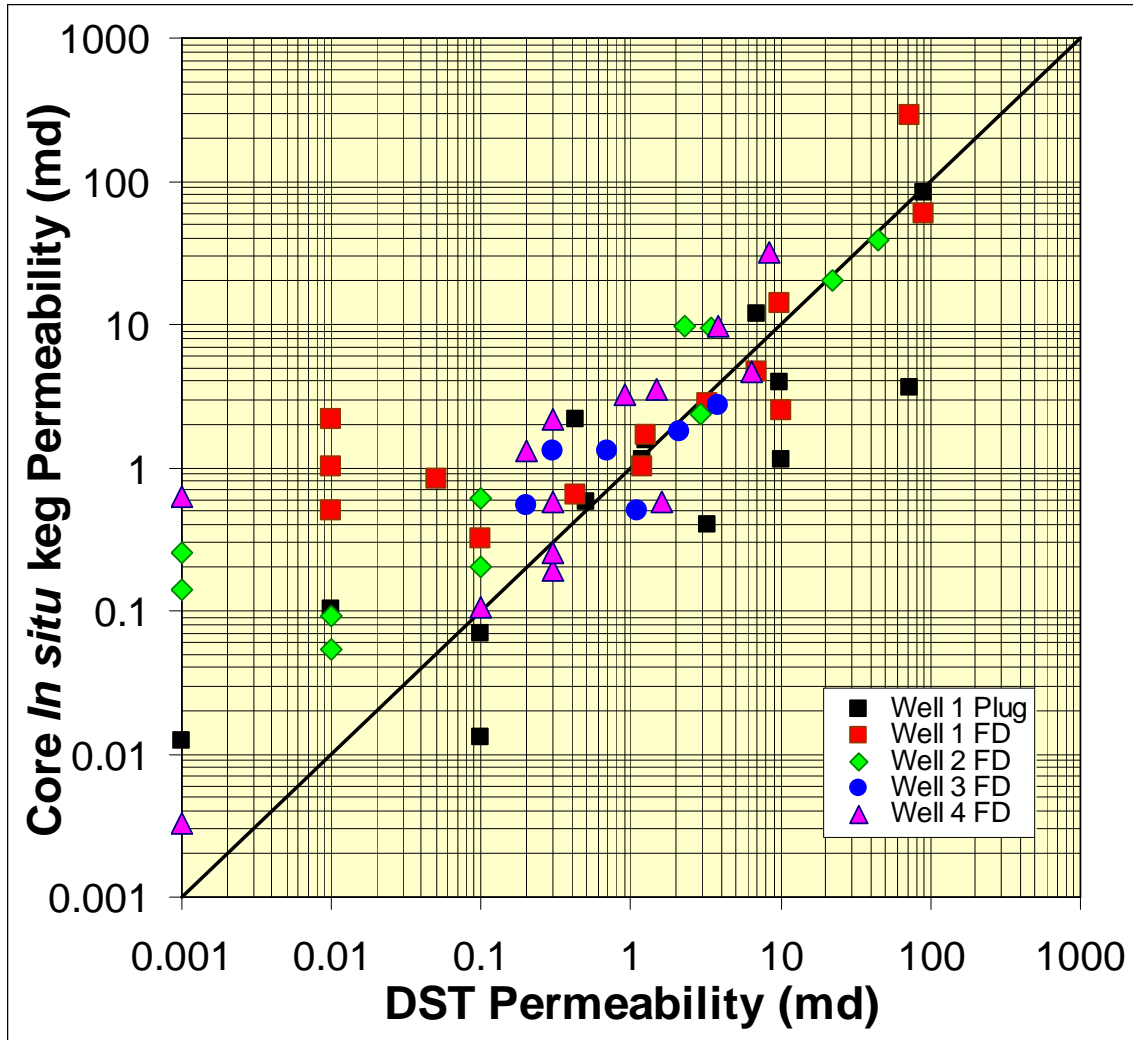


Figure 4.2.94. Crossplot of calculated interval drill stem test (DST) formation permeability versus average interval permeability calculated from full-diameter (FD) core for four wells and from core plugs in well 1. Routine core data were corrected for confining stress, Klinkenberg, and relative permeability effects so as to correspond to reservoir-condition values. Good correlation down to ~0.5 md shows matrix-scale control of flow in the region of DST investigation. Below 0.5 md microfractures in full-diameter core result in permeabilities higher than in the unfractured reservoir. Higher DST than core plug permeabilities can be interpreted to indicate that formation is not fractured in the range of investigation and that plug sampling density was probably not adequate to properly sample lower range of permeability.

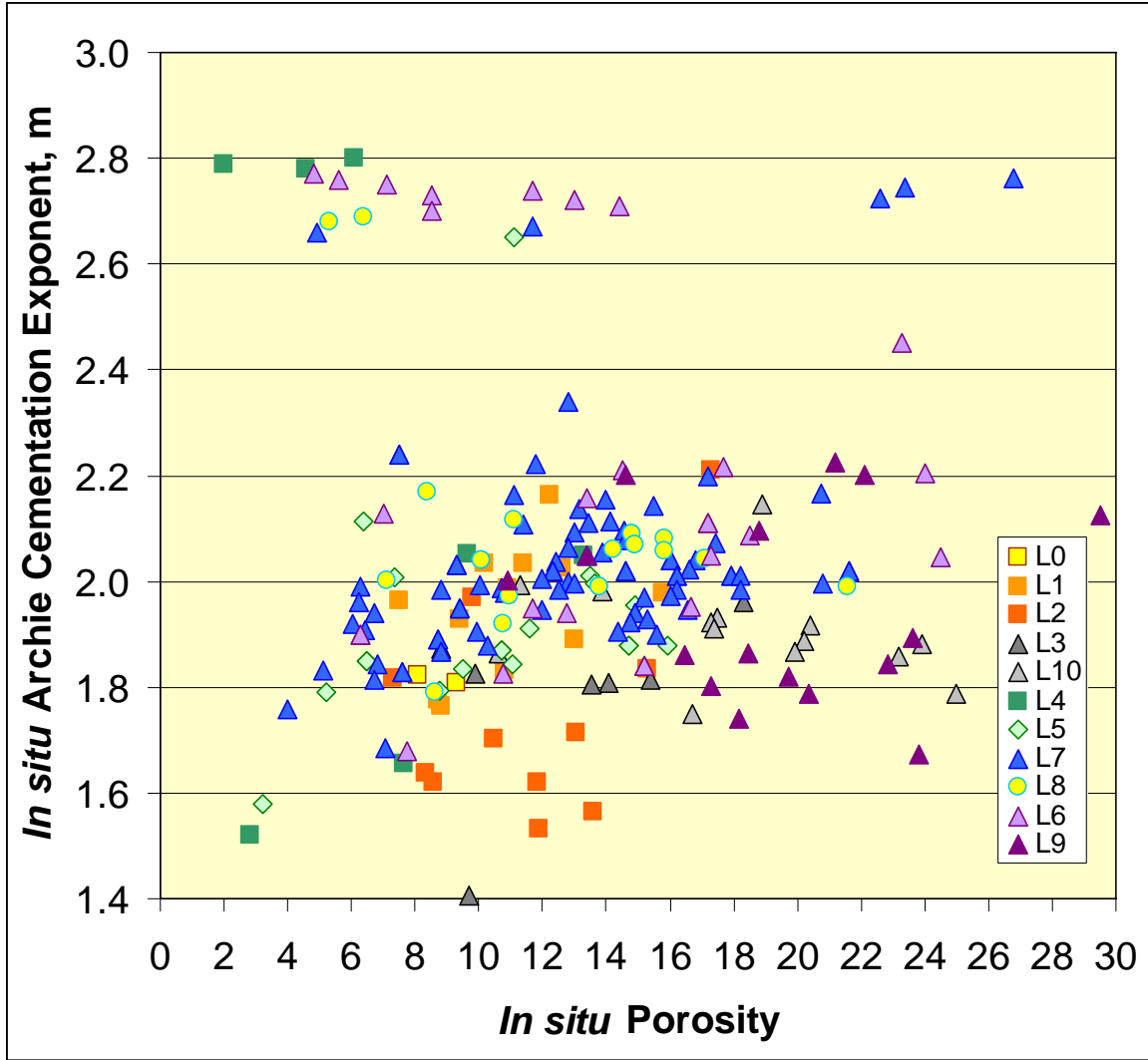
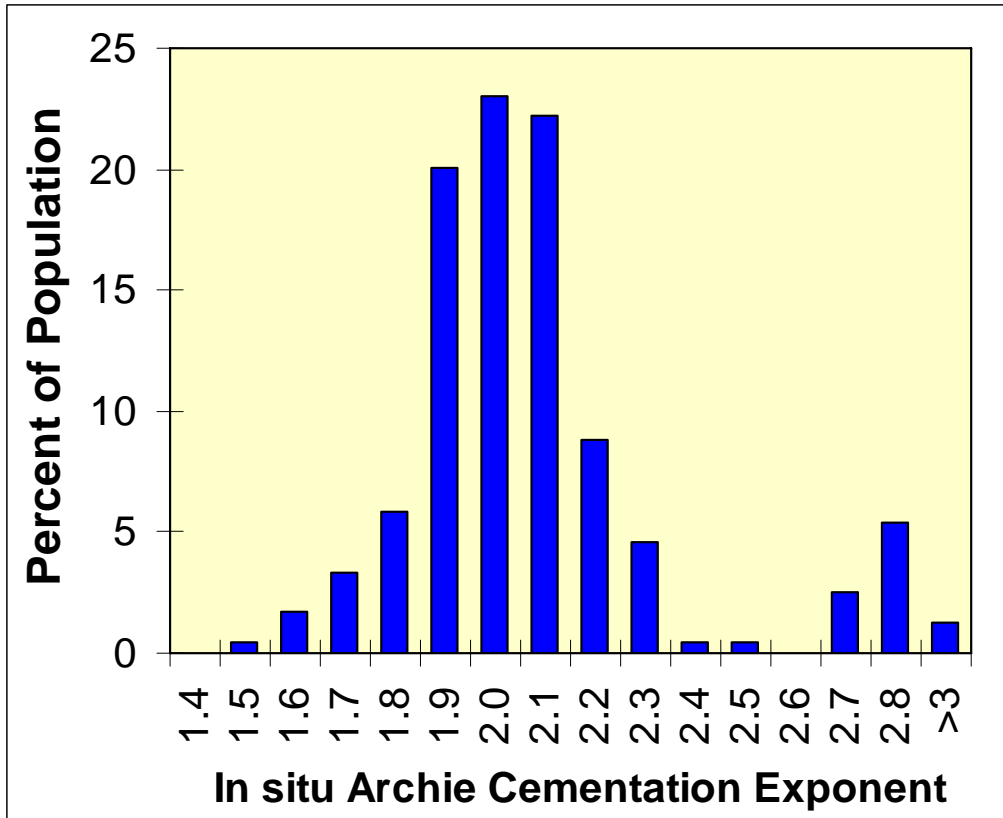
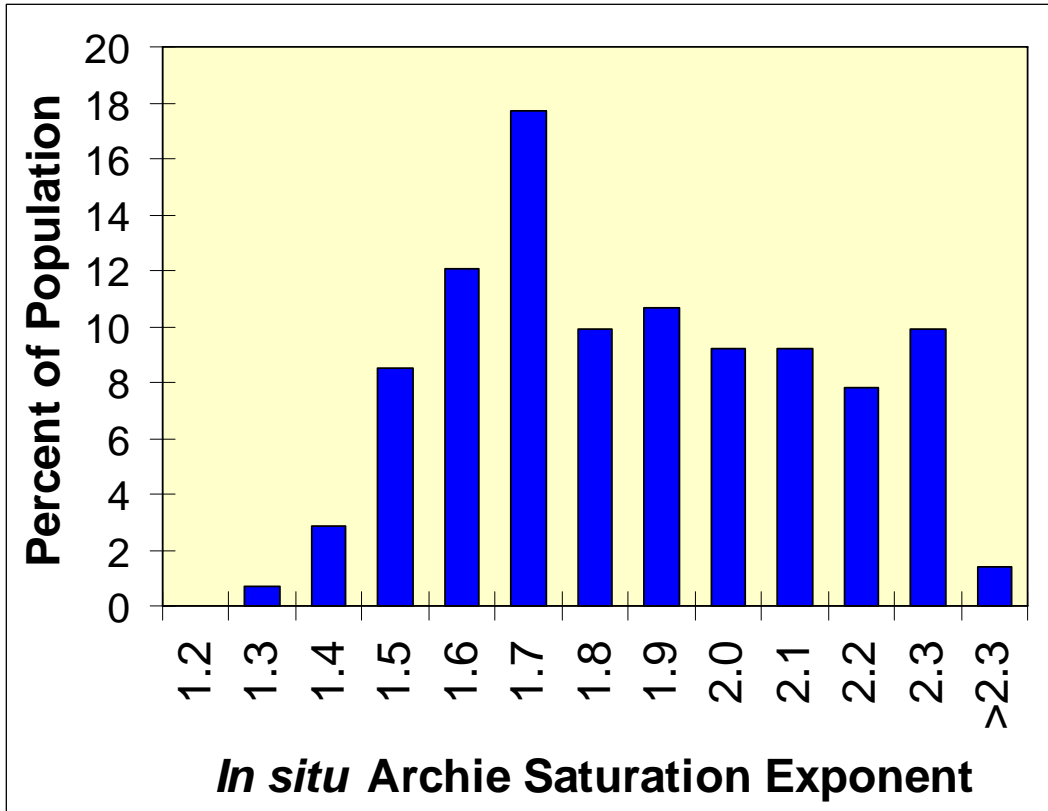


Figure 4.2.95. Crossplot of *in situ* Archie cementation exponent (*m*) versus *in situ* porosity for all lithofacies in Hugoton. Most lithofacies exhibit no correlation with porosity though lithofacies L7 (packstone/pack-grainstone) exhibits a slight decrease in *m* with decreasing porosity. Cementation exponent values greater than 2.6 represent samples with significant moldic porosity. Individual cementation exponent values assume the Archie intercept, *a*, is equal to 1.0.



Lithofacies Code	Lithofacies Description	Count <i>In situ</i> Archie Cementation Exponent (m, A=1)	Mean <i>In situ</i> Archie Cementation Exponent (m, A=1)	Standard Deviatoin <i>In situ</i> Archie Cementation Exponent (m, A=1)
0	NM Sandstone	2	1.82	0.01
1	NM Crs Siltstone	12	1.95	0.12
2	NM ShlySiltstone	11	1.75	0.20
3	Marine Siltstone	7	1.78	0.18
4	Mdst/Mdst-Wkst	4	1.82	0.27
5	Wkst/Wkst-Pkst	18	1.88	0.11
6	vf xln Sucrosic Dol	20	2.03	0.18
7	Pkst/Pkst-Grnst	79	2.00	0.11
8	Grnst/PA Baff	19	2.03	0.08
9	fn-med xln Dol	16	1.95	0.18
10	Marine Sandstone	14	1.91	0.09
	All	202	1.96	0.15

Figure 4.2.96. Frequency distribution of Archie cementation exponent values (upper) and summary statistics (lower) for all Hugoton Chase and Council Grove rocks showing a mean $m = 1.96 \pm 0.15$ (1 s.d.) for all rocks excluding the moldic porosity samples that exhibit $m > 2.6$.



Lithofacies Code	Lithofacies Description	Count <i>In situ</i> Archie Saturation Exponent (n)	Mean <i>In situ</i> Archie Saturation Exponent (n)	Standard Deviatoin <i>In situ</i> Archie Saturation Exponent (n)
0	NM Sandstone	2	1.68	0.18
1	NM Crs Siltstone	8	1.61	0.24
2	NM Shly Siltstone	0		
3	Marine Siltstone	2	1.69	0.16
4	Mdst/Mdst-Wkst	0		
5	Wkst/Wkst-Pkst	10	1.93	0.29
6	vf xln Sucrosic Dol	16	1.93	0.31
7	Pkst/Pkst-Grnst	61	1.80	0.31
8	Grnst/PA Baff	9	2.17	0.07
9	fn-med xln Dol	7	1.66	0.17
10	Marine Sandstone	11	1.66	0.12
	All	126	1.83	0.31

Figure 4.2.97. Frequency distribution of Archie saturation exponent values (upper) and summary statistics (lower) for all Hugoton Chase and Council Grove rocks showing a mean $m = 1.83 \pm 0.31$ (1 s.d.) for all rocks.

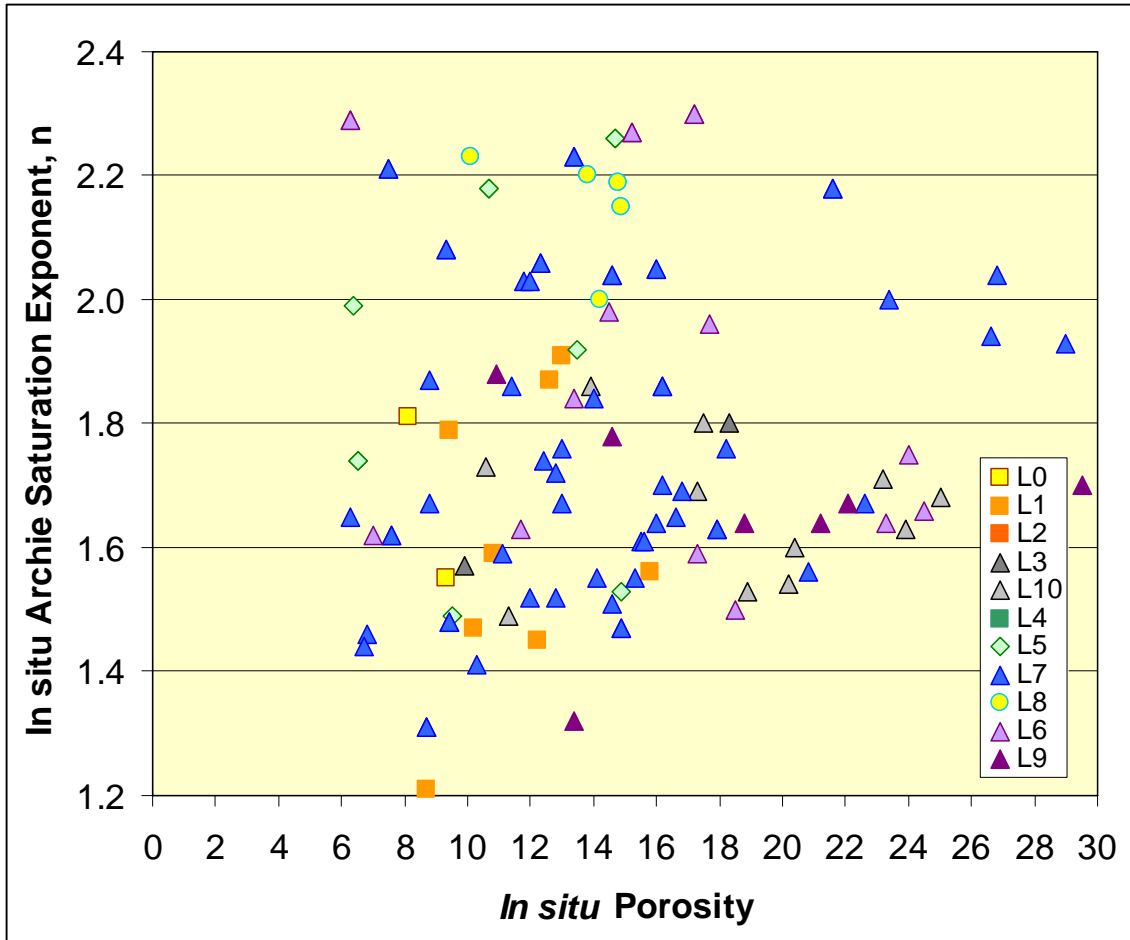


Figure 4.2.98. Crossplot of *in situ* Archie saturation exponent (*n*) versus *in situ* porosity for all lithofacies in Hugoton. All lithofacies exhibit no correlation with porosity.

4.3 WIRELINE-LOG PETROPHYSICS

John H. Doveton

Introduction

The log analysis of porosity and fluid saturations in the Hugoton field is complicated by a variety of formation properties in the Chase and Council Grove Groups and these are discussed below.

Uranium mineralization of carbonate units

Significant contents of uranium occur locally in dolomitized formations and can be misidentified as shales or shaly carbonates when using standard gamma-ray logs. This problem has been widely recognized and it has been common industry practice to run spectral gamma-ray logs, so that shaly material (associated with potassium and thorium content) can be discriminated from uranium mineralization. Luczaj and Goldstein (2000) concluded from fluid-inclusion studies and U-Pb chronology that the uranium was emplaced as one of several diagenetic events of dolomitization in the Late Permian. Within the HAMP project, the correct identification of radioactive carbonates has been accommodated by a neural network procedure that applies multiple log responses calibrated to core lithofacies.

Deep invasion by drilling fluids

Low pressures in the Chase and Council Grove Groups in the Hugoton field cause deep invasion of these units when drilled with a conventional mud program. The magnitude of the invasion is such as to adversely affect deep resistivity measurements, so that water saturations can be significantly overestimated. Comparison of resistivity logs in closely neighboring wells, one drilled with foam and the other with mud, has provided a systematic demonstration of invasion effects as reported by George et al. (2004). Because mud programs are almost universally used in drilling throughout the field, conventional Archie equation estimates of water saturation are considered unreliable and have been replaced in the HAMP project by saturations estimated from a capillary pressure model.

Variability in lithology

The Chase and Council Grove Groups consist of interbedded carbonates, clastics, and evaporites so that calculations of porosity from wireline logs must accommodate frequent changes in matrix properties with depth. The HAMP project subdivision of the groups into distinctive lithofacies enabled porosity calibration of logs from core to be established as facies-specific functions for porosity prediction.

Gas effects

The presence of gas close to the borehole wall causes major effects on both the density and neutron logs, which are scaled with water (matched with mud-filtrate in the flushed zone) as the reference pore fluid. Predictive equations were developed to incorporate this effect as a regression analysis rooted in a petrophysical model of the gas-water-mineral system.

Washouts

The erosion of thin, friable layers in the drilling operation results in loss of contact of the neutron and density pads with the borehole wall and deleterious effects on the log measurement of porosity with the recording of excessively high values. Many of these washouts were discriminated and removed by the application of a maximum cut-off for the caliper measurement of hole diameter. The remainder were recognized by their localized anomalously high values and eliminated using porosity cut-offs of 20 to 22.5%. Removal of washout zones from the calibration phase excluded highly deviant outliers from the analysis; the prediction of porosities in washout zones was equated with the average porosity for the predicted assigned to the interval. The procedure was found to be effective in removing washout effects and was executed as an automated process with some limited manual intervention to preserve intervals with high, but real, porosities such as occur in coarsely crystalline dolomites (L9). Following environmental correction, the calculation of porosities from logs can then be developed as a reliable procedure, particularly when validated through the use of porosities from the extensive core database as the calibration standard.

Prediction of porosity from logs calibrated to core

The HAMP project subdivided the Chase and Council Grove into lithofacies identified from observation of core. The matrix properties that regulate the transform of porosity log response to pore volume are determined by mineral composition rather than textural and other aspects of facies. Consequently, the porosity calibration sets for carbonates were grouped into limestones (L5, L7, and L8) and dolomites (L6 and L9). However, clastic facies (L1-4, L10-11) were analyzed separately to allow for the influence of possible differences in accessory minerals associated with their depositional environments. For each calibration, a prediction of porosity was made from regression analysis applied to a petrophysical equation using density and neutron logs scaled to the common standard of equivalent limestone porosity units. Prior to each analysis, lithologies that were mis-assigned to their lithofacies (such as a limestone within a dolomite lithofacies) were removed by applying appropriate cutoff criteria from the core grain-density and the log photoelectric factor. Subsequent to the regression analysis, extreme outliers were removed through the application of Chauvenet's criterion, and recomputation of the regression function.

In the first phase of analysis, a fundamental distinction was found between the clastic and carbonate facies. Functions that utilized the density log alone proved to be the best

predictors within clastic facies. The neutron log appeared to be adversely and erratically affected by clay minerals within the fine fractions. The similarity of clay mineral densities with that of quartz results in a calibrated density log as a reasonably robust estimator of effective porosity. The result contrasted with carbonate facies where predictions of porosity were more closely matched by a weighted function of the density and neutron logs to accommodate both changes in mineralogy and gas effects.

Calibrated density log predictions of porosity in nonmarine siltstones (L1 and L2) and marine siltstones (L3 and L4) showed strong commonality within environment and differentiation between environments (Figure 4.3.1). As a result, the data for the nonmarine siltstones were pooled in a single function:

$$\phi = 1.78 + 0.84 \phi_d \quad (4.3.1)$$

and marine siltstones by the function:

$$\phi = 1.85 + 0.66 \phi_d \quad (4.3.2)$$

where the predicted porosity and density log porosity are in percentage units. Independent regression analysis of nonmarine sandstone data (lithofacies 11) gave the prediction function:

$$\phi = 1.32 + 0.84 \phi_d \quad (4.3.3)$$

and for marine sandstone (lithofacies 10):

$$\phi = 6.37 + 0.56 \phi_d \quad (4.3.4)$$

In all cases, the density porosity is calibrated in equivalent limestone porosity units. The distinctive offset between the marine and nonmarine functions can be attributed to the slightly higher grain densities measured in core samples from the nonmarine facies.

Although gas effects are minor in the Council Grove and compensated by the averaging of neutron and density porosities, they can be significant in the Chase Group (see Figure 4.3.2) and must be accommodated in an expanded equation set. The equation commonly applied to estimate the porosity with a compensation for gas takes the form:

$$\phi = \sqrt{\frac{(\phi_n^2 + \phi_d^2)}{2}} \quad (4.3.5)$$

The equation closely approximates the formula derived by Gaymard and Poupon (1968) from a petrophysical model of a gas-filled reservoir. An alternative and empirical equation that is also widely used is a simple weighted average of the neutron and density porosities with a weighting of one-third applied to the neutron porosity and a two-thirds weighting of the density porosity (Asquith and Krygowski, 2004). This empirical

equation closely emulates the gas correction shown on service company neutron-density crossplots (Figure 4.3.3). A regression analysis of core porosities related to neutron and density fractional log porosities resulted in an equation of the form:

$$\phi = 0.62 \phi_d + 0.39 \phi_n \text{ for limestones (L5, L7, and L8)} \quad (4.3.6)$$

$$\phi = 4.75 + 0.58 \phi_d + 0.26 \phi_n \text{ for dolomites (L6 and L9)} \quad (4.3.7)$$

The extra term in the dolomite equation accommodates the lithology correction required for logs calibrated to a limestone matrix.

The application and validation of statistical and petrophysical concepts to porosity estimation is an important factor in reserve calculations. As always, accuracy is a major concern but special attention must be paid to potential bias introduced by gas effects and lithology variation whose cumulative effects can result in significant underestimation or overestimation of total hydrocarbons in place.

References

Asquith, G., and Krygowski., D., 2004, Basic Well Log Analysis (2nd Edition), American Association of Petroleum Geologists, Tulsa, 244 p.

Gaymard, R., and Poupon, A., 1968, Response of neutron and formation density logs in hydrocarbon bearing formations : The Log Analyst, v. IX, no. 5, p. 3 - 12.

George, B.K., Torres-Verdin, C., Delshad, M., Sigal, R., Zouioueche, R., and Anderson, B., 2004, Assessment of in-situ hydrocarbon saturation in the presence of deep invasion and highly saline connate water: Petrophysics, v. 45, no. 2, p. 141-156.

Luczaj, J.A., and Goldstein, R.B., 2000, Diagenesis of the Lower Permian Krider Member, southwest Kansas, U.S.A.: Fluid-inclusion, U-Pb, and fission-track evidence for reflux dolomitization during latest Permian time: Journal of Sedimentary Research, v. 70, no. 3, p. 762-773.

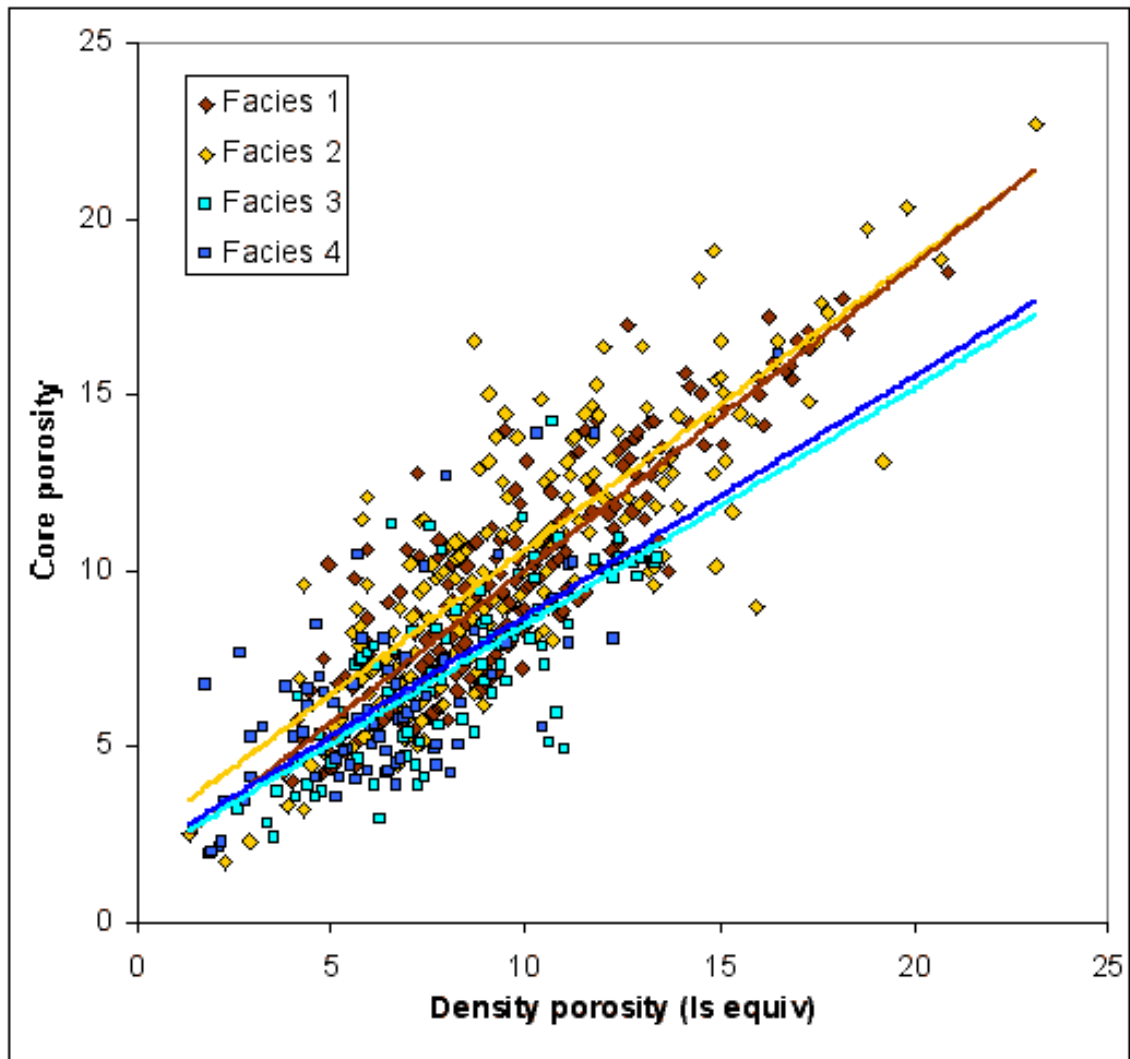


Figure 4.3.1. Porosity calibration of siliciclastic zones based on regression of core measurements on density log porosity in limestone-equivalent units for continental facies (L1 and L2) and marine facies (L3 and L4).

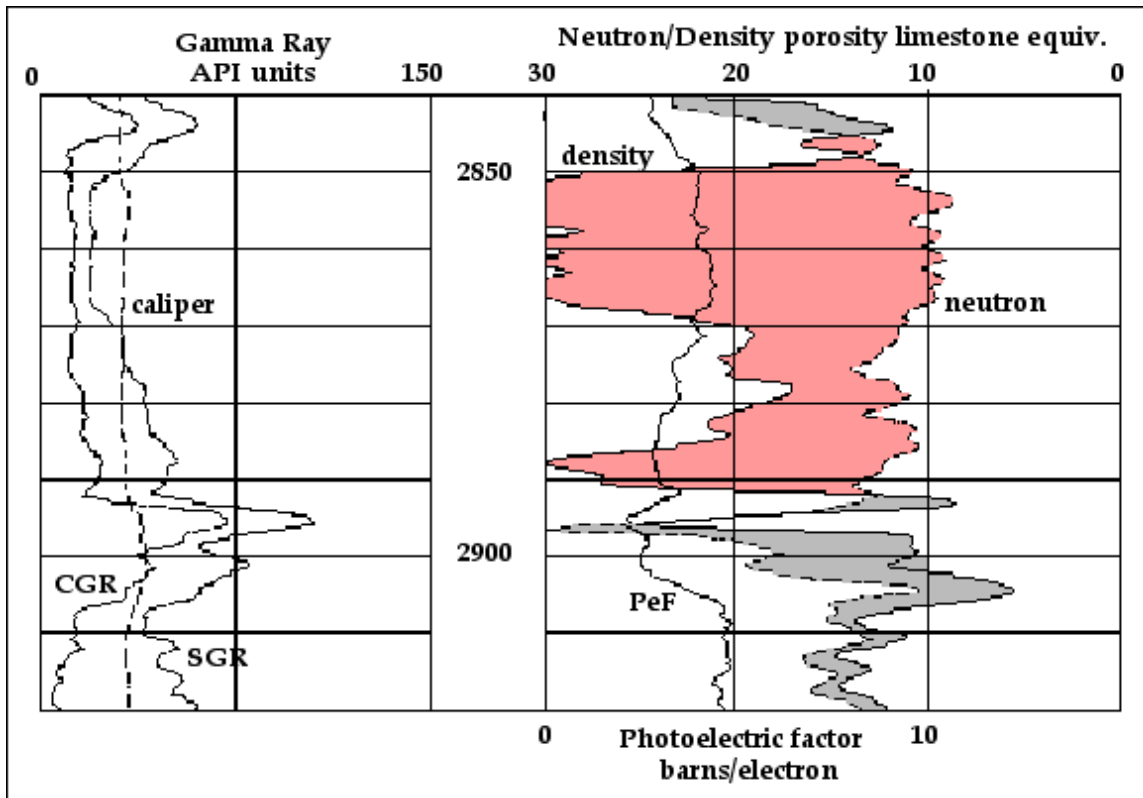


Figure 4.3.2. Example of strong (and atypical) gas effect on the neutron and density porosity logs in the Towanda Limestone Member of a well in Stevens County, Kansas.

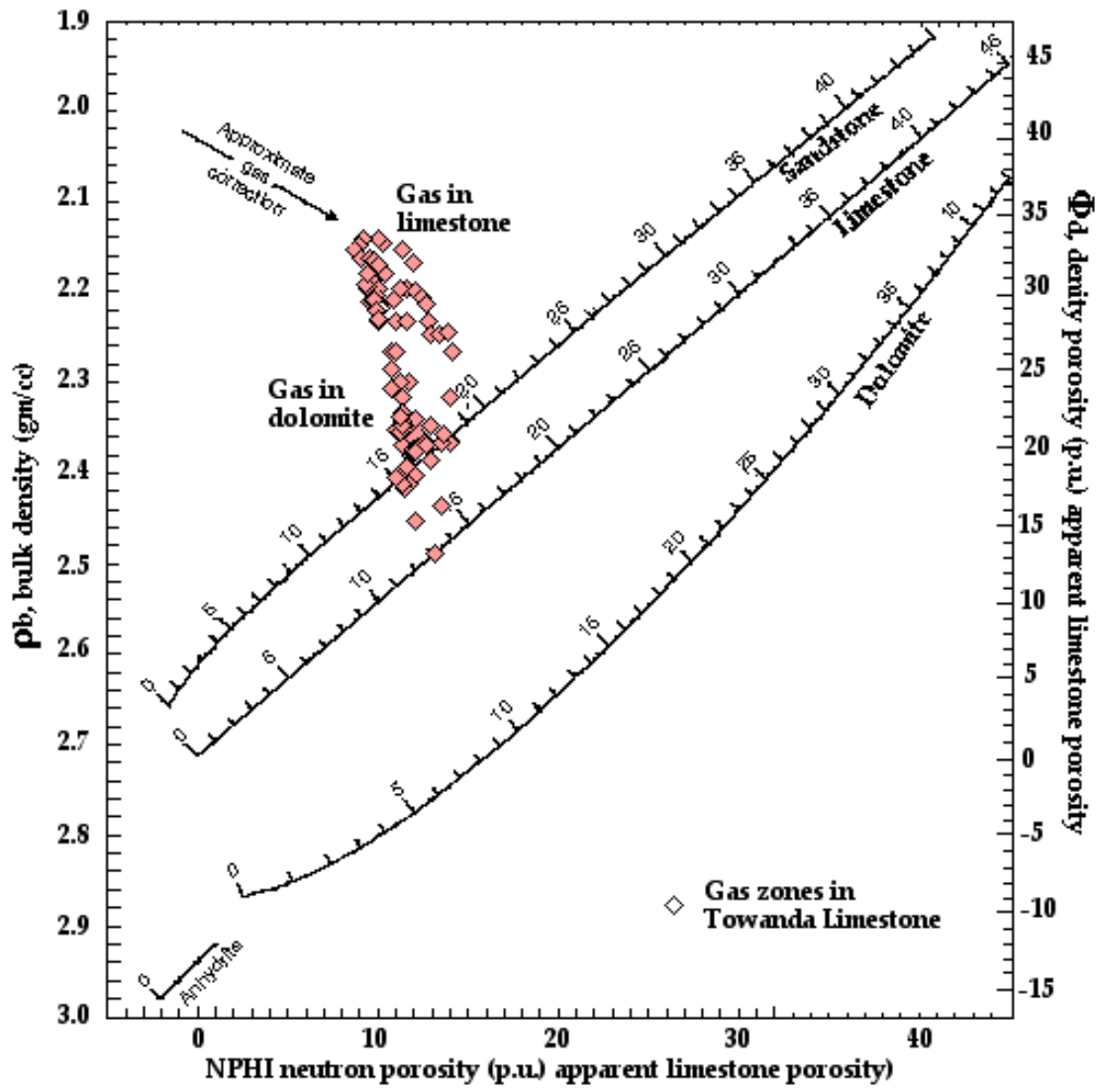


Figure 4.3.3. Neutron- density porosity log crossplot of gas zones in the Towanda Limestone Member from the example Stevens County well (see Figure 4.3.2).